Full 3D Blood Velocity Mapping and Flow Quantification from Doppler Echocardiographic Images

Gomez, Alberto

Awarding institution:
King's College London

Division of Imaging Sciences and

Biomedical Engineering

School of Medicine

KING'S College LONDON

Full 3D Blood Velocity Mapping and Flow Quantification from Doppler Echocardiographic Images

by Alberto Gómez

A thesis submitted in partial fulfilment of the requirements for the degree of Doctor of Philosophy of the University of London

June 2013

Supervisors:

Dr. Graeme Penney

Prof. Tobias Schaeffter

Examiners:

Dr. Vicente Grau

Dr. Jeffrey Bamber

Abstract

This thesis contributes to knowledge by describing two novel methods to calculate 3D blood velocity and flow within the heart using 3D colour Doppler images. The principal goal of both methods was to overcome the main limitation of Doppler systems which is that the Doppler effect only measures one component of the velocity (parallel to the beam direction). For that reason, measured velocity and calculated flow depend on the angle between the beam direction and the flow.

The first method was developed to reconstruct 3D intracardiac velocity vector fields. This is the first time that such vector fields have been obtained from 3D colour Doppler images. The novelty of the proposal lies not only in the 3D velocity reconstruction, but also 1) a new noise model for colour Doppler images was proposed which improves the realism of simulation studies, 2) an efficient patch-wise implementation was introduced and 3) ventricle wall motion was used to enable full ventricular coverage. Based on simulations minimum acquisition requirements for accurate reconstruction were established. These requirements were: view angles over 20 degrees and noise below 10% of the Doppler maximum velocity. The method was tested on healthy volunteers and on paediatric patients and an accuracy of 15% compared to flow Magnetic Resonance Imaging (MRI) was obtained, when acquisition and data conditions were close to the optimum range.

The second method proposes an algorithm to calculate angle-independent flow rates through surfaces within the heart and vessels. Built on the Gauss's theorem, this method enables to increase coverage beyond the Field of View (FoV) of individual colour Doppler images by combining images acquired from multiple views. The method was validated in patients with Hypoplastic Left Heart Syndrome. Results were compared with the current clinical gold standard measurement of flow MRI, agreeing on flow values and volumes to less than 10%.

The novel methods proposed in this thesis have shown encouraging results using volunteer and patient data. I hope that the methods proposed will in the future be able to offer advanced flow measurements using echo. The ability to improve the information available from echo imaging, due to its ease of use and cost effective nature, has the potential for widespread improvements in clinical care.

To my family: Paloma, Ángel, Samuel, Pablo and Daniela.

Acknowledgement

First of all, I would like to thank my supervisors Graeme and Tobias for their guidance and support. It is very hard to express in just a few words all Graeme has done for me. He has been a permanent source of encouragement, motivation and advice; I guess what I appreciate most is that he has trusted my judgement and has given me the freedom to develop my own ideas. Tobias was my first contact with KCL, and he gave me the chance to come to London when I was only a Masters intern in Hamburg, for what I am deeply grateful. I would also like to thank Reza Razavi for the trust he placed in me.

In my time in the Department of Biomedical Engineering, I have been lucky enough to meet a good number of great people to share research pain and glories with. I want to thank Chris Burguer, my KCL *buddy* and excellent pub-mentor and squash instructor; Markus (O')Henningsson, eternal squash rival and official cider boy; Daniel Giese, my cycle mate, who taught me all I know about 4D flow MRI and much more; Nico Toussaint, colleague, flatmate and friend, always there to give a hand with C++; and Tobias Voigt, the best German "tandem" I never had. I would like to thank Cheng Yao, Shahrum Gilani and Devis Peresutti for their help with echo image registration and processing, and Nick Gaddum and Rachel Clough for the help with the pulsatile flow phantom. I would also like to thank Andreas, Jen, Christoph, Ghislain, Harry, Maite, Catalina, Radek, Jack and Andy for the nice moments and fruitful discussions over the past three years.

I'd like to thank Alberto Figueroa for his advice, in general, and his help particularly on the physics of fluid dynamics; Adelaide de Vecchi, for her help with computational models; and Andy King, for giving me the opportunity to "perform" for the undergraduate students.

My thoughts are also with the memory of Philip Batchelor. I was lucky to learn

a few tricks on matrix algebra from him.

During my PhD I had many opportunities to be in the clinic and see the clinical practice from very close. I would like to thank John Simpson for the clinical support and advice; I am also extremely grateful to my team-mate Kuberan Pushparajah, for all the time, effort and joy that we have shared; and to my friend Isra "quillo" Valverde, who always has a smile to offer and can answer flow-related clinical questions as good as run matlab and python scripts. Also thanks to Gerald Greil and the colleagues from the Academic Surgery Department for acting as mock audience for my clinically-oriented presentations.

I would like to thank the admin team from the Division of Imaging Sciences and Biomedical Engineering, in particular Davide Poccecai, Mick Barnes and Melanie Beasley who have helped me a lot during these years.

During my thesis, access to echo data has always been an issue, to some extent. It would have been definitely worse if it was not for the help of Graeme, John, Tobias (Voigt and Schaeffter), Kawal and Gerald; and also external partners and colleagues: Helko Lehman, Irina Waechter-Stehle, Felix Achilles, Alexandra Groth, Jurguen Weese, from Philips; and Mark Hillecke from Imperial College, which provided me with very useful tips.

In the past three years I had the opportunity to travel to a lot to conferences, meetings and even to a summer school in Sicily. In those travels I have met very interesting people with whom I have exchanged ideas, points of view and also sightseeing, breathtaking views and good food and drink. Some of these moments come particularly to my mind. I would like to thank Markus, Daniel and Nico for the great time in Barcelona; Graeme and Andy for the delicious (although largely overdimensioned) pizza in Chicago; Maxime, Oscar and Mathieu for the amazing week in Nice (as in every other project meeting); and Kuberan, John, and all the Evelina's group for the excellent time in Athens, and especially Marieta for the superb dinner by the Acropolis.

I would also like to thank Carlos López Barrio and Chus Ledesma Carbayo from UPM (Madrid) for always having their doors open to me; and Valérie Burdin from Télécom Bretagne for her support at beginning of my thesis.

These past three years have been an amazing period of my life not only professionally, but also personally. I have to thank my friends for the endless good times

in London, in particular Sergio, Antonio (Torpín), Emilio, Boris, Jon, Fátima, Tom, Victor, and the people from the London Assembly; and Rado, Lolla, Shauna, Adam and all the former and current flatmates at 58 Leman Street. I have to give a special thanks to my friends from *SpanishSpokers*, because no matter where I am I know I can always count on them, and especially, Kike, Samu, Emilio, Hadrien, Charles, Moreyba, Maria (Costris), Silvia, Julen, Eukeni, Aritz and Fer, to whom I owe a visit to the Canary Islands; and my friends from Brest, particularly Ángela, Dani, Patri and Diego.

I do not forget my friends from Madrid, my home town, who have been a safe reference during all these years around Europe. Thanks to Alex, Jaime and Victor, for all we have lived together and for still much more ahead; and Natalia, David (Pipa), Ministro, Moreno and Mario from UPM. And of course my friends from childhood, because the mere fact that I can still call them my friends after all these years and all these kilometres deserves the greatest gratitude: Dani, Darío, Carla, Adri, Mónica, Jose and Sparrowe, thanks for being there.

I would like to finish by thanking my family because none of this would have been possible without them. Thanks to my aunt Carmela, for her advice; thanks to Anicarmen and Marco for their hospitality and encouragement; thanks to my brothers Pablo and Samuel, for when we talk I travel back to were I belong; and thanks to my parents Paloma and Ángel, for their love, patience, understanding and for following me to the end of the world.

The biggest thanks of all is for Daniela. She has had infinite patience and love; she fed my heart and my tummy and took care of me when I was too busy to do it myself because I was working on my thesis (which was nearly everyday for the last three years). My world is a better place since you are in it, and I love you for that.

Last, I would like to thank you for reading my thesis. I guess that when one puts the soul on his work, some of it remains forever imprinted, and flows back to every reader. And there cannot be a more beautiful reward.

Alberto Gómez, March 2013.

Contents

List of Figures

List of Tables

List of Notation

a	Variable
$a^\star$	Complex conjugate of a
$\overline{a}$	Mean value of a
$a^{(n)}$	$n-th$ derivative of a
A	Point
$\overline{AB}$	Vector from point A to point B
A_x	A_x component of vector A
$\mathbf{A}$	Matrix
$\mathbf{A}^\top$	Transposed matrix
$\mathbf{a}$	Column vector
a_x	x component of vector $\mathbf{a}$
$\mathbf{a}^\top$	Transposed column vector (row vector)
$\hat{\mathbf{a}}$	Normalized column vector
$\beta^n_{s,l}(t)$	Scaled and displaced version of a B-spline β^n, $\beta^n_{s,l}(t) = \beta^n(t/s - l)$
$\dot{\beta}^n_{s,l}(t)$	Derivative of the B-spline $\dot{\beta}^n_{s,l}(t) = \frac{\partial}{\partial t}\beta^n_{a,l}(t)$

Abbreviations

2D Two-dimensional.

2D+t Flow MRI temporally resolved through-plane flow-encoded 2D MRI.

3D Three-dimensional.

3D+t Flow MRI temporally resolved 3 directional flow-encoded 3D MRI.

A-Mode Amplitude Mode.

BDBM Bilinear Deformable Block Matching.

BFS Breadth-First Search.

B-Mode Brightness Mode.

CDMA Code Division Multiple Access.

CT Computerised Tomography.

CWD Continuous Wave Doppler.

d_{Bs} B-spline degree.

DB Directional Beamforming.

DFS Depth-First Search.

ECG electrocardiogram.

Echo Echocardiography.

EMF Electromagnetic Flow Meter.

FCR Flow Convergence Region.

FFT Fast Fourier Transform.

FoV Field of View.

FP7 Framework Programme 7.

Fps Frames per second.

GT Ground Truth.

LMS Least Mean Squares.

LV Left Ventricle.

M-Mode Time-Motion Mode.

MR Magnetic Resonance.

MRI Magnetic Resonance Imaging.

PC-MRI Phase Contrast Magnetic Resonance Imaging.

PDE Partial Differential Equation.

PISA Proximal Isovelocity Surface Area.

PSF Point Spread Function.

PWD Pulsed Wave Doppler.

PWE Planar Wave Excitation.

Q Image quality.

RF Radio Frequency.

RoI Region of Interest.

SA Synthetic Aperture.

SFI Speckle Flow Index.

SNR Signal to Noise Ratio.

SpA Spatial Averaging.

SPWD Spectral Pulsed-Wave Doppler.

SQ Spatial Quadrature.

SSD Sum of Squared Differences.

ST Speckle Tracking.

TA Temporal Averaging.

TGC Time Gain Compensation.

TO Transversal Oscillation.

TOE Transesophageal Echo.

TRE Target Registration Error.

TTE Transthoracic Echo.

US Ultrasound.

Medical Abbreviations

AO Aorta.

ASD Atrial Septal Defect.

AV Aortic valve.

AVVa Atrio-ventricular valve.

BMI Body Mass Index.

CHD Congenital Heart Disease.

CVD Cardiovascular Disease.

EF Ejection Fraction.

HLHS Hypoplastic Left Heart Syndrom.

LA Left atrium.

LV Left ventricle.

LVOT Left ventricular outflow tract.

MV Mitral valve.

PA Pulmonary artery.

PS Pulmonic Stenosis.

PV Pulmonary valve.

Q Cardiac Output.

QPQS Pulmonary to Systemic Flow Ratio.

RA Right atrium.

Reg. Fr. Regurgitant Fraction.

RV Right ventricle.

SV Stroke Volume.

ToF Tetralogy of Fallot.

TV Tricuspid valve.

VSD Ventricular Septal Defect.

Chapter 1

Introduction

“ El ojo que ves no es
ojo porque tú lo veas;
es ojo porque te ve. ”

(The eye you see is not / an eye because you see it; / it is an eye because it sees you.).

“Campos de Castilla”, Antonio Machado (1921)

Contents

The work presented in this document is focused on three-dimensional (3D) cardiovascular flow and velocity quantification from multiple 3D colour Doppler images, and is presented in partial fulfilment of the requirements for the degree of Doctor of Philosophy of the University of London. This chapter provides a brief summary of the objectives pursued, the structure of the document and the main scientific contributions of the described work.

1.1 Motivation

Cardiovascular imaging is an essential resource for cardiologists and researchers in order to understand cardiac morphology, physiology and pathology. There exist nowadays a number of well-established non-invasive modalities for morphological imaging of heart and vessels –e.g. echocardiography (echo), Magnetic Resonance Imaging (MRI) and Computerised Tomography (CT).

The function of the heart is to pump blood to all organs. Indeed, a heart which might be morphologically different to a "normal" heart (e.g. a congenital heart) can still be a functional heart if delivers blood to the body. Therefore, the ability to *see* blood flow is the ability to observe a heart's pumping function. For this reason, over recent years there has been an increasing interest in non-invasive techniques to image cardiovascular flow. The most commonly used technique is Spectral Pulsed-Wave Doppler (sPWD), which only measures one component of blood velocity at a single position over time. Improvements in Phase Contrast Magnetic Resonance Imaging (PC-MRI) –also referred to as *flow MRI*– over the past years has enabled accurate multi-dimensional velocity measurement through a plane or even a volume.

Flow MRI is still not a widely used technique. Reasons for this include high cost, reduced availability, long exam time, incompatibility with ferromagnetic implants and need for anaesthesia in young children. Nevertheless, temporally resolved through-plane flow-encoded 2D MRI (2D+t Flow MRI) is considered the gold standard for non-invasive flow rate measurements. Moreover, temporally resolved 3 directional flow-encoded 3D MRI (3D+t Flow MRI) is an active research field to obtain 3D time-resolved images of blood flow throughout the cardiovascular system.

Echo is nearly always the first imaging modality used for cardiac diagnosis (in terms of number of exams and availability of the equipment). Echo Doppler techniques are very widely used and are part of standard routine for blood flow measurements. Unfortunately echo Doppler has important limitations, in particular only the component of the velocity aligned with the ultrasound beam can be measured. As a result, Doppler measurements are inaccurate: measured velocity is dependent on the angle between the beam axis and the blood flow. In addition, standard Doppler techniques assume that flow is laminar and that measured velocity is constant over the whole cross section of the vessel or that the velocity profile has a parabolic shape.

All these assumptions can lead to errors in flow rate of up to 30% (Thrush, 2010).

In this thesis, multiview approaches (*i.e.* combined processing of images acquired from multiple views) have been investigated in order to overcome this major limitation of Doppler measurements. Two main research objectives have been investigated:

1. **Investigation of 3D flow and velocity reconstruction from multiple 3D colour Doppler views**. Figure 1.1 illustrates the 3D velocity reconstruction concept: blood flow is complex and of 3D nature (Fig. 1.1(a)), but colour Doppler images only measure a 1D projection (Fig. 1.1(b)). The main aim of this research was to recover all 3 components of the velocity, as shown in Fig. 1.1(c).

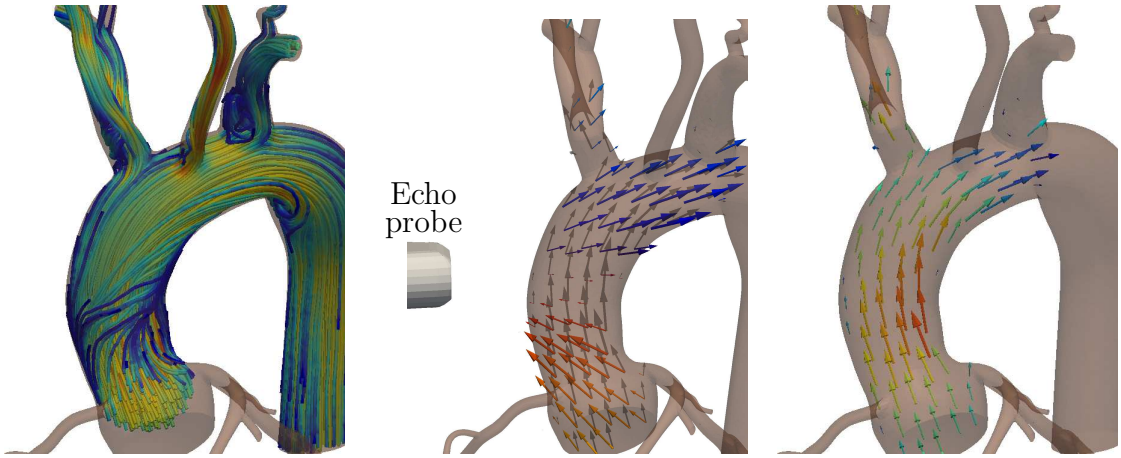

(a) True flow through the ascending aorta during systole. (b) Velocity measured with a colour Doppler image. (c) Reconstructed 3D velocity.

Figure 1.1: Concept diagram: 3D velocity reconstruction. (a) Representation of blood flow through the aortic outflow tract and the aortic arch. (b) Hypothetical velocities measured with a colour Doppler image. The red and blue vectors represent the beam direction along which Doppler velocity would be measured with the echo probe (transducer) located on the left. (c) Reconstructed 3D velocity, where all components of the velocity are recovered.

2. **Investigation of angle-independent flow quantification methods from multi-view composite surfaces.** Following Gauss's theorem, the flux of a vector field through a surface depends only on the component of the vector field orthogonal to that surface. As a result, blood flow rate through a surface can be calculated with only one component of the blood velocity, as long as this component is orthogonal to the surface and the surface completely includes

the blood pool. Such a geometric arrangement occurs in ultrasound imaging if the velocity is integrated over surfaces equidistant from the transducer. Figure 1.2 illustrates the idea that has been investigated in this thesis. If the cross section of the target structure (e.g. a vessel) is totally contained in the Field of View (FoV) of a 3D colour Doppler image (Fig. 1.2(a)) flow rate can be calculated independently on the angle of insonation. In the more general case where the echo FoV does not necessarily contain the whole cross section of the vessel or that part of the FoV is affected by shadowing or other image artefacts, combining multiple 3D colour Doppler views (Fig. 1.2(b)) enables the calculation of accurate angle-independent flow rate by integrating velocity over composite spherical surfaces (Fig. 1.2(c)).

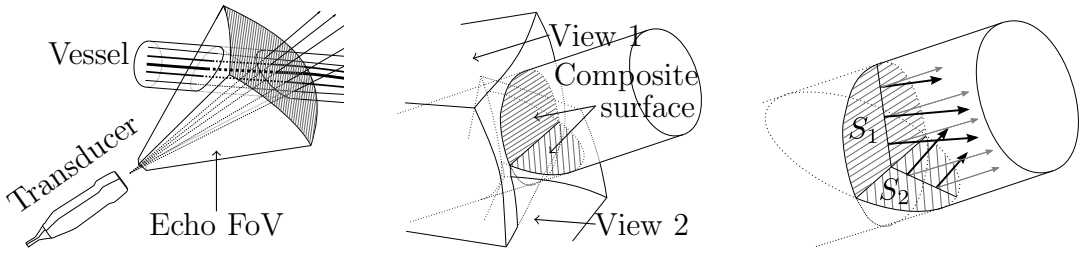

(a) Echo FoV containing the whole cross section of the vessel of interest. Angle independent flow can be calculated. From a 3D colour Doppler volume.

(b) Two views, each of which partially covers the cross section of the vessel, are combined to produce a composite surface which totally include the vessel.

(c) Velocity measured from each view is integrated over all the spherical patches (here S_1 and S_2) which form the composite surface.

Figure 1.2: Concept diagram: Angle-independent flow by velocity integration over spherical surfaces using multiple 3D colour Doppler images.

1.2 Summary of the Thesis

This thesis is structured in 9 chapters. Chapters 2, 3 and 4 describe the technical background, the clinical motivation and review state-of-the-art techniques for velocity reconstruction and flow quantification with echo Doppler systems.

The **original work** of this thesis is described in chapters 5, 6, 7 and 8, where novel methods for 3D blood velocity reconstruction and accurate flow rate and volume quantification are proposed.

Last, chapter 9 summarises the main points of this thesis, putting the original contributions into context and covering the technical and clinical implications of

the developed methods. In the next paragraph, the contents of each chapter are described one by one.

Chapter 2 describes the clinical context of the research carried out in this thesis. Cardiac anatomy and physiology are summarised, highlighting the clinical aspects of cardiac blood flow. Then an overview on cardiaovascular disease and Congenital Heart Disease (CHD) is provided to put into context the patient group to which the techniques developed have been applied, and in particular to describe Hypoplastic Left Heart Syndrom (HLHS). Flow-related clinical parameters are explained, as well as standard and advanced techniques for blood flow measurement used in the clinic, focusing on MRI and echo.

Chapter 3 provides an overview of the physics and engineering of ultrasound image acquisition and formation. Special detail is given to formation of 3D colour Doppler images, including Doppler measurement, image formation, artefacts and sources of inaccuracy. A brief section on flow MRI and other techniques for clinical flow measurement is included at the end of the chapter.

Chapter 4 provides a comprehensive literature review on state-of-the-art flow quantification with echo techniques. In the first half of the chapter, echo techniques for 2D and 3D blood velocity recovery are studied. Special attention is given to methods which use multiple views. The second half of chapter 4 is dedicated to techniques to calculate flow rate and volume from echo Doppler measurements. The techniques covered include standard and advanced spectral Doppler methods, angle-independent methods and the Proximal Isovelocity Surface Area (PISA) method.

Chapter 5 is the first of the four chapter which contain the original contributions of this thesis. This chapter describes a novel technique to recover a 3D velocity field from three or more 1D projections. The reconstruction algorithm is presented in three versions of increasing complexity and performance, from the simple geometrical backprojection approach, to a more general voxel-wise Least Mean Squares (LMS) approach and finally to a regularised patch-wise approach to recover a smooth field of 3D vectors from an arbitrary number of projections using a B-Spline grid.

Chapter 6 studies the applicability of the novel method described in chapter 5 to the clinical problem of recovering 3D cardiovascular blood velocity from three or more 3D colour Doppler images. First, a sensitivity analysis is presented, describing the ranges of parameters (noise in Doppler data, view angles and registration accuracy) required for accurate reconstruction. This analysis is carried out with simulated data generated with a new multi-scale noise model. The reconstruction technique is tested on three volunteers and three paediatric patients, and validated by comparison with flow MRI measurements.

Chapter 7 Introduces a new method to recover 3D velocity in the entire ventricle by incorporating ventricle wall motion into the method used in chapter 6. Wall motion is calculated from a standard B-Mode sequence, and is incorporated into the flow reconstruction method using a multi-scale implementation. 3D+t flow patterns such as the ventricular filling vortex are recovered and compared to 3D+t Flow MRI on a paediatric patient.

Chapter 8 describes a new technique to calculate angle-independent, highly time-resolved flow rate and volume. The method is based on integration of Doppler velocities over spherical surfaces orthogonal the the beam direction, without the need to recover the 3D velocity field. High temporal resolution is achieved by temporal interleaving of time delayed sequences. Full coverage of the region of interest is achieved by combining multiple views and thus producing a composite spherical surface over which velocity is integrated to calculate flow rate. Three novel methods to combine multiple views are proposed and compared to flow rate and volumes obtained from 2D+t Flow MRI on four HLHS patients.

Chapter 9 summarises the main conclusions of this work, and puts into context the original contributions described in the previous chapters. The future research directions and the technical and clinical implications of the developed techniques are also discussed.

1.3 Original Contributions

The original work described in this thesis can be summarised in two main contributions:

1. For the first time, **3D blood velocity vectors** are available from echo images. This allows the **quantification** and **qualitative analysis** of 3D flow patterns, flow profiles, flow rate and flow volume.

   Impact of the novelty. Understanding of cardiac function both in healthy and diseased subjects can be highly improved by the means of improved imaging of cardiac flow. In particular, and since blood flow is of 3D nature, 3D flow recovery allows the study of flow patterns and allows calculation of important clinical parameters such as flow rates and flow volumes in arbitrary regions and through arbitrary planes. The ability to calculate 3D velocity vectors using echo allows application of these techniques to a broad range of subjects. Not only can 3D velocity vectors be obtained in reduced time and cost compared to flow MRI (the current gold standard), but also most cardiac patients undergo an echo examination before any other imaging procedure and some patients (in particular very small babies) are not eligible for flow MRI.

2. A method is proposed to **quantify angle-independent** flow rate and volume, overcoming current limitations such as **reduced frame** rate and the **small FoV** of 3D colour Doppler acquisitions, providing arbitrarily high frame-rate and broad spatial coverage.

   Impact of the novelty. Two major limitations of flow quantification with 3D colour Doppler are the reduced FoV and reduced temporal resolution, in particular in congenital paediatric patients (which have high heart rates) and in patients with enlarged cardiac structures. The proposed technique overcomes both limitations, allowing accurate flow quantification, even before the patient has to be sent to an MR scan.

Chapter 2

Clinical Background

"Cardiology is about flow. (...) Flow should therefore be a primary focus by which we explain where lesions form, why they degrade and decompensate, and how we grade the extent of restoration of function after vascular intervention"

"Cardiology is Flow", Richter and Edelman (2006)

Contents

Pumping blood is the function of the heart, and therefore accurate cardiac assessment cannot be conceived without accurate and reliable assessment of cardiac flow. Along the cardiac cycle, blood is conducted through the three-dimensional (3D) space of the different chambers of the heart and the vessels, thus, full 3D characterisation of blood velocity and flow is needed for a complete understanding of the cardiac condition.

Cardiac pathologies are indeed very common, and they modify normal heart function *i.e.* they produce perturbations of flow shape and pattern and significant variations of flow parameters. Early imaging modalities focused on heart anatomy, but over the last decades flow imaging has become a focus of interest and active research. Although analysis of heart anatomy gives important insight on cardiac physiology, full 3D velocity and flow quantification are of particular clinical relevance since they constitute a direct observation of cardiac function.

This chapter starts with a basic overview on heart anatomy and physiology, focusing on dynamics of blood flow. It follows a brief analysis of cardiac diseases and conditions and how they affect the heart and cardiac flow. The chapter finishes with a description of techniques and methods for flow analysis, measurement and imaging, emphasizing the role of echocardiography (echo) in clinical practice.

2.1 Cardiac Anatomy and Physiology

The human heart is a muscular organ which pumps blood to the body through the circulatory system, in order to deliver oxygen and nutrients to every cell.

2.1.1 Anatomy of the heart

The heart is surrounded by a membrane called the pericardium, which protects and lubricates the heart. The cardiac wall consists of three layers: the epicardium is the outer layer, and has mainly a protective function; the myocardium is a thick layer responsible for cardiac contraction; and the endocardium is the innermost layer coating the cardiac chambers and valves, which provides continuity with inner vessel

walls.

Figure 2.1 depicts the anatomy of the heart. A healthy heart is divided into four chambers: two ventricles and two atria. The atria are separated from the ventricles by the atrioventricular groove, where the coronary artery lies. The wall between the atria is called atrial septum, and the wall between the ventricles is the ventricular septum.

The right atrium (RA) receives oxygen-depleted blood from the cava veins and the coronary sinus, and passes it to the right ventricle (RV) through the tricuspid valve (TV). The RV ejects the blood to the pulmonary artery through the pulmonary valve (PV).

The left atrium (LA) receives oxygenated blood from the pulmonary veins, and circulates it to the left ventricle (LV) through the mitral valve (MV). The LV ejects the oxygenated blood to the aorta through the aortic valve (AV). The three cusps of the TV and the two cusps of the MV are attached to the ventricular walls by the papillary muscles via the cordal apparatus (*chordae tendinae*).

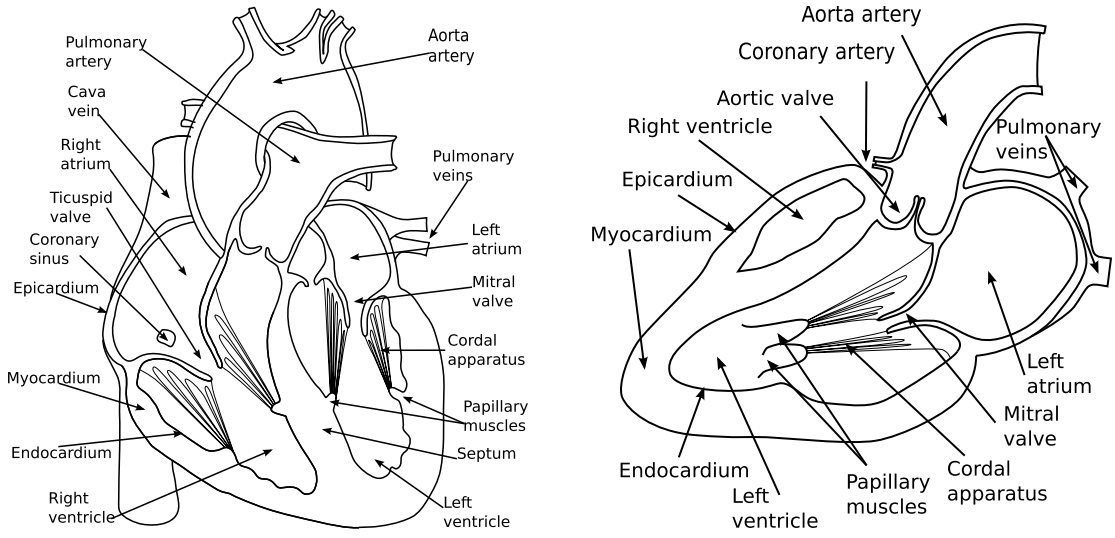

(a) 4 chamber plane.

(b) Long axis plane.

Figure 2.1: Cardiac anatomy.

2.1.2 Physiology of the heart

Cardiac activity is governed by an electrical impulse which propagates through cardiac tissue and triggers the different phases of the cardiac cycle. This impulse can be measured with an electrocardiogram (ECG). The ECG is a widespread indicator

of the phase of the cardiac cycle.

The function of the heart is to pump blood to the body. Each side of the heart is actually a single pump on its own. The left heart (LA and LV) is responsible for the systemic circulation and the right heart (RA and RV) is responsible for the pulmonary circulation.

Blood circulation from one chamber to another is controlled by two mechanisms: active muscular contraction, which is triggered by an electrical impulse, and passive valve openings, triggered by changes in intracardiac pressure.

Figure 2.2 illustrates the physiology of the heart through the cardiac cycle. Contraction and relaxation of the myocardium and valve opening and closing are depicted in Figs. 2.2(a) to 2.2(f). Changes in intracardiac pressure and volume are represented in Figs. 2.2(g) and 2.2(h).

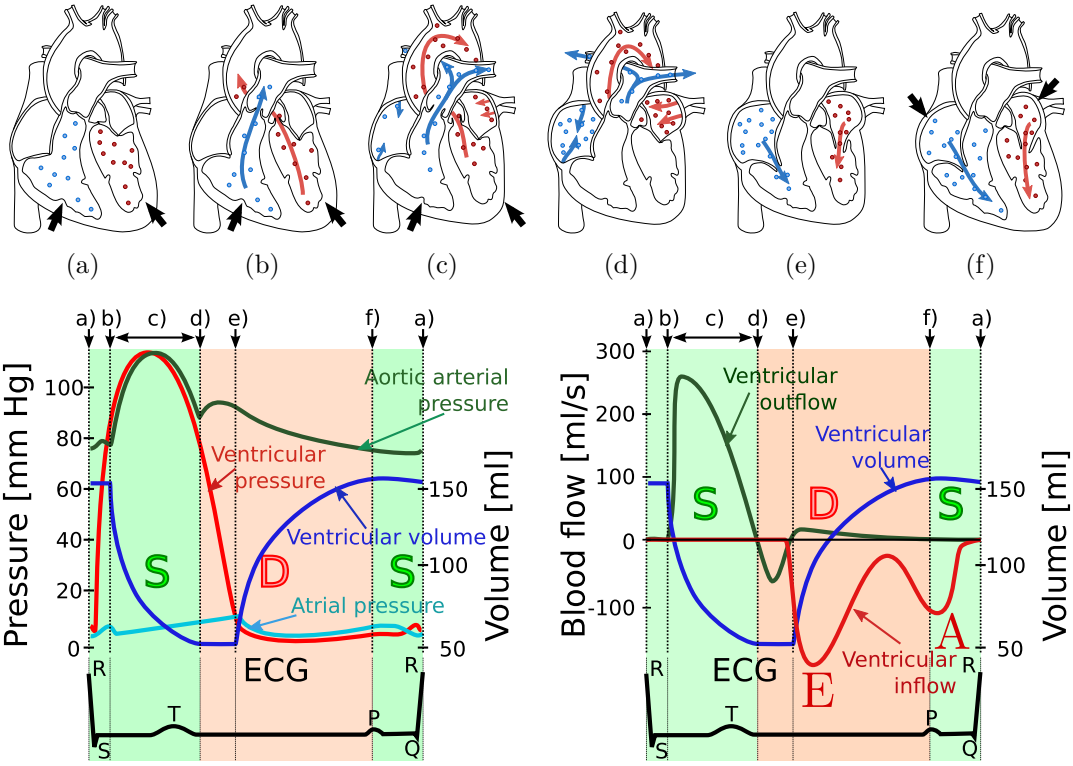

(g) Pressure and left ventricular volume during the cardiac cycle.

(h) Blood flow in a normal left ventricle during the cardiac cycle.

Figure 2.2: Cardiac physiology. (a)–(f) Different instants of the cardiac cycle. (g) Pressure in left ventricle and ascending aorta and ventricular volume through the cardiac cycle. (h) Normal flow rate through the aortic and mitral valves through the cardiac cycle. Systole (S) is indicated with green background and diastole (D) with red background.

In the vast majority of the literature on physiology, the cardiac cycle is explained

starting at the P wave of the ECG. However, in most cardiac imaging modalities image acquisition is triggered by the R wave, which means that the first frame acquired is when ventricle contraction begins. In consequence for the purpose of this thesis all images shown and all analysis will assume that the cardiac cycle begins and ends at the R wave. The R wave indicates the commencement of ventricular contraction (Fig. 2.2(a)). The atrial and ventricular pressures equal, and the atrio-ventricular valves start to close. Then follows the isovolumetric contraction, during which the ventricle muscles contract, until the ventricular pressure gets above the aortic pressure (first crossing of red and green lines in Fig. 2.2(g)) and the AV and the PV open (Fig. 2.2(b)). The ventricles contract during the rest of the systole (Fig. 2.2(c)), rapidly first and slower later (note the decrease in the steepness of the ventricular volume curve in Fig. 2.2(g)). As the ventricle ejects the blood, ventricular pressure decreases. During this time, the atria receive blood from veins. When ventricular pressure drops below the aortic pressure, a suck effect brings blood back from the arteries to the ventricle, causing the closing of the AV and the PV (Fig. 2.2(d)). The closing of all four valves is the beginning of the diastole with the isovolumetric relaxation. The atria continue filling with blood until the atrial pressure is higher than ventricular pressure (Fig. 2.2(e)). Then the atrio-ventricular valves open and lead to the early ventricular filling. A few ms later, the P wave of the ECG triggers atrial contraction which results in active ventricular filling (Fig. 2.2(f)), after which the cardiac cycle starts again.

Further details on cardiac physiology are widely available in clinical literature (Guyton and Hall, 2006; Oh et al., 2007; Segadal and Matre, 1987).

2.1.3 Dynamics of Cardiac Blood Flow

It is of clinical interest to relate cardiac flow and cardiac physiology. In particular, normal flow waveforms through the AV, PV, MV and TV (Yoganathan et al., 2007) are illustrated in Fig. 2.2(h).

In the left heart, as soon as the AV opens (Fig. 2.2(b)) aortic flow rises rapidly until the ventricular pressure drops below the aortic pressure. This causes some backward flow until the AV closes. At the end of the isovolumetric relaxation the MV opens (Fig. 2.2(e)). Then follows two flow peaks as shown in Fig. 2.2(h). The

first one (E wave) corresponds to the early ventricular filling due pressure difference between the atrium and the ventricle. The second peak (A wave) corresponds to active filling due to atrial contraction, and is in general smaller than the first one (Kim et al., 1994). In the right heart, blood flow waveforms through the PV and the TV are similar to the left heart, but pressures are lower. PV and AV are morphologically similar, except the pulmonary orifice is slightly bigger. The velocity through the PV is also lower than through the AV, but flow waveforms are similar (Sloth et al., 1994). Velocity through the TV is lower than through the MV because the valve annulus is larger in the first one (Yoganathan et al., 2007).

The described cardiac dynamics are valid for healthy subjects. In presence of cardiovascular disease, heart function is modified in a number of ways that are briefly described in the following sections.

2.2 Cardiovascular Disease

Cardiovascular Disease (CVD) refers to diseases of the heart and its main arteries and veins. According to the World Health Organisation, CVDs are the cause of 23% of world deaths and the highest cause of death in middle and high income countries. In 2007, the death rate (number of deaths in a population at risk during one year) associated to Cardiovascular Disease (CVD) was 251.2 per 100000 (Roger et al., 2011). CVD are classified into two types: non congenital and Congenital Heart Disease (CHD).

Non congenital cardiac diseases are those acquired during lifetime, e.g. chronic diseases such as atherosclerosis. Cardiovascular chronic diseases have emerged over past years as a major contributor to global mortality (Fuster and Kelly, 2010).

Congenital Heart Disease (CHD) consists of structural cardiac defects presents at birth. CHD is the largest cause of birth defect-related deaths. The incidence of moderate and severe forms of CHD is of 6/1000 to 19/1000 live births world wide (Hoffman and Kaplan, 2002). Most common manifestations of CHD are atrial and ventricular septal defects (totalling a 38.9% of CHD) (Roger et al., 2012).

An example of CVD is the condition known as Hypoplastic Left Heart Syndrom (HLHS), which accounts for about a 2.2% of the CHD (Roger et al., 2012). HLHS has been found (Robbins et al., 2003) to account for the most expensive average

charges for neonate hospitalization ($199,597 in 2003 in USA), and involves the more recent development in advancing the limits of CHD interventions in surgery. Because images from patients with HLHS are used later in this thesis, HLHS is now explained in more detail.

2.2.1 Hypoplastic Left heart Syndrome

Hypoplastic Left Heart Syndrom is a congenital cardiac condition in which the left heart and the ascending aorta are severely underdeveloped, and was first proposed by Noonan and Nadas (1958). In this condition, the right heart is forced to provide systemic and pulmonary circulations. The disease and the 3 surgery stages that are usually carried out are described in Fig. 2.3.

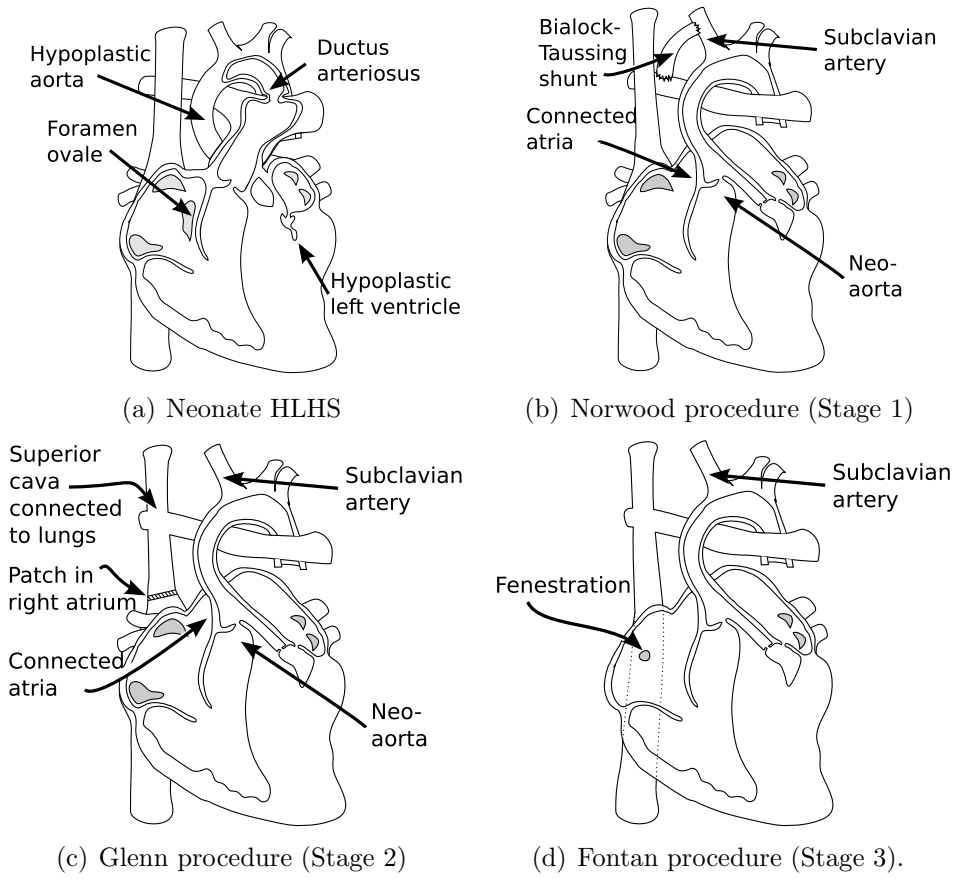

(a) Neonate HLHS

(b) Norwood procedure (Stage 1)

(c) Glenn procedure (Stage 2)

(d) Fontan procedure (Stage 3).

Figure 2.3: Hypoplastic Left Heart Syndrome.

The most typical cardiac morphology for a HLHS neonate patient is represented in Fig. 2.3(a). All babies are born with an opening between left and right atria, called *foramen ovale*, and a small blood vessel connecting aorta and pulmonary artery, called *ductus arteriosus*, and these are essential for survival at birth. These

connections are kept open by using medication until the first surgical intervention takes place. The three surgical stages are the following:

Stage 1: shortly after birth, the Norwood procedure (Norwood et al., 1983) is carried out (Fig. 2.3(b)). The procedure consists in disconnecting the right ventricle from the pulmonary artery and connecting it to the aorta, to pump blood to the systemic circulation. The new outflow valve is called neo-aortic valve. Since this operation stops the pumping of blood to the lungs connecting the neo-aorta to the pulmonary circulation is required. This can be achieved by connecting the subclavian artery and the pulmonary artery (Blalock-Tausig shunt). The septum between the atria is removed so that both atria send blood to the right ventricle.

Stage 2: After the Norwood procedure, the heart has an extremely high workload and the pulmonary system is exposed to the high systemic pressures. Therefore another surgical intervention, known as the Hemi-Fontan or bi-directional Glenn procedure (Glenn, 1958) is needed 4 to 6 months after the first procedure. Figure 2.3(c) represents the heart after the Glenn procedure. The Blalock-Tausig shunt is removed and the superior vena cava is disconnected from the RA and connected to the pulmonary circulation.

Stage 3: the Glenn procedure relieves the pressure in the lungs by connecting to venous pressures. There is no more mixing of oxygenated and venous blood from the upper body, but some mixing still occurs from the lower body, producing some oxygen desaturation. To complete the treatment of the HLHS, a last surgical stage is performed, the Fontan procedure (Fontan and Baudet, 1971; de Leval, 2005), when the child is between 1 or 3 years old. The final morphology of the repaired heart is shown in Fig. 2.3(d). The inferior vena cava is connected to the pulmonary circulation and disconnected from the RA, so there is no more blood mixing. The pulmonary circulation is no longer pumped by the heart but it is passively conducted by the low venous pressure. To regulate intracardiac and arterial pressures, a small hole (fenestration) is left connecting the vena cava to the RA.

The completion of this three-stage procedure dramatically increases early and

mid term survival. However, because this reconstructive surgery was only introduced in the early 1980s (Lai et al., 2006), it is still too soon to study the long term impact on patients' health. However, late death and need for heart transplant have been found uncommon (Mahle et al., 2000).

2.2.2 Impact of CVD on Blood Flow

Cardiovascular diseases are related to abnormalities in cardiac morphology and function which result in to abnormal flow parameters and patterns. Abnormal blood flow is reflected by flow parameters (flow rate, cardiac output, and other quantities which are explained in Sec. 2.3), and blood velocity patterns (changing flow laminarity or producing vortices or other flow processes). The most common variations are described hereinafter.

Blood flow parameters are affected by physiological changes, such as heart rate and blood pressure. For example, an increase in heart rate (not necessarily pathological) usually results in an increase in the amount of blood pumped per minute, a decrease in left-ventricular end-diastolic pressure and no change in regurgitation, if present (Laniado et al., 1982). In the case of cardiac defects, septal holes and defective valves produce variations in normal flow curves (Fig. 2.2(h)). For example, in the case of aortic insufficiency (leaking of the aortic valve), the mitral peak flow increases, and almost all transmitral flow seems to concentrate in the E wave (see Fig. 2.2(h)) (Judge et al., 1971).

Three-dimensional blood velocity patterns also change with pathology. The presence of a stenosis increases blood velocity through the narrowing and usually produces small vortices immediately after (Long et al., 2001). Valvular regurgitation produces high velocity jets which may be projected into a single or multiple directions opposite to the natural flow (Hope et al., 2007). Septal defects can produce blood mixing between the two sides of the heart, although typically the blood velocity through the defect are lower than in regurgitant jets (Uribe et al., 2009).

Modified blood flow parameters and velocity patterns are complex phenomena which require advanced imaging and measuring techniques for adequate characterisation.

2.3 Standard Measurement of Cardiac Flow

Currently, blood velocity and flow measurements can be carried out using invasive, minimally invasive and non invasive modalities:

- **Invasive** modalities include the use of devices like the electromagnetic flow meter (EMF) (Nichols and O'Rouke, 1997) and the transit-time flow meter (Beldi et al., 2000). These kind of measurements are very accurate but also require placing the device in the vessel where measurements are to be made, which needs open surgery.

- **Minimally invasive** techniques require introducing probes in the patients body but without open surgery, like intravascular Doppler probes during catheterisation procedures, for example for measuring coronary flow (Wilson et al., 1987).

- **Non invasive** techniques are the most common and include echo, 2D+t Flow MRI (Gatehouse et al., 2005), 3D+t Flow MRI (Wigstrom et al., 1996) and x-ray angiography (Shpilfoygel et al., 2000).

In practice, clinical assessment of flow is reduced to the quantification of a number of parameters, shown in Table 2.1.

Echo imaging is now a mature technology, which has a well-established place in clinical practice (Evangelista et al., 2008; Stadlbauer et al., 2009) where it currently accounts for about one in four of all medical imaging procedures worldwide (Wells, 2006). Transthoracic echo is the dominant imaging modality for assessing cardiac function in general, and CHD in particular, because of its simplicity and availability, and because pediatric patients (the majority of CHD patients) have excellent acoustic windows in the chest (Lovato et al., 2007). Transthoracic echo examinations are carried out 75 times more often than cardiac Magnetic Resonance Imaging (MRI) (Tsai-Goodman et al., 2004), which means that MRI is used on selected patients only and always after an echocardiographic exam. Echo is the modality used throughout this thesis, and for this reason the echocardiographic examination will be covered in more detail than the other modalities.

Parameter	Description
Flow rate	is the volume of blood that moves through a given surface per time unit. Typically, flow rate is measured through the MV and the TV, and through the AV and the PV (ventricular inflows and outflows respectively)
Volume flow	is the time integral of the flow rate, and measures the volume of blood that has moved through a given surface during a period of time.
Stroke volume (SV)	is the volume of blood ejected from the ventricle per cardiac cycle.
Cardiac output (Q)	is the volume of blood pumped by the heart (left or right ventricle) per minute, and can be calculated as Q=SV$\times$*heart rate*.
Pulmonary to systemic flow ratio (QPQS)	is the ratio between the right ventricular output (pulmonary output) and the left ventricular output (systemic output). In healthy subjects this ratio is $1:1$, whereas in children with CHD can range from $1:2$ to $4:1$ or even more in severe cases (Kitabatake et al., 1984; Sanders et al., 1983).
Ejection fraction (EF)	is the percentage of blood that is ejected from a ventricle at one beat, out of all the ventricular volume. In healthy subjects it is in the range $55\% - 70\%$. Ejection fraction below 40% may indicate disease[1].
Regurgitant fraction (Reg. Fr.)	is the fraction of blood that enters back to a cardiac chamber from which it was ejected. For example, mitral regurgitation goes from mild ($< 30\%$) to severe ($\geq 50\%$) (Enriquez-Sarano et al., 2009).

Table 2.1: Clinical parameters related to cardiac flow.

2.3.1 The Echocardiographic Examination

Echo is highly operator dependent. Therefore, reproducibility may be achieved by using standardised views and techniques (Anderson, 2007). Standard echocardiographic views are defined for Two-dimensional (2D) planes which fit into the acoustic windows of the body.

There are four commonly utilised echocardiographic acoustic windows: parasternal, apical, subcostal and suprasternal (fig. 2.4(a))

Standard nomenclature such as sagittal, coronal and axial planes are not used in echo. Instead, echocardiographic nomenclature is described with respect to the way in which the imaging plane transects the heart itself. Thus, three orthogonal planes are routinely employed in 2D echocardiography: long axis, short axis and four chamber plane. (fig. 2.4(b)).

Standard image views can be obtained from the standard acoustic windows orienting the probe along the standard image planes (Fig. 2.5). Note however that

[1]Guidelines from the American Heart Association, http://www.heart.org

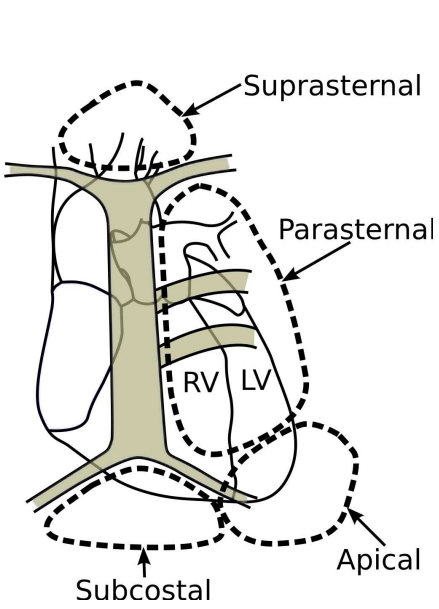

(a) Standard acoustic windows (left side of the chest). The dotted lines enclose the regions where the probe should be placed to acquire images.

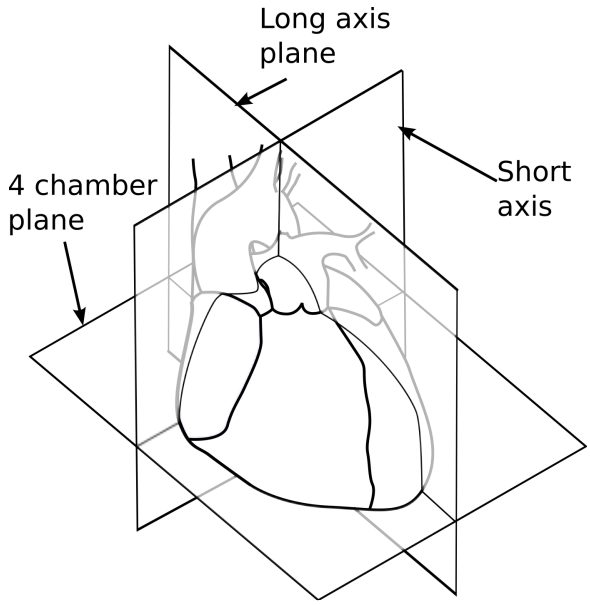

(b) Imaging planes of the heart. The three orthogonal planes define the standard cuts of a human heart.

Figure 2.4: Standard echo views. A standard 2D echo view is characterised by an acoustic window and an imaging plane.

in 3D echo not only a plane but a full volume is acquired. This means that, for example, the parasternal long axis and short axis will be the same views.

Further description of echocardiographic nomenclature can be found in the book by Anderson (2007).

2.3.2 Standard Assessment of Cardiovascular Flow with Echo

Echo systems provide several tools for hemodynamic assessment (Oh et al., 2007). Left ventricular stroke volume (SV) is routinely calculated by segmenting the left ventricle and measuring variations in volume through the cardiac cycle (Yamani et al., 2012) as shown in Fig. 2.6(a). However, most of the flow-related measurements are performed by using echo Doppler technology, which measures the component of the velocity aligned with the echo beam, and is therefore dependent on the angle of insonation (Doppler imaging will be covered in detail in Sec. 3.3.1). Spectral Doppler is used for measuring velocity waveforms at a point (Fig. 2.6(b)), which can be used to approximate pulmonary to systemic flow ratio (QPQS) and ejection fraction (EF). Flow rate can also be estimated using spectral Doppler, however this is rarely done in clinics since this measurement is known to be prone to errors (Evans

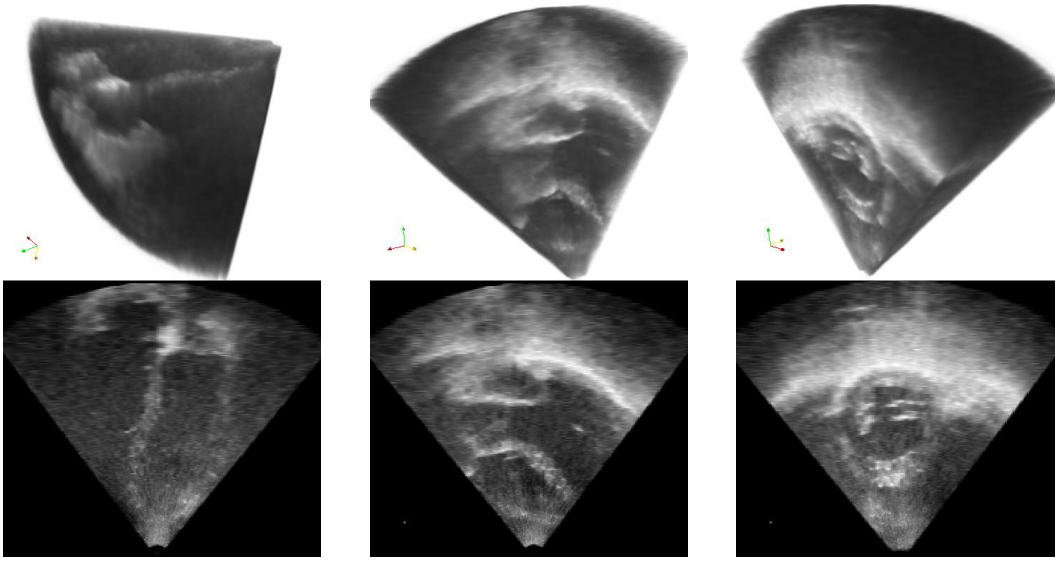

(a) Apical four chamber image.

(b) Parasternal long axis image.

(c) Parasternal short axis image.

Figure 2.5: Example of standard echo imaging images. 3D render of the volumes (top row) and 2D slice (bottom row).

and McDicken, 2000), which can be as high as 30% overestimation (Thrush, 2010).

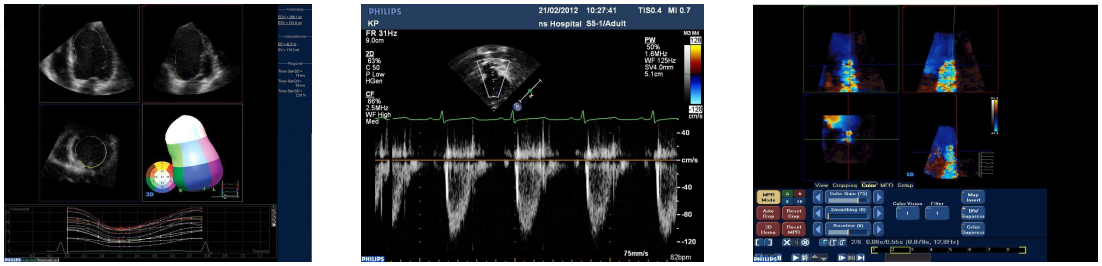

(a) Volume estimation by segmentation of 3D B-Mode sequences.

(b) Spectral Doppler measurement of neo-aortic outflow in a HLHS patient.

(c) View of a 3D colour Doppler image.

Figure 2.6: Standard flow measurements with echo. Figures produced with Philips QLab software.

Currently, quantitative measurement of flow-related parameters with echo still suffers from several limitations due to artefacts, aliasing and angle dependency. However, 2D and more recently 3D colour Doppler echo (Fig. 2.6(c)) are widely used for qualitative analysis of cardiac function, jets, shunts and valvular regurgitation.

The next section describes advanced flow imaging and measuring techniques, using echo and other modalities, which are not routinely used in the clinic but have shown great potential in research studies.

2.4 Advanced Measurement and Imaging of Cardiac Blood Flow

Flow imaging and measurement is an area of great clinical interest and an active field of research. In the last decade, many new advances in flow measurement, reconstruction and visualization have been introduced, in particular in MRI and echo (Sengupta et al., 2012).

2.4.1 Advanced Flow Measurements with MRI

Latest developments in temporally resolved through-plane flow-encoded 2D MRI (2D+t Flow MRI) techniques allow the accelerated acquisition of through plane velocities on a 2D slice with high temporal and spatial resolution ($25ms$ and $1.5mm^2$ respectively) within a breathold (Giese et al., 2012), as shown in Fig. 2.7(a). Accelerated temporally resolved 3 directional flow-encoded 3D MRI (3D+t Flow MRI) provides 3D velocity images with lower spatial resolution (around $2.5mm^3$) and a temporal resolution of $40ms$ to $70ms$ and an acquisition time significantly longer than in 2D (around $20min$ scan) using an accelerated sequence (Markl et al., 2011), as shown in Fig. 2.7(b). This allows the study of patterns, variations, vorticity and turbulence of blood flow, mixing and transport of blood through the cardiac chambers (Kilner et al., 2000).

However powerful 3D+t Flow MRI can be, it has some inconveniences and limitations. Accuracy is lower than 2D+t Flow MRI (Gatehouse et al., 2010), and acquisition time is much longer. Turbulence is difficult to image because of the spatial resolution and the averaging along the acquisition time. Also, MRI may be contraindicated for patients with metal implants, claustrophobia, or body mass index (BMI) $> 40kg/m^2$ (Hamdan et al., 2009). In addition, MRI is significantly more expensive than echo, is not as widely available and infants have to be anaesthetised to undergo the scan. For this reasons clinical guidelines recommend that MRI should be used only if specific clinical questions have not been answered by another imaging technique like echo.

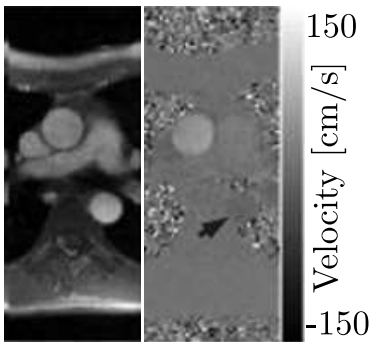

(a) 2D PC-MRI (courtesy of Dr. Daniel Giese).

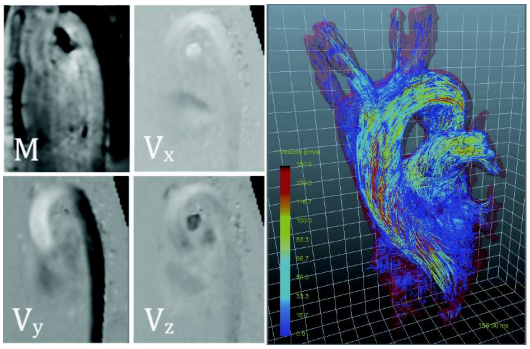

(b) 4D PC-MRI (Courtesy of Dr. Isra Valverde).

Figure 2.7: Advanced flow measurement with MRI. (a) 2D Phase Contrast MRI. The figure shows the magnitude image (anatomical, on the left) and the phase-encoded image representing through-plane velocity (right). (b) 4D Phase Contrast MRI. The four subfigures on the left show the magnitude image (top left, anatomy) and the three phase-encoded components of velocity, at a given slice of the 3D volume. On the right, 3D rendering of velocity using streamlines (GyroTools GTFlow software).

2.4.2 Advanced Flow Measurements with Echocardiography

The introduction of 2D matrix phased array transducer technology has allowed rapid acquisition of 3D time-resolved echo sequences of both B-Mode and colour Doppler volumes. Using 3D B-Mode images, EF and volume flow (Yamani et al., 2012), cardiac output (Q) and SV can be estimated (Hung et al., 2007). In the past years, 3D colour Doppler has show potential to evaluate valvular function (Cai and Ahmad, 2012), flow rate, and other cardiovascular parameters.

Echo is usually the first imaging technique used on cardiac patients, and remains the most widely used modality for examination of flow abnormalities (Budoff et al., 2012). Although there is an increasing interest in using 3D colour Doppler for flow quantification (Ge, 2012), accurate flow rate, Reg. Fr. and QPQS are currently measured with 2D+t Flow MRI, which is considered the reference technique. However, as mentioned before, echo imaging systems have many advantages: they are inexpensive compared to other modalities, non-invasive, real-time, and compatible with cardiac implants such as pacemakers. For all these reasons, there is a great interest in obtaining as much information as possible from the echo examination. In particular, 2D and 3D colour Doppler images may be acquired to evaluate blood flow patterns, morphology of regurgitant and stenotic jets and septal defects (Lang

et al., 2012).

2.5 The Future of Flow Analysis with Echo

Echo has great potential for quantitative and qualitative analysis of cardiovascular flow. Echo Doppler provides direct, nearly real-time quantification of blood velocity in space and time, while remaining an affordable, fast and widely available technique which is routinely used in clinics worldwide. For this reason, echo is closest to the patient than any other imaging modality. For this reason, improvements in echo systems, and in the information that echo systems provide, may have a major impact in patient health.

Observation of cardiovascular flow is the direct observation of the function of the heart. Clinicians want to have better access to flow information, including flow quantification and visualization of flow patterns. Being able to combine the benefits of echo systems with improvements in quantitative flow calculations, particularly from Doppler imaging, would have widespread clinical benefits. Addressing this clinical challenge is the subject of this thesis.

Chapter 3

Physical Principles of Blood Flow Imaging

Photograph by D. Arancibia, 2011.

"It is almost to be accepted with certainty that this will in the not too distant future offer astronomers a welcome means to determine the movements and distances of such stars which, because of their unmeasurable distances from us and the consequent smallness of the parallactic angles, until this moment hardly presented the hope of such measurements and determinations."

"On the coloured light of double stars and certain other stars from the heaven", Doppler (1842)

Contents

Non-invasive, non ionising flow imaging technologies, like Doppler echocardiography (echo) and flow Magnetic Resonance Imaging (MRI) have experienced an enormous improvement in the past 20 years. MRI was only developed in the late 1970s, and was not intensively used in clinical practice until the mid 1980s (Geva, 2006). Flow MRI imaging was first proposed by Moran (1982). Spectral Doppler ultrasound has been in existence since the mid 1950s (Edler and Lindstr om, 2004), but colour Doppler images were not generated until 1984 (Omoto et al., 1984), and only became part of standard clinical practice from the 1990s onwards. In the last decade, 3D Colour Doppler and 2D and 3D time resolved flow MRI are gaining the interest of clinical and technical communities for the potential and added value they may provide.

In this chapter, the physical principles of different flow measurement techniques are described. Focus is put on non-invasive techniques, particularly echo. First, the physics behind echocardiography (echo), whose clinical relevance has been stated in chapter 2, is described, with emphasis on the physics of echo Doppler. Second, basic physics of flow MRI, which constitutes the current gold-standard for non-invasive flow measurements, are briefly discussed. Third, some notes on other flow measurement modalities are given. Last, the main technical limitations of current flow measurement systems are analysed, motivating the research lines followed within this thesis.

3.1 Physics of Ultrasound

This section contains a summary of physics of echo imaging. Throughout this thesis, the term ultrasound (US) will be used within the context of physics (ultrasonic waves). In the medical context, and in particular in cardiac applications, systems which use US waves to produce images will be termed *echo systems* or *echo imaging systems*.

US consists of mechanical waves with frequencies above the upper auditory limit of $20kHz$. Medical US devices use longitudinal waves with a frequency range of about $2 - 15MHz$. Mechanical (*i.e.* pressure) waves must travel through some physical medium. Each particle of the medium oscillates about its resting location, in the direction of propagation of the wave (therefore the wave is called longitudinal), but does not undergo any net motion during propagation (Hangiandreou, 2003).

3.1.1 Sonic and Ultrasonic Waves

Sound waves are pressure waves that propagate through a medium of density ρ_0. If the velocity of propagation of the wave in that medium is denoted by c, the wave propagation is governed by the following three equations (Möser, 2009):

- The law of compression

$$\nabla \cdot \mathbf{v}(\mathbf{r}, t) = -\frac{1}{\rho_0 c^2} \frac{\partial p(\mathbf{r}, t)}{\partial t} \tag{3.1}$$

- The acoustic inertia law

$$\rho_0 \frac{\partial \mathbf{v}(\mathbf{r}, t)}{\partial t} = -\nabla p(\mathbf{r}, t) \tag{3.2}$$

- The wave equation, which can be inferred from (3.1) and (3.2).

$$\frac{1}{c^2} \frac{\partial^2 p(\mathbf{r}, t)}{\partial t^2} = \Delta p(\mathbf{r}, t) \tag{3.3}$$

where p is the pressure wave, $\mathbf{v}$ is the velocity wave and t is the time. The velocity wave $\mathbf{v}$ indicates the velocity of a particle of the medium, located at the position $\mathbf{r}$,

about its mean position, whereas the velocity of propagation, c indicates the velocity at which the wave propagates through the medium.

The complex pressure wave $\bar{p}$ is the solution to the wave equation (3.3):

$$\bar{p}(\mathbf{r}, t) = p_0 e^{-i\phi_0} e^{-i(\mathbf{k}\cdot\mathbf{r}-\omega t)} \tag{3.4}$$

where ϕ_0 is the initial phase, $\omega = 2\pi f$ is the angular frequency of the wave, and $\mathbf{k}$ is the vector wavenumber, whose direction $\hat{\mathbf{k}}$ indicates the direction of propagation of the wave and whose magnitude $\|\mathbf{k}\|$ is the inverse of the wavelength λ. A reminder of the relationship between some wave quantities is shown in Table 3.2. The velocity

Quantity	Equal to	Units
wavenumber, $\|\mathbf{k}\|$	$\omega/c = 2\pi/\lambda$	$[1/m]$
wavelength, λ	c/f	$[m]$
angular frequency, ω	$2\pi f = 2\pi/T$	$[rad/s]$
acoustic impedance, Z	$c\rho$	$[kg/s/m^2]$
period, T	$2\pi/\omega = 1/f$	$[s]$

Table 3.2: Showing equations and units of quantities related to sound waves.

wave can be obtained by integration of (3.2) over time, which yields

$$\bar{\mathbf{v}}(\mathbf{r}, t) = \frac{\bar{p}(\mathbf{r}, t)}{c\rho_0}\hat{\mathbf{k}} \tag{3.5}$$

the quantity $Z \equiv c\rho_0$ which relates the amplitude of the pressure wave and the velocity wave is called *characteristic acoustic impedance* of the medium (Dendy and Heaton, 1999) .

The representation of sound waves as complex exponentials is mathematically convenient. However, in practice only real valued sound signals can be observed and measured. The observable pressure p and velocity $\mathbf{v}$ can be obtained from their complex representation by taking the real part:

$$\begin{aligned} p &= Re\{\bar{p}\} \\ \mathbf{v} &= Re\{\bar{\mathbf{v}}\} \end{aligned}$$

Throughout this document, p and $\mathbf{v}$ are used to denote either the complex waves or the real parts. In case of ambiguity, the nature of the wave is explicitly stated.

Depending on the source of the sound wave, the directionality of the wave can take different forms. A wave which propagates along one direction, where the wavefront describes a plane is called a *planar wave*. A wave which is generated at a point source and propagates the same energy to all directions of the space, where the wavefront describes a sphere is called a *spherical wave*.

3.1.2 Interaction of US Waves with Biological Tissue

When an acoustic wave propagates within a medium, several phenomena occur related to the presence of changes in acoustic impedance of the medium or interfaces between different materials. The physics of these interactions are now described. These interactions are also depicted in figure 3.1.

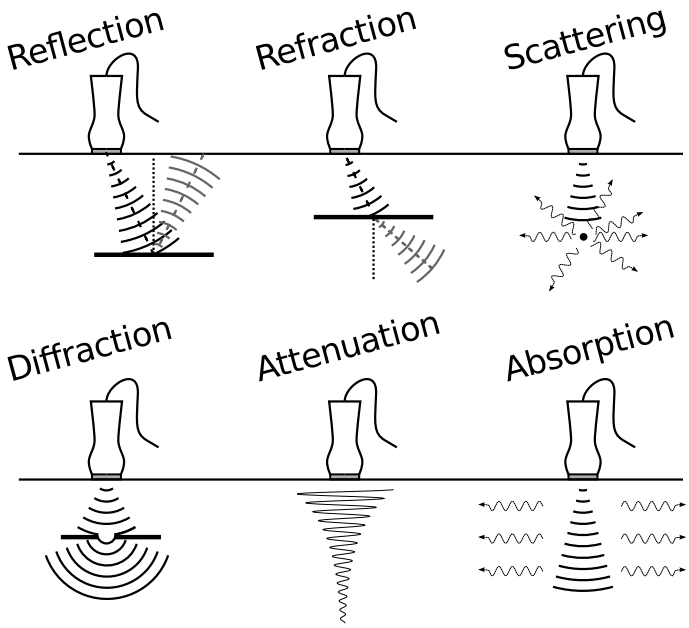

Figure 3.1: Interactions of sound waves with structures, inspired by Anderson (2007). The received echo is a combination of all the above processes.

In the following, we use the terms *structure* or *tissue structure* to denote regions within the tissue which have a different acoustic impedance value, so that part of the transmitted wave returns back to the transducer.

- Reflection and Refraction

  When a wave encounters an interface, part of the wave is reflected from the boundary and part of the wave is transmitted across the boundary. Thus, two waves are generated (fig. 3.2(a)):

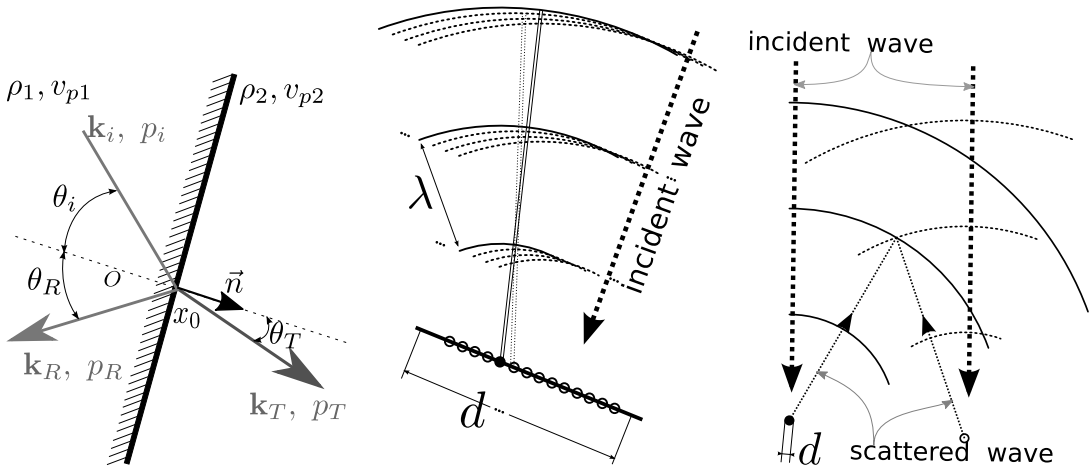

(a) Reflection and refraction (b) Reflection ($d \gg \lambda$) (c) Diffuse scattering ($d < \lambda$)

Figure 3.2: Interaction of sound waves with structures of different sizes with respect to λ. (a) Incident (i), reflected (R) and refracted (T) sound waves. Snell's law defines: incident angle and reflection angle are equal ($\theta_i = \theta_R$), and incident angle and refraction angle are determined by the condition $\frac{c}{v_{p1}} \sin\theta_i = \frac{c}{v_{p2}} \sin\theta_T$. (b) If the structure is smooth and much larger than λ, the wave is reflected following Snell's law. (c) If the structure size is much smaller than λ, the structure scatters sound in all directions, and signal from different scatterers can be out of phase.

- Reflected wave p_R. Also called echo wave. This propagates back inside the same medium as the incident wave, $p_R(\mathbf{r}, t) = p_{R0} e^{-i(\mathbf{k}_R \cdot \mathbf{r} - \omega t + \phi)}$.
- Refracted wave p_T. Also called transmitted wave. This propagates across the interface to the second medium, $p_T(\mathbf{r}, t) = p_{T0} e^{-i(\mathbf{k}_T \cdot \mathbf{r} - \omega t + \phi)}$.

The direction of both p_R and p_T is characterised by Snell's law:

$$\begin{aligned} \mathbf{k}_i(\mathbf{r}) \times \hat{\mathbf{n}}(\mathbf{r}) &= \mathbf{k}_R(\mathbf{r}) \times \hat{\mathbf{n}}(\mathbf{r}) = \mathbf{k}_T(\mathbf{r}) \times \hat{\mathbf{n}}(\mathbf{r}) \\ &\qquad at\ \mathbf{r} = \mathbf{r}_{interface} \end{aligned} \tag{3.6}$$

where $\mathbf{r}_{interface}$ is any point in the interface and $\hat{\mathbf{n}}(\mathbf{r})$ is the vector normal to the interface.

The relationship between the amplitudes of the three waves must satisfy the condition that both pressure and the normal component of the velocity at the interface are continuous in the interface. This means that:

$$\left.\begin{aligned} p_i(\mathbf{r}, t) + p_R(\mathbf{r}, t) &= p_T(\mathbf{r}, t) \\ [\mathbf{v}_i(\mathbf{r}, t) + \mathbf{v}_R(\mathbf{r}, t)] \cdot \hat{\mathbf{n}} &= \mathbf{v}_T(\mathbf{r}, t) \cdot \hat{\mathbf{n}} \end{aligned}\right|_{\mathbf{r}=\mathbf{r}_{interface}} \tag{3.7}$$

Using (3.5) as input into the second equation in (3.7) yields

$$\frac{p_i(\mathbf{r},t)\cos\theta_i - p_R(\mathbf{r},t)\cos\theta_R}{Z_1} = \frac{p_T(\mathbf{r},t)\cos\theta_T}{Z_2}\bigg|_{\mathbf{r}=\mathbf{r}_{interface}} \tag{3.8}$$

where the $-$ sign in the reflected wave is justified because the angle between $\hat{\mathbf{k}}_{\mathbf{R}}$ and $\hat{\mathbf{n}}$ is $\pi-\theta_R$. From (3.7) and (3.8) we obtain the reflection and transmission coefficients for the pressure:

$$\begin{aligned} R_p &= \tfrac{p_R}{p_i} = \tfrac{Z_2\cos\theta_i - Z_1\cos\theta_T}{Z_2\cos\theta_i + Z_1\cos\theta_T} \\ T_p &= 1 + R_p = \tfrac{p_T}{p_i} = \tfrac{2Z_2\cos\theta_i}{Z_2\cos\theta_i + Z_1\cos\theta_T} \end{aligned} \tag{3.9}$$

Note that when $R_p < 0$ the reflected wave experiences a phase shift of $\pi/2$. If the ultrasonic wave hits the interface orthogonally, the amount of energy returning back to the transducer (and therefore contributing to produce the echo image) depends upon the acoustic impedance of the mediums. Table 3.5 (a) shows typical ranges of sound velocity (c), density (ρ) and acoustic impedance (Z) in soft tissue (ST), air (A) and bones (B). Table 3.5 (b) shows the resulting reflection coefficient (R_p) when a sound wave goes from one medium (Med. 1) to another (Med. 2). Three cases are of particular interest:

- In the interface between two different soft tissues, R_p is usually less than 1%, and most of the energy is transmitted to generate new echoes at deeper interfaces. Similarly, when the echo returns from a deep layer, most of this reflected echo will arrive back to the transducer and contribute to form the image.
- In the interface **soft tissue** to **air**, $R_p \approx 0.99$, which means that almost no energy is transmitted and therefore nothing deeper than that interface will be detected.
- In the interface **soft tissue** to **bone**, $R_p \geq 0.5$, and therefore very little energy continues to deeper layers and comes back to the transducer.

When the ultrasound wave encounters bones (or other rigid mediums) or air, the resulting image will show a shadow extending from that depth onwards, because very little energy is transmitted through the interface. The resulting

Med.	$c\ [m/s]$	$\rho\ [kg/m^3]$	$Z\ \times 10^6\ [kg/m^2/s]$
ST	1450 ± 110	1065 ± 235	1.6 ± 0.25
A	330	1.21	0.0004
B	3500	2300	7.8

(a) Material properties of the medium.

		Med. 2		
		ST	A	B
Med. 1	ST	0 ± -0.14	0.99	-0.65 ± 10
	A	-0.99	0	-0.99
	B	0.65 ± 10	0.99	0

(b) Reflection coefficient R_p.

Table 3.5: Medium properties and impact on wave propagation. Data from Evans and McDicken (2000) and Martin and Ramnarine (2010).

artefact is known as *shadowing*. An example of shadowing due to bones is shown in Fig. 3.3(a). In cases when R_p is very close to 1 and the interface is large and smooth, e.g. in tissue-air interfaces, mirror artefacts can occur, as shown in Fig. 3.3(b). In this case, most of the signal energy is reflected back from the interface following Snell's law. However, after reflection, the wave encounters other scatterers which change the wave's path increasing the return time, and therefore the returning echo will be interpreted as originated at a larger depth. The resulting image will show structures beyond the highly reflective interface which in reality are a mirror of the tissue before the interface.

The reflection and refraction processes as described above occur when the interface is large with respect to the wavelength λ. This means that the particles that form the interface are tightly placed together constructing a smooth surface (Fig. 3.2(b)), and the wave *sees* a surface much larger than its wavelength. Ultrasonic waves used for echocardiography have a frequency range between $2MHz$ and $15MHz$ (Martin and Ramnarine, 2010), which means that their wavelength is in the range of $0.01mm$ to $0.77mm$. Boundaries between tissues are in general larger that these values, and sound propagation through them are explained by Snell's law. However, there are changes in acoustic tissue properties (e.g. acoustic impedance) at a scale smaller than λ. For these cases, reflection from tissue particles (scatterers) require a different propagation model.

- Diffuse Scattering

(a) Bone shadowing. (b) Mirror image.

Figure 3.3: Artefacts in B-Mode images due to large differences in acoustic impedance through an interface. (a) The presence of a bone produces a shadow which extends axially. (b) In the interface liver-lung (diaphragm), most of the energy of the incident wave $\mathbf{k_i}$ is reflected following Snell's law in the direction $\mathbf{k_R}$, which would miss the transducer. However, on its way the reflected wave encounters a scatterer at position p which reflects part of the signal in the direction $\mathbf{k'_R}$ towards the transducer. The transducer interprets the receive echo as coming from the direction of $\mathbf{k_i}$ but further than the interface (point p') since the time delay is larger. The result is a mirrored image on the other side of the interface.

When the ultrasonic wave hits a structure (scatterer) whose size is much smaller than λ, sound is scattered in all directions (Faran, 1951). Note how this is different to hitting a smooth surface ($> \lambda$) in which case sound is reflected with the same angle as the incident angle, as shown in Fig. 3.2(a) and described above). This particular kind of reflection by small structures is called *diffuse scattering*.

Scatterers within a resolution cell (*i.e.* a region where two separate structures in tissue are too close to be resolved in the image) are due to small changes in acoustic impedance within a tissue which would otherwise be regarded as being homogeneous, and may be changes in compressibility or density or both (Evans and McDicken, 2000). Their location is regarded as random since it is not correlated with the underlying structure of the tissue (Dantas et al., 2005), however the resulting signal produces a deterministic pattern called *speckle*. Speckle appears in echo images as a texture pattern, and under the same scanning conditions the resulting pattern is always the same, thus its deterministic nature (Burckhardt, 1978). Since speckle formation depends on

the scanning conditions, the resulting speckle pattern is dependent on the imaging system.

Mathematically, speckles are generated by the summation of random phasors (complex waves with random phase), therefore the resulting wave amplitude can be thought of as a random walk problem (Anderson and Trahey, 2000). If there is a large number of scatterers per resolution cell, the resulting amplitude is assumed to be a random variable which follows a Rayleigh distribution (Burckhardt, 1978; Gill, 1985). However this assumption appears to be not always true, and therefore texture characterization has been an active field of study since the 1970s (Dantas et al., 2005; Meunier and Bertrand, 1995; Rao et al., 1990; Tuthill et al., 1988; Zemp et al., 2003).

Figure 3.4 represents the formation of the speckle pattern by two scatterers. Intuitively, each scatterer becomes a point source of ultrasound when the incident wave reaches its location. The same applies to other scatterers randomly distributed in its neighbourhood, and therefore depending on the relative distances of the scatterers and on the wavelength constructive and destructive interference occurs (Fig. 3.4(a)), producing differences in the amplitude of the resulting backscattered signal which results in the speckle pattern that contributes to texture formation in the images (Fig. 3.4(b)).

Since the speckle pattern does not represent morphology of tissue, it has been regarded as noise and therefore many publications have proposed its elimination or reduction (Achim et al., 2001; Gupta et al., 2004; Tay et al., 2010). However, consistency of the speckle pattern has been exploited for tissue tracking (Amundsen et al., 2006; Bohs et al., 2000) and tissue classification (Kadah et al., 1996; Thijssen, 2003).

- Diffraction

  Diffraction may be described as the apparent bending and the spreading out of waves when they encounter structures in the wave direction. Diffraction occurs independently of the size of those structures, but it is more pronounced when the diffracting objects are of a size approximately equal to λ. Diffraction can be understood by the Huygens-Fresnel principle (Fresnel, 1816; Huygens,

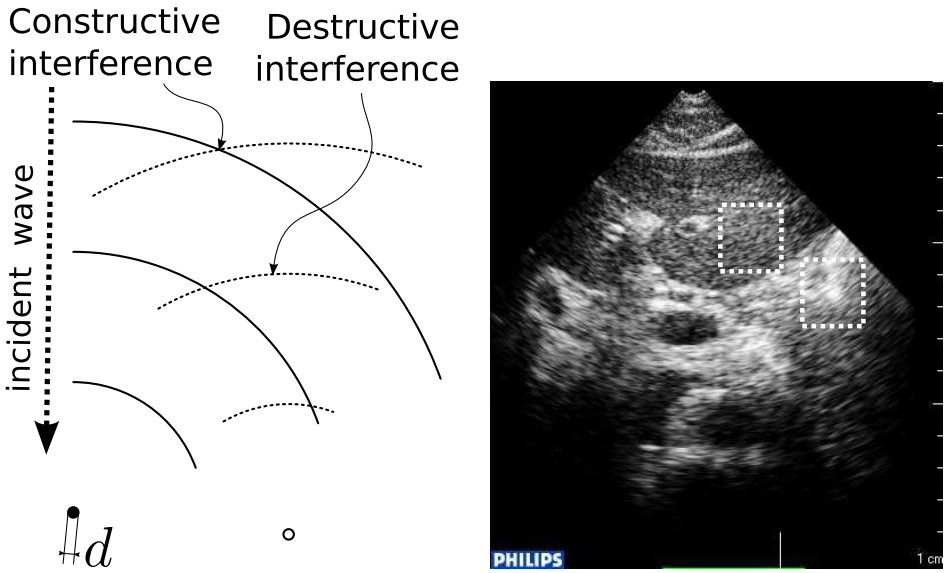

(a) Speckle formation. (b) Speckle patterns.

Figure 3.4: Speckle B-Mode images. (a) Phase difference in the reflected wave from two small scatterers produces constructive and destructive interference which is responsible for the speckle pattern. (b) Resulting speckle patterns in a B-Mode image showing the liver and surrounding tissue, where the two white blocks show different textures belonging to different kinds of tissue. The texture, which does not reflect the underlying morphology, is a combined effect of speckle and variation with depth of the system point spread function (PSF).

1690), which establishes that every point in the interface reached by the wavefront acts as a punctual source of the wave. For example when a planar wavefront, made up by the sum of (ideally) infinite punctual spherical wavefronts, reaches a small structure such as the an edge of a small window, the absence of punctual wavefronts beyond the edge curves the planar wave near the edges, changing the direction of propagation.

The difference between diffuse scattering and diffraction is subtle, sometimes even ambiguous (Laven, 2010). Diffraction can be regarded as a particular case of scattering, in which the wave hits an obstacle which blocks part of the wavefront, and the part of the wave which is not blocked propagates towards the blocked region of the space, bending around the obstacle.

- Attenuation

  When sound travels through a medium, its intensity diminishes with distance. This loss of intensity is called *attenuation*. Attenuation is due to two processes: absorption or dissipation and scattering (Babick et al., 2000). Absorption is

the conversion of the sound energy to other forms of energy, typically heat, during the propagation of the pressure wave due to relaxation mechanisms (Wells, 1975). Scattering, as explained before, results in some energy of the wave being reflected into different directions which will not be captured by the transducer, and energy is therefore lost.

Other processes, such as reflection, refraction, non linear propagation and beam-divergence (Evans and McDicken, 2000) also contribute to attenuation, and they are in general dependent on the wave frequency, with attenuation increasing rapidly at higher frequencies. Attenuation is typically characterised as a decaying exponential driven by the frequency-dependent attenuation coefficient $\alpha(f)$ as follows:

$$A(x) = A_0 e^{-\alpha(f)x} \tag{3.10}$$

In this expression A_0 is the unattenuated amplitude of the propagating wave at some location. The amplitude $A(x)$ is the reduced amplitude after the wave has travelled a distance x from that initial location. The value of α depends on the material and the frequency, and most ultrasound textbooks include tables with values for tissues and frequencies related to medical ultrasound. When α is measured in dB/cm, the relationship with frequency is roughly linear (Martin and Ramnarine, 2010).

Since attenuation is dependent on depth, images need to be compensated for its effects in order to show homogeneous intensity for organs and tissues which extend along the beam direction.

3.2 Ultrasound Imaging

This section explains how the physical interactions of ultrasound waves with biological tissue described before can be used to build an image of the inside of a patient. If the velocity of the sound in tissue is known, the time between emission and reception is used to calculate the depth of the structure which generated the echo. The intensity of the returned signal is translated into brightness for image construction.

Briefly, ultrasound images are produced as follows: an ultrasonic transducer (Sec. 3.2.1) sends a pulse into the tissue, and receives the backscattered echo a few

ms later. The received signal is pre-processed to compensate for attenuation and time delay and is then converted into pixel brightness at a particular location of the output image (3.2.2). Different ways of processing echo signals and converting them into pixel brightness produce different imaging modes (3.2.3).

3.2.1 Transducers

Echo transducers are devices that convert electric energy into mechanic energy (pressure waves) and *vice versa*. Most of them are manufactured with piezoelectric crystals. Transducers are usually constituted by arrays of 64, 128 or 256 crystals (Whittingham and Martin, 2010).

There are a wide variety of transducers in the market with different shapes and functions: linear arrays, 1D sector (phased) arrays, curved arrays, and 2D phased arrays. Figure 3.5 shows three cardiac transducers, which are compatible with the Philips iE33 echo system and were used for the experiments in this thesis. The X3-1 (Fig. 3.5(a)) is a 2D phased array transducer which produces 3D Brightness Mode (B-Mode) and Doppler (3 to $1MHz$), the S5-1 (Fig. 3.5(b)) is a sector array transducer which produces 2D B-Mode and Doppler images (5 to $1MHz$) and the X7-2 (Fig. 3.5(c)) is a high frequency (7 to $2MHz$) 2D phased array transducer for 3D B-Mode and colour Doppler imaging. The X3-1 was used on volunteers and big paediatric patients, whereas the X7-2 was only used on small babies. The S5-1 was used on all patients for Pulsed Wave Doppler (PWD) and Continuous Wave Doppler (CWD) measurements.

(a) 3D probe X3-1 (b) 2D probe S5-1 (c) 3D probe X7-2

Figure 3.5: Two cardiac echo transducers by Philips, for for the iE33 echo system.

3D imaging is achieved with the 2D phased array technology (Rabben, 2011). In a

2D phased array, transducer elements are placed in a regular 2D array on the surface of the transducer. Each crystal can be activated individually and electronically in order to generate or receive a small wavefront. Composition of individual wavefronts results in the full US beam by the previously mentioned process of beamforming. Beamforming consists of producing a desired beam shape and direction by combining the sound wave from many transducer elements. The basic idea is represented in 2D in Fig. 3.6. Since sound propagation is linear, the contribution of each element will sum up, and if they are all in phase this will create a planar wavefront. By delaying the pulse from each transducer element, the resulting wavefront can be oriented to a desired direction (Fig. 3.6(a)). Similarly, delays can be used to focus the beam to a point at a particular depth (Fig. 3.6(b)). Analogously, received echoes can be delayed to receive ultrasonic waves coming from a particular location and direction.

In addition, the amplitude of the wave produced by each transducer element can be weighted to alter the transmit function. This is known as *apodization*.

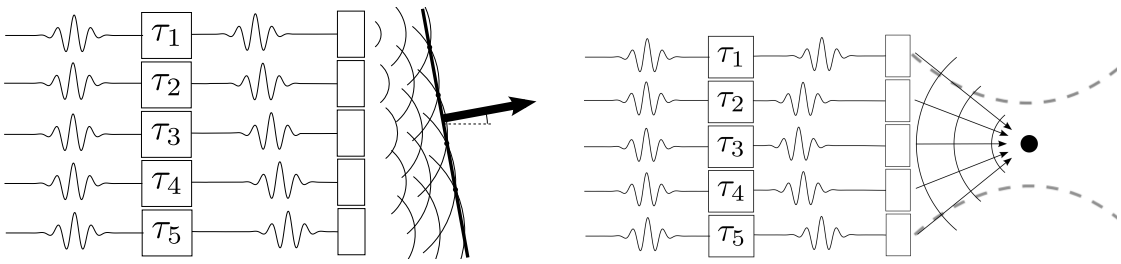

(a) Beamforming of a planar wavefront.

(b) Focusing of the beam to a point.

Figure 3.6: Beamforming process. The introduction of a different delay τ_i in the excitation of each crystal allows for beam focusing to a particular direction or location.

3.2.2 Echo Image Formation

The image formation process has several steps (Bamber, 1999), that are represented in figure 3.7.

1. Transmit US signal

   The signal processing in an ultrasound scanner begins with the shaping and delaying of the excitation pulses applied to each element of the transducer array to generate a focused, steered and apodized pulsed wave (Fig. 3.6) that

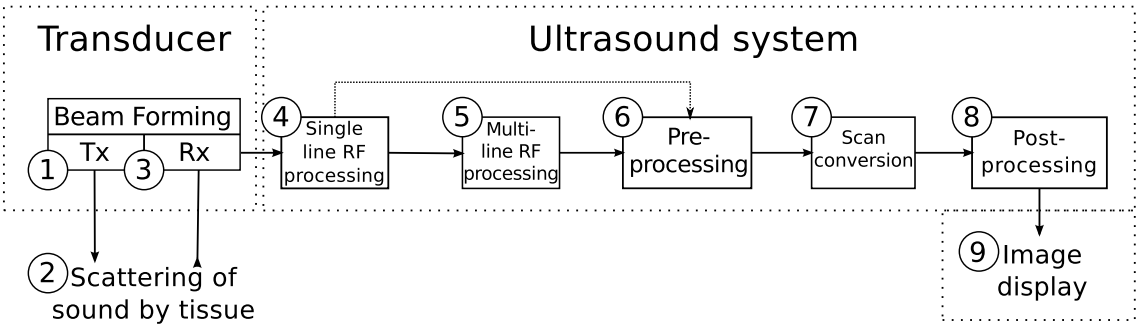

Figure 3.7: Echo image formation process. Inspired by the lecture notes by Bamber (1999).

propagates into the tissue. Modern 3D imaging systems usually perform part or all of this process in the transducer (Rabben, 2011).

2. Scattering of sound by tissue

   The transmitted signal propagates across the tissue. Then, the returned signal is a combination of all the phenomena described in section 3.1.2.

3. Receive returned wave

   The echoes resulting from scattering of the sound by tissue are received by all elements within the transducer array. The electronic signal produced by each element is processed by applying apodization and delays for reception beamforming, analogous to those performed during transmission (Szabo, 1998).

4. Single line Radio Frequency (RF) processing

   Signals corresponding to individual axial lines undergo different filtering operations, e.g. frequency analysis to extract velocity information (Wells, 1998), amplification to compensate for signal attenuation *i.e.* Time Gain Compensation (TGC), also called *swept gain*.

5. Multi-line RF processing

   In some systems multiple RF lines are processed together e.g. interpolation between lines, phase comparison or other filtering (Bamber, 1999) is applied to improve image quality.

6. Pre-processing

Sometimes, once all lines have been processed, they are jointly filtered before the actual image is formed. Examples of pre-processing techniques that may be applied are resolution enhancement, contrast enhancement, speckle reduction or suppression, etc. (Lizzi and Feleppa, 2000).

7. Scan conversion

   The shape of the scanned region depends on the beamforming and beam steering, which may differ from one application to another. In cardiac applications, echo transducers typically insonate a frustum shaped region. The Field of View (FoV) is sampled into a polar (2D) or spherical (3D) grid. Scan conversion consists in resampling the pre-processed data into a cartesian rectangular grid.

8. Post-processing

   Post-processing can consist of several operations on the scan-converted image, including image enhancing, smoothing, denoising or combination of overlay of information from different sources e.g. anatomical information and velocity from blood or tissue in colour Doppler imaging.

9. Display

   Most echo systems include a display which show the images as well as other information related to the exam, the patient and acquisition parameters.

3.2.3 Echo Imaging Modes

Echo systems are capable of acquiring and representing data in different forms. The main imaging modes are represented in Fig. 3.8.

- Amplitude Mode (A-Mode)

  This mode shows the intensities of the received signal plotted against depth for a single 1D line (Fig. 3.8(a)).

- Brightness Mode (B-Mode)

  The combination of multiple 1D lines (*i.e.* multiple A-Mode images) yields 2D and 3D images of the anatomy within the FoV (Fig. 3.8(b)). Signal intensity in now represented as pixel/voxel brightness.

- Time-Motion Mode (M-Mode)

  This technique generates a 2D image showing depth against time. At each time point, a 1D line is displayed, the result being a trace of the motion of the structures within the scan line (Fig. 3.8(c)).

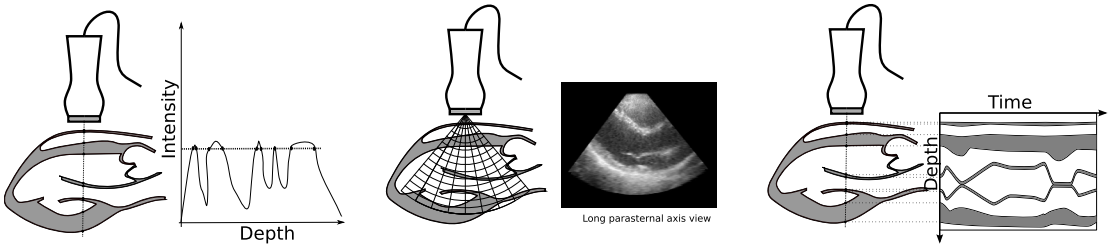

(a) A-Mode. The output image is a 1D curve representing the amplitude of the echo against the depth.

(b) B-Mode. The output image can be seen as a set of A-Mode curves where the amplitude of the echo is represented as brightness along the beam direction.

(c) M-Mode. The output image is a 1D + time image in which the amplitude is represented as brightness and the horizontal axis represents the time.

Figure 3.8: Echo imaging modes: A-Mode, B-Mode and M-Mode.

In addition, most systems also feature Doppler modes, which are used for measuring and imaging tissue and blood velocities, and are covered in section 3.3.

3.2.4 Image Resolution

Image resolution is defined as the smallest distance between two distinct structures that yields two differentiable objects in the image (Ng and Swanevelder, 2011). In echocardiography, three types of resolution must be considered:

- **Axial resolution** is the ability to resolve two structures which are close to each other along the beam direction. A fine axial resolution means that two structures which are very close along the beam direction can be distinguished in the image (Martin, 2010). Axial resolution depends mostly on the pulse length. Shorter pulses are reflected from interfaces close to each other in the axial direction without interfering. Shorter pulses require higher frequencies. Unfortunately, attenuation increases rapidly with frequency and therefore high frequencies will be severely attenuated with depth. This establishes a trade-off between depth of the image and axial resolution.

- **Lateral resolution** is the ability to resolve two structures which lie close to each other on the plane orthogonal to the beam direction. Lateral resolution depends on the beam width. The narrower the beam is, the finer the lateral resolution will be. Beam width depends on the aperture size, and the density of transducer elements. A large aperture produces a narrow beam. Usually, the aperture size is relatively small, so narrowing of the beam may be achieved by focusing. Focusing is achieved by using many transducer elements to produce a single beam (Sec. 3.2.2). In theory, under ideal conditions, the effective resolution is half the the beamwidth (defined as the width of the beam at half the peak power) (Martin, 2010). In practice, many factors can reduce the ability to resolve two structures thus the beamwidth is often taken as the effective lateral resolution.

- **Temporal resolution** is the time from the beginning of one frame to the beginning of the next. Temporal resolution increases with shorter depths (the pulse has to travel a shorter distance) and with fewer scan lines. In general, the bigger the image and the higher spatial resolution, the lower the temporal resolution.

Current systems achieve typical values of around 20 images per second of $200 \times 200 \times 200$ voxels (scan-converted) with a spatial resolution of the order of $0.7mm^3$ for 3D+t B-Mode sequences.

3.3 Echo Doppler Imaging

Echo Doppler is a modality that provides information about the velocity of scatterers based on the Doppler effect, discovered by Doppler (1842). This section explains how echo Doppler is used to measure tissue and blood velocity and the main characteristics of the resulting images.

3.3.1 The Doppler Effect

When a wave source moves relative to the observer, the observed frequency is different to the original frequency sent by the moving source. The phenomenon is illustrated in Fig. 3.9.

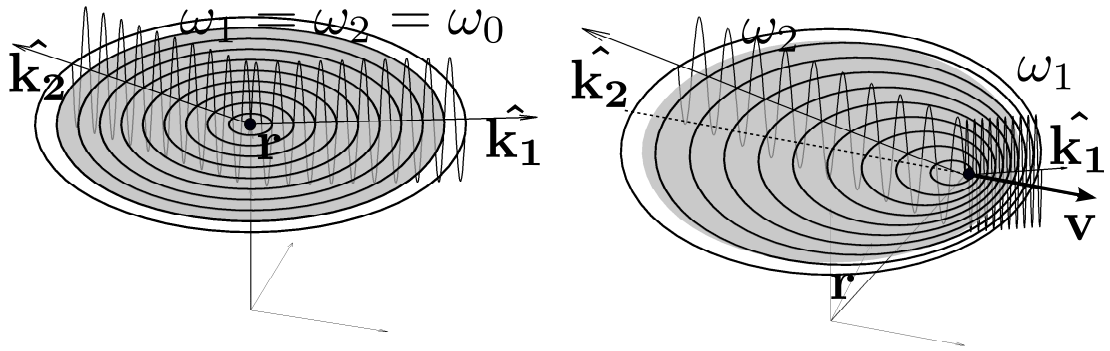

(a) Static source and observers (b) Moving source and static observers

Figure 3.9: Doppler Effect. (a) When the source is static with respect to the observers, all observers receive the same frequency $\omega_1 = \omega_2 = \omega_0$. (b) When the source moves, observers receive waves with shifted frequencies. If the source moves towards the observer, the frequency appears increased and if it moves away from the source it appears decreased with respect to the original frequency: $\omega_1 > \omega_0$ and $\omega_2 < \omega_0$.

If the source and the observer (or observers) are stationary with respect to each other (Fig. 3.9(a)), all observers to which the wave arrives in the direction of $\hat{\mathbf{k}}_\mathbf{i}$ see the same frequency, ω_0, which is the frequency emitted by the source. Numerically, the observed frequency $\omega_1 = \omega_2$ can be computed by differentiation of the phase of the wave in (3.4) with respect to time:

$$\omega_i = \partial_t \arg\left[\bar{p}(\mathbf{r}, t)\right] = \omega_0 \qquad i = 1, 2 \tag{3.11}$$

If the source moves with a velocity $\mathbf{v}$, the wave will arrive at each observer with a different frequency (in general $\omega_1 \neq \omega_2 \neq \omega_0$) depending on the direction of observation $\hat{\mathbf{k}}_\mathbf{i}$, because the wavefront is compressed in the direction of $\mathbf{v}$.

If the observer moves with respect to a static source, with a velocity $\mathbf{v_R}$, the observed wave becomes

$$\bar{p}(\mathbf{r}, t) = p_0 e^{-i\phi_0} e^{-i(\mathbf{k}\cdot(\mathbf{r}+\mathbf{v_R}t)-\omega t)} \tag{3.12}$$

and the received frequency can be obtained by differentiation:

$$\omega_i = \partial_t \left[-\mathbf{k_i} \cdot (\mathbf{r} + \mathbf{v_R}t) + \omega t\right] = \omega\left(1 - \hat{\mathbf{k}}_\mathbf{i} \cdot \frac{\mathbf{v_R}}{c}\right) = \omega\left(1 - \frac{\|\mathbf{v_R}\|\cos\theta}{c}\right) \tag{3.13}$$

where $\mathbf{k} = \hat{\mathbf{k}}\frac{\omega}{c}$ and θ is the angle between the direction of motion of the observer and the direction of observation. The case when the source moves with a velocity

$\mathbf{v}$ while the observer stays still (Fig. 3.9(b)) needs to be approached differently, because from the point of view of the source, the medium through which the sound waves propagates also moves. This can be accounted for by introducing a new wave vector $\mathbf{k_s}$. The increase in velocity of the wave in the medium is:

$$\Delta c = -\hat{\mathbf{k}} \cdot \mathbf{v} = -\frac{c}{\omega}\mathbf{k} \cdot \mathbf{v} \tag{3.14}$$

where the $-$ sign is due to the medium having an apparent velocity of $-\mathbf{v}$ with respect to the source. The new velocity of the wave in the medium is then $c' = c + \Delta c$, and the new wave vector is

$$\mathbf{k_S} = \hat{\mathbf{k}}\frac{\omega}{c'} = \hat{\mathbf{k}}\frac{\omega}{c\left(1 - \frac{\mathbf{k}\cdot\mathbf{v}}{\omega}\right)} = \mathbf{k}\frac{1}{1 - \frac{\mathbf{k}\cdot\mathbf{v}}{\omega}} = \mathbf{k}\frac{1}{1 - \frac{\|\mathbf{v}\|\cos\theta}{c}} \tag{3.15}$$

which yields an observed frequency

$$\omega' = \partial_t \left[-\mathbf{k_S} \cdot (\mathbf{r} - \mathbf{v}t) + \omega t\right] = \omega\left(\frac{1}{1 - \frac{\mathbf{v}\cdot\hat{\mathbf{k}}}{c}}\right) = \omega\left(\frac{1}{1 - \frac{\|\mathbf{v}\|\cos\theta}{c}}\right) \tag{3.16}$$

In echo Doppler imaging the transducer is static with respect to the scatterer which moves with blood or tissue. First, the scatterer is the observer, and receives a wave with shifted frequency ω_1, as described by (3.13). Then, the scatterer reflects the sound wave back to the transducer, this time the scatterer being the moving source and the transducer an static observer, and therefore the transducer receives a wave with a different frequency ω_2, as governed by (3.16). The relation between the original frequency ω_0 and the received frequency ω_2 is

$$\left.\begin{array}{rcl} \omega_2 & = & \omega_1\left(\frac{1}{1-\frac{\mathbf{v}\cdot\hat{\mathbf{k}}}{c}}\right) \\ \omega_1 & = & \omega_0\left(1 - \hat{\mathbf{k}}\cdot\frac{\mathbf{v_R}}{c}\right) \end{array}\right\} \omega_2 = \omega_0\frac{1 - \hat{\mathbf{k}}\cdot\frac{\mathbf{v_R}}{c}}{1 - \hat{\mathbf{k}}\cdot\frac{\mathbf{v}}{c}} = \omega_0\frac{1 - \hat{\mathbf{k}}\cdot\frac{\mathbf{v_R}}{c}}{1 + \hat{\mathbf{k}}\cdot\frac{\mathbf{v_R}}{c}} \tag{3.17}$$

where $\mathbf{v} = -\mathbf{v_R}$.

In Doppler ultrasound, ω_0 is known and ω_2 can be measured, and the goal is to calculate the velocity of the scatterer. Rearranging (3.17):

$$\Delta\omega = \omega_0\frac{-2\hat{\mathbf{k}}\cdot\frac{\mathbf{v}}{c}}{1 + \hat{\mathbf{k}}\cdot\frac{\mathbf{v}}{c}} \approx -2\omega_0\hat{\mathbf{k}}\cdot\frac{\mathbf{v}}{c} \tag{3.18}$$

where the approximation is justified when $c \gg \|\mathbf{v_R}\|$, which is the case in echo Doppler, where $c \approx 1540 m/s$ and blood velocity is in the order of 1 to $10 m/s$.

In Doppler imaging, the emitted frequency w_0 is known and the frequency shift $\Delta\omega$ is measured. The goal is to calculate the velocity of the scatterer. Equation (3.18) yields

$$\hat{\mathbf{k}} \cdot \mathbf{v} = \|\mathbf{v}\| \cos\theta \approx -c\frac{\Delta\omega}{2\omega_0} \tag{3.19}$$

where θ is the angle between the direction of the scatterer (e.g the direction of blood flow) and the direction of observation (*i.e.* the direction of the ultrasonic beam). Two important remarks can be extracted from (3.19).

Remark 1. *Doppler system does not measure the true velocity of the scatterer, but only the component of the velocity along the direction of observation,* $\hat{\mathbf{k}}$ *i.e. the beam direction.*

Remark 2. *In a standard 3D echo system, the beam is electronically steered to cover a spherical frustum shaped region. The beam direction changes for each imaged point, and is orthogonal to spherical surfaces centred at the transducer surface. The direction along which velocity is measured by a Doppler system is therefore orthogonal to spherical surfaces of increasing depth.*

3.3.2 From the Doppler Effect to Velocity Measurements: Spectral Doppler

This section explains how a returning echo with a phase shift is translated into a velocity value, and how this velocity can be displayed as a function of time. This kind of representation is called a time-velocity spectrum or spectral Doppler. There are two different ways of producing spectral Doppler traces:

- Continuous Wave Doppler (CWD). In this mode, US waves are continuously sent and continuously received. To accomplish this, one or more transducer elements permanently emit a pressure wave and one or more transducer elements permanently receive the echoes. Since the transmission and reception is performed continuously, pulse length is infinite and spatial localization is done exclusively by focusing and beamforming (Fig. 3.10(a)). For this reason, the scatterers are poorly localized in depth, since all the return signals

coming from the same beam line are integrated. The main advantages of this technique are high temporal resolution, high sensitivity to low velocities and absence of aliasing artefacts.

Figure 3.10(b)) shows the process of measuring the frequency shift $\Delta\omega = \omega_2 - \omega_0$ in CWD. Echo signal is continuous in time. The demodulation consists of mixing the transmitted with the reference signal (*i.e.* signal multiplication). The mixed signal (also called *Doppler signal*) has a high frequency component $(\omega_2 + \omega_0)$ and a low frequency component $(\omega_2 - \omega_0)$. Therefore low pass filtering can be used to remove the high frequency component and yield a wave whose frequency is $\Delta\omega$. The frequency can be then calculated by a Fast Fourier Transform (FFT), which provides the distribution of frequencies (*i.e.* following to (3.19), the distribution of velocities along the beam direction). An example of a resulting velocity sonogram is shown in Fig. 3.10(c). The sonogram is displayed as an image where the horizontal axis (t) represents the time and the vertical axis (v) represents velocity (along the beam direction). The brightness is proportional to the power density of the received signal originated at scatterers moving at the velocity v at time point t.

- Pulsed Wave Doppler (PWD). In this mode all the active elements work in both emission and reception (Fig. 3.11(a)). They emit a short burst of ultrasound and then switch to receive mode. The received signal is time-gated to resolve the depth from which it comes. Figure 3.11(b) shows the demodulation process. In this case, the reference signal is continuously generated, as in CWD. The received pulses, however, are very short in time so the frequency shift due to the Doppler effect is not noticeable. Instead, each received pulse has been reflected by the scatterer from a different position, and therefore arrives at the transducer delayed (or advanced) with respect to the reference signal, which is equivalent to a phase shift. The amplitude of the mixed (multiplied) signal depends on this phase shift. As shown in Fig. 3.11(b), each individual pulse contributes with one sample to the demodulated signal (Hoskins, 2010). Once the signal has been demodulated, the frequency distribution can be computed using the FFT.

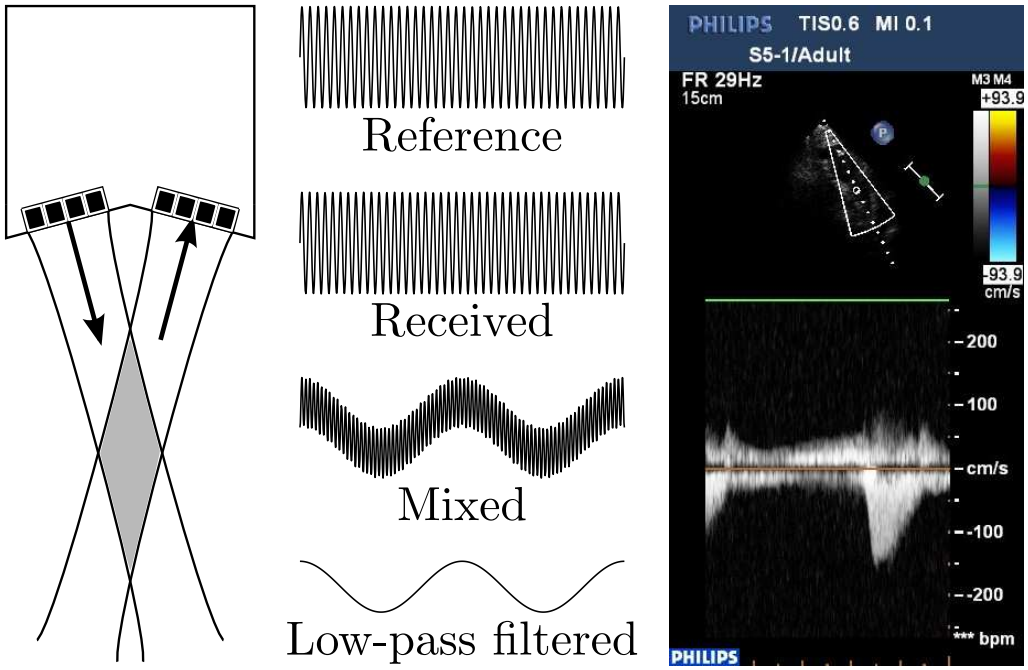

(a) Simultaneous emission and reception. (b) Demodulation of the Doppler signal. (c) Example of CWD trace.

Figure 3.10: Continuous Wave Doppler (CWD). (a) One or more elements are permanently working in emission and one or more are permanently in reception. (b) Received echo with shifted frequency is mixed with a reference signal with the original frequency, and the demodulated signal, whose frequency is the frequency shift, is obtained by low pass filtering. (c) CWD sonogram acquired on a healthy patient, showing the velocity distribution in the ascending aorta from a suprasternal window.

Figures 3.10(c) and 3.11(c) show the sonograms of the two modalities when imaging the same structure in a healthy volunteer. The envelope of both curves is very similar, with a velocity peak at the same time point and of similar magnitude.

There are therefore a few important differences between CWD and PWD. Homogeneity of the traces is different: intensity values in CWD are produced by integration in a much broader region, where many different velocities contribute to signal, and therefore the resulting trace has an homogeneous white colour from averaging, whereas Pulsed Wave Doppler (PWD) can resolve in depth by time-gating and also axially by focusing. Therefore the measured velocity correspond to a smaller region within the vessel and the sonogram is less blurred. The velocity range is much larger with CWD (the only limitation is the sampling rate of the digitized image). In the case of PWD, the range of velocities that can be measured is limited by the pulse repetition frequency, f_{pr}. As mentioned before, each pulse contributes with one sample to the demodulated signal. This means that the sampling rate of the demodulated

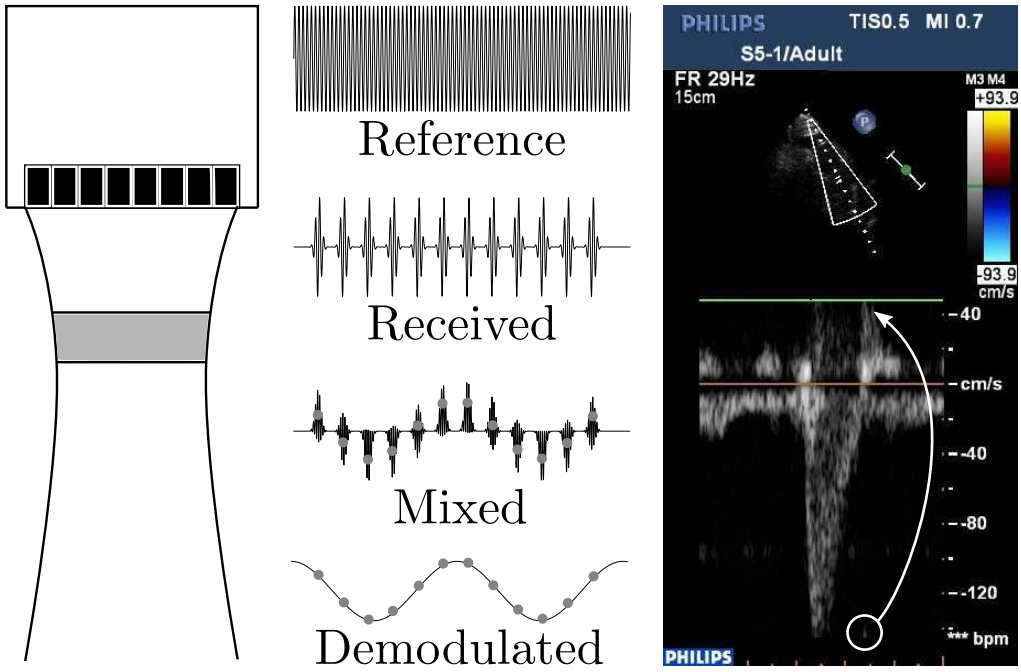

(a) Alternate emission and reception using the same transducer elements.

(b) Signal demodulation.

(c) Example of PWD trace.

Figure 3.11: Pulsed Wave Doppler (PWD). (a) All the transducer elements alternate from emission to reception. In reception, received echoes are time-gated to resolve depth. (b) Each received echo contributes to the demodulated signal with one sample, whose amplitude is proportional to the phase shift between the received pulse and the reference signal. (c) Spectral PWD trace acquired on a healthy patient, showing the velocity trace in the ascending aorta from a suprasternal window.

signal is equal to f_{pr}. The Nyquist-Shannon sampling theorem (Shannon, 1949) establishes that the maximum frequency than can be represented unambiguously by a sampled signal is half the sampling frequency, and aliasing occurs beyond this value. Therefore, the maximum frequency shift that can be detected with PWD is $f_{pr}/2$. In the PWD trace, this appears as signal folding for velocities beyond the maximum measurable velocity, as can be seen in Fig. 3.11(c) where the positive peak at $40cm/s$ folds back to $-140cm/s$. Note that no pulse can be sent if the transducer is in reception mode, and it will be longer in reception mode if echoes are expected at larger depths; therefore the maximum measurable velocity decreases with depth. This can be an important limitation in particular in cardiac applications.

3.3.3 From Velocity values to Images: Colour Doppler

PWD technology allows the velocity of the scatterers at a given depth to be calculated by time-gating. Combining PWD with beam steering and focusing (Sec. 3.2) allows velocity values to be mapped to anatomy within a region of space and over time. This technology can be used to measure blood velocity, known as *colour Doppler* imaging which is the focus of this thesis, and also to measure motion of tissue (known as *tissue Doppler*).

In colour Doppler images, the measured velocity is mapped to colours for visualisation. They can then be displayed, typically overlaid onto a B-Mode image (fig. 3.12) for anatomical reference.

Producing a velocity map within a region requires to estimate velocity at many locations in a plane or a volume, which can be very time consuming. Additionally, since each measured location will be mapped to a single colour, the velocity distribution is not needed; instead only the mean velocity is typically mapped[1]. As a consequence, the FFT is not used to calculate the frequency, instead the so called autocorrelation techniques (Kasai et al., 1985; Torp et al., 1994), described in appendix A, are used. These techniques are faster than the FFT and provide the mean velocity, the velocity variance and the signal power.

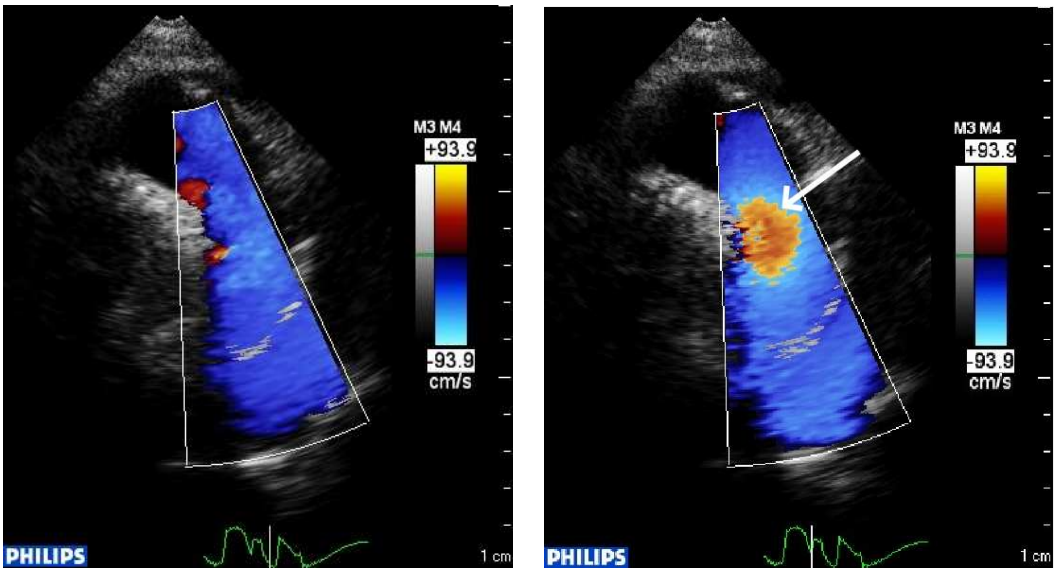

(a) Standard 2D colour Doppler image.

(b) Aliasing artefact in a colour Doppler image.

Figure 3.12: Doppler velocity image (colour), overlaid onto a B-Mode image.

[1]Some colour maps use both average velocity and variance to produce a colour, to give information on turbulence.

Current echo systems provide 2D and 3D colour Doppler imaging capabilities. In spite of the speed-up achieved by autocorrelation techniques, image formation requires a large amount of processing compared with spectral Doppler, and therefore the frame rate is significantly lower. To form an image, the average frequency of the Doppler signal has to be computed for each voxel using the autocorrelation technique. Current systems use two complementary techniques to increase frame rate (Hoskins and Criton, 2010): colour Doppler images are acquired over several cardiac cycles, *i.e.* at each cycle a sector of the image is acquired; and a smaller FoV than the B-Mode image is typically manually selected by the user. Figure 3.12(a) shows an example of the reduced FoV (also called *colorbox*) used in 2D colour Doppler imaging. This way, current systems can achieve frame rates of up to $17 fps$ in 3D colour Doppler images.

3.3.4 Artefacts in Colour Doppler images

Colour Doppler images are formed by echoes reflected back to the transducer by moving scatterers. However, an important difference with anatomical echo imaging modes (Fig. 3.8) is that the phase of the echo is used rather than the amplitude. The phase of the signal is affected by diffraction and attenuation in a different way than the amplitude, e.g. phase modulations can be introduced. However, colour Doppler images are affected by shadowing and mirroring similarly to B-Mode images. In addition, colour Doppler images suffer from some artefacts exclusive to PWD.

- Aliasing

  As explained before, if the velocity along the beam direction is higher that the maximum measurable velocity, the velocity value folds around producing high contrast colour changes in the colour Doppler image, as shown in Fig. 3.12(b).

- Velocity resolution

  Velocity resolution is defined as the smallest difference in the velocity of two spatially (or temporally) distinguishable scatterers that yields two different intensity values in the colour Doppler image, and is mostly determined by the electronics of the echo system (e.g. number of signal quantification levels). Velocity resolution is therefore expressed as a percent of the maximum mea-

surable velocity. Early colour Doppler systems provided a velocity resolution usually worse than 10% Evans and McDicken (2000). Recent studies (Rojo-Álvarez et al., 2007) show velocity resolutions of over 5%, and conclude that velocity resolution has an important impact in accuracy when colour Doppler images are used for quantification.

- Random noise

  Several sources of random noise contaminate colour Doppler images. For example, electronic noise may appear especially when gain is set too high, in which case saturation of electronic circuits may produce random colour in regions where there is no flow. Sounds produced by the body may induce Doppler shifts above the threshold of the clutter filter.

- Spectral broadening

  The angle of insonation is slightly different for each transducer element. The beam direction of each individual element is the direction from the element to the scatterer of interest. In practice, this means that the velocity measured at one point will be measured along different beam directions and therefore a range of velocity values are measured by the ensemble of transducer elements. In spectral PWD this phenomenon appears as a thickening of the velocity trace. In colour Doppler, this translates into a certain ambiguity of the velocity value in the voxel.

- Speckle

  The Random distribution of scatterers produces fluctuations on the phase of the reflected wave which can modify the phase shift produced by the actual velocity of the scatterer (Sec. 3.1.2), and thus yield an erroneous velocity value. Several methods have been proposed to overcome this effect (Hoskins et al., 1990), and most commercial systems use temporal averaging to smooth fluctuations in velocity value.

- Clutter filtering

  Tissue moves much more slowly than blood, therefore tissue motion (e.g. cardiac motion) produces frequency shifts much smaller than blood motion, but

scattered waves from tissue are of greater amplitude. These two facts are used to separate blood motion from tissue motion when producing colour Doppler images, by the means of the so-called clutter filter. In practice, clutter filters are designed so that velocities lower than about $10cm/s$ (which is typically the maximum velocity of tissue in cardiac applications, not taking into account valves) and especially when the amplitude of the echo is high are considered as related to tissue motion and are discarded, producing a signal drop-out in small vessels or low blood velocities.

- Flash artefact

  When the transducer moves quickly with respect to the body, some colour may appear in large areas of the FoV. This artefact is usually easily detected by the operator.

- Signal from side lobes

  It is considered that the echo beam is only the main lobe in the sound radiation pattern of the transducer aperture. However, side lobes may also produce low amplitude echoes which if not attenuated before returning to the transducer, will be processed as if sent by the main lobe.

3.4 Blood Velocity and Flow Measurement with Magnetic Resonance Imaging

Magnetic Resonance Imaging (MRI) is an imaging modality which uses the magnetic resonance phenomenon of protons to produce images of the inside of the body. Further to morphological imaging, MRI can be used to non-invasively measure velocity of moving particles including blood.

The nuclear magnetic moment of protons present in the human body is randomly oriented, therefore the bulk magnetization is zero. However, when inside a magnetic field $\mathbf{B_0}$, the average magnetic momentum aligns with the direction of this magnetic field (defined as the longitudinal z direction). Using a RF pulse, the net magnetization can be flipped into the transverse plane (xy plane). The angular velocity at which the magnetization precesses around the z direction is proportional to the

magnitude of $\mathbf{B_0}$. This rotation produces a time-varying electromagnetic field that induces an electric signal in the receive coils. The signal in the coils can be used to generate an image. To form an image the received signal has to be coded in space. This is achieved by the use of magnetic field gradients along the three directions of the space, which effectively impose a different resonance frequency and phase for each point of the space inside the MRI scanner (Conolly et al., 2000; McRobbie et al., 2006).

Phase-Contrast MRI (PC-MRI) allows the measurement of the velocity of moving protons inside the body. The physical principle behind velocity measurement is that the accumulated phase of a magnetization vector moving along a gradient is proportional to its velocity. To eliminate phase shift originating from non-moving protons, two acquisitions (with different gradient strength) are acquired and the phase difference is taken. Static protons will have identical phase changes in both acquisitions and exhibit zero net phase. However, moving particles will show a net phase difference proportional to their velocity. The measured velocity will be the projection of the true velocity of the particles along the direction of the gradient. In consequence, to obtain a 3D velocity field several acquisitions are required. The maximum measurable velocity (v_{enc}) depends on the strength and duration of the bipolar gradient, and must be set by the user. The velocity of any particle moving faster than v_{enc} will be aliased (phase wrapping). Of all the phenomena which contribute to artefacts and inaccuracy in PC-MRI images, the presence of eddy currents originating from fast-switching gradients has been shown to have a very important effect causing offsets in measured velocity. Gatehouse et al. (2010) showed that small eddy current related errors (e.g. 0.4% of v_{enc}) can potentially cause a 10% error in flow quantification.

In the last years, PC-MRI has become the reference technique for non-invasive flow and velocity quantification, and many authors have used it to assess Doppler based techniques (Garcia et al., 2010; Ge et al., 2005). In the work carried out in this thesis, PC-MRI has been used to validate and assess the accuracy of the proposed methods. Throughout this document, PC-MRI velocity measured along one direction on a 2D slice is defined as temporally resolved through-plane flow-encoded 2D MRI (2D+t Flow MRI), also referred to as *2D flow MRI*. Full velocity mapping over a volume is defined as temporally resolved 3 directional flow-encoded 3D MRI

(3D+t Flow MRI), also referred to as *4D flow MRI*.

3.5 Other techniques for Measuring Blood Velocity and Flow

Many other techniques and methods have been proposed and are used to measure blood velocity or flow, for clinical purposes or as validation for other methods. In this section, some of the most commonly used techniques are described. These techniques have been included because they have been used to compare, assess and validate echo Doppler techniques over the past years.

3.5.1 Cardiac Catheterisation

Cardiac catheterisation consists of introducing catheters (thin surgical tubes) into the patient's heart through the vascular system. A variety of measuring devices and contrast agents can be introduced through the catheters to measure blood flow.

3.5.1.1 Flow measurements with diluted contrast agents

Dilution methods consist of diluting some agent into blood and measure the change in concentration of this agent through the cardiac cycle. *Thermodilution* (Kadota, 1985) is a dilution method where the agent is a different fluid which is at a different temperature than the blood. Another catheter is used to measure the temperature of blood at the region where flow rate is to be calculated. The change in temperature of the blood is linearly related to the concentration of the agent, so the flow rate can be computed from the resulting concentration-time curve (Weisel et al., 1975). Thermodilution is an invasive, well established technique and has been used in the past to validate flow rate estimated from spectral Doppler (Gill, 1985).

Another option is to inject a contrast agent (dye-dilution). The dye can be fluorescent (Riva et al., 1978), and then its concentration can be measured with a fluorometer, or can be radio-opaque, and then the concentration is measured by X-ray angiography (Rhode et al., 2005; Shpilfoygel et al., 2000). Dye-dilution techniques have also been used to asses the accuracy of flow measurement with Doppler on patients (Evans et al., 1989a; Vargas-Barron et al., 1984).

3.5.1.2 Flow measurements with intravascular devices

Instead of introducing contrast agents, thin devices can be introduced through the catheter. Most common intra-vascular flow measurement devices include PWD transducers of less than $1mm$ diameter (Schumacher et al., 2001), which measure average velocity over the vessel cross-sectional area, and are very accurate if flow is laminar since good alignment with the vessel is usually achieved.

3.5.1.3 Oximetry

Another technique for measuring volume flow, called *oximetry*, is based on the Fick principle. The Fick principle establishes a relationship between the amount of a certain substance consumed by an organ and the concentration of that substance in the arteries irrigating the organ and in the veins leaving the organ. In Fick's original method the substance was oxygen and the organ was the whole body (Fishman, 2000). Cardiac output (Q) can be computed using Fick's principle (Wilkinson, 2001) as

$$Q = \frac{VO_2}{a - v} \tag{3.20}$$

where VO_2 is the volume of oxygen consumed by the body per beat, and a and v are the oxygen concentration in the arteries and veins delivering blood from and to the left ventricle. In practice, this technique is mostly used to calculate pulmonary to systemic flow ratio (QPQS), in which case measurement of VO_2 is not necessary:

$$QPQS = \frac{a_s - v_s}{a_p - v_p} \tag{3.21}$$

where a_s, v_s are the systemic oxygen saturations and a_p, v_p are the pulmonary oxygen saturations. Both are measured with an intravascular probe through a catheter.

Several authors (Kitabatake et al., 1984; Migliavacca et al., 2000; Sun et al., 1995) have used oximetry to compare and assess Doppler based methods.

3.5.2 Electromagnetic Flowmeters

Electromagnetic flow meters (Nichols and O'Rouke, 1997; Tsujino et al., 2001) are very accurate, but need surgical intervention to be placed around the vessel through which flow computation is desired. This limits their use to open surgery procedures.

3.6 Summary

This chapter has described the physics behind blood flow imaging and measurement using non-invasive modalities, in particular echo Doppler which is used throughout this thesis. Advantages and limitations of this and other modalities have been analysed from a theoretical perspective.

Physics of flow measurement with MRI have been described briefly, because 2D+t Flow MRI and 3D+t Flow MRI are the references against which results have been compared. Finally a few other modalities for blood flow measurement, which have been used for accuracy assessment and validation of echo and Doppler based flow measurement methods by other authors, have also been included for completeness.

Physics of echo and colour Doppler image formation have been described in detail because these image modes are input into the algorithms described later on this thesis. The methods described correspond to the standard and most common way to produce echo and Doppler images. However, echo systems can be improved with advanced techniques which alter standard image formation and image processing to provide enhanced images and measurements of blood flow. Chapter 4 gives an overview of such techniques over the past 40 years.

Chapter 4

Literature Review

"If I have seen further it is by standing on ye sholders of Giants."

"Letter from Isaac Newton to Robert Hooke", Turnbull et al. (1959)

Contents

This chapter contains a review on advanced image processing methods to extract angle-independent flow and velocity information from colour Doppler images. The aim is to provide a comprehensive review of the current state-of-the-art.

Colour Doppler images measure velocity only along the direction of the ultrasound beam (Remark 1 in Sec. 3.3.1). For this reason, two components of the velocity are unknown, and therefore a Doppler velocity-derived flow rate depends on the angle of insonation. Over the past 30 years, several authors have proposed different approaches to overcome this limitation. Section 4.1 reviews flow reconstruction methods that have been proposed to recover multi-dimensional velocity fields with echo. Section 4.2 covers the major contributions on angle-independent flow quantification from echo Doppler.

4.1 2D and 3D Velocity Reconstruction from Echo

Current echo imaging systems provide colour-coded velocity information in addition to the traditional B-Mode images in 2D and increasingly also in 3D. Nevertheless, the velocity provided represents only one component of the real 3D velocity of the scatterers (Sec. 3.3), *i.e.* the projection of the true 3D velocity vector onto the US beam direction. Several methods and techniques have been proposed in the last 30 years to provide full velocity information. These techniques can be classified into the following categories:

- Methods which use special focusing and beam-forming schemes to detect transverse motion.
- Methods which track image features to estimate motion.
- Methods which use multiple Doppler views to remove direction and magnitude ambiguity.
- Methods which use physical *a priori* knowledge in addition to Doppler information to recover the missing velocity components.

The reviewed methods often combine several of these techniques, and this classification refers to the main idea behind each proposed method. However, most of the methods use pulsed-wave Doppler and share the same underlying principle: several short echoes consecutively received from a moving scatterer will be shifted

in frequency[1], and the frequency shift will be proportional to the velocity of the scatterer along the direction of the ultrasound field modulation. If this frequency shift can be obtained along multiple directions, then multiple components of blood velocity can be calculated.

Sections 4.1.1, 4.1.2, 4.1.3 and 4.1.4 cover the state-of-the-art of each of these categories, and section 4.1.5 gives a comparative overview of them all.

4.1.1 Methods which Use Advanced Beam-forming and Focusing

Standard echo Doppler is only sensitive to velocity along the beam direction because that is the direction of propagation of the ultrasound wave (Sec. 3.2). However, special apodization (weighting of the pulses at each transducer element) can enable measurement of transverse motion.

4.1.1.1 Transversal Oscillation and Spatial Quadrature

The use of complex functions during receive beamforming allows the generation of a point spread function (PSF) which oscillates both in the axial and the lateral direction. The lateral oscillation appears when the transducer aperture is apodized with a symmetric function with two peaks[2] (Fig. 4.1).

The received echo will therefore experience a frequency shift if the true velocity has nonzero axial or lateral components. The received signal is real and one-dimensional, where the frequency shift is a function of two variables –the axial and lateral components of the velocity–. To remove the ambiguity, a quadrature phase detector is used, similar to that used conventionally with standard PWD methods (Sec. A.5). Briefly, the received echo is demodulated with the two reference waves (the axial and the lateral oscillations) and with versions of these shifted 90°. This yields four equations to resolve the two components and the two directions of the velocity of the scatterer.

[1] In the case of PWD, each pulse is actually shifted in phase (Sec. 3.3.2). In the end, the addition of consecutive phase-shifted pulses produces a wave whose main frequency is shifted with respect to the reference wave.

[2] Indeed the Fraunhofer approximation states that the far field lateral distribution can be approximated by the Fourier transform of the aperture function (*i.e.* the apodization), which, in the case of two peaks (deltas) would be a sinusoid (pure oscillation) in the lateral direction.

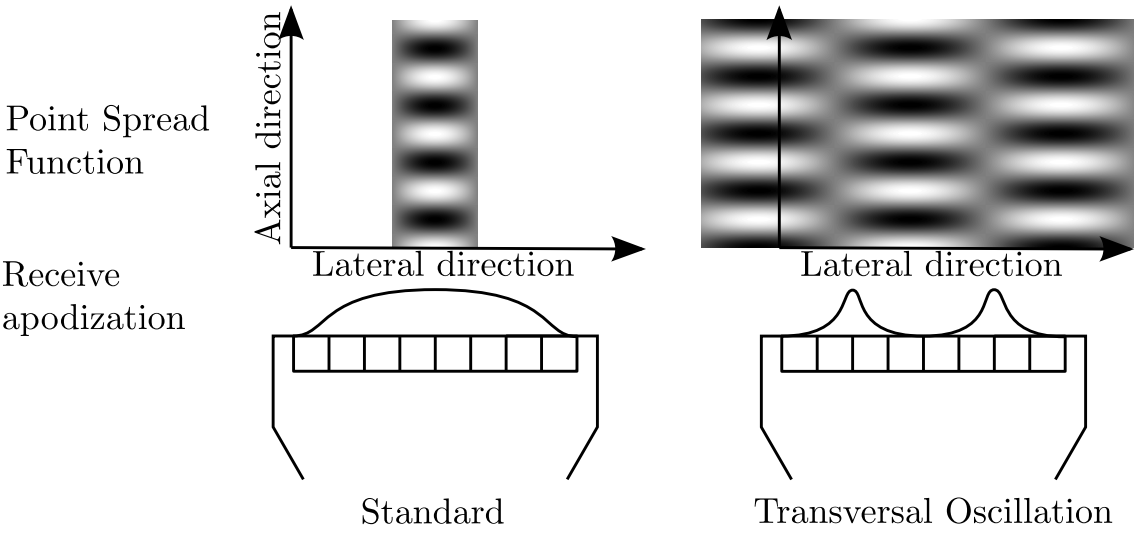

Figure 4.1: Transversal Oscillation (TO) method. In the standard beamforming scheme, the ultrasound field only oscillates along the axial direction (left). The complex apodization function used in TO (right) produces oscillations both in the axial and the lateral direction, therefore velocity components in both directions produce a frequency shift in the received signal. However, narrower sub-apertures produce broader lobes in the PSF this reducing lateral resolution.

The method was proposed by Aderson (1998) who called it Spatial Quadrature (SQ), and also by Jensen and Munk (1998), who called the method Transversal Oscillation (TO). A comprehensive evaluation of accuracy with respect to different parameters was carried out by Udesen and Jensen (2006), who concluded that the method was capable of estimating two components of the velocity within an accuracy of 10% for angles between the axis of the transmitted beam and flow direction between 60° and 90°, but was inaccurate for smaller angles. The method was tested *in-vivo* by Hansen et al. (2009), on 11 volunteers and compared to 2D+t Flow MRI with a mean error on volume flow of $12.6\% \pm 9.5\%$. Although Spatial Quadrature (SQ) and TO can in theory be extended to 3D, this has not been done so far.

Note that the complex apodization is only done in reception, therefore the transmitted beam is the same as in a standard system.

4.1.1.2 Subdivision of the Receive Aperture

The receive aperture can be subdivided into several apertures by apodization. This subdivision effectively converts the transducer in several smaller transducers which receive beams at different angles. Each beam is therefore processed separately and contributes with a different component of the velocity (along the direction of each

beam).

In practice, this idea is very similar to TO, because in both cases the receive apodization is such that two peaks divide the aperture in two regions. They differ in the way the received echoes are further processed[1].

Tanter et al. (2002) proposed a technique in which the aperture was divided into two synthetic sub-apertures during reception. For each sub-aperture, 1D speckle tracking was performed along the scan line, yielding a 1D motion component per image point. Combining the two sub-apertures resulted in 2D motion maps. However, this technique is restricted to small depths ($< 6cm$) since the angle between both apertures decreases with depth.

Another approach, proposed by Niita and Shiina (1998), consisted of dividing the aperture into two circular and concentric sub-apertures. The inner sub-aperture worked as the transmitting aperture, and the outer sub-aperture worked as the receiving aperture. By calculating the phase difference of the received echoes at each receive element, the lateral components of the velocity can be estimated using a Least Mean Squares (LMS) approach, thus yielding a 3D velocity vector field –in theory over a volumetric region. However, this method has only been validated with simulation studies, and might be limited to small depths.

4.1.1.3 Synthetic Aperture

Synthetic Aperture (SA) is an imaging technique which aims to increase image resolution and frame rate by synthetically enlarging the transducer aperture without increasing the physical dimensions of the aperture itself. This is achieved by transmitting an unfocused wave (e.g. an spherical wave which therefore has a broader beam than a focused wave using the same aperture) and focusing in receive only. To achieve this, the transmit aperture is divided in N groups of one or more transmit elements which send successive spherical waves (Fig. 4.2 left) each time from a different location of the transducer aperture (Nock and Trahey, 1992). Each spherical wave is then scattered by particles and received with all transducer elements to produce a low resolution image. All the low resolution images can then be put together to produce a high resolution image.

[1] Anderson (2001) and Lovstakken (2007) propose that the two methods are equivalent for some apodization functions.

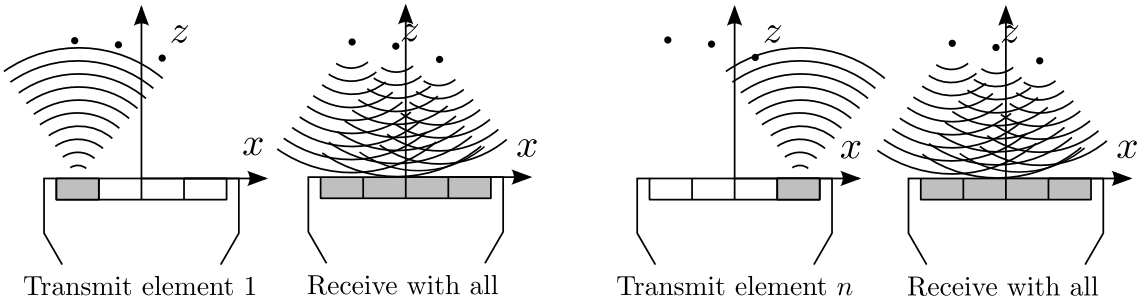

Figure 4.2: Synthetic Aperture (SA) method. Many spherical (unfocused) waves are sent sequentially and focused in receive, generating a low resolution image per spherical wave. Then all the low resolution images can be compounded to generate a high resolution image, or to retrieve all the components of the velocity.

(Nikolov and Jensen, 2001) proposed a receive beamforming scheme so that each low resolution image could be focused along a different direction, by using the time-delay method proposed by (Jensen and Lacasa, 1999). The velocity of the scatterers along each direction was calculated by cross correlation.

Synthetic Aperture (SA) has been tested *in-vivo* in Jensen and Nikolov (2002) and in Nikolov and Jensen (2003), with promising yet very experimental results. Jensen et al. (2006) offers an overview on the method as well as possible applications of SA including 2D velocity vector reconstruction.

The application of SA as well as of TO to complex flow patterns, e.g. intracardiac flow, has not been proven and is still under investigation (Hansen et al., 2009).

4.1.1.4 Finite Aperture Formulation

The classical theory of Doppler shift assumes that a planar wavefront can be produced by beam-forming, and therefore the propagating wave travels in a single, straight direction through the medium until it reaches an obstacle, where scattering and reflection occur. However, this is strictly valid only for planar waves of infinite extent, which can only be generated by apertures of infinite width. The finite width of real beams introduces aberrations and spectral broadening (Censor, 1977) due to the presence of oblique sound waves. Newhouse et al. (1987) proposed that this effect has potential to detect transverse motion and therefore to allow 2D vector reconstruction, where the accuracy of the reconstruction for the transverse component of the velocity was comparable to the accuracy for the axial component. The main limitations of this method is the difficulty to accurately calculate Doppler

bandwidth (Lovstakken, 2007). This method remains experimental and has never been used in commercial systems.

4.1.2 Feature Tracking Methods

Some methods for velocity vector computation are based on tracking the temporal or spatial position of a structure which has moved by maximising the similarity between the original structure and its displaced version at a later time point. The approaches presented in this section use correlation as a similarity measure.

4.1.2.1 Time Domain Shift Estimation

The calculation of multiple components of blood velocity by temporal correlation of received echoes was first proposed by (Bonnefous, 1988), extending a previous work on 1D velocity measurement (Bonnefous and Pesqué, 1986). In their paper, they propose that the velocity component orthogonal to the beam axis can be calculated by correlation of contiguous scan lines. Time shift is calculated by maximising the cross-correlation between echoes. The method can therefore be regarded as a low-level speckle tracking technique. As such, a fundamental limitation is the sensitivity to false peaks in the correlation function (Walker and Trahey, 1995), also called *peak-locking* (Corpetti et al., 2006).

4.1.2.2 Speckle Tracking

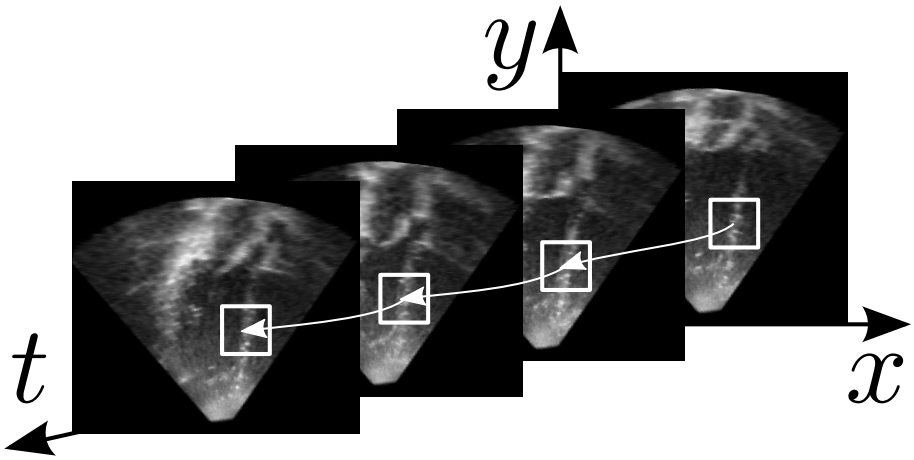

Figure 4.3: Speckle Tracking (ST). In this example, in-plane cardiac wall motion is calculated by tracking the speckle pattern (enclosed by a white square) along time in a 2D+t BMode sequence.

Trahey et al. (1987) applied Speckle Tracking (ST) to 2D blood motion estimation. The method was improved by optimising the metric used (Bohs and Trahey, 1991), and integrated with a system with very good results obtained in phantom studies with laminar flow (Bohs et al., 1993). ST in blood has also been extended to 3D (Morsy and Von Ramm, 1999). However, signal intensity from red blood cells is generally very weak (particularly compared to signal from tissue), which is why blood motion is typically invisible in B-Mode, and may need specific amplification and pre-processing in order to enable speckle tracking in blood (Chiao et al., 2000). Bjaerum et al. (2002) proposed a speckle enhancement step prior to the speckle tracking to overcome this limitation. Their method consists of processing each received echo before forming the full B-Mode image. The processing chain consists of high-pass filtering followed by an amplitude normalisation. Other ways to enhance blood contrast include the injection of micro-bubbles for imaging intra-cardiac flow patterns (Gao et al., 2012), however these techniques remain experimental.

Marion and Vray (2009) proposed another method based on spatio-temporal filtering to estimate the apparent velocity vector for each pixel of the sequence of ultrasound images. They assumed that a moving object is represented by a group of pixels travelling from image to image in the sequence, leaving a trace in the spatio-temporal volume. A bank of filters was designed to estimate a local texture orientation related to the velocity of the object. With their method, the velocity estimates obtained for one and two components of the velocity showed mean errors less than 5% and 12%, respectively, which is an improvement with respect to other methods described in this section, and to this day the best results achieved using ST for estimating blood motion. However, this method has been only applied to phantom studies.

Inspired by this idea, (Udesen et al., 2008) proposed to use Planar Wave Excitation (PWE) receiving with a single aperture and perform 2D speckle tracking to compute 2D motion fields, without the depth limitation of the other approach. Their method was tested on simulated data and on the carotid artery of a healthy volunteer, and then compared to 2D+t Flow MRI, showing an accuracy in flow volume of 9%. This method was used by Hansen et al. (2008) to study relatively complex flow features in several peripheral vessels close to the skin surface: carotid bifurcation, femoral bifurcation, brachiocephalic trunk, subclavian artery bifurcation, jugular

vein and great saphenous vein, of four healthy volunteers, showing plausible flow patterns.

A recent comparison of different methods based on ST for blood flow reconstruction has been published by Marion et al. (2010).

4.1.3 Multiple View Methods

Methods described in this section use multiple colour Doppler images, acquired from different positions, to reconstruct multi-dimensional blood velocity information. Figures 4.4 and 4.5 show a scheme of the different multi-beam configurations proposed over the last years.

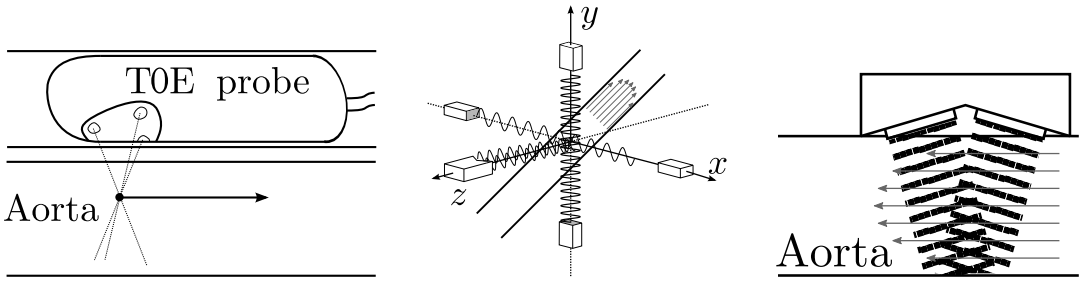

(a) 3D Velocity at one point by Daigle et al. (1975).

(b) 3D Velocity at one point by Fox (1978).

(c) 2D Velocity on a 2D section by Farthing and Peronneau (1979).

Figure 4.4: Scheme of some of the most relevant multi-beam configurations proposed over the last years (I).

Early multi-view approaches focused on retrieving 2D and 3D velocity at a single point using multiple transducers simultaneously measuring spectral PWD. One of the first attempts to reconstruct multi-dimensional velocity from multiple Doppler measurements was carried out by Daigle et al. (1975) (Fig. 4.4(a)). They proposed the use of a transesophageal probe with three pulsed wave transducers to measure aortic velocity at one point without angle dependency. Fox (1978); Fox and Gardiner (1988) proposed to use three transmitter-receiver systems (Fig. 4.4(b)), oriented in three orthogonal directions to simultaneously compute the three components of the velocity at a single point. His paper shows the theoretical development for flow reconstruction, intended for a transcutaneous Doppler flow meter, and showed encouraging results on a phantom study. Farthing and Peronneau (1979) used a dual-transducer system proposed by Péronneau et al. (1974) (Fig. 4.4(c)) to characterise 2D velocity profiles in the ascending aorta and branches. The transducer was placed

during an open surgery operation and was directly attached to the aorta.

After the encouraging results obtained on phantoms and animals, and contemporary to the consolidation of 2D colour Doppler systems, research interest moved forward to colour Doppler images and applications in volunteers and patients with transthoracic echo. A review on different approaches based on cross-beam designs was carried out by Dunmire et al. (2000). A more recent review on 2D velocity vector recovery can be found in Swillens et al. (2010). Wei-qi and Lin-xin (1982) proposed a clinically oriented device consisting of two simultaneous transcutaneous transducers to measure true in-plane velocity magnitude in one point (Fig. 4.5(c)). The proposed device yields two measurements of velocity (sum and subtraction velocities from the two transducers). When the sum velocity is zero the true velocity is at an angle of $\pm\delta/2$ with both beams. The true velocity can then be calculated as the subtraction of both measurements divided by $2\cos(\delta/2)$, yields twice the true velocity.

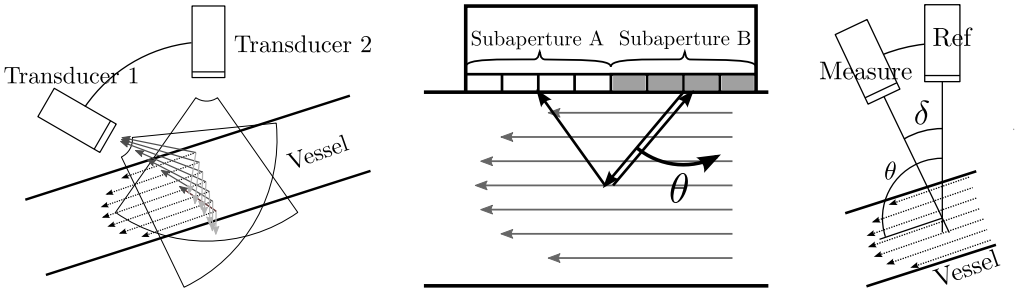

(a) 2D Velocity on a 2D section by Arigovindan et al. (2007); Xu et al. (1991).

(b) 2D Velocity on a 2D section by Phillips et al. (1995).

(c) 2D Velocity on a 2D section by Tortoli et al. (2006); Wei-qi and Lin-xin (1982).

Figure 4.5: Scheme of some of the most relevant multi-beam configurations proposed over the last years (II).

Xu et al. (1991) derived the general formulae for reconstructing the vector field in 2D, using two or more 2D colour Doppler views (Fig. 4.5(a)) and tested their method on a flow phantom. Two methods were proposed: a weighted averaging of the vector images, and a Least Mean Squares (LMS) approach which uses the information of several views to improve the Signal to Noise Ratio (SNR). The weighted averaging method consists of computing several reconstructed vector images and then averaging them. The weights are given depending on the angle between the two views. The LMS approach computes a single velocity vector image using all colour

Doppler images by minimising the noise influence in a statistical sense. Overbeck et al. (1992) proposed the use of two emitters and one receiver to reconstruct 2D velocity vectors, and was tested on a phantom and on a carotid artery. Maniatis et al. (1994) compared different strategies for 2D velocity vector reconstruction, including those proposed by Xu et al. (1991), and concluded that the angle between views was a major factor affecting reconstruction accuracy. Phillips et al. (1995) proposed a 2D velocity reconstruction scheme with a single transducer (Fig. 4.5(b)). Their method consisted of subdividing the transducer aperture into two regions, one of which would emit the pulses, and both of them would receive the scattered echoes. Since each region receives the echoes from a point at a different angle, two components of the velocity are measured simultaneously. Error increased with depth because the angle between the two beams decreased. The same idea was exploited by Capineri et al. (2002); Scabia et al. (2000), who tested a similar device on laminar flow from phantom data. Recent applications of subaperture techniques for 2D velocity recovery on *in-vivo* data have been investigated by Pastorelli et al. (2008). Note the similarity with the techniques described in Sec. 4.1.1.2. The focus on processing rather than acquisition in these papers justify their inclusion within this section.

Over the last ten years interest on removing the direction ambiguity of Doppler measurements has increased, not only for multi-dimensional velocity vector reconstruction but also for accurate flow quantification. Tortoli et al. (2006) proposed a dual-beam approach to remove angle ambiguity for laminar flows (Fig. 4.5(c)), similar to the work by Wei-qi and Lin-xin (1982). Their method consists of two transducers rigidly assembled together, where the relative orientation between the two transducers is known. One transducer is used to measure blood velocity, and the other is used to measure the angle between the beam axis and the flow direction. The dual probe is tilted until the measured signal from the second transducer is zero, in which case the second beam is at 90° with blood direction and the measurement from the first transducer can be angle compensated. This method was tested on volunteers by Ricci et al. (2009), with an accuracy over 95% on peak systolic velocity.

Arigovindan et al. (2007) proposed the mathematical framework for regularised reconstruction of 2D velocity vector fields from multiple 2D colour Doppler images,

using an acquisition protocol similar to the one proposed by Xu et al. (1991) (Fig. 4.5(a)). Their method used a B-spline basis to incorporate irregularly sampled input data and up to four regularisation parameters that allowed the introduction of *a priori* knowledge related to the physical nature blood, such as its compressibility and its vorticity. The focus of the paper was to develop an efficient mathematical formulation of the optimisation problem by proposing a structure of the linear system optimised for numerical solvers. The regularisation parameters were tuned to minimise noise variance, and therefore different parameters were used for each dataset. They used their algorithm to reconstruct 2D velocity vectors in a phantom as well as in the carotid bifurcation (at a depth of 3cm) and the cardiac wall. Since no ground truth velocity field was available, part of the input data, which was not used for reconstruction, was used for validation. In the carotid bifurcation, relative position and orientation of the multiple views was known by calibration, whereas for cardiac wall motion, 2D images were registered. Reconstruction accuracy reported on a rotating tissue-mimicking phantom achieved errors of 3° in angle and 3.5% of the peak velocity in magnitude. The accuracy for real volunteer was only given as the residual of minimisation process which fitted the resulting vector field to input data, which is difficult to interpret.

So far, no crossed-beam multiview approach has been proposed to reconstruct 3D velocity fields within the cardiac chambers.

4.1.4 Physically Constrained Methods

Some of the previously mentioned methods rely on the use of physical *a priori* knowledge as supplementary information to improve the accuracy of the velocity vector reconstruction. This section describes methods which use physical knowledge (e.g. mathematical models) to remove ambiguity on magnitude and direction intrinsic to Doppler measurements, *i.e.* methods which require physical constrains in addition to echo data to reconstruct velocity vector fields.

Ohtsuki and Tanaka (2006) proposed a technique to reconstruct 2D velocity from a single 2D colour Doppler image called *echo dynamography*. The method was based on decomposing the total velocity into a base velocity and a divergence-free vorticity velocity (Fig. 4.6(a)). Since in 2D the divergence-free condition couples

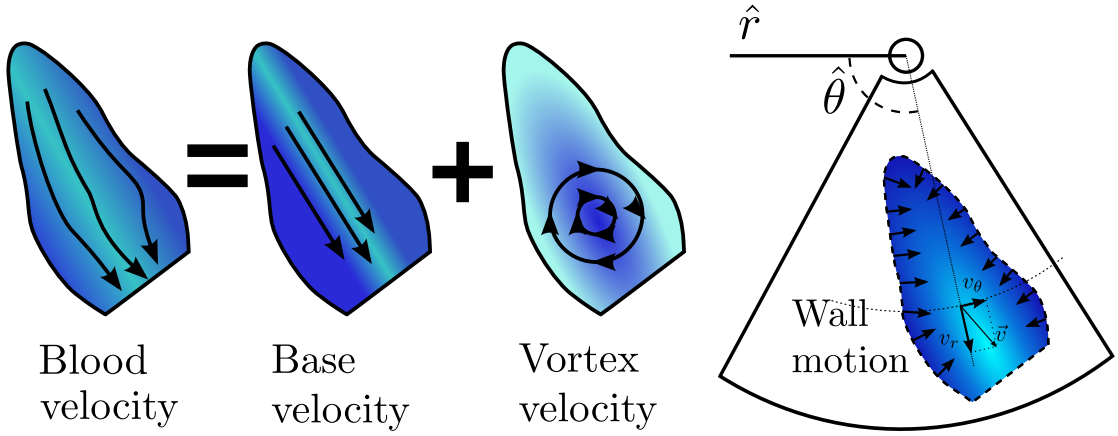

(a) Echo dynamography.

(b) Mass conservation plus wall motion.

Figure 4.6: Physically constrained methods for multidimensional velocity reconstruction.

both components of a vector, the total velocity can then be recovered from the vorticity velocity and the base velocity along the beam direction. This technique was tested on volunteer data for 2D intraventricular velocity reconstruction, and was used to analyse blood flow patterns like vortices and spirals during ventricular ejection by Tanaka et al. (2010), and during ventricular filling by Tanaka et al. (2011).

Garcia et al. (2010) proposed another method to recover 2D intraventricular velocity vectors from a single 2D colour Doppler image and wall motion estimated from speckle tracking computed on a 2D B-Mode image (Fig. 4.6(b)). They imposed that the reconstructed vector field was divergence-free, which introduced, as in Ohtsuki and Tanaka (2006), a coupling between the known and the unknown components of the 2D velocity. Estimated wall motion was used as free-slip boundary condition (*i.e.* at the wall-blood pool interface, the wall motion in the direction orthogonal to the wall has to be continuous with blood velocity in that direction). In this work they focused on the large flow structures in apical long-axis plane of the Left Ventricle (LV), passing through the LV apex, the centre of the mitral and of the aortic valves in the apical long-axis view. The flow is assumed to be planar in the apical plane, an assumption which they claim results in an error of 15%.

4.1.5 Discussion on Multi-dimensional Velocity Reconstruction Methods

A summary on the described techniques and methods is presented in Table 4.2. The most relevant publications on multi-dimensional velocity reconstruction have been sorted in chronological order. In order to understand the contents of the table, some clarifications shall be made. Dimensionality of the reconstructed vector field covers two aspects: first, the dimensionality of the region where velocity is reconstructed, noted *single point* (0D), *linear* (1D), *planar* (2D) or *volumetric* (3D); second the dimensionality of the reconstructed velocity vectors, which is either 2D or 3D. In all cases, the reconstructed velocity as well as the input data is available over the temporal dimension. The "input" column refers to the system used to acquire the input signals or images, and the number of inputs needed. Note that in most of the multiview methods, the relative position and orientation between the multiple views was assumed to be known which, in clinical practice, is not necessarily the case, especially if the multiple acquisitions are not simultaneous. The only exception is the paper by Arigovindan et al. (2007), in which they use landmark based registration only for wall motion estimation, for which they report an error ten times larger than for the carotid bifurcation. The "region" column indicates the region of interest where velocity was reconstructed. Note that all regions can be classified as either laminar flows (mostly carotid artery) and complex flow (bifurcations and intracardiac flow). Authors reported accuracy in various ways. In order to offer comparable error values, the "error" column indicates the average relative error (in percent) when available. When absolute error values were given, the percent with respect to the peak value is shown. Although error value was sometimes given for velocity and sometimes for flow rate, the use of relative error is dimensionless and therefore allows the inclusion of both error types. When accuracy was given only qualitatively, or in a non-comparable way, accuracy is described with a word (e.g. "low").

Starting at the top of table 4.2, early approaches, carried out with spectral PWD systems, aimed at the total removal of the direction and magnitude ambiguity, and therefore tried to recover 3D velocity at the point of interest (Daigle et al., 1975; Fox, 1978). Since the set-up required the use of several transducers, and clinical applica-

tion was complicated, some authors decided to assume axial symmetry of laminar flow and reconstruct 2D velocity in a plane containing the axis of the vessel (Farthing and Peronneau, 1979; Wei-qi and Lin-xin, 1982), which is known to introduce large errors (Evans and McDicken, 2000). During these years, flow visualisation was still undeveloped, and most interest was put on reliable velocity quantification. In most cases, validation was carried out with phantoms or animals. The development of 2D B-Mode and the introduction of ST allowed for the first time the estimation of 2D velocity maps. However, the speckle pattern in blood is very weak compared to tissue, therefore although this technique has been proposed in the past (Marion et al., 2010; Morsy and Von Ramm, 1999), it has not been widely investigated beyond a few phantom studies and an isolated experiment on carotid flow (Bjaerum et al., 2002).

In 1990, advances in echo systems enabled the acquisition of many electronically steered scan lines in a very short time, therefore high frame rate 2D B-Mode and 2D colour Doppler were available. Multiview methods were proposed to reconstruct 2D velocity vector maps within a region covered by several 2D colour Doppler images (Maniatis et al., 1994; Overbeck et al., 1992; Phillips et al., 1995; Xu et al., 1991). Also, quicker and more accurate systems allowed the development of advanced beam-forming techniques, like SQ, which provided sensitivity to transverse motion (Anderson, 1997; Jensen and Munk, 1998). During the 1990s, many novel methods were proposed, but in most cases experimentation was limited to phantom data, and obtaining 2D velocity vectors from *in-vivo* data was rarely achieved and only for relatively simple flow patterns.

In the 2000s, most of the velocity reconstruction approaches aimed to recover 2D in-plane velocity vectors for study of velocity profiles in laminar blood flows (Arigovindan et al., 2007; Bjaerum et al., 2002; Capineri et al., 2002; Hansen et al., 2008; Nikolov and Jensen, 2003; Pastorelli et al., 2008; Ricci et al., 2009; Udesen et al., 2008). The difficulty of obtaining multiple 2D images of the same structure within the heart has prevented, to date, the calculation of 2D or 3D velocity fields within the cardiac chambers, or cardiac inlets or outlets using crossed-beam methods. Some recent publications have tried to avoid the acquisition of several colour Doppler views and instead have obtained additional velocity information by imposing physical constraints (Garcia et al., 2010; Ohtsuki and Tanaka, 2006; Tanaka

Publication	Method	Velocity	Input	In vitro	In vivo	Region	Validation	Error
Daigle (1975)	Multiview	Point 3D	3xTOE	-	dog	Aorta	Flowmeter	5%-20%
Fox (1978)	Multiview	Point 3D	3xTC	phantom	-	-	GT	low
Farthing (1979)	Multiview	Point 2D	2xPeri.	-	dog	Aorta	Theory	low
Wei-qi (1982)	Multiview	Point 2D	2xTC	phantom	1 pat	Carotid	GT	5%*
Trahey (1987)	ST	Planar 2D	1x2D-BM	-	1 vol	Popliteal vein	Visual	low
Bonnefous (1988)	TS	Point 2D	1xTC	sim.	-	-	-	-
Xu (1991)	Multiview	Planar 2D	Nx2D-CD	phantom	-	-	Visual	low
Overbeck (1992)	Multiview	Planar 2D	2x2D-CD	phantom	1 vol	Carotid	GT	10%*
Bohs (1993)	ST	Planar 2D	1x2D-BM	phantom	-	-	GT	< 6%
Maniatis (1994)	Multiview	Planar 2D	2x2D-CD	sim.	-	-	GT	angle dependent
Phillips (1995)	Multiview	Planar 2D	SubAp	sim. + phantom	-	-	GT	5%*
Anderson (1997)	SQ	Point 2D	1xTC	phantom	-	-	Theory	-
Jensen (1998)	SQ	Point 2D	1xTC	sim.	-	-	GT	1% to 5%
Niita (1998)	TO	Volumetric 3D	1xTC	sim.	-	-	GT	low
Morsy (1999)	ST	Volumetric 3D	42 x 42 AM	phantom	-	-	-	low
Capineri (2002)	Multiview	Planar 2D	SubAp	phantom	-	-	Visual	low
Bjaerum (2002)	ST	Planar 2D	1x2D-BM	-	-	Carotid	-	-
Nikolov (2003)	SA	Planar 2D	1xTC	sim. + phantom	1 vol	Carotid	Flowmeter	<11%
Tortoli (2006)	Multiview	Point 2D	2xTC	phantom	-	-	Flowmeter	<5%
Udesen (2006)	SQ	Linear 2D	1xTC	sim. + phantom	-	-	GT	<10%*
Ohtsuki (2006)	Phys. Cons.	Planar 2D	1x2D-CD	phantom	1 vol + 1 pat	Intracardiac	Visual	low
Arigovindan (2007)	Multiview	Planar 2D	Nx2D-CD	sim. + phantom	1 vol	Carotid bifurcation	Theory	3.5% (Phantom)
Pastorelli (2008)	Multiview	Planar 2D	SubAp	sim. + phantom	2 vol	Carotid	Flowmeter	<22%
Ricci (2009)	Multiview	Point 2D	2xTC	phantom	21 vol	Carotid	Variability	<10%
Hansen (2009)	SQ	Planar 2D	1xTC	-	11 vol	Carotid	PC-MRI	10% to 24.1%
Marion (2009)	ST	Planar 2D	1x2D-BM	phantom	-	-	GT	<15%
Garcia (2010)	Phys. Cons.	Planar 2D	1x2D-CD	phantom	2 vol + 2 pat	Intracardiac	PC-MRI	15%-25%
Tanaka (2011)	Phys. Cons.	Planar 2D	1x2D-CD	phantom	10 vol	Intracardiac	Visual	low

Table 4.2: Comparison of multi-dimensional flow reconstruction methods from echo and echo Doppler data. Notation for methods: ST = Speckle Tracking. TS = Time Shift. SA = Synthetic Aperture. SQ = Spatial Quadrature. Notation for Input: TOE = Transesophageal Echo. TCE Transcutaneous Echo. BM = B-Mode. AM = A-Mode. CD = Colour Doppler. SubAp = Sub Aperture. Error values marked with "*" are valid only under optimal conditions of other parameters.

et al., 2011) with very encouraging results for 2D intracardiac flow pattern analysis. These methods are based upon the coupling of the two components of the velocity imposed by the continuity equation for incompressible fluids assuming that the through plane velocity component is negligible. This assumption, which is only valid for certain planes (e.g. four chamber plane) of normal hearts, prevents the direct extension of this method to 3D and to arbitrary planes.

Over the last 30 years, there has been a tendency to obtain multi-dimensional velocity information over larger and larger regions. The first methods reconstructed 2D and 3D velocity over a punctual or a very small region. During the 1980s and 1990s, interest moved to 2D velocity maps, mainly in small peripheral vessels like the carotid artery, where flow patterns are relatively simple and echo access is not restricted by air or bones. Latest publications target more ambitious regions like full 2D velocity mapping of intracardiac blood flow, which allows visualisation and measurement of complex vortices and non-laminar flow patterns.

The increasing interest in complex intracardiac flow patterns and in accurate flow and velocity quantification (Sengupta et al., 2012), as well as recent developments in 3D echo and echo Doppler imaging, will naturally direct velocity reconstruction techniques towards full 3D velocity reconstruction. In addition, 3D, temporally resolved velocity vector fields, which are currently achievable with 3D+t Flow MRI, have shown potential for numerous clinical and research applications (Markl et al., 2011).

The aims of this thesis included the study of new methods which enable 3D velocity vector reconstruction from 3D colour Doppler images. This, has not been previously reported in the literature. Of all the methods described in this section, only multiview methods (Sec. 4.1.3) and physically constrained methods (Sec. 4.1.4) can be applied to images obtained with standard commercial echo systems. In particular, multiview approaches have been investigated within this thesis, because 1) they have shown promising results in 2D, 2) current clinical echo systems (CE marked and FDA approved) can be used and therefore data can be easily acquired from patients and 3) extension to 3D is in theory possible if three or more views are provided.

4.2 Flow Quantification with Echo

This section reviews methods to calculate blood flow rate and volume, rather than calculation of 3D velocity vectors. Early Doppler systems (e.g. spectral CWD and PWD) provided average velocity values at a sampling volume along time, weighted by the cosine of the angle between the beam axis and the flow direction. The resulting trace was used to measure several flow parameters such as peak velocity, average velocity and to detect the presence of regurgitation. Several methods have been proposed over the last 40 years to quantify these and other flow-related parameters which are not directly provided by Doppler signal (Table 2.1). It is of particular interest to quantify flow rate within the cardiovascular system, since other quantities such as cardiac output, stroke volume and regurgitant fraction can be directly calculated from the former.

Blood flow rate is defined as the volume of blood that goes through a given surface per time unit. Gauss' theorem allows defining flow in terms of blood velocity along the direction orthogonal to a given surface. Therefore, quantification of blood velocity has the potential to provide flow rate values. This section discusses a number of different methods to calculate volume flow and flow rate from velocity measured with Doppler systems.

Section 4.2.1 covers the standard method for flow quantification using echo Doppler, which uses a single spectral PWD trace plus an anatomical B-Mode scan. Section 4.2.2 describes improvements over the standard method, which provide better results but are still angle dependent. Section 4.2.3 describes more advanced methods which overcome the angle dependency problem but rely on other assumptions such as vessel geometry. Section 4.2.4 is included for the sake of completeness and covers the Proximal Isovelocity Surface Area (PISA) method which provides angle independent flow estimations through small orifices. Section 4.2.5 summarises, providing a comparison of the different techniques.

4.2.1 Standard Flow Quantification Based on Spectral PWD

The most widely used method is to carry on a duplex exam, *i.e.* acquire simultaneous B-Mode and PWD or CWD. Mean velocity over a sample volume located in the centre of the vessel is measured with spectral Doppler (Fig. 4.7 left). The B-

Mode image is then used to calculate the angle between the vessel and the beam axis, which is used to compensate the measured velocity value, and to measure the cross-sectional diameter of the vessel. Cross-sectional area is computed assuming circular symmetry of the vessel, and flow rate is calculated as the product of the mean velocity times the cross-sectional area (Fig. 4.7 right). Volume flow was then calculated by the time integral of the flow rate curve. One of the first authors to propose this technique was Gill (1979), who assumed that the value measured by the Doppler system was the mean velocity value across the vessel. This assumption can introduce errors of up to 35% (Evans and McDicken, 2000) into the flow rate calculation, especially for large vessels.

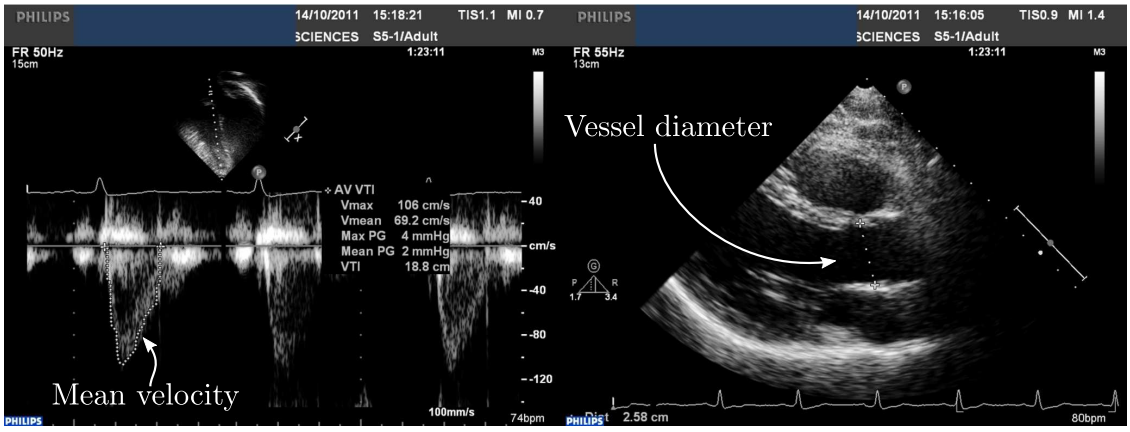

Figure 4.7: Standard flow quantification using echo Doppler. The echo beam is aligned with the vessel of interest (ascending aorta, on the left). The measured velocity is assumed constant over the cross section. Then, a B-mode image is used to measure the diameter of the cross section (assumed circular, on the right). The resulting flow is calculated as the product of the circular surface and the integral of the measured velocity over time.

Additional error is introduced when measuring the cross sectional area of the vessel. First, the cross section is assumed to be a perfect circle, which is not necessarily the case. Second, the cross section may change through the cardiac cycle, which is rarely taken into account with this technique. Struyk et al. (1985) reported errors up to 19% on volume flow in an animal study due to variations on selected aortic diameter. Third, velocity measurement is angle-dependent. The usual practice is to estimate the angle between the beam axis and the vessel axis and divide the measured velocity by the cosine of this angle. Small errors in angle estimation can introduce large errors in flow measurement. For example, a 5° error introduces an error of 15% for a vessel-to-beam angle of 60°, and increases as the vessel-to-beam

angle approaches 90° (Evans and McDicken, 2000). In addition, angle compensation assumes laminar flow along the direction parallel to the vessel walls, which may be true only in very simple vessels, but will not be true at bifurcations or within cardiac chambers.

A slight variation of this method is to assume a velocity profile shape over the vessel cross section instead of assuming that the measured velocity is simply the average over the entire cross section. The velocity is then measured within a small sample volume in the centre of the vessel and assumed to be the maximum velocity. Then a profile is assumed (often a flatten paraboloid) over the vessel cross section. This method is still actively used (de Vecchi et al., 2012).

4.2.2 Improved Angle Dependent Flow Quantification Methods

Two improvements over the method discussed in Sec. 4.2.1 are represented in Fig. 4.8. One technique is to measure velocity not only at a single sample volume in the centre of the vessel, but in a series of contiguous small sample volumes placed along the scan line all the way through the vessel (Fig. 4.8(a)). This allows the use of a profile velocity (using circular symmetry) instead of a single velocity for the flow rate measurement (Foster et al., 1990). In practice, this technique is performed with M-Mode colour Doppler images which provide velocity measurements at multiple depths along time (Bohs et al., 1995; Forsberg et al., 1995; Picot and Embree, 1994).

As a substitute to the circular symmetry assumption, 2D colour Doppler images can be used to measure velocity (the component along the beam direction) over the whole cross section of a vessel, instead of a single line (Fig. 4.8(b)). This technique was investigated by Embree and O'Brien (1990) on a flow phantom with errors $< 10\%$ in volumetric flow. However, the angle between the beam axis and flow direction still had to be compensated for, and the frame rate was significantly lower than any of the previously mentioned approaches.

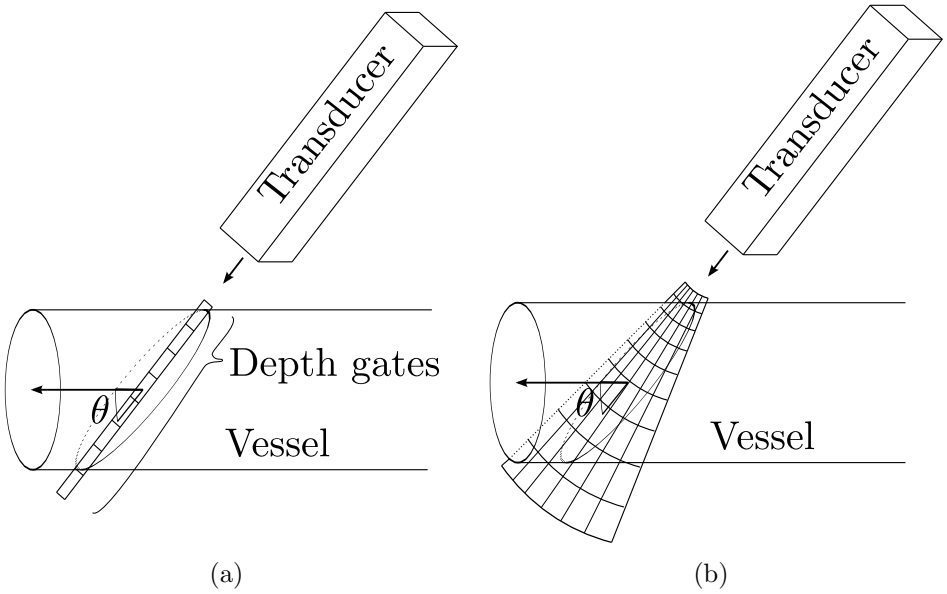

Figure 4.8: Improved angle-dependent flow quantification using echo Doppler. (a) Velocity is measured at different depth gates along a line crossing the vessel. After compensating for the angle θ between the flow and the beam axis, flow through the circular cross-section can be calculated by imposing circular symmetry. (b) Alternatively, a 2D colour Doppler image can be obtained to remove the circular symmetry assumption.

4.2.3 Angle Independent 2D Flow Quantification Methods

All the previously described techniques suffer from angle dependency. In order to compensate for the angle, principal flow direction can be estimated for simple (*i.e.* tubular) geometries. However, in general blood cells move in many directions and flow patterns can be complex resulting in inaccurate flow calculations.

Previous approaches computed flow rate through a plane orthogonal to the vessel. In addition, blood was assumed to flow parallel to the vessel walls, and therefore measured velocity needed to be angle-compensated. A more generic approach, first suggested by Hottinger and Meindl (1975), uses the measured component of velocity (along the beam axis) to compute flow through a surface not necessarily orthogonal to the vessel, but orthogonal to the beam axis. In their approach, the transducer is set to send a planar wavefront, therefore the sampling surface is a plane. If the plane cuts completely the cross-section of a vessel, independently of the angle at which the plane intersects the vessel, flow rate can be calculated unambiguously (Fig. 4.9). This method was put into practice by Evans et al. (1989a,b), testing their device on a flow phantom and validating it by measuring cardiac output on 54 patients, with a correlation coefficient of 0.96 compared to thermodilution. A

similar method, but using a spherical wavefront with an intravascular probe was proposed by Gibson et al. (1994), later extended to non-intravascular by Poulsen and Kim (1996a) and tested on phantom data with errors $< 15\%$ on volume flow estimation. Hottinger and Meindl (1979) proposed a variation of this method where the combined effects of scattering and attenuation where compensated yielding an angle-independent measurement of blood flow through a vessel with independence of changes in cross-sectional area. In vitro results showed very promising although it was stated than locating a sampling volume inside the vessel might be of practical importance.

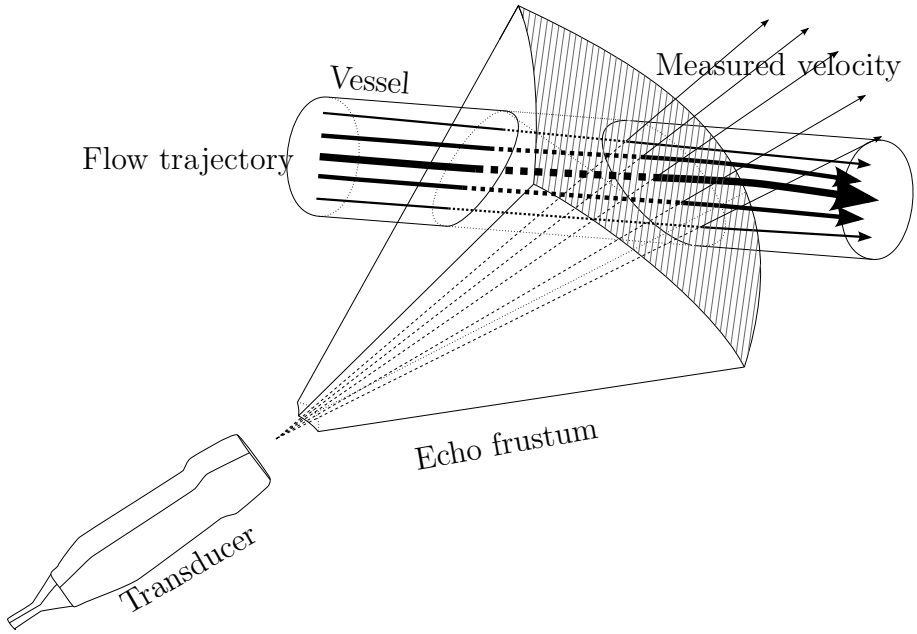

Figure 4.9: Angle-independent flow quantification using echo Doppler. Flow can be calculated as the integral of the measured velocity (along the beam direction) over a spherical surface (orthogonal to the beam direction) which completely intersects the vessel of interest.

Li et al. (2001) proposed a method using conventional 2D colour Doppler systems. They measured volume flow with a 2D transoesophageal echo (TOE) probe on a flow phantom. The probe was rotated to obtain velocity measurements over a volume, and a spherical surface, orthogonal to the beam direction at each point and cutting the synthetic vessel, was used to compute flow. Mori et al. (2002) proposed the use of a similar set-up (a rotational TOE probe) to measure volume flow on sheep. The method showed good correlation with measurements using an electromagnetic flow meter (EMF) ($r = 0.91$ to $r = 0.95$).

Recent development of 3D colour Doppler imaging allowed use of colour Doppler

images for angle independent flow quantification with a single acquisition. Ge et al. (2005) used 3D colour Doppler sequences to measure volume flow on 13 paediatric patients through the mitral valve, and compared the results to 2D+t Flow MRI obtaining a standard error estimate of around 15%. However, they obtained flow rate curves with only 7 data points during ventricular filling, which may not be enough to ensure reliability and robustness of the method. Pemberton et al. (2005) analysed the increase of error with depth using the same method, and concluded that when depth is such that image quality and especially frame rate decreases, then the error increases beyond acceptable values. Very recently, Thavendiranathan et al. (2012) proposed the use of a state-of-the-art echo system, which provided 14 to 33 volumes per second, each of which covered the whole aortic and mitral valves. Using a single acquisition, they computed input and output ventricular volumes to study regurgitation, by obtaining flow rate curves over spherical surfaces coincident with the ultrasonic wavefront. Their method consisted of several steps: first, the endocardial surface of left ventricle was automatically segmented. Second, the mitral annulus and aortic outflow tract were automatically detected by an advanced model-based atlas search algorithm. The location of the valves was used to select the sampling spherical surface, and therefore flow measurement was automatically motion-corrected. Results were compared to 2D+t Flow MRI, obtaining a mean dissimilarity around a 5% over 44 patients. However, an important limitation of this technique segmentation and detection methods based on statistical atlases are known to perform poorly in congenital hearts, which is an important patient group as shown in Sec. 2.2.

In all angle independent techniques presented in this section, the surface through which flow can be computed is limited by acoustic windows of patients and view angle, preventing their use when the spherical surface of the frustum does not completely intersect the cross section of the vessel or structure of interest. Nevertheless, angle-independent flow quantification with 3D colour Doppler images has great potential for clinical applications and further improvements on the technique can be expected in the near future (Ge, 2012).

4.2.4 Proximal Isovelocity Surface Area

One of the first authors to apply the Proximal Isovelocity Surface Area (PISA) method were Utsunomiya et al. (1991), following previous work by Simpson et al. (1989) and Cape et al. (1989). The method aims to quantify flow rate through stenotic orifices where high velocity jets are present since blood flow converges towards the orifice at increasing velocity. The principle of the PISA method is represented in Fig. 4.10. The isosurfaces of the velocity field in the proximal side of the orifice (*i.e.* proximal isovelocity surfaces) approximate spherical surfaces centred at the orifice when measured close to the orifice (Bargiggia et al., 1991). By tuning the Doppler range, aliasing occurs, eventually showing an ellipsoidal isovelocity surface where the velocity is equal to the selected Doppler range (*i.e.* in the limit between the aliased and the non aliased region). The surface area is then that of an ellipsoid and flow rate can be calculated as the product of velocity times surface area.

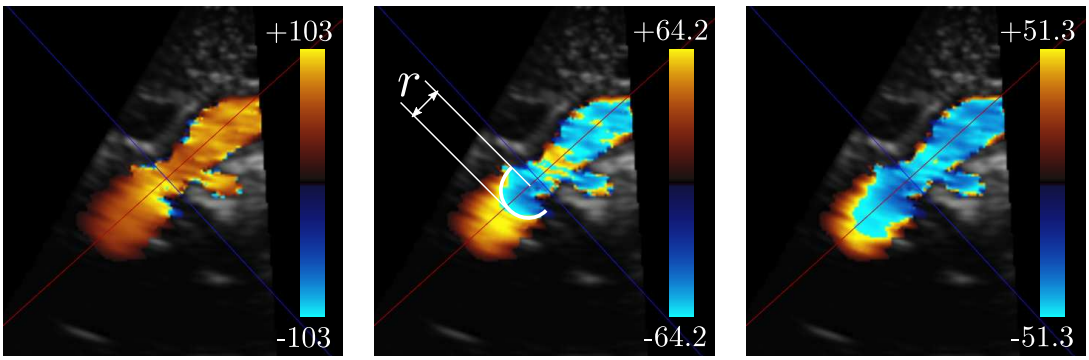

(a) $V_{max} = 103cm/s$ (b) $V_{max} = 64.2cm/s$ (c) $V_{max} = 51.3cm/s$

Figure 4.10: Proximal Isovelocity Surface Area (PISA) method for flow quantification through stenotic orifices. The figures show the flow through the ascending aorta in a young patient with aortic stenosis from a suprasternal view, with a decreasing Doppler velocity range (v_{max}) from left to right. (a) The Doppler range is selected so that there is no aliasing. (b) The range has been selected so that there is some aliasing near the stenotic orifice, describing approximately an semi-circular cap. The shape of the orifice is assumed spherical and then the flow rate can be calculated as $+64 \times 2\pi r$. (c). The range has been selected so that there is too much aliasing occurs at too low velocities, therefore too far from the orifice where the assumption that isovelocity surfaces are spherical does not hold.

Rodriguez et al. (1993) carried out a validation of the method by comparing the effective stenotic area (*i.e.* the resulting flow rate divided by the velocity at the orifice) with the area of the orifice measured with other methods, in 40 patients with mitral stenosis. The velocity range was tuned so that aliasing occurred close to the

orifice, so that the maximum velocity was taken as the constant velocity and the isovelocity hemisphere passed by the point where aliasing started. Enriquez-Sarano et al. (1995) carried out a study on 119 patients with isolated mitral regurgitation. The effective regurgitant orifice measured with the PISA method tended to overestimate the area when flow convergence was non-optimal (*i.e.* shape of isosurfaces were not close to a sphere), which was found to be relatively rare. Other authors have investigated the applicability of the method to patients with mitral regurgitation to assess severity (Hall et al., 1997), study orifice area variation (Hung et al., 1999) and general evaluation of the condition (Zoghbi et al., 2003).

Very recently, Goncalves et al. (2011) described the integration of the PISA method within latest commercial echo systems. Capable of acquiring 3D temporally resolved colour Doppler images in just one heart beat with a temporal resolution of 16 volumes per second, these systems show great potential for improved quantification of mitral regurgitation and flow through stenotic orifices.

The PISA method has proven high potential and accuracy for quantification of regurgitant flows. However, it assumes that the direction of the measured velocity in the aliasing region is parallel to the beam axis, which is in general not true, and may limit the application of the PISA method to regions other than very small orifices.

4.2.5 Summary and Discussion

Most of the widely used and new emerging methods for flow quantification with echo have been described in this section. Table 4.4 shows some of the most relevant publications over the last 30 years. During the 1980s, most echo flow quantification methods used spectral PWD, assuming that the measured velocity was the average over the circular cross-section (Gill, 1979; Struyk et al., 1985). Although this technique has been superseded by several other methods described above, it is still used for its simplicity and readiness, either as a quick means to see blood velocity in real-time that gives clinicians a rough idea of patient's flow dynamics, or even for advanced applications like intracardiac flow modelling e.g. the work by de Vecchi et al. (2012).

In the early 1990s, the standard method was improved by measuring velocity in several segments within a 1D scan line (Forsberg et al., 1995; Foster et al., 1990)

or a 2D scan plane (Embree and O'Brien, 1990). These techniques introduced complexity into the measurement and required special probes, thus have been barely investigated since.

The idea of integrating velocity values over a surface orthogonal to the direction of the measured velocity was tested *in-vivo* already in the late 1980s (Evans et al., 1989b), although the method was still relatively cumbersome. It was not until well into the 1990s (Gibson et al., 1994) that colour Doppler images were used to sample a surface orthogonal to the beam axis, first by mechanical rotating the 2D scan plane (Li et al., 2001; Mori et al., 2002; Poulsen and Kim, 1996a), and then with true 3D Doppler echo systems (Ge et al., 2005). This method has shown very promising results, especially in very recent years where high frame rate and wide FoV full 3D systems are available (Thavendiranathan et al., 2012). However, in all methods the surface through which flow can be computed depends on the echo view, which is limited by the anatomy of the patient.

In the last 20 years, great interest has been shown on quantification of mitral flow and mitral regurgitation. Although no echo Doppler method has proven to robustly and reliably achieve this, very promising methods have been proposed. In particular the PISA method has shown potential to calculate flow rate through stenosis and small orifices under favourable conditions of view angles and velocity range. The method was first proposed with 2D colour Doppler images (Enriquez-Sarano et al., 1995; Hung et al., 1999; Rodriguez et al., 1993; Utsunomiya et al., 1991), and the recent introduction of 3D colour Doppler systems promises significant improvements (Goncalves et al., 2011). However this method imposes some assumptions on velocity distribution, described in Sec. 4.2.4, which may introduce error into the flow measurement.

4.3 Remaining Challenges in Velocity and Flow Quantification with Echo Doppler

This chapter has covered from the first stages to the state-of-the-art techniques for cardiovascular velocity mapping and flow quantification using echo systems.

The main limitation regarding velocity measurement and characterisation is that

Publication	Method	Ang. Dep.	system	In vitro	In vivo	Region	Validation	Error
Gill (1979)	standard	yes	sPWD	phantom	15 pat	fetal umbilical	GT	14%
Hottinger (1979)	custom	no	sPWD	phantom	-	-	GT	r=0.99*
Struyk (1985)	standard	yes	sPWD	phantom	sheep + 16 pat.	ascending aorta	flowmeter	<19%
Evans (1989)	planar scanning	no	custom	phantom	1 pig + 54 pat	ascending aorta	dlution	r=0.96
Foster (1990)	1D profile	yes	sPWD	sim.	-	-	GT	low
Embree (1990)	2D profile	yes	2D PWD	phantom	-	-	GT	<10%
Utsunomiya (1991)	pisa	yes	2D CD	phantom	-	-	timed collection	<5%
Rodriguez (1993)	pisa	yes	2D CD	-	40 patients	mitral valve	area measurement	r=0.91
Gibson (1994)	spherical scanning	no	custom	phantom	-	-	flowmeter	<15%
Forsberg (1995)	1D profile	yes	1D CD	phantom	5 dogs	carotid + femoral	flowmeter	<30%
Enriquez-Sarano (1995)	pisa	yes	2D CD	-	119 patients	mitral valve	CWD	r=0.97
Poulsen (1996)	spherical scanning	no	2Dr CD	phantom	-	-	timed collection	10%
Hung (1999)	pisa	yes	M CD	-	30 patients	mitral valve	CWD	<5%*
Li (2001)	spherical scanning	no	2Dr CD	phantom	-	-	timed collection	r=0.98
Mori (2002)	spherical scanning	no	2Dr CD	-	8 sheep	pulmonary / aortic	flowmeter	r=0.95
Ge (2005)	spherical scanning	no	3D CD	-	13 children	mitral valve	PC-MRI	15%
Goncalves (2011)	pisa	yes	3D CD	-	-	mitral valve	-	-
Thavendiranathan (2012)	spherical scanning	no	3D CD	-	44 patients	aorta	PC-MRI	r>0.91

Table 4.4: Comparison of flow quantification methods from echo Doppler data. Notation for system: sPWD = spectral PWD. 1D/2D/3D CD = 1D/2D/3D Colour Doppler. 2Dr CD 2D rotational Colour Doppler (produces 3D images). M CD = M-Mode Colour Doppler. Notation for validation: GT = Ground Truth. PC-MRI = Phase Contrast MRI. CWD = Continuous Wave Doppler. Notation for error: when in percent, represents deviation from the reference technique. Otherwise, r stands for the correlation coefficient between the published method and the reference technique. Error values marked with "*" are valid only under optimal conditions of other parameters.

echo Doppler only measures a 1D component of the true 3D velocity. Although several authors have proposed methods to reconstruct 2D velocity fields, so far there has been no attempts to perform full 3D velocity mapping of blood velocity with echo Doppler. In this thesis, a method to reconstruct 3D velocity vectors from multiple registered echo Doppler views has been proposed (chapters 5, 6 and 7).

Several methods have been proposed for cardiovascular flow quantification with echo Doppler. From these methods, the angle-independent methods, based on velocity integration over surfaces orthogonal to the beam axis, have shown the most promising results. However, these methods still have several limitations. Frame rate is, even in the latest systems, much lower than the reference technique (2D+t Flow MRI). In addition, full coverage of the region of interest is not always possible because the entire cross section of the structure of interest has to be completely intersected by an ultrasonic wavefront within the FoV. Last, the orientation of the surface through which flow can be computed is limited by anatomy and view angle. In this thesis, a method which overcomes all these limitations has been proposed (chapter 8).

Chapter 5

Reconstruction of 3D Velocity Fields from Multiple 1D Projections

> " I saw a Line that was no Line; Space that was no Space: I was myself and not myself. When I could find a voice, I shrieked aloud in agony, 'Either this is madness or it is Hell'. 'It is neither,' calmly replied the voice of the Sphere, 'it is Knowledge; it is Three Dimensions: open your eye once again and try to look steadily'."
>
> *"Flatland: a Romance of Many Dimensions"*, Abbott (1884)

Contents

This chapter describes one of the original contributions of this thesis. Starting from a simple geometrical approach, a method for 3D flow reconstruction from projections is refined through three approaches of increasing complexity and performance.

This chapter is organised as follows. Section 5.1 explains the clinical motivation of 3D velocity reconstruction and describes the problem to be solved. Section 5.2 describes how multiple colour Doppler images are registered to each other. Sections 5.3, 5.4 and 5.5 describe three methods which incrementally improve 3D velocity reconstruction from 1D projections. Section 5.6 describes the applicability and limitations of the three methods. Finally, section 5.7 summarises the main points of this chapter.

5.1 Introduction

As explained in section 3.3 (remark 1), 3D colour Doppler images only provide a 1D projection of the true 3D velocity within a volumetric region of interest. The availability of 3D velocity would be of great clinical interest (as already discussed in sections 2.5 and 4.1.5) because blood velocity is a 3D phenomena, thus 3D quantification and analysis of 3D blood flow would provide a more comprehensive insight into blood flow patterns and clinical flow measurements. This chapter proposes a technique to recover the underlying 3D velocity from multiple registered 3D colour Doppler volumes. The proposed technique has two steps:

1. Image registration

   Multiple colour Doppler images are input to the reconstruction algorithms. To calculate the relative position and orientation of these views, image registration is performed. The proposed two step registration process is described in Sec. 5.2.

2. Velocity reconstruction from projections

Each colour Doppler image provides a 1D projection of blood velocity. By combining these projections, the underlying 3D velocity can be retrieved. Inspired by previous work in 2D (Sec. 4.1.3), a novel 3D velocity reconstruction method is proposed. Building from a simple geometrical approach, the algorithm is refined first by enabling the incorporation of an arbitrary number of views and last by providing a B-spline based framework in which scattered data from an arbitrary number of views can be used as input. These three versions of the algorithm are described in three different sections:

- Geometrical backprojection, described in Sec. 5.3.
- Voxel-wise Least Mean Squares (LMS), described in Sec. 5.4.
- B-spline based scattered LMS, described in Sec. 5.5.

5.2 Image Registration

In order to combine Doppler information from multiple N_v views the relative position between these views must be known. We calculate these relative positions using a registration algorithm which uses the phase-based similarity measure proposed by Grau et al. (2007), specifically designed for registration of multi-view 3D B-Mode echo images acquired from different acoustic windows. This similarity measure is based on the fact that the Fourier terms of an image are in-phase at edges (Mulet-Parada and Noble, 2000), and therefore high phase congruency across scales indicates presence of edges or features that can be used for registration. As proposed by Grau et al. (2007), registration was initialized by a point wise registration from three manually picked landmarks. In order to restrict the evaluation of the similarity measure to significant voxels, a mask of the shape of the 3D frustum, eroded 10 voxels to remove border effects in the phase images, was used. Target and source images where blurred with a Gaussian kernel of isotropic $\sigma = 5mm$.

Colour Doppler acquisitions contain a B-Mode image and a colour-coded velocity image (e.g. Fig. 3.12(a)). However, these B-mode images have a small Field of View (FoV) due to the increased processing required for the Doppler acquisition (Hoskins and Criton, 2010), as detailed in appendix A. This reduces the accuracy and capture range of the registration algorithm. In our data, the angular width of the frustum

for images with reduced FoV was $40° \times 38°$, whereas for standard B-Mode images was $68° \times 62°$.

Our solution is to use a two-step registration approach where we acquire a standard B-Mode image directly after each Doppler acquisition. The two steps of the registration are represented in Fig. 5.1. Our method firstly registers the reduced FoV B-Mode image to the corresponding standard (wide FoV) B-Mode image, which yields the matrix $M_{L_i}^{r_i}$, where r_i indicates the i-*th* reduced FoV image and L_i indicates the i-*th* wide FoV image. This registration is easy to achieve as the images have been acquired from the same position. Then one of the wide FoV B-Mode images is arbitrarily chosen as the reference image and all the other $N_v - 1$ wide FoV B-Mode images are registered to this reference, which yields a set of matrices $M_{L_{ref}}^{L_i}$ $(i = 1 \dots N_v)$. Therefore the resultant transformation between two Doppler views can be calculated from $M_{reg,i} = M_{L_{ref}}^{L_i} \times M_{L_i}^{r_i}$.

5.3 Geometric Voxel-Wise Reconstruction of 3D Vectors

If, at a given point $P \in \mathbb{R}^3$, three linearly independent projections $\mathbf{p_1}$, $\mathbf{p_2}$ and $\mathbf{p_3}$ of the velocity vector $\mathbf{v}(P)$ are known, then $\mathbf{v}(P)$ can be retrieved by geometrical means (Fig. 5.2 (a)). Let $\pi_i,\ i = 1 \dots 3$ be three planes defined by a normal vector $\hat{\mathbf{n}}_\mathbf{i} = \mathbf{p_i}/\|\mathbf{p_i}\|$ and a point $Q_i = P + \mathbf{p_i}$.

The velocity vector $\mathbf{v}(P)$ that generates the projections $\mathbf{p_i}$ can be calculated as the vector $\overline{PQ}$ where Q is the intersection of the three planes π_i (Fig. 5.2 (b)). The equations of the three planes define the linear system to solve:

$$\begin{cases} \pi_1 \equiv (Q - Q_1) \cdot \hat{\mathbf{n}}_\mathbf{1} = 0 \\ \pi_2 \equiv (Q - Q_2) \cdot \hat{\mathbf{n}}_\mathbf{2} = 0 \\ \pi_3 \equiv (Q - Q_3) \cdot \hat{\mathbf{n}}_\mathbf{3} = 0 \end{cases} \tag{5.1}$$

The system (5.1) can be expressed in matrix form:

$$\begin{bmatrix} \hat{\mathbf{n}}_\mathbf{1} & \hat{\mathbf{n}}_\mathbf{2} & \hat{\mathbf{n}}_\mathbf{3} \end{bmatrix}^\top Q = \begin{bmatrix} Q_1^\top \hat{\mathbf{n}}_\mathbf{1} \\ Q_2^\top \hat{\mathbf{n}}_\mathbf{2} \\ Q_3^\top \hat{\mathbf{n}}_\mathbf{3} \end{bmatrix} \tag{5.2}$$

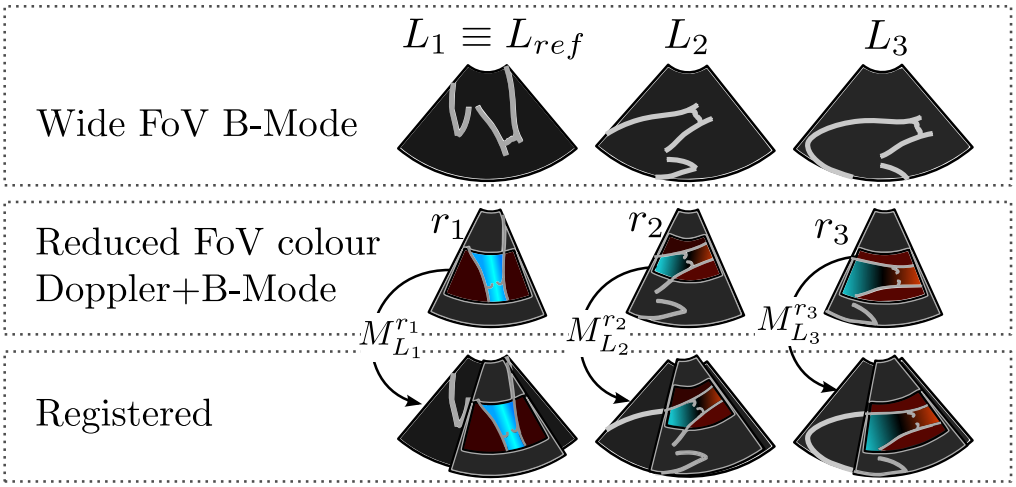

(a) Registration of the standard wide FoV B-Mode images to the B-Mode images from the colour Doppler acquisitions, which yields the matrices $M_{L_i}^{r_i}$.

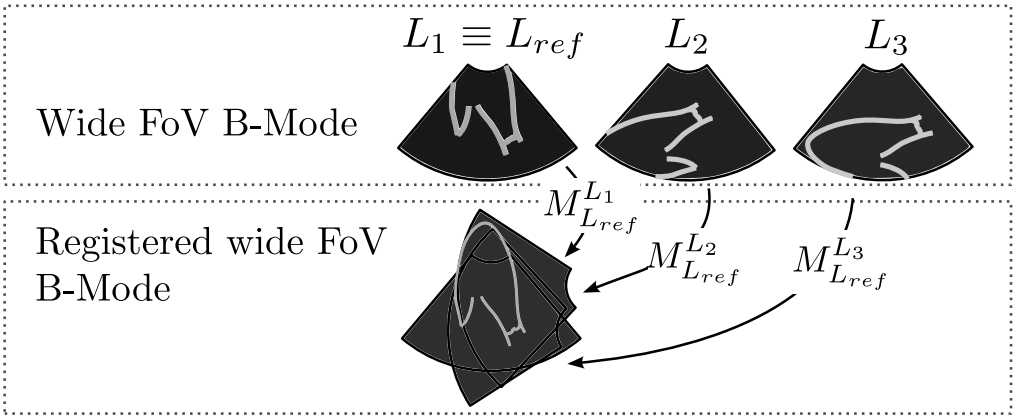

(b) Registration of the standard wide FoV B-Mode images to the reference wide FoV B-Mode image, which yields the matrices $M_{L_{ref}}^{L_i}$.

Figure 5.1: Two step registration process. Since the background B-Mode images acquired in a colour Doppler scan have reduced FoV, they are first registered to a standard B-Mode image (wide FoV) acquired from the same view, which is then registered to a reference B-Mode image acquired from a different view. The matrix to transform the colour Doppler images to the reference B-Mode image is $M_{reg_i} = M_{L_{ref}}^{L_i} \times M_{L_i}^{r_i}$.

Because the three projections must be independent, the matrix $\left[\begin{array}{ccc} \hat{\mathbf{n_1}} & \hat{\mathbf{n_2}} & \hat{\mathbf{n_3}} \end{array}\right]^\top$ is invertible and therefore the intersection of the planes is

$$Q = \left(\left[\begin{array}{ccc} \hat{\mathbf{n_1}} & \hat{\mathbf{n_2}} & \hat{\mathbf{n_3}} \end{array}\right]^\top \right)^{-1} \left[\begin{array}{c} Q_1^\top \hat{\mathbf{n_1}} \\ Q_2^\top \hat{\mathbf{n_2}} \\ Q_3^\top \hat{\mathbf{n_3}} \end{array}\right] \tag{5.3}$$

The 3D velocity is then $\mathbf{v}(P) = PQ$. Without any loss of generality, the system can be considered centred at the origin, thus $Q_i = \mathbf{p_i}$ and $\mathbf{v}(P) = Q$. In the case

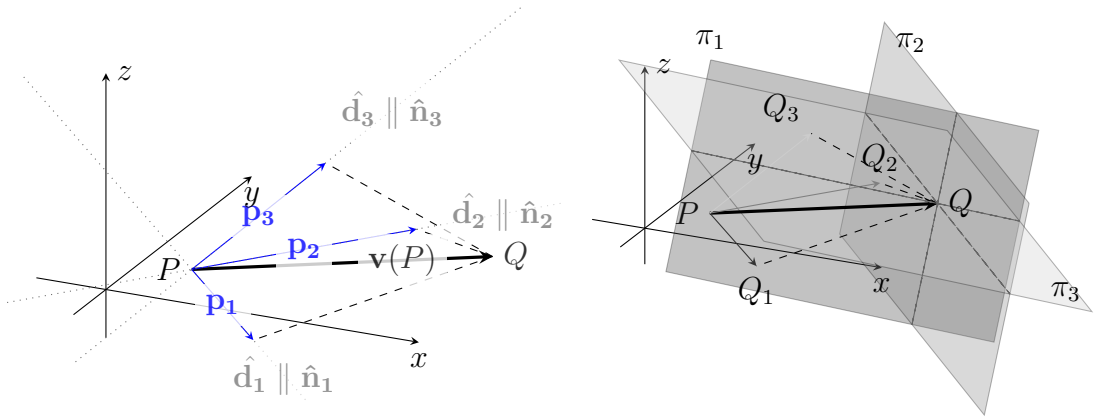

(a) 3D velocity $\mathbf{v}(P)$ and its projections.

(b) Geometrical approach based on plane intersection.

Figure 5.2: Geometrical approach. (a) Velocity vector $\mathbf{v}(P)$ and three projections $\mathbf{p_1}$, $\mathbf{p_2}$ and $\mathbf{p_3}$ along three independent directions $\hat{\mathbf{d}}_\mathbf{1}$, $\hat{\mathbf{d}}_\mathbf{2}$ and $\hat{\mathbf{d}}_\mathbf{3}$. (b) An orthogonal plane π_i is traced at the end of each projection vector $\mathbf{p}_i$ and orthogonal to the projection direction. The intersection of the 3 planes yields the original velocity vector $\mathbf{v}$.

of multiple colour Doppler views, the projections are, at each voxel, the measured Doppler velocity m_i along the direction of the beam $\hat{\mathbf{d}}_\mathbf{i}$, *i.e.* $\mathbf{p_i} = \hat{\mathbf{d}}_\mathbf{i} m_i$. Since the direction of the projection is parallel to the beam direction, $\hat{\mathbf{d}}_\mathbf{i} \cdot \hat{\mathbf{n}}_\mathbf{i} = 1$ (5.3) which results in the following equation:

$$\mathbf{v}(P) = \left(\begin{bmatrix} \hat{\mathbf{d}}_\mathbf{1} & \hat{\mathbf{d}}_\mathbf{2} & \hat{\mathbf{d}}_\mathbf{3} \end{bmatrix}^\top \right)^{-1} \begin{bmatrix} m_1 \\ m_2 \\ m_3 \end{bmatrix} \tag{5.4}$$

which can be solved to give the 3D blood velocity vector at each voxel.

The presented method is fast and simple, but is limited to 3 input views, because it requires that the matrix to be inverted is square (3×3 in 3D). However, if more views are available, using all of them to retrieve velocity should yield more accurate results and be more robust against noise. Therefore a more flexible method would be desired. For this reason, next section introduces an extension of the geometrical backprojection to an arbitrary number of views.

5.4 Voxel-Wise Least Mean Squares Reconstruction of 3D Vectors

Vector reconstruction from an arbitrary number of projections can be achieved using a LMS approach, which consists of the following. At a given voxel, where projections from N views are available, each measured velocity $\{m_i\}_{i=1...N}$ is defined by

$$m_i = \hat{\mathbf{d}}_\mathbf{i} \cdot \mathbf{v} + g_i \tag{5.5}$$

where g_i is a random variable representing noise in the measurement. The LMS approach consists of finding the value of $\mathbf{v}$ that minimises the energy term $j(\mathbf{v}) = \sum \|g_i\|^2$,

$$j(\mathbf{v}) = \sum_{i=1}^{N} \|\hat{\mathbf{d}}_\mathbf{i} \cdot \mathbf{v} - m_i\|^2 \tag{5.6}$$

For convenience, (5.6) can be re-written in matrix form as follows

$$\begin{aligned} j(\mathbf{v}) &= \left(\begin{bmatrix} \hat{\mathbf{d}_1}^\top \\ \vdots \\ \hat{\mathbf{d}_N}^\top \end{bmatrix} \mathbf{v} - \begin{bmatrix} m_1 \\ \vdots \\ m_N \end{bmatrix} \right)^\top \left(\begin{bmatrix} \hat{\mathbf{d}_1}^\top \\ \vdots \\ \hat{\mathbf{d}_N}^\top \end{bmatrix} \mathbf{v} - \begin{bmatrix} m_1 \\ \vdots \\ m_N \end{bmatrix} \right) \\ &= (\mathbf{D}\mathbf{v} - \mathbf{M})^\top (\mathbf{D}\mathbf{v} - \mathbf{M}) \end{aligned} \tag{5.7}$$

To minimise (5.7) it suffices to take the derivative of $j(\mathbf{v})$ and make it equal to zero:

$$\begin{aligned} \tfrac{\partial j(\mathbf{v})}{\partial \mathbf{v}} &= \tfrac{\partial}{\partial \mathbf{v}} (\mathbf{D}\mathbf{v} - \mathbf{M})^\top (\mathbf{D}\mathbf{v} - \mathbf{M}) \\ &= \tfrac{\partial}{\partial \mathbf{v}} (\mathbf{v}^\top \mathbf{D}^\top \mathbf{D}\mathbf{v} - 2\mathbf{v}^\top \mathbf{D}^\top \mathbf{M}) \\ &= 2\mathbf{v}^\top \mathbf{D}^\top \mathbf{D} - 2(\mathbf{D}^\top \mathbf{M})^\top \\ &= \mathbf{v}^\top \mathbf{D}^\top \mathbf{D} - \mathbf{M}^\top \mathbf{D} = 0 \end{aligned} \tag{5.8}$$

which yields

$$\begin{aligned} \mathbf{v}^\top &= (\mathbf{M}^\top \mathbf{D})(\mathbf{D}^\top \mathbf{D})^{-1} \Longrightarrow \\ \mathbf{v} &= (\mathbf{D}^\top \mathbf{D})^{-1} (\mathbf{D}^\top \mathbf{M}) \end{aligned} \tag{5.9}$$

Note that if $\mathbf{D}$ is square and invertible, which only happens when there are three input views, then

$$\mathbf{v} = \mathbf{D}^{-1} (\mathbf{D}^\top)^{-1} \mathbf{D}^\top \mathbf{M} = \mathbf{D}^{-1} \mathbf{M} \tag{5.10}$$

which is the same result as in (5.4) obtained by the geometrical approach.

This approach is fast and has flexibility to incorporate an arbitrary number of projections. However, this method operates voxel-wise. This means that at each point where a velocity vector is to be reconstructed all the input views must have a Doppler measurement. This is in general not the case, because input data can be irregularly sampled. For that reason, each input image must, after registration, be resampled into the output grid. The choice of the output grid and the interpolation scheme used during resampling have an impact on the accuracy of the solution. The next section describes a method which uses input projections sampled at scattered positions, and in addition facilitates incorporation of regularisation based on the derivatives of the reconstructed velocity field. Availability of the derivatives enables the incorporation of physical knowledge into the problem.

5.5 Patch-wise B-Spline Based Reconstruction of 3D Vectors

Arigovindan et al. (2007) proposed a mathematical framework for 2D velocity reconstruction based on a LMS formulation where velocity was expressed in a B-spline basis. This approach integrates the interpolation step within the reconstruction process and therefore input data can be arbitrarily scattered without any need for resampling. In this section an improved version of the method proposed by Arigovindan et al. (2007) is described in detail. Two major improvements of the method are proposed:

1. Extension of the LMS/B-spline approach to 3D.

   The extension to 3D not only provides a full velocity mapping but also allows incorporation of physical constraints (e.g. a penalisation on a compressibility term) which are of a 3D nature. The use of physical constraints has been previously proposed in the literature to regularise (Arigovindan et al., 2007) and to restrict the solution (Garcia et al., 2010; Uejima et al., 2010) for 2D velocity reconstruction. Although the use of the div-curl regulariser is a mathematically valid approach to condition a linear system, imposing that a 2D projection of 3D incompressible flow is incompressible does not necessarily lead to more

realistic results, unless the through-plane velocity is constant (in which case $\partial v_z/\partial z = 0$). In 3D, where all the spatial components of the velocity are available, penalising divergence helps both to condition the linear system and to impose physically meaningful constraints.

2. Patch-wise formulation of the solution.

   The ability to split the system to be solved into smaller pieces becomes a requirement when incorporating a third dimension to the reconstruction. This is because the use of 3D volumes instead of 2D images greatly scales up the computational resources needed for solving the linear system. Therefore the proposed method provides a scalable, patch wise velocity reconstruction scheme which allows the method to a) be computationally more efficient and b) reconstruct 3D velocity within arbitrary regions by defining a patch over the desired region.

5.5.1 LMS Formulation of the Reconstruction in a B-spline Grid

B-splines are smooth functions which are very widely used in signal and image processing for their numerous advantages (Unser, 1999). Additional details on B-splines are provided in Appendix B, in particular: origin, definition and usual approximation, interpolation and data fitting with B-splines. The proposed method consists in solving a B-spline based linear system.

Let $\mathbf{v}(P) = [v_x(P)\ v_y(P)\ v_z(P)]^\top$ be the fluid velocity field evaluated at the point $P = [P_x\ P_y\ P_z]^\top$. $\mathbf{v}(P)$ can be expressed in the space of uniform B-splines of degree n:

$$v_\gamma(P) = \sum_{i=1}^{N_g^i} \sum_{j=1}^{N_g^j} \sum_{k=1}^{N_g^k} c_{i,j,k}^\gamma \beta_{s,i}^n(P_x) \beta_{s,j}^n(P_y) \beta_{s,k}^n(P_z) \tag{5.11}$$

where $\gamma \in \{x, y, z\}$, the B-spline grid has a size of $N_g^i \times N_g^j \times N_g^k$, and $\{c^x, c^y, c^z\}_{i,j,k}$ are the B-spline coefficients. Notation for B-Spline functions has been shortened as follows:

$$\beta_{s,i}^n(t) = \beta^n(t/s - i)$$

where $\beta^n(t)$ is the B-spline of degree n and s is the distance between grid nodes and

determines the finest resolution of the resulting vector field (*i.e.* its scale).

Each registered input view $i = 1 \dots N$ provides an input Doppler data set $\{m_k, P_k, \hat{\mathbf{d}}_k\}_i$ where for each point $k = 1 \dots K_i$, m_k is the (projected) velocity measurement at position P_k where the echo beam direction is $\hat{\mathbf{d}}_k$. Appending input data from all N views, the resulting $\sum K_i$ input data points can be used to calculate the 3D velocity field $\mathbf{v}$ by minimising the following energy term:

$$j_{proj}(\mathbf{v}) = \sum_{k}^{\sum K_i} \|\hat{\mathbf{d}}_\mathbf{k} \cdot \mathbf{v}(P_k) - m_k\|^2 \tag{5.12}$$

The problem can be posed in matrix form by defining the beam direction matrix (5.13), the coefficient matrix (5.14) and the B-Spline sampling matrix (5.15):

$$\begin{gathered} \mathbf{D} = [\mathbf{D_x} \quad \mathbf{D_y} \quad \mathbf{D_z}] \\ \{\mathbf{D_x}\}_{ii} = d_{x,i} \quad \{\mathbf{D_y}\}_{ii} = d_{y,i} \quad \{\mathbf{D_z}\}_{ii} = d_{z,i} \end{gathered} \tag{5.13}$$

$$\begin{gathered} \mathbf{C} = [\mathbf{C_x} \quad \mathbf{C_y} \quad \mathbf{C_z}]^\top \\ \{\mathbf{C}_\gamma\}_{((i-1)N_g^j + j - 1)N_g^k + k, 1} = c_{i,j,k}^\gamma \quad \gamma = x, y, z \end{gathered} \tag{5.14}$$

$$\begin{gathered} \mathbf{S} = \begin{bmatrix} \mathbf{S_s} & 0 & 0 \\ 0 & \mathbf{S_s} & 0 \\ 0 & 0 & \mathbf{S_s} \end{bmatrix} \\ \{\mathbf{S_s}\}_{r,((i-1)N_g^j + j - 1)N_g^k + k} = \beta_{s,i}^n(p_{r,x})\beta_{s,j}^n(p_{r,y})\beta_{s,k}^n(p_{r,z}) \end{gathered} \tag{5.15}$$

These matrices allow (5.12) to be expressed in matrix form:

$$\begin{aligned} j_{proj}(\mathbf{C}) &= \|\mathbf{D_x S_s C_x} + \mathbf{D_y S_s C_y} + \mathbf{D_z S_s C_z}\|^2 = \\ &= \|\mathbf{DSC} - \mathbf{m}\|^2 = \\ &= (\mathbf{DSC} - \mathbf{m})^\top (\mathbf{DSC} - \mathbf{m}) \end{aligned} \tag{5.16}$$

where $\mathbf{m} = [m_1 \dots m_{\sum K_i}]^\top$. B-spline coefficients $\mathbf{C}$ are calculated by minimising (5.16) by taking the derivative of the energy function j with respect to $\mathbf{C}$, and

equating to zero, analogously to (5.8):

$$\begin{aligned} \tfrac{\partial}{\partial \mathbf{C}} J(\mathbf{C}) &= \tfrac{\partial}{\partial \mathbf{C}} \left((\mathbf{DSC})^\top (\mathbf{DSC}) \right) - 2 \tfrac{\partial}{\partial \mathbf{C}} \left((\mathbf{DSC})^\top \mathbf{m} \right) \\ &= \tfrac{\partial}{\partial \mathbf{C}} \left(\mathbf{C}^\top (\mathbf{DS})^\top (\mathbf{DS}) \mathbf{C} \right) - 2 \tfrac{\partial}{\partial \mathbf{C}} \left(\mathbf{C}^\top (\mathbf{DS})^\top \mathbf{m} \right) \\ &= 2\mathbf{C}^\top (\mathbf{DS})^\top (\mathbf{DS}) - 2\mathbf{m}^\top (\mathbf{DS}) = 0 \end{aligned} \tag{5.17}$$

which yields

$$\begin{aligned} \mathbf{C}^\top &= \mathbf{m}^\top (\mathbf{DS}) \left[(\mathbf{DS})^\top (\mathbf{DS}) \right]^{-1} \\ \mathbf{C} &= \left[(\mathbf{DS})^\top (\mathbf{DS}) \right]^{-1} (\mathbf{DS})^\top \mathbf{m} \\ \mathbf{C} &= \mathbf{A}_{proj}^{-1} \mathbf{b} \end{aligned} \tag{5.18}$$

where $\mathbf{A}_{proj} = \mathbf{S}^\top \mathbf{D}^\top \mathbf{DS}$ and $\mathbf{b} = \mathbf{S}^\top \mathbf{D}^\top \mathbf{m}$. The reconstructed 3D velocity field at the points sampled by $\mathbf{S}$ can be obtained as $\mathbf{V} = \mathbf{SC}$.

5.5.2 Incorporation of Physical Constraints

The proposed linear system may not always be well posed, e.g. A_{proj} might not be invertible. The system can be regularised by introducing a penalty term proportional to the divergence of the velocity. By penalising the divergence in 3D, we are imposing that the flow should be incompressible, which should yield a more realistic result since blood flow is assumed incompressible. This strategy is particularly well suited to the approach presented here for two reasons:

- The derivative of B-splines can be analytically computed, therefore divergence can be expressed as a function of B-spline coefficients. For this reason the problem can be formulated as a linear matrix equation and is thus solvable by LMS as in the previous section.

- Penalising the divergence in 3D is equivalent to imposing that the flow should be incompressible, which should yield a more realistic result since blood flow is assumed incompressible. This is not necessarily true in 2D, where a penalisation term based on the divergence enforces through-plane velocity to be considered constant.

The solution to the regularised problem consists of the minimisation of a new energy function:

$$j(\mathbf{v}) = (1 - \lambda) j_{proj}(\mathbf{v}) + \lambda j_{div}(\mathbf{v}) \tag{5.19}$$

where λ is a weighting factor and

$$j_{div}(\mathbf{v}) = \sum \|\nabla \cdot \mathbf{v}\|^2 \tag{5.20}$$

The term on the right hand side of (5.20) can be expressed in matrix form. Given that $\nabla \cdot \mathbf{v} = \partial_x v_x + \partial_y v_y + \partial_z v_z$,

$$\partial_x v_x(P) = \sum_{i=1}^{N_g^i} \sum_{j=1}^{N_g^j} \sum_{k=1}^{N_g^k} c^x_{i,j,k} \dot{\beta}^n_{a,i}(P_x) \beta^n_{a,j}(P_y) \beta^n_{a,k}(P_z) \tag{5.21}$$

where

$$\dot{\beta}^n_{a,l}(\gamma) = \frac{d}{d\gamma}\left(\beta^n_{a,l}(\gamma)\right) \qquad \gamma = \{x, y, z\} \tag{5.22}$$

The derivative B-spline sampling matrices are defined as follows

$$\{\dot{\mathbf{S}}_x\}_{r,((i-1)N_g^j + j - 1)N_g^k + k} = \dot{\beta}^n_{a,i}(p^r_x) \beta^n_{a,j}(p^r_y) \beta^n_{a,k}(p^r_z) \tag{5.23}$$

$$\{\dot{\mathbf{S}}_y\}_{r,((i-1)N_g^j + j - 1)N_g^k + k} = \beta^n_{a,i}(p^r_x) \dot{\beta}^n_{a,j}(p^r_y) \beta^n_{a,k}(p^r_z) \tag{5.24}$$

$$\{\dot{\mathbf{S}}_z\}_{r,((i-1)N_g^j + j - 1)N_g^k + k} = \beta^n_{a,i}(p^r_x) \beta^n_{a,j}(p^r_y) \dot{\beta}^n_{a,k}(p^r_z) \tag{5.25}$$

Let $\dot{\mathbf{S}} = [\dot{\mathbf{S}}_x \ \dot{\mathbf{S}}_y \ \dot{\mathbf{S}}_z]$, then the energy term corresponding to the divergence of the velocity (5.20) can be written in matrix form as

$$j_{div}(\mathbf{C}) = (\dot{\mathbf{S}}\mathbf{C})^\top (\dot{\mathbf{S}}\mathbf{C}) \tag{5.26}$$

and the full energy term, equivalent to (5.19) is

$$j(\mathbf{C}) = (1 - \lambda) j_{proj}(\mathbf{C}) + \lambda j_{div}(\mathbf{C}) \tag{5.27}$$

Taking the derivative and equating to zero, analogously to (5.8) yields

$$\begin{aligned} \tfrac{\partial}{\partial \mathbf{C}} j(\mathbf{C}) &= (1 - \lambda)\, \tfrac{\partial}{\partial \mathbf{C}} j_{proj}(\mathbf{C}) + \lambda \tfrac{\partial}{\partial \mathbf{C}} (\dot{\mathbf{S}}\mathbf{C})^\top (\dot{\mathbf{S}}\mathbf{C}) \\ &= (1 - \lambda) \left[2\mathbf{C}^\top (\mathbf{D}\mathbf{S})^\top (\mathbf{D}\mathbf{S}) - 2\mathbf{m}^\top (\mathbf{D}\mathbf{S})\right] + \\ &\quad + \lambda 2 \mathbf{C}^\top \dot{\mathbf{S}}^\top \dot{\mathbf{S}} \\ &= 0 \end{aligned} \tag{5.28}$$

and therefore

$$\begin{aligned}
& (1-\lambda)\mathbf{C}^\top(\mathbf{DS})^\top(\mathbf{DS}) + \lambda\mathbf{C}^\top\dot{\mathbf{S}}^\top\dot{\mathbf{S}} = (1-\lambda)\mathbf{m}^\top(\mathbf{DS}) \Longrightarrow \\
\mathbf{C}^\top &= (1-\lambda)\mathbf{m}^\top(\mathbf{DS})\left[(1-\lambda)(\mathbf{DS})^\top(\mathbf{DS}) + \lambda\dot{\mathbf{S}}^\top\dot{\mathbf{S}}\right]^{-1} \Longrightarrow \\
\mathbf{C} &= (1-\lambda)\left[(1-\lambda)(\mathbf{DS})^\top(\mathbf{DS}) + \lambda\dot{\mathbf{S}}^\top\dot{\mathbf{S}}\right]^{-1}(\mathbf{DS})^\top\mathbf{m} \\
&= (1-\lambda)\left[(1-\lambda)\mathbf{A}_{proj} + \lambda\mathbf{A}_{div}\right]^{-1}\mathbf{b} \\
&= (1-\lambda)\mathbf{A}^{-1}\mathbf{b}
\end{aligned} \tag{5.29}$$

5.5.3 Efficient Formulation of the Linear System

The linear system proposed in Sec. 5.5.1, defined by the matrices $\mathbf{A}$ and $\mathbf{b}$, is sparse and has a very particular structure due to the way it is generated:

$$\begin{aligned}
A &= \mathbf{S}^\top\mathbf{D}^\top\mathbf{S}\mathbf{D} \\
&= \begin{bmatrix} \mathbf{S_s}^\top & . & . \\ . & \mathbf{S_s}^\top & . \\ . & . & \mathbf{S_s}^\top \end{bmatrix}\begin{bmatrix} \mathbf{D_x}^\top \\ \mathbf{D_y}^\top \\ \mathbf{D_z}^\top \end{bmatrix}\begin{bmatrix} \mathbf{S_s} & . & . \\ . & \mathbf{S_s} & . \\ . & . & \mathbf{S_s} \end{bmatrix}\begin{bmatrix} \mathbf{D_x} & \mathbf{D_y} & \mathbf{D_z} \end{bmatrix} \\
&= \begin{bmatrix} \mathbf{Dx}^\top\mathbf{Ss}^\top\mathbf{SsDx} & \mathbf{Dx}^\top\mathbf{Ss}^\top\mathbf{SsDy} & \mathbf{Dx}^\top\mathbf{Ss}^\top\mathbf{SsDz} \\ \mathbf{Dy}^\top\mathbf{Ss}^\top\mathbf{SsDx} & \mathbf{Dy}^\top\mathbf{Ss}^\top\mathbf{SsDy} & \mathbf{Dy}^\top\mathbf{Ss}^\top\mathbf{SsDz} \\ \mathbf{Dz}^\top\mathbf{Ss}^\top\mathbf{SsDx} & \mathbf{Dz}^\top\mathbf{Ss}^\top\mathbf{SsDy} & \mathbf{Dz}^\top\mathbf{Ss}^\top\mathbf{SsDz} \end{bmatrix}
\end{aligned} \tag{5.30}$$

Matrix $\mathbf{A}$ is a 3×3 block matrix. Since $\mathbf{Dx}$, $\mathbf{Dy}$ and $\mathbf{Dz}$ have similar shape, all the blocks are banded matrices with the nonzero elements concentrated near the block diagonal. Figures 5.3(a) and 5.3(b) show the typical shape of $\mathbf{S}$ and $\mathbf{A}$ respectively. It should be noted that the shape of $\mathbf{A}$ is not particularly well suited for linear solvers, which are more efficient if the matrix is closer to diagonal.

The formulation of the matrix equations can be slightly modified to improve the matrix shape. Instead of filling $\mathbf{S}$ by blocks corresponding to x, y and z coordinates, as presented before, the rows of $\mathbf{S}$ can be arranged so that the three components of each input data point are consecutive, as shown by the red lines in Fig. 5.4(a). Similarly, the columns of $\mathbf{S}$ can be arranged so that the c_i^x, c_i^y and c_i^z are also consecutive, as shown by the green lines in Fig. 5.4(a). The columns of $\mathbf{D}$ have to be rearranged accordingly too. Figure 5.4(b) shows the resulting $\mathbf{A}$ matrix, where

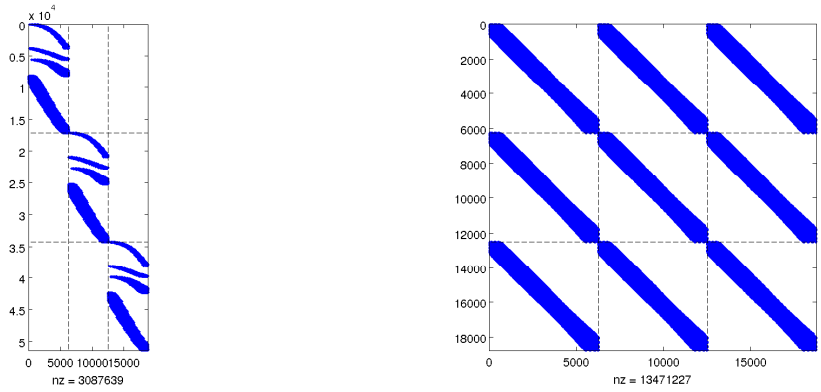

(a) **S** matrix. There is one row per input data point and one column per B-spline grid node.

(b) **A** matrix.

Figure 5.3: Structure of matrices in the LMS B-spline approach.

all the nonzero elements are disposed in bands close to the diagonal. As a result, the system $\mathbf{A}x = \mathbf{b}$ can be more efficiently solved, e.g. iterative methods will converge in fewer iterations and have a smaller residual.

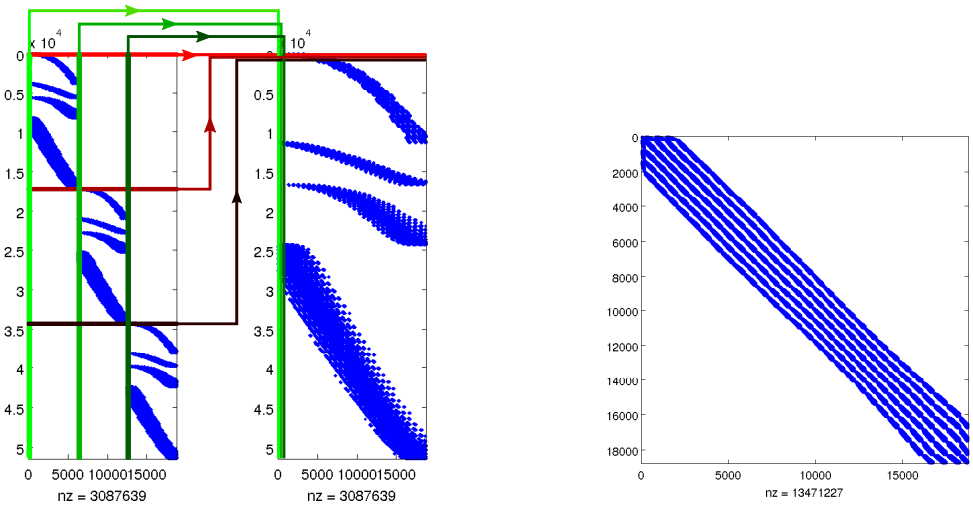

(a) Reordering of **S** .

(b) **A** matrix reordered.

Figure 5.4: Restructuration of matrices in the LMS B-spline approach. (a) Matrix reordering process. The $i-$th row of each block matrix $\mathbf{S_s}$ are relocated in contiguous rows, as shown for $i = 1$ following the red lines. Similarly, the $j-$th column of each block matrix are relocated at contiguous columns, as shown for $j = 1$ following the green lines. (b) Resulting **A** when built from reordered matrix **S**.

5.5.3.1 Grid Resolution

The separation between the nodes of the B-spline grid has a strong effect on the result and on the computational complexity.This can be illustrated by the simplified problem of fitting a B-spline curve to one component of the velocity, as shown in Fig.

5.5. Coarse grids are computationally lighter but also approximate input data with a higher residual error (Fig. 5.5(a)). On the other hand, very fine grids produce overfitting to the data and, although the resulting curve exactly passes through the input data points, undesired oscillations occur between the input data points (Fig. 5.5(d)). In between these extremes, the spacing between grid nodes determines a trade-off between smoothing input data (Fig. 5.5(b)) and potentially fitting to noise in the input data (Fig. 5.5(c)).

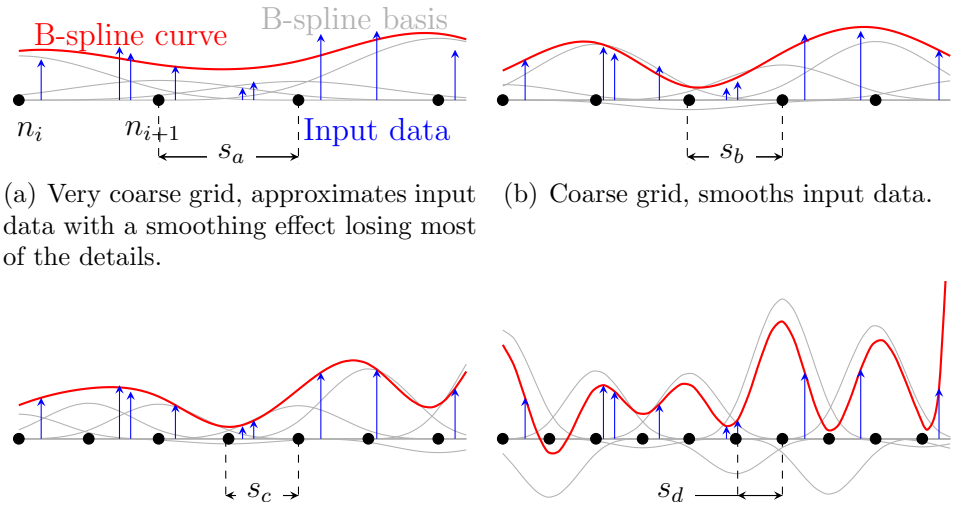

(a) Very coarse grid, approximates input data with a smoothing effect losing most of the details.

(b) Coarse grid, smooths input data.

(c) Fine grid, achieves almost perfect fit of input data, which includes fitting to noise.

(d) Very fine grid, produces data overfitting and introduces undesired oscillations in the resulting curve.

Figure 5.5: Effect of grid spacing on B-spline reconstruction. As the distance between nodes $\{n_i\}$ decreases, *i.e.* $s_a > s_b > s_c > s_d$, the B-spline curve better fits input data, until grid nodes are too close and oscillations appear.

As a general rule, it is desirable to have at least one input data point between two grid nodes to avoid oscillations. In the case of 3D vector reconstruction from multiple views, best results are observed if there is one input data point from at least three different views between grid nodes.

In multi-view echo, where input data points are irregularly sampled in spherical coordinates, and input data is available within a sparse domain (the overlap between at least three views) there is another phenomenon related to the B-spline grid which produces badly conditioned matrices. Some grid nodes might not have any input data points within the support of the corresponding B-spline basis function, introducing a full zero column into the matrix $\mathbf{S}$. This zero column will become a zero element in the diagonal of the matrix $\mathbf{A}$. Moreover, a node with some input data

points which are within the B-spline support but close to the edge of the B-spline grid will produce very small elements in the diagonal of $\mathbf{A}$ (note that this is more critical in the 3D case since building up $\mathbf{A}$ involves the product of x, y and z B-splines). All these factors contribute to increase the condition number of $\mathbf{A}$, enlarge the computational cost of solving the linear system and magnify the oscillations in the output function. In other words, because the input data is sparse, a regular grid cannot achieve stability and detail at the same time.

A solution to this is to remove the columns of $\mathbf{S}$ that sum to less than a certain threshold. As a result, nodes surrounded by many input data points will have a higher weight whereas nodes far from input data will be set to zero. This is equivalent to removing grid nodes during the calculation of the node weight, *i.e.* using an irregular sampling grid, but keeping all the advantages of regular grids. The impact on the final solution is illustrated in Fig. 5.6.

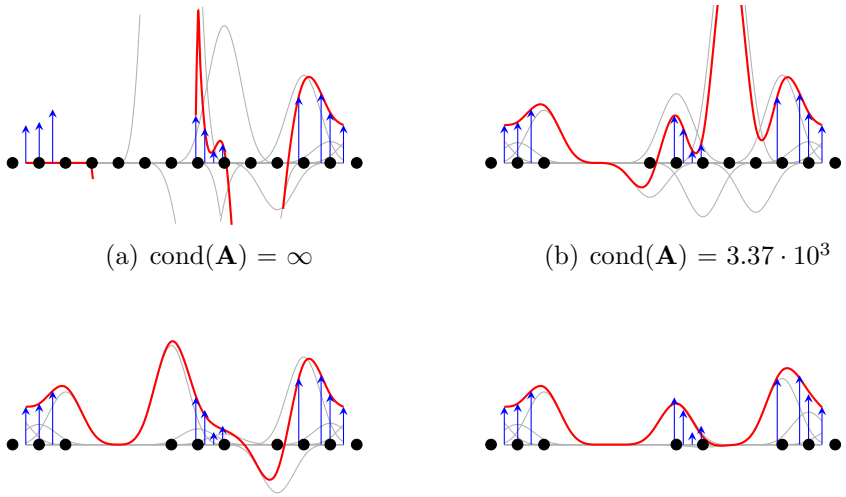

(a) $\text{cond}(\mathbf{A}) = \infty$ (b) $\text{cond}(\mathbf{A}) = 3.37 \cdot 10^3$

(c) $\text{cond}(\mathbf{A}) = 578.0$ (d) $\text{cond}(\mathbf{A}) = 59.1$

Figure 5.6: Effect of node removal on B-spline reconstruction. Removing nodes where there is no input data improves matrix condition and avoids undesired oscillations in the B-spline curve.

5.5.4 Computational Complexity, Scalability and Patch-Wise Computation

3D velocity reconstruction, as described in Sec. 5.5 can be conceived as a matrix-based linear problem. Matrix size depends on two factors: the number of input data points ($\sum K_i$) and the size of the B-spline grid ($N_g^i \times N_g^j \times N_g^k$). For 3D velocity re-

construction from three or more colour Doppler views, matrix size increases rapidly. The matrices **S**, **D** and **C** have $K \times 3$ rows, and matrix **S** has $N_g^i \times N_g^j \times N_g^k \times 3$ columns. For example, in the minimal case of 3 colour Doppler images, each one having $200 \times 200 \times 200$ voxels (scan converted), and a B-spline grid with a distance between nodes of twice the voxel size, **S** will be $24 \cdot 10^6 \times 3 \cdot 10^6$. Although this matrix is sparse, if each nonzero value is stored as a double (8 Bytes) and there are 16 non zeros per row, **S** would take up more than 2GB of memory. Therefore, the number of input views, the extension to the third dimension and the use of fine grids may cause severe memory limitations, and lacks scalability.

This problem, which is inherent to the way scattered data is approximated in a B-spline grid, has been addressed by Tustison and Gee (2006). As they remark, "*for large data sets, it* [the coefficient matrix] *may be poorly conditioned*". They propose to use just one input data point at a time. For each input data point, they calculate the coefficients of all the grid nodes within a neighbourhood of diameter equal to the support of the B-spline functions. Therefore, for each input data point they calculate $(n+1)^D$ coefficients (in the D-dimensional case). Some of the nodes are shared by multiple input data points, therefore, for those nodes, the final coefficient is computed as an average of each value computed weighted by the distance from each input data point to the node. This approach can be related to the formulation proposed in Sec. 5.5.1 by using only one input data point at a time (*i.e.* matrix **S** would have one row) and taking into account the $(n+1)^D$ neighbouring nodes (*i.e.* removing the columns from **S** corresponding to all the other nodes), and finally averaging the coincident nodes. This approach requires far less memory than solving for all the coefficients at once, but requires many calculations (The solution of a $(n+1)^D \times (n+1)^D$ matrix for each input data point plus the weighted averaging).

In this section, a different approach to reduce the computational requirements is proposed. Calculating all the nodes at the same time is extremely expensive. Calculating just one input data point requires many non-trivial operations. Instead the method proposed here is to divide the B-spline grid into patches where 3D velocity is computed independently, as shown in 2D (for ease of illustration) in Fig. 5.7. Because B-splines have a finite support, the coefficients in a patch can be computed by only using data within a small subset of the input domain. The computation patch P is then stepped across the B-Spline grid so as to cover all the

nodes as shown in Fig. 5.7.

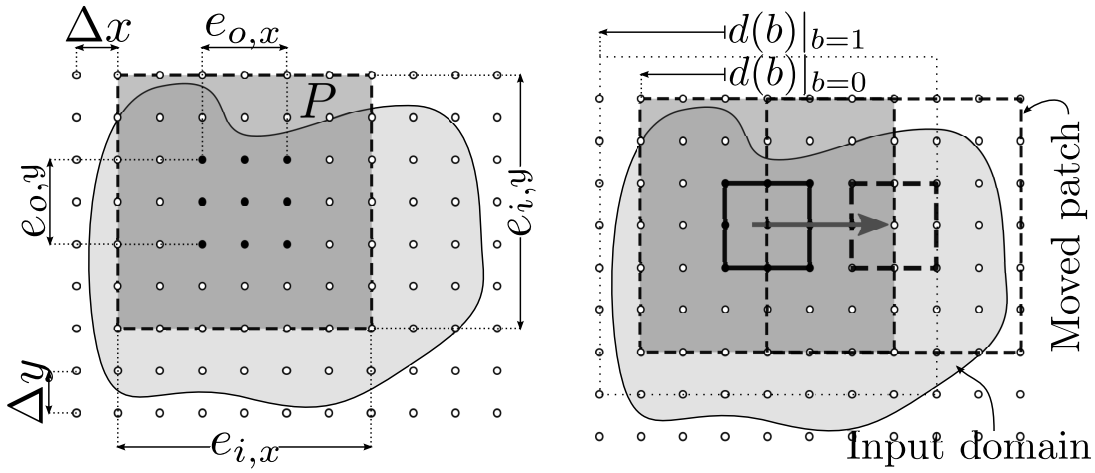

(a) Patch definition. (b) Patch overlap.

Figure 5.7: 2D representation of the patch-wise division of the reconstruction grid, for B-splines of degree $n = 3$. (a) The patch size is defined by the input extent (e_i, region of input data used to calculate the coefficients of this patch) and output extent (e_o, region covering the coefficients that are calculated in this patch). (b) Example of e_i for values of the border $b = 0$ and $b = 1$. The dashed patch on the right represents where the patch is moved next to compute the next set of coefficients.

The patch P is defined by two extents (Fig. 5.7(a)): the output extent e_o, which encloses calculated coefficients; and the input extent e_i, which covers the input data used for computing the coefficients. The exact solution is obtained if a single patch covers the whole input domain (*i.e.* $e_i \supseteq \Omega$) as done by Arigovindan et al. (2007). In the more general case where $e_i \subseteq \Omega$ the solution is approximated but the memory usage is reduced. If the coefficients within a region $e_o \subseteq G$ are calculated, the approximation improves as more input points are used. Since a B-Spline of degree n extinguish at $(n+1)/2$ grid points from the B-spline centre, to calculate each coefficient, all the points within a minimum distance $d_{min} = (n+1)/2 \times [\Delta x\ \Delta y\ \Delta z]^\top$ shall be taken into account, as represented in Fig. 5.7(b). To improve accuracy, d_{min} can be extended by an amount b (border parameter) selected by the user. This way, we include in the calculation of each coefficient all the input data within a distance $d = [(n+1)/2 + b] \times [\Delta x\ \Delta y\ \Delta z]^\top$.

This approach is equivalent to building matrix $\mathbf{S}$ with rows corresponding to input data points within e_i and columns corresponding to grid nodes within e_o and can therefore be regarded as an intermediate solution where the patch size is an input parameter which can be tuned to the available computational resources.

To reconstruct the velocity field across the whole region of interest, the patch is moved in such a manner that the external points of two consecutive patches overlap (Fig. 5.7(b)). The overlap is therefore of $[(n+1)/2+b]$ nodes. Because of the overlap, the coefficients at the overlapping region are computed several times; however, all the coefficients outside e_o are discarded.

5.6 Discussion

This chapter has proposed an approach for 3D velocity reconstruction. Three versions of the reconstruction algorithm have been described in sections 5.3, 5.4 and 5.5 with increasing complexity, flexibility and accuracy. Table 5.2 summarises the main differences between the three versions.

The geometrical and the LMS versions have similar memory usage, because they operate voxel-wise. Therefore, all the matrices they require are very small. For the same reason, for both of these versions of the reconstruction method the resulting linear systems can be solved by direct methods. The accuracy achieved by the LMS method should be superior to the Geometric method, since the inclusion of more input data should improve the solution, except for the case where the number of views is three in which case both methods give exactly the same solution. However, LMS approach is computationally more complex because it requires three times more matrix multiplications.

	Memory Usage	Complexity	Accuracy	Solver	Physical Constraints	Input
Geometric	*	*	**	Direct	N/A	Resampled
LMS	*	**	***	Direct	N/A	Resampled
B-spline LMS	*****	*****	****	Iter.	$\nabla \cdot \mathbf{v} = 0$	As is

Table 5.2: Comparison of three methods to reconstruct 3D vectors from multiple 1D projections.

The final B-spline based version is computationally more expensive than the other two, both in terms of memory usage, as explained in Sec. 5.5.4 and in terms of complexity for the large size of the linear system to be solved. In general, the use of direct methods for such large matrices is discouraged, in favour of iterative methods. However, the B-spline approach allows to easily incorporate physical knowledge

by penalising the divergence of the velocity field (which should be zero because blood flow is incompressible), because the derivatives of a B-spline curve are linearly dependent on the coefficients of the B-spline curve.

In spite of the large resources needed by the proposed B-spline framework, the method has significant advantages over simpler implementations. Firstly, it should achieve better accuracy, for two reasons. a) to reconstruct velocity at a single point, a neighbourhood of input data points is used (depending on the patch size), which helps smooth the result and remove noise from input data; and b) the ability to incorporate physical constraints brings the result closer to the underlying divergence-free flow. Secondly, voxel-wise methods require that input data is resampled into a defined output grid. The B-spline based method allows input data points to be arbitrarily scattered within the region covered by the output B-spline grid. When the multiple input views are 3D colour Doppler images acquired from different acoustic windows, input data points will be arbitrarily scattered, therefore the B-spline method can incorporate 3D colour Doppler data with no need to previously resample or interpolate it to a common grid.

The B-spline method proposes a patch-wise implementation of the reconstruction algorithm which allows a trade-off between execution time and required computational resources with little loss in accuracy. In addition, it allows the incorporation of physical constraints based on the derivatives of the vector field, which is convenient for flow-related problems.

5.7 Conclusion

This chapter has presented a method for 3D velocity reconstruction from multiple 3D colour Doppler views. The method has two steps: 1) a registration step to calculate the relative position and orientation of the input colour Doppler images, and 2) the solution of a linear system to retrieve 3D velocities from registered data.

A B-spline based regularised LMS approach to 3D velocity reconstruction has been described. This method should provide better accuracy and robustness with respect to noise than simpler methods, in exchange for longer execution times and requires more computational resources.

The experimental protocol and results of 3D velocity reconstruction are described

in the next chapter. The goal of these experiments is to show feasibility, potential and accuracy of 3D velocity reconstruction from multiple registered colour Doppler views. For all the advantages described in Sec. 5.6, experiments have been carried out with the B-spline based regularised LMS approach.

Chapter 6

Application of the Multiview Vector Reconstruction Method Using 3D Colour Doppler images

" Accurate retrieval and display of flow-related information remains a challenge because of the processes involved in mapping the flow velocity fields within specific chambers of the heart "

"Emerging Trends in CV Flow Visualization", Sengupta et al. (2012)

Contents

This chapter describes the application and assessment of the patch-wise B-spline Least Mean Squares (LMS) method described in Sec. 5.5 to recover 3D intracardiac blood velocity and flow from multiple colour Doppler images. In order to study the applicability of the method to a real clinical scenario, a sensitivity study was carried out to determine the ranges of view angles, noise in input data and registration errors that are required for an accurate reconstruction. This sensitivity study took simulated data as input, which enabled a comprehensive manipulation of the parameters under study. The method was then tested on healthy volunteers and paediatric patients.

This chapter is organised as follows. Section 6.1 contains a brief overview of the chapter. Section 6.2 describes how synthetic colour Doppler images were generated from temporally resolved 3 directional flow-encoded 3D MRI (3D+t Flow MRI) datasets. Section 6.3 explains how noise and variations in colour Doppler images were modelled with a novel multi-scale Gaussian approach. Section 6.4 describes the experimental protocol for simulated and real data, and Sec. 6.5 shows the results of the sensitivity analysis and the 3D velocities obtained in three volunteers and three paediatric patients.

6.1 Introduction

Multiview echocardiographic techniques present some specific challenges. In particular, in order to obtain images of anatomy and velocity from the heart, ultrasound waves must avoid bones from the ribs and the sternum and air from the lungs, for the reasons pointed out in Sec. 3.1.2. This limits the number of independent views which can be acquired to just few, and with limited angle between them. In addi-

tion, the relative position and orientation between acquired views must be known, e.g. by image registration. In the particular case of multiview 3D colour Doppler images, noise from each component of the velocity may have a strong impact on the reconstructed 3D velocity.

These three parameters (view angles, registration accuracy and noise of input data) and their impact on reconstruction accuracy were investigated with simulated colour Doppler images. A novel noise model for colour Doppler images is introduced in order to ensure that simulation studies were relevant to real cases. The goal of this noise model is to capture variability between colour Doppler images in a reliable but simple manner, without modelling the underlying physics and image formation process.

In summary, the original contributions of this chapter are three-fold: 1) to identify and characterise the main parameters which contribute to inaccuracy of 3D velocity reconstruction in a clinical scenario; 2) to provide the range of these parameters for which 3D flow can be accurately reconstructed, and 3) to show the first-ever 3D velocities reconstructed from multiple 3D colour Doppler images of volunteers and paediatric patients.

6.2 Simulation of Colour Doppler Images from 3D+t Flow MRI

Simulated colour Doppler images were generated from 3D+t Flow MRI acquired in a healthy volunteer. 3D+t Flow MRI data covering the heart and great vessels was acquired on a 3 Tesla MR System (Achieva Philips, Best, The Netherlands) using a k-space segmented acquisition triggered with the subject's electrocardiogram (ECG). Parameters included: spatial resolution: $2.5 \times 2.1 \times 2.5 mm^3$, temporal resolution: $35 ms$, velocity encoding range: $150 cm/s$. Data was acquired during free breathing using a respiratory navigator (Markl et al., 2007). To decrease acquisition time, a spatio-temporal undersampling factor of 8 was used in combination with a dedicated constrained reconstruction algorithm (Pedersen et al., 2009).

Figure 6.1 shows how synthetic colour Doppler images were generated from 3D+t Flow MRI data. Three virtual probe locations were manually selected from

clinically-feasible locations with respect to the anatomy in the MR images. From these locations, velocity was projected along virtual scan lines from the tip of the transducer towards the aortic valve (Fig. 6.1(a)). Colour Doppler images were simulated by interpolating the projected values in a Cartesian grid (Fig 6.1(b)). The resulting synthetic images then had noise added, using the multi-scale noise model described in Sec. 6.3. The resulting views, plus the knowledge of their relative positions, were used by our algorithm to produce a reconstructed 3D flow field.

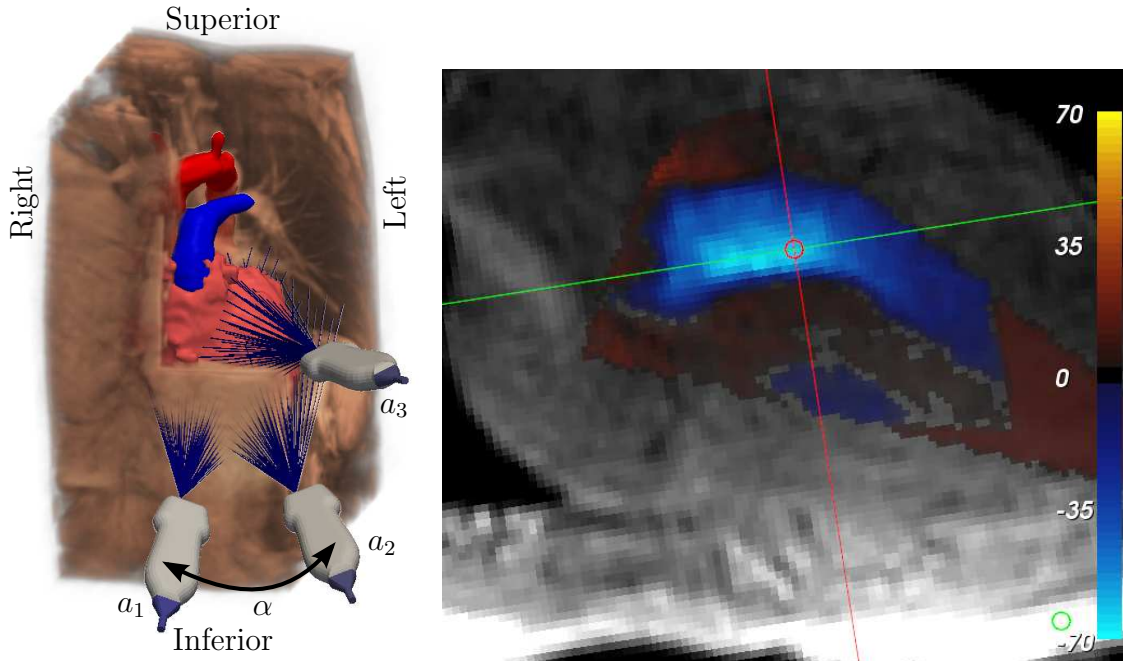

(a) Virtual probe locations.

(b) Slice of an image acquired from a_1.

Figure 6.1: Virtual probe locations in the PC-MRI dataset from which simulated colour Doppler images are generated. (a) a_1 and a_2 show transducer position located at an apical window, separated by a view angle $\alpha = 25°$, and p_1 shows transducer position located at a parasternal window. The virtual probe is oriented towards the aortic valve. As an example, (b) shows a zoomed 2D slice through the resulting 3D colour Doppler image, during systole, for probe position a_1.

6.3 Novel Noise Model for Colour Doppler Images

Previous work (Arigovindan et al., 2007; Maniatis et al., 1994; Xu et al., 1991) assumes that noise in Doppler images is voxel-wise additive Gaussian noise. However, observations of real Cartesian colour Doppler images suggest that voxel-wise noise is not the only type of variability in the images, as can be appreciated in Fig. 6.2,

where a slice of three images acquired from the same view and almost the same time (and so should be almost identical) are shown. Clear differences between these images, which are in a much larger scale than voxel-wise noise, are shown.

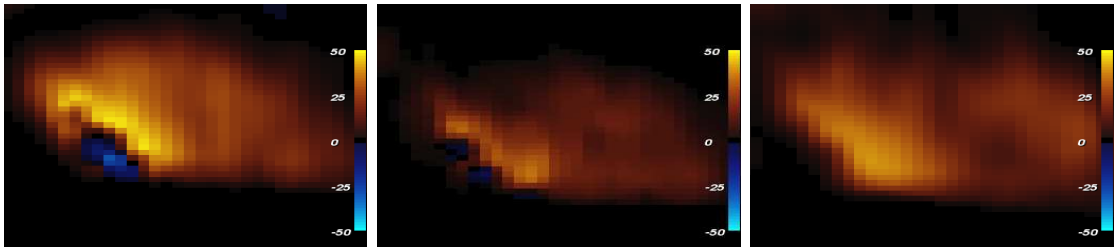

(a) (b) (c)

Figure 6.2: Variation in real colour Doppler images. (a)–(c) Slice of three real colour Doppler images acquired consecutively from the same view and at a similar time frame, showing unintended variations that occur in scan-converted colour Doppler images.

For the remainder of this chapter, any undesired and involuntary variations in colour Doppler images are referred to as "noise". In particular, noise is used here in a wide sense, comprising the traditional definition of noise (*i.e.* random error introduced by the measurement device, electronics, etc) and any other phenomena that can distort intensity values of the final image by any means.

Using this definition of noise, it can be appreciated in Fig. 6.2 that in real scan-converted images noise occurs not only at a voxel-wise scale, but also at a much larger scale. Moreover, the process of scan-conversion, interpolation and filtering prior to display greatly reduces any voxel-wise noise. Therefore, a new multi-scale model is proposed to enable realistic modelling of variations in colour Doppler images:

$$I = D + G(\sigma_f) + L_s(\sigma_L) \tag{6.1}$$

where D is the noiseless image where voxel intensity represents the value of the underlying velocity projected along the echo beam direction, G is the voxel-scale noise component, L_s is the large scale noise component of scale s, and I is the noise-perturbed realistic image. Both G and L_s are centred and with standard deviations σ_f and σ_L respectively. If I is regarded as a discrete sampling of a continuous $3D$ signal Υ over a discrete grid with spacing $(\Delta x, \Delta y, \Delta z)$, the terms of (6.1) are mathematically defined by

$$D = \Upsilon \times \sum_i \sum_j \sum_k \delta(\frac{x}{\Delta x} - i)\delta(\frac{y}{\Delta y} - j)\delta(\frac{z}{\Delta z} - k) \tag{6.2}$$

$$G(\sigma_f) = \sum_i \sum_j \sum_k g_{i,j,k}(\sigma_f)\delta(\frac{x}{\Delta x} - i)\delta(\frac{y}{\Delta y} - j)\delta(\frac{z}{\Delta z} - k) \tag{6.3}$$

$$L_s(\sigma_L) = \sum_u \sum_v \sum_w g_{u,v,w}(\sigma_L)\delta(\frac{x}{s\Delta x} - u)\delta(\frac{y}{s\Delta y} - v)\delta(\frac{z}{s\Delta z} - w) \tag{6.4}$$

where $g(\sigma_f)$ and $g(\sigma_L)$ are random values following a centred Gaussian distribution with variances σ_f^2 and σ_L^2 respectively. L_s is defined over a grid of spacing $(s\Delta x, s\Delta y, s\Delta z)$, *i.e.* the scale s is the ratio between the voxel spacing of the original image D and the large scale noise grid. To perform the sum in (6.1) we resampled $L_s(\sigma_L)$ to the grid defined by D by using cubic B-spline interpolation.

The Gaussian voxel-wise model is often justified because the received Doppler signal is related to the concentration of scatterers in blood (i.e. red cells), which is also believed to have a Gaussian distribution (Angelsen, 2000; Pastorelli et al., 2008). However, many non Gaussian effects contribute to noise in the final colour Doppler image, from acquisition phenomena such as Rayleigh fading, intrinsic spectral broadening of Doppler signal and non-uniformity of the ultrasound beam (Gill, 1985; Hoskins et al., 2010) to preprocessing of the data such as filtering and scan-conversion. In addition, uncontrolled external changes, like physiological changes, involuntary changes in probe location, pressure of the probe against the skin and small changes in velocity scale (Fan et al., 1994) also contribute to changes in Doppler images. All these combined effects can produce important intra-machine and inter-machine variability of colour Doppler images, as discussed by Fan et al. (1994).

The goal of our noise model is not to represent the underlying physics of colour Doppler image formation, but to produce realistic perturbations on Cartesian converted colour Doppler images in a simple way. Therefore (6.1) models all the acquisition and preprocessing chain, which includes Cartesian conversion, filtering and smoothing for display.

The noise model proposed in this section needs three input parameters: the scale s for the large scale noise component L_s, the variance of the voxel-scale noise component σ_f^2 and the variance of the large scale noise component σ_L^2. In the

following sections first how to estimate the value of s is described, and then a value for the ratio between the amounts of large (σ_L^2) and small (σ_f^2) scale noise is proposed, so the proposed model can be compared with a standard voxel-scale noise model.

6.3.1 Finding the appropriate scale for the noise model

To obtain the scale for the proposed noise model, several consecutive colour Doppler images were acquired without moving the probe and were then compared using the Sum of Squared Differences (SSD) measure, at different values of the scale s. The representation I^s of an image I at a scale s is defined as the best approximation, in a LMS sense, of I in a B-spline grid where node spacing is determined by s:

$$\begin{aligned} I^s(\mathbf{p}, \mathbf{C^s}) &= \textstyle\sum_i \sum_j \sum_k c^s_{i,j,k} \beta^n_{s,i}(p_x) \beta^n_{s,j}(p_y) \beta^n_{s,k}(p_z) \iff \\ \mathbf{I^s} &= \mathbf{S}(s)\mathbf{C^s} \end{aligned} \tag{6.5}$$

where $\mathbf{I}$ and $\mathbf{I^s}$ are column vectors with all the voxel values of I and I^s, $\mathbf{S}$(s) is the B-spline sampling matrix at the scale s, defined in (5.15), and the coefficients $\mathbf{C^s} = [\ldots c^s_{i,j,k} \ldots]^\top$ are calculated by minimising the dissimilarity between I^s and I, in a least mean squares sense analogous to (5.12):

$$\begin{aligned} & \min_{\mathbf{C^s}} \textstyle\sum \|I^s(\mathbf{p}, \mathbf{C^s}) - I(\mathbf{p})\|^2 \\ \Rightarrow \quad & \mathbf{C^s} = (\mathbf{S}(s)^\top \mathbf{S}(s))^{-1} \mathbf{S}(s)^\top \mathbf{I} \\ \Rightarrow \quad & \mathbf{I^s} = \mathbf{S}(s)(\mathbf{S}(s)^\top \mathbf{S}(s))^{-1} \mathbf{S}(s)^\top \mathbf{I} \end{aligned} \tag{6.6}$$

To estimate the size of the large scale noise, the mean sum of squared differences $mSSD(s)$ between the n images at scale s is calculated:

$$mSSD(s) = \frac{2}{n(n-1)} \sum_{i=2}^{n} \sum_{j=1}^{i-1} \overline{\|I_i^s - I_j^s\|^2} \tag{6.7}$$

where $\overline{\|\cdot - \cdot\|^2}$ indicates the average SSD between two images.

Figure 6.3 illustrates how the large scale is chosen. Figure 6.3 (a) represents a slice of I^1 and I^2 at different scales. The comparison between both images is shown in Fig. 6.3 (b), which shows values of $mSSD(s)$ over a range of scales. At large scales (right hand side of Fig. 6.3) the images will be very blurred and $mSSD(s)$ will represent the squared difference between the mean values of the images. As the

scale is reduced, features in the individual images become more distinct, and there is a scale at which features between the different Doppler images match (s_M). As the scale is further decreased we observe large scale variations between the images which initially increase $mSSD(s)$ slightly, but $mSSD(s)$ remains constant over a range of values of s. This region is denoted by the dashed ellipse in Fig. 6.3, and it is over these range of values that we propose our large scale noise should be calculated. As s is further reduced $mSSD(s)$ increases which is caused by small scale, (voxel-wise when $s = 1$) differences between the images. Therefore, $s = 15$ was chosen for the size of the large scale noise, which is approximately in the middle of the range for the datasets tested.

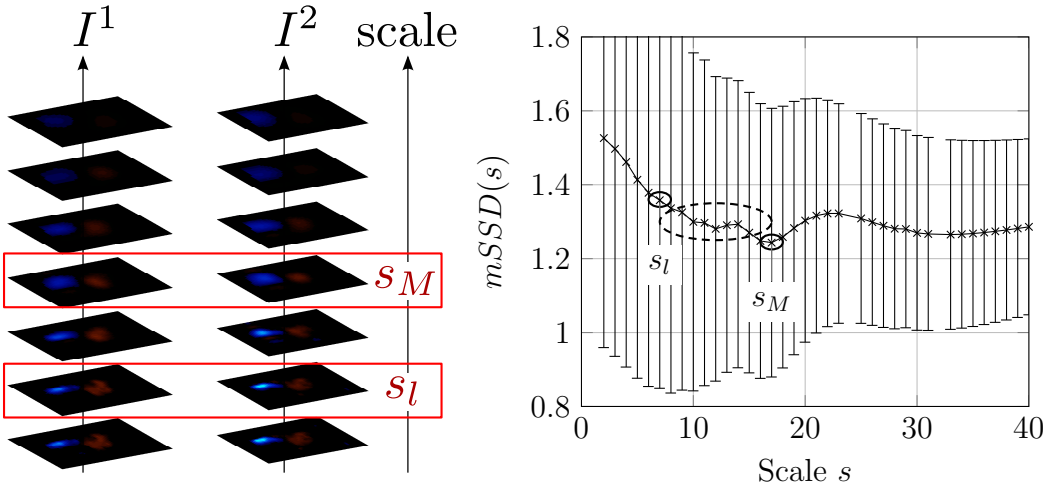

(a) Two images at different scales.

(b) mSSD between images.

Figure 6.3: Finding the scale at which variations occur. (a) Slices of two images represented at different scales. (b) Mean value and standard deviation of the mSSD, between images from one view (averaged over all frames), with respect to the scale s. The x axis represents the scale. The curve minimum, indicates the scale s_M for which the large scale features of both images best match. A dashed ellipse indicates the range of scales where the large scale variations occur.

6.3.2 Finding the ratio between amount of large-scale noise σ_L and voxel-scale noise σ_f

The ratio between σ_L and σ_f was chosen so that the proposed multi scale noise model and the standard voxel-wise noise model (of variance σ_{vw}) could be compared. The level of noise represented in both models is similar if the reconstructed velocity vectors have similar average angle and magnitude error. Figure 6.4 shows the average

absolute difference in angle and in magnitude for a voxel-wise noise model compared to a large scale noise model, when $\sigma_{vw} = \sigma_L$ for different values of σ_f. It can be shown that the curves agree well for $\sigma_f = \sigma_L/2$, thus this was the value chosen for the proposed model.

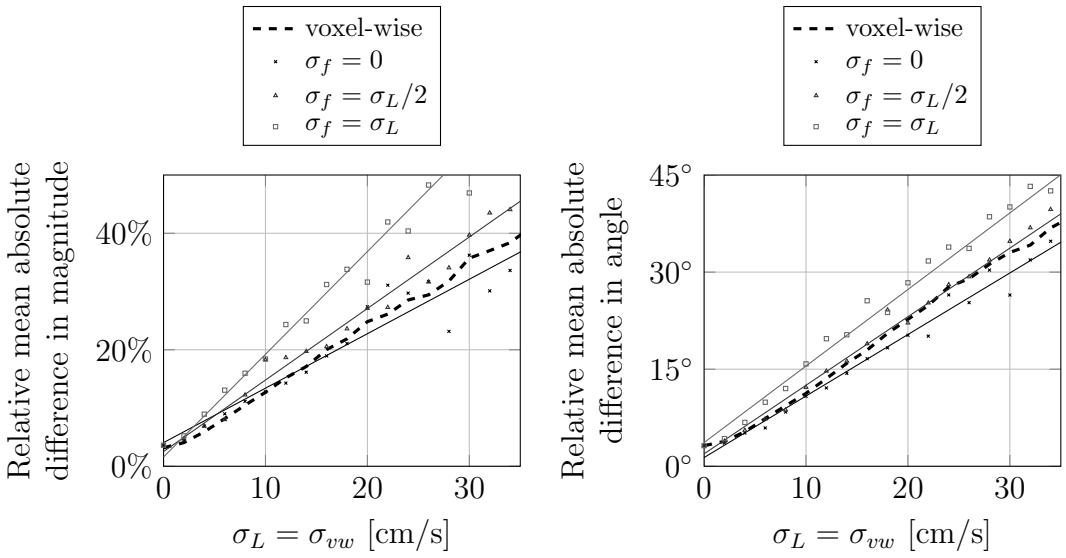

(a) Absolute difference in magnitude (b) Absolute difference in angle

Figure 6.4: Noise dependence in velocity magnitude in simulated data, for different values of the ratio between large scale and voxel scale noises, σ_f/σ_L.

The proposed multi-scale noise model produces more visually realistic variations in colour Doppler images than the standard Gaussian voxel-wise model. Figure 6.5 shows a comparison of variation in real images and variation with Gaussian voxel-wise and with the proposed multi-scale noise models. Three real images acquired from the same view, duplicated from Fig. 6.2 are shown in Fig. 6.5(a)–6.5(c), and similar images simulated with the proposed method Fig. 6.5(d)–6.5(f) and with the standard voxel-wise approach Fig. 6.5(g)–6.5(i). From visual inspection it can be appreciated that the proposed method models variation in colour Doppler images which are much more realistic when compared to real Doppler acquisitions than the voxel-wise approach.

6.4 Materials and Experiments

This section describes the experiments carried out on simulated data and real data. Experiments on simulated data were designed to estimate view angles, noise level of

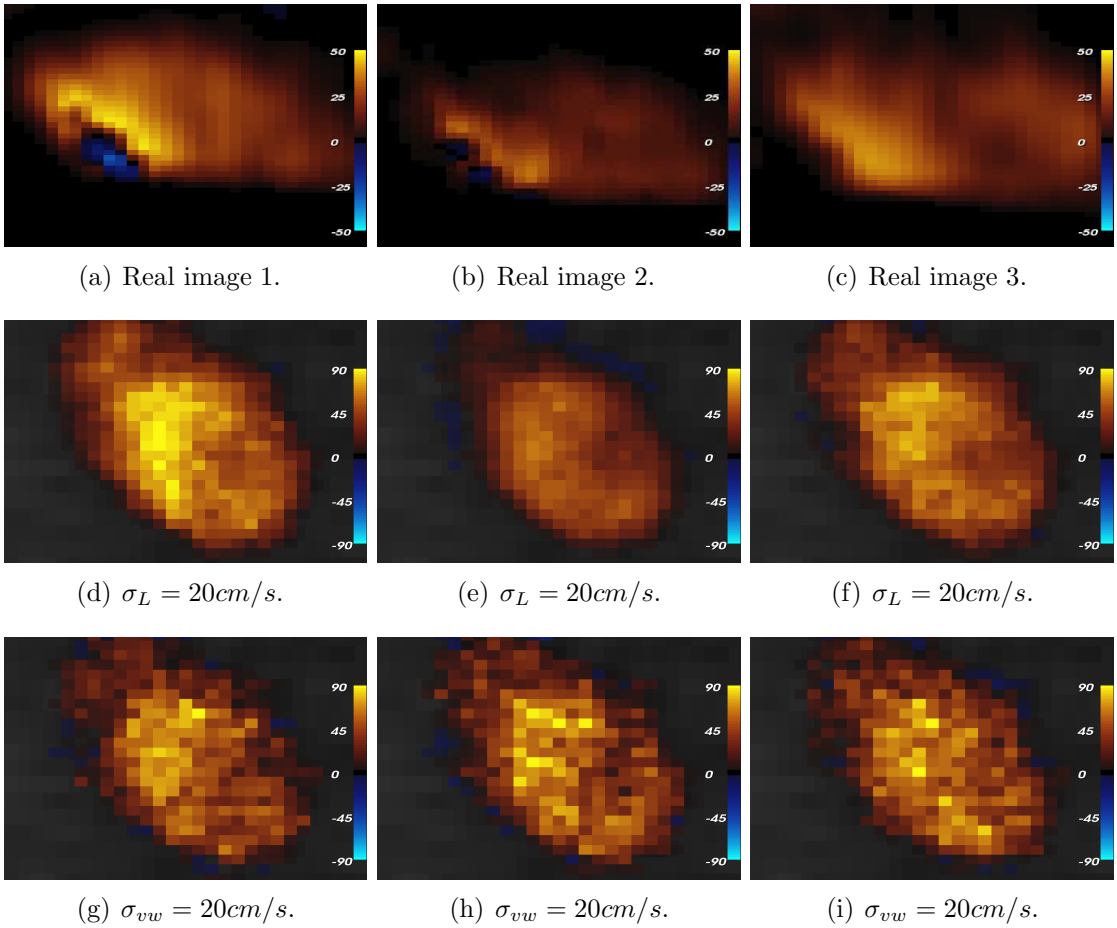

(a) Real image 1. (b) Real image 2. (c) Real image 3.

(d) $\sigma_L = 20cm/s$. (e) $\sigma_L = 20cm/s$. (f) $\sigma_L = 20cm/s$.

(g) $\sigma_{vw} = 20cm/s$. (h) $\sigma_{vw} = 20cm/s$. (i) $\sigma_{vw} = 20cm/s$.

Figure 6.5: Comparison of real and simulated colour Doppler images. (a)–(c) Slice of three real colour Doppler images acquired consecutively from the same view, duplicated from Fig. 6.2. (d)–(f) Three simulated colour Doppler images, produced from 3D+t Flow MRI, acquired from a virtual view manually chosen to be close to the view position of (a)–(c), and approximately the same cardiac phase. For each of them the proposed multi-scale noise has been used ($\sigma_L = 20cm/s$, $\sigma_f = \sigma_L/2$). (g)–(i) Simulated images produced in a similar way as (d)–(f) but with added voxel-wise noise ($\sigma_{vw} = 20cm/s$). The multi-scale noise model produces more realistic variations than the typical voxel-wise Gaussian model.

input data and registration accuracy required to enable accurate 3D blood velocity reconstruction. The outcome of the simulation study was verified with real data from three healthy volunteers. A preliminary test on three paediatric patients is also included, to show feasibility and compliance with current clinical protocols.

6.4.1 Experiments on Simulated Data

Experiments were carried out to evaluate the sensitivity of flow reconstruction to two different kinds of parameters:

- Algorithmic parameters: the error introduced by the method itself, which is

produced by the combined effect regularisation and patch-wise computation.

- External factors: three parameters that could have a major impact on reconstruction accuracy are considered:
  - Noise in colour Doppler images.
  - Registration accuracy.
  - Range of view angle.

The reconstructed velocity fields obtained were compared to the ground truth in the following way, which allowed to extrapolate results to real data. Three error measurements were carried out: mean absolute difference in velocity magnitude, in velocity angle, and in flow rate through the ascending aorta, using exactly the same surface and the same segmentation in the simulated data as in the ground truth. Although mean absolute difference in flow rate represents an indirect measurement of accuracy of the 3D velocity field through a scalar, it was chosen because it can also be compared to real volunteer data, for which a ground truth velocity field was not available, but flow rate could be calculated from 2D+t Flow MRI.

6.4.1.1 Sensitivity to Algorithmic Parameters

Experiments on the dependence of the reconstructed velocity field with the value of two algorithmic parameters are reported: effect of the border width (b), and effect of regularisation (5.19) on the three errors described above, for different values of λ.

6.4.1.2 Sensitivity to External Factors

In subsequent experiments, noise in input data in the range $0cm/s \leq \sigma_L < 40cm/s$ are used, which are consistent with Doppler noise levels described in the literature (Arigovindan et al., 2007; Pastorelli et al., 2008) and cover the range of values experienced in volunteer experiments (Sec. 6.5.2 and Fig 6.5).

6.4.1.2.1 Noise in colour Doppler data Reconstruction accuracy for different amounts of multi-scale noise (6.1) is assessed. As described in Sec. 6.3, the multi-scale noise model has three parameters: scale at which large variations occur, which is fixed to $s = 15$; standard deviation of the large scale component of

the multi-scale noise model, σ_L; and standard deviation of fine scale component of the multi-scale noise model, σ_f, which is fixed to $\sigma_f = \sigma_L/2$. For each case, the experiment was repeated 50 times, and statistics were calculated over the 50 trials.

6.4.1.2.2 Registration accuracy Registration errors are simulated by adding Gaussian noise to the rigid registration parameters of one of the three views. The phase-based similarity measure used to register the three views (Grau et al., 2007), reports Target Registration Error (TRE) as described by Fitzpatrick (2001) below $2mm$ in more than 70% of the cases, the rest of which are in the range $[2mm, 5mm]$. Therefore, registration error is modelled by perturbing the rigid parameters of the registration matrix in order to obtain values of the TRE in the interval $[0mm, 5mm]$. This was achieved as follows: 1000 random rigid transformation matrices were produced and used to transform one of the three views. For each matrix, the TRE was calculated as the average displacement, in mm, of 100 landmarks randomly placed within a 15mm radius from the centre of the Left Ventricular Outflow Tract (LVOT) segmentation used for flow rate computation. The 1000 trials were grouped in 20 bins by their TRE, with a minimum of 20 trials per bin. The transformed images were used to reconstruct velocity vectors.

6.4.1.2.3 View angle At least three colour Doppler views are required to reconstruct 3D velocity. The angle between these views has an important impact on reconstruction accuracy. In clinical practice, view angles are limited by anatomy and acoustic windows. A clinically feasible protocol was simulated by using three standard views: two apical and one parasternal, as represented in Fig. 6.1 (a). The angle between the apical views and the parasternal is usually fixed by anatomy. The echocardiographer can more easily move the probe within the four-chamber plane to separate the two apical views by an angle α. For this reason the impact of angle between views is studied through the influence of α three error measurements described above. The parasternal view and one apical view (beam sources at p_1 and a_1 respectively) were kept fixed while the second apical view (beam source at a_2) was placed at the apical window separated from a_1 by an angle α which was varied from 0° to 60° at intervals of 1°. For each angle, the experiment was repeated 50 times, and statistics were calculated over the 50 trials.

6.4.2 Experiments on Real Data From Volunteers

3D Colour Doppler data was acquired on volunteers targeting the blood flow through the LVOT, for 3 reasons: Firstly, flow velocity patterns through the aortic valve have been thoroughly studied with other techniques and therefore velocity profile in healthy subjects is well-known (Paulsen and Hasenkam, 1983; Segadal and Matre, 1987), which allows the assessment of the flow patterns obtained. Second, availability of temporally resolved through-plane flow-encoded 2D MRI (2D+t Flow MRI) through the aortic valve allowed a quantitative assessment of the technique. Third, the aortic valve is a region which can be imaged by a standard transthoracic probe from 3 or more views, which is a requirement for our multi-view approach.

Echo exams were acquired using a Philips iE33 system, equipped with a X3-1 transducer for cardiac applications. Image acquisitions consisted of 3D+t sequences acquired from 3 different views. At each view, an expert echocardiographer acquired three consecutive sequences without moving the transducer, to measure noise between similar acquisitions. Under ideal conditions these three sequences would be identical, however images vary due to involuntary changes in anatomy or in probe location and noise and variability in colour Doppler images. Access to reformatted Cartesian echo images was via the Philips Healthcare QLab software, using either 2D+t screenshots (colour Doppler) or via a dedicated software patch (B-Mode images). Details on image extraction can be found in appendix C.

Any sequences which failed registration or where the image quality was clearly poor were discarded. This was done by visual inspection. In the three volunteers, 7.5% of the input images were discarded. When for the same view colour Doppler images differed significantly, the colour Doppler image with more signal was assumed the most accurate. Only this image was then used as input for the velocity reconstruction process described in Sec. 5.5.

The reconstructed velocity fields were evaluated qualitatively and quantitatively. Qualitative analysis was carried out by clinicians who scored the image quality and plausibility of the resulting flow patterns and velocity profiles (bad – average – good).

Quantitative accuracy measurements were carried out comparing flow rate curves obtained from our proposed method to flow rate obtained from standard 2D+t Flow

MRI, calculated at the ascending aorta. Flow curves were integrated through time to compute stroke volume, which was also compared between the two modalities. 2D+t Flow MRI was acquired on a 3 Tesla MR System (Achieva Philips, Best, The Netherlands) including a clinically used phase contrast sequence with the following parameters: k-space segmented acquisition retrospectively triggered with the subjects ECG, spatial resolution: $2.5 \times 2.1mm^2$, slice thickness: $8mm$, temporal resolution: $25ms$, velocity encoding range: $150cm/s$. Data was acquired during a breathhold of approximately $18s$. Care was taken to align the acquired slice perpendicularly to the main flow direction.

6.4.3 Experiments on Patient Data

The method was applied to data from three paediatric congenital patients, and compared to 2D+t Flow MRI acquired immediately before the echo. Patient 1 was 2 years old with Hypoplastic Left Heart Syndrom (HLHS) post Hemifontan procedure. Five colour Doppler views were acquired with a Philips X3-1 probe during breath-holds, targeting the tricuspid valve: 2 apical, 1 parasternal, 1 subcostal and 1 parasternal oblique. A standard B-Mode sequence was acquired in each view for image registration. Patient 2 was 3 months old with HLHS post stage 1 procedure. Three colour Doppler views were acquired with a Philips X7-2 probe during breath-holds, targeting the tricuspid valve: 1 apical, 1 parasternal and 1 subcostal. Patient 3 was 2 months old with repaired critical aortic stenosis and residual mitral stenosis. Three colour Doppler views were acquired with a Philips X7-2 probe during breath-holds, targeting the left ventricular chamber: 1 apical, 1 parasternal and 1 subcostal. At each view, the probe was tilted along three orientations in order to achieve maximum ventricular coverage (therefore in total 9 images were acquired).

6.4.4 Dealiasing of Real Colour Doppler Images

Care was taken when selecting the Doppler velocity range to avoid aliasing. However some first-order aliasing still occurred. In situations where aliasing is a common artefact, an automatic dealiasing method is preferred. Many such methods are available in the literature, mostly dedicated to meteorological sciences and flow MRI. For example, Liang (1996) proposed a method to dealiase (commonly referred

to as *unwrap*) the phase of the complex phase-contrast MRI bivariate signal by using a polynomial model. Unfortunately, this and other methods based on phase analysis of the complex signal are not applicable to colour Doppler images, which are real-values (if it is assumed there is no access to raw echo signals). Other methods have been developed to specifically dealiase colour Doppler images, for example the method by Shahin et al. (2000) which is automatic but requires a training data base of colour Doppler images. Very recently, Muth et al. (2011) proposed a fully automated method for dealiasing of colour Doppler images. This method showed very good results in 2D images, however it relies on several assumptions (e.g. the aliased region is smaller that the non-aliased region of the image; the noise is Gaussian; etc) and ignores the influence of interpolation during scan conversion.

For the images used in this thesis, aliasing was rare, therefore the number of images to dealiase was small and they were corrected using a semi-automatic method. The dealiasing method consisted of manually selecting a point within the aliased region, which was used as a seed point for a region-growing algorithm to segment the whole aliased region. The threshold for the region growing process was tuned manually. Once the aliased region was correctly segmented, the velocity values were unfolded by adding or subtracting the Doppler range (*i.e.* twice the maximum measurable velocity) depending on whether the aliased region contained negative or positive velocities respectively. Second or higher order aliasing was extremely rare and was corrected for using a completely manual process.

6.5 Results

6.5.1 Results on Simulated Data

6.5.1.1 Inaccuracies Intrinsically Introduced by the Proposed Method

Figure 6.6 (a) shows the dependency of reconstruction error with the size of the patch border b. Larger values of b rapidly yield values of the patch coefficients closer to the true solution. Since the computation time increases exponentially with b, $b = 3$ was chosen for B-spline degree (d_{bs})= 1, and $b = 5$ for d_{bs}= 3 which assure less than 2% mean absolute difference in flow rate. The size of the patches did not have any effect on accuracy for values of b greater than 1.

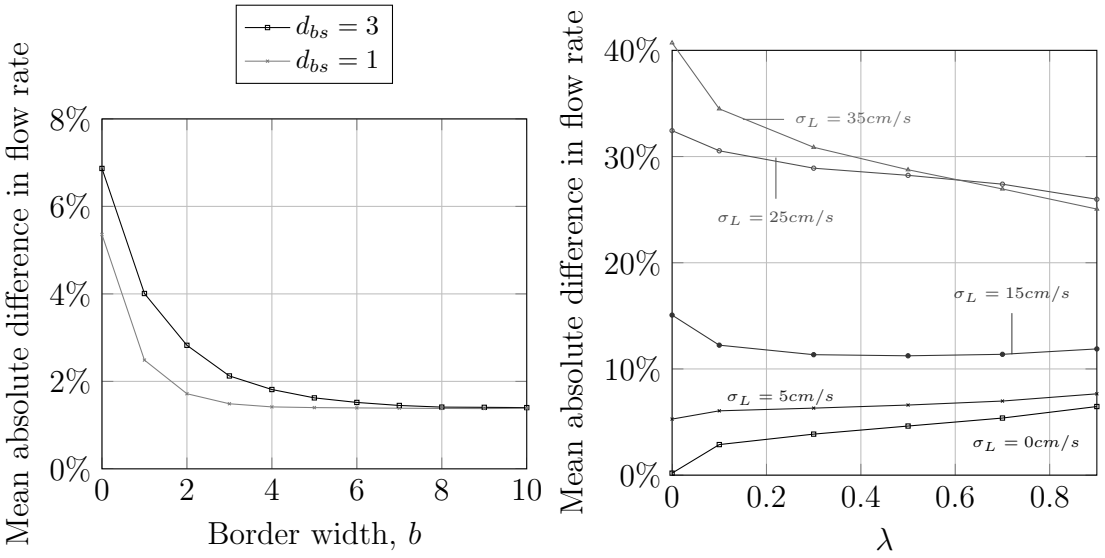

(a) Error in flow rate for different values of b

(b) Error in flow rate for different values of λ

Figure 6.6: Relative reconstruction error in simulated data, with respect to the ground truth, for different values of algorithmic parametres.

Figure 6.6 (b) shows the effect of regularisation on accuracy of reconstructed velocity fields for different amounts of noise. The amount of regularisation is driven by the value of λ, as described in (5.27). In absence of noise, regularization forces the reconstructed velocity to move away from the input data (see curve for $\sigma_L = 0cm/s$) because of the smoothing effect of the regularization. For noisy data ($\sigma_L > 5cm/s$), just a small amount of regularisation ($\lambda \geq 0.1$) improves results. For the experiments on real data, $\lambda = 0.3$ was used.

6.5.1.2 Contribution of Noise in Colour Doppler Data

Figure 6.7 shows the evolution of the mean absolute difference in flow rate, as a percentage of the maximum flow rate of the ground truth, with respect to the amount of noise, both for the proposed noise model (6.1) and the voxel-wise noise model. Although both errors increase linearly with the amount of noise, with the proposed multi-scale noise model error increases much more rapidly. Therefore, a standard additive voxel-wise noise model could greatly overestimate algorithm accuracy.

The reconstruction algorithm is much less sensitive to voxel-wise Gaussian noise than it is to the multi-scale noise model for two reasons: 1) Flow rate is computed by integration, which acts as a low pass filter removing spatial-high frequency noise inherent to voxel-wise scale, and 2) the LMS minimization is optimal for Gaussian

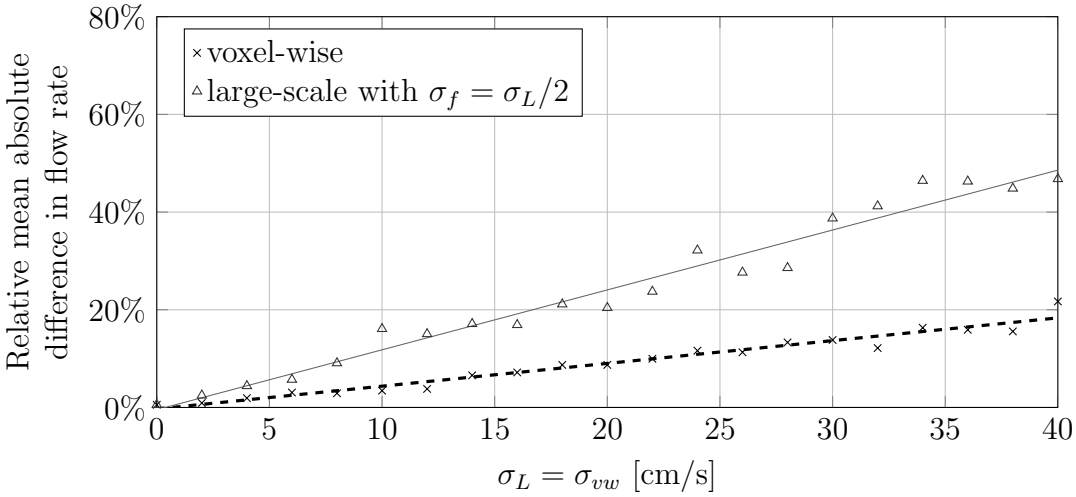

Figure 6.7: Error in the calculation of flow rate from simulated data, with respect to the amount of noise, for two noise models: the proposed multi-scale noise (6.1) for which the horizontal axis represents σ_L, and $\sigma_f = \sigma_L/2$; and voxel wise noise of standard deviation $\sigma_{vw} = \sigma_L$ added to simulated colour Doppler images.

noise.

6.5.1.3 Contribution of Registration error

Figure 6.8 shows the influence of registration accuracy on the accuracy of the reconstructed velocity, for $\sigma_L = 20cm/s$ and $\sigma_f = \sigma_L/2$. The plots of flow rate, angle and magnitude mean absolute differences are all almost flat for registration errors between 0 and $2.5mm$, indicating that registration errors $< 2.5mm$ have very little effect on vector reconstruction accuracy which is dominated by the $\sigma_L = 20cm/s$ noise used in this simulation.

6.5.1.4 Contribution of View Angle

Figure 6.9 shows the impact of the view angle on the reconstruction accuracy, for simulated data with added noise with $\sigma_L = 20cm/s$, and $\sigma_f = \sigma_L/2$. Reconstruction error increases steeply with decreasing angles particularly for small angles ($\alpha < 20°$). Larger angles keep the mean absolute difference almost flat. From this it is inferred that if the view angles are above 20°, the reconstruction error is mostly determined by the noise in colour Doppler data.

6.5.1.4.1 Summary Table 6.1 shows a summary of the impact and ranges of different parameters on reconstruction accuracy. Typical values for noise and view

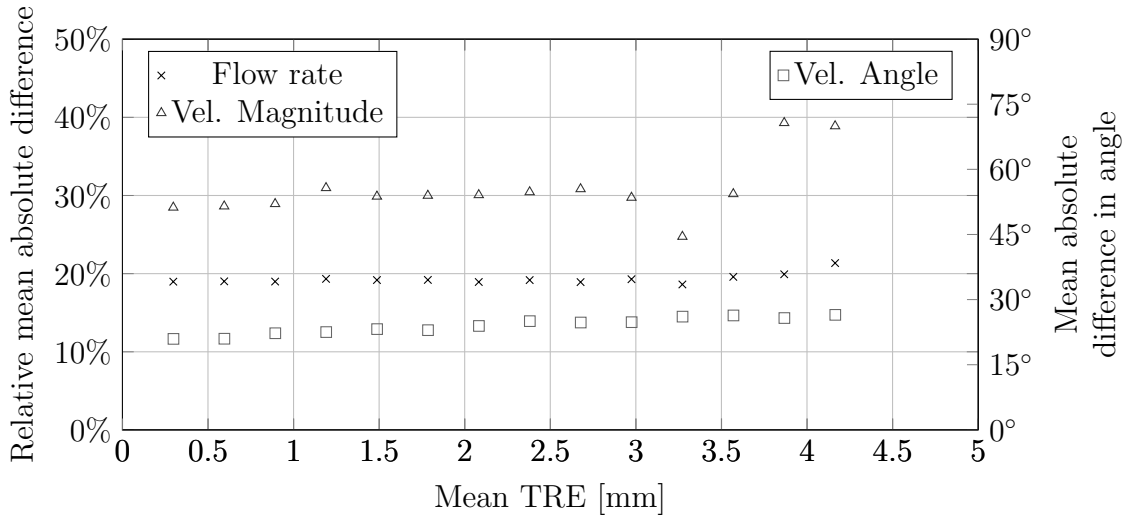

Figure 6.8: Effect of Target Registration Error (TRE) on accuracy of flow rate and velocity magnitude (left y-axis) and velocity angle (right y-axis), for $\sigma_L = 20cm/s$, and $\sigma_f = \sigma_L/2$.

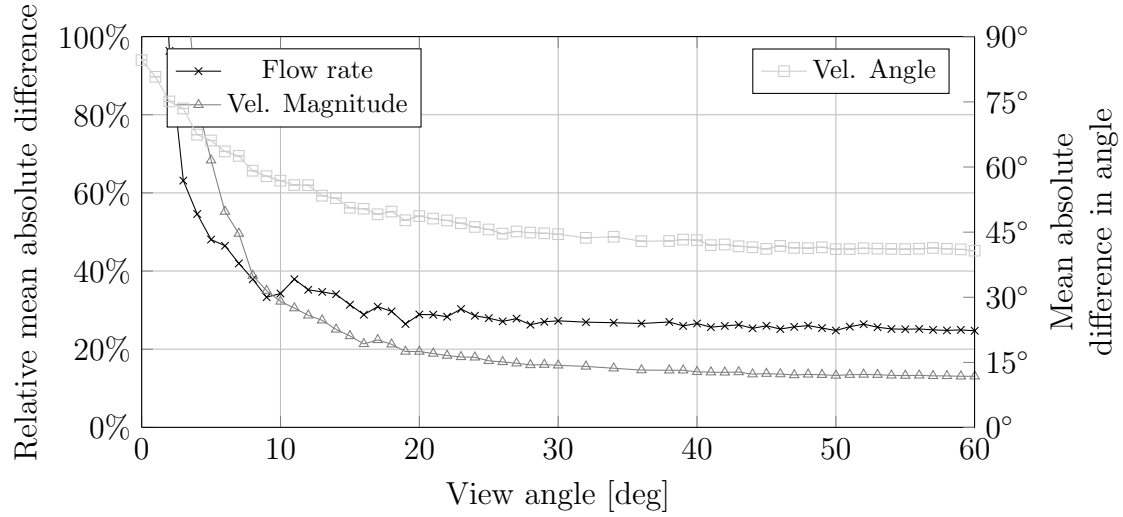

Figure 6.9: Effect of view angle on accuracy of flow rate and velocity magnitude (left y-axis) and velocity angle (right y-axis), for a noisy case with $\sigma_L = 20cm/s$ and $\sigma_f = \sigma_L/2$.

angle were calculated from our experiments on adult volunteer data (Fig. 6.10), and the values for registration accuracy that are reported by Grau et al. (2007).

	Impact	Required Range	Typical Range
Noise	Large	$< 10cm/s$	$5 - 60cm/s$
TRE	Small	$< 2.5mm$	$< 2mm$
View Angle	Large	$> 20°$	10°–40°

Table 6.1: Summary of contributors to inaccuracy of 3D velocity reconstruction: noise of input data, Target Registration Error (TRE) and view angles.

6.5.2 Results on Volunteer Data

The reconstruction method was applied to three healthy volunteers, who varied greatly in terms of their image quality and acoustic access. This variation allowed the validation of the results of the simulation studies presented in Sec. 6.5.1, by producing simulated data with noise and view angles measured from the three volunteers. The flow predicted from these simulations was compared to the results obtained from volunteer data.

6.5.2.1 Quantitative Assessment of Reconstruction Accuracy

Figure 6.10 (a) shows measurements of angles and image quality and Fig. 6.10 (b) shows measurements of noise of the input data for each volunteer. Noise measurements were calculated for both models: voxel-wise noise and multi-scale noise ($s = 15$). As expected, data which visually showed good or average image quality (volunteers 1 and 3) had lower amount of noise than data which showed bad image quality (volunteer 2). Only one (volunteer 1) of three volunteers had all three view angles above 20°. It was therefore expected that reconstruction for volunteer 2 would be inaccurate due mainly to high noise, and that reconstruction for volunteer 3 would be inaccurate due to a small view angle ($< 15°$).

	Volunteer		
	1	2	3
$\alpha[deg]$	44°	17°	39°
$(\mathbf{p_1}\hat{,}\mathbf{a_1})$	37°	31°	15°
$(\mathbf{p_1}\hat{,}\mathbf{a_2})$	22°	39°	29°
Q	avg.	bad	good

(a)

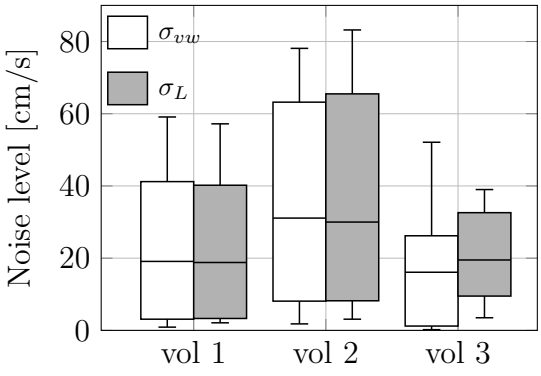

(b)

Figure 6.10: Measurements on volunteer data. (a) View angles: angle between apical views (α), and angle between the parasternal view and each of the apical views ($(\mathbf{p_1}\hat{,}\mathbf{a_i})$). Angles lower than 20° are expected to cause large errors (Fig. 6.9). Image quality (Q) was assessed by a clinician, blinded to results, based on the quality of B-Mode images. (b) Box and whisker plots of noise level (box shows median and inter-quartile range, whiskers show 10% and 90% percentiles) from volunteers, measured first voxel-wise (σ_{vw}) and then at a scale $s = 15$ (σ_L).

Table 6.2 shows the relative mean absolute difference in stroke volume measured in real data compared to the expected relative mean absolute difference calculated from simulations with the standard voxel-wise noise model and with our multi-scale noise model. The first column (Real) shows the disagreement between volume calculated from 2D+t Flow MRI and from our proposed technique in the three volunteers. To ascertain how realistic the simulation study was, 3D colour Doppler data was simulated with the view angles and noise (both voxel-wise and multi-scale noise models) measured for the three volunteers and shown in Fig. 6.10. For each volunteer, simulated data was generated 5 times, and statistics were calculated over the 5 trials. Results suggest that voxel-wise noise overestimates the accuracy of the algorithm while the proposed multi-scale noise model showed good agreement with real data.

	Real	Simulation	
		Voxel-wise	Proposed
Volunteer 1	15.0%	$1.4\% \pm 3.7\%$	$10.8\% \pm 9.6\%$
Volunteer 2	61.9%	$37.9\% \pm 27.3\%$	$61.2\% \pm 59.6\%$
Volunteer 3	74.5%	$1.6\% \pm 2.4\%$	$63.6\% \pm 31.2\%$

Table 6.2: Error in stroke volume on three healthy volunteers with respect to 2D+t Flow MRI (*Real*), and error on 3 simulated datasets with similar parameters to the real cases. Simulations have been performed using two approaches: the voxel-wise Gaussian noise (*Voxel-wise*) and the multi-scale noise model (*Proposed*).

Flow volumes were estimated by the time integral of flow rate curves, shown (dashed lines) in Fig. 6.11, compared to the reference from 2D+t Flow MRI (solid lines) on volunteers. As predicted by the multi-scale noise model, accurate reconstructed flow was achieved for volunteer 1 and large errors were observed for volunteers 2 and 3, compared to 2D+t Flow MRI.

6.5.2.2 Qualitative Assessment of Reconstruction Accuracy

In addition to the numeric results, the reconstructed 3D velocity fields are qualitatively analysed. Figure 6.12(a) shows an example of the reconstructed velocity field through the aortic valve, for volunteer 1, in mid systole. The anatomy is represented by three orthogonal slices of a 3D B-Mode image acquired from an apical view. Velocity vectors are colour coded by velocity magnitude. To facilitate interpretation of this image, Fig. 6.12(b) shows the projection of the reconstructed velocity field

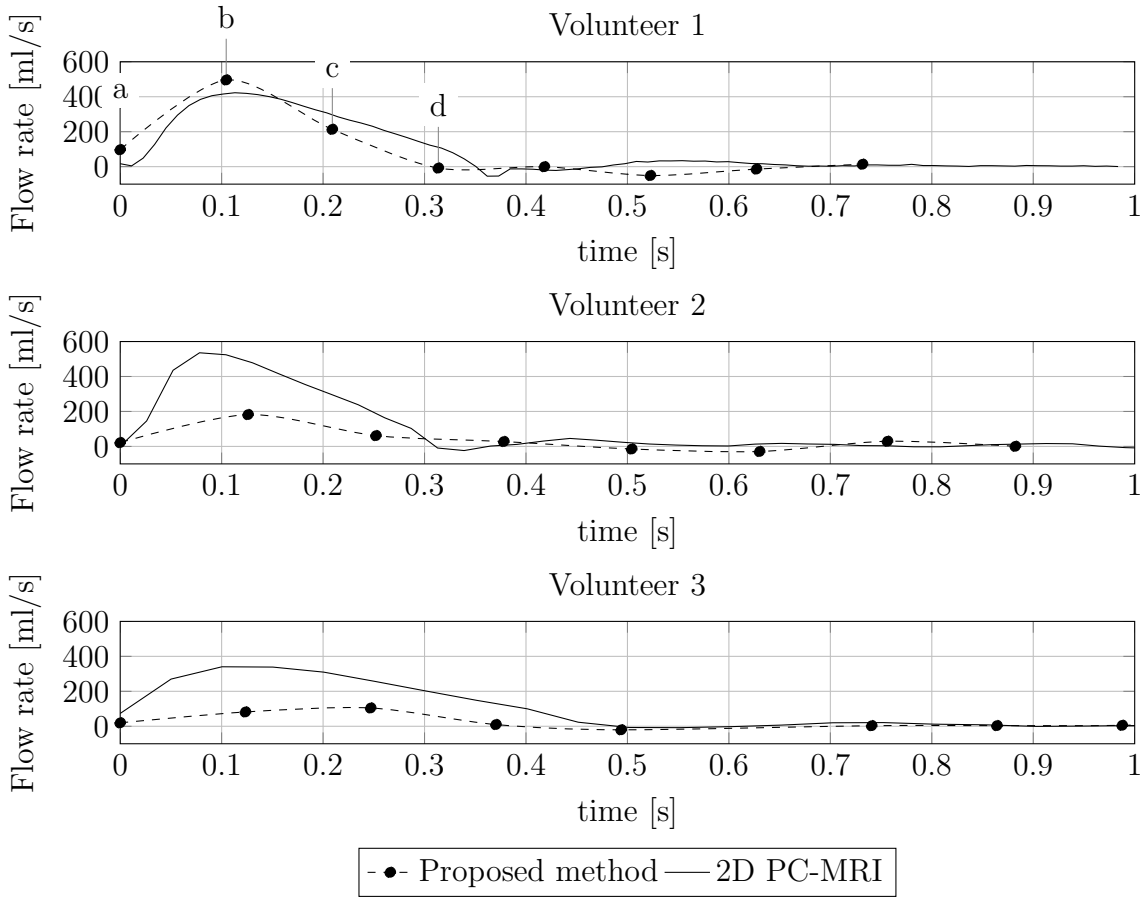

Figure 6.11: Flow rate for three volunteers, using the proposed method (dashed) compared to 2D+t Flow MRI (solid). Sampling planes were located at the ascending aorta (2D+t Flow MRI) and the aortic valve (our method). Volunteer 1 had all view angles $> 20°$ and relatively low noise level. Volunteer 2 had small angles and very high noise level. Volunteer 3 had relatively low and noise level but very small view angles.

onto a long axis plane of the left ventricle centred in the LVOT.

Qualitative analysis of the 3D flow patterns throughout the cardiac cycle was carried out by a clinician, who considered patterns from volunteer 1 visually plausible (Fig. 6.12). Velocity increases when blood goes through the valve narrowing, and the maximum velocity is not observed along the midline but nearer to the outside of the aortic arch.

Figure 6.13 shows through plane velocity profiles for volunteer 1 corresponding to the phases of the cardiac cycle indicated by letters (a)–(d) in Fig. 6.11 (top), together with a slice of the B-Mode image on the sampling plane for anatomical reference. The resulting through plane velocity profile follows the expected paraboloid shape (Segadal and Matre, 1987) skewed towards the aortic wall as has been found in the past by Paulsen and Hasenkam (1983). Since the echo acquisition is ECG-triggered,

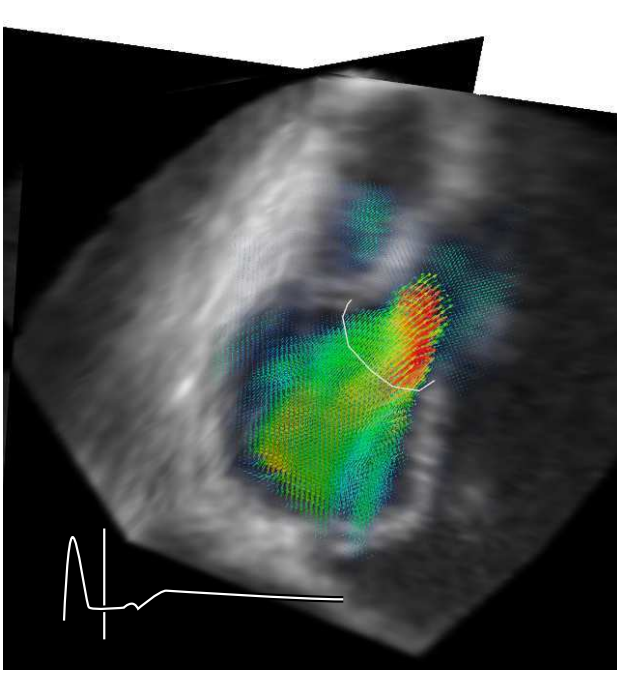

(a) 3D rendering of the velocity field with and three orthogonal cuts of a registered B-Mode image for anatomical reference. A white ring represents the plane through which flow was computed..

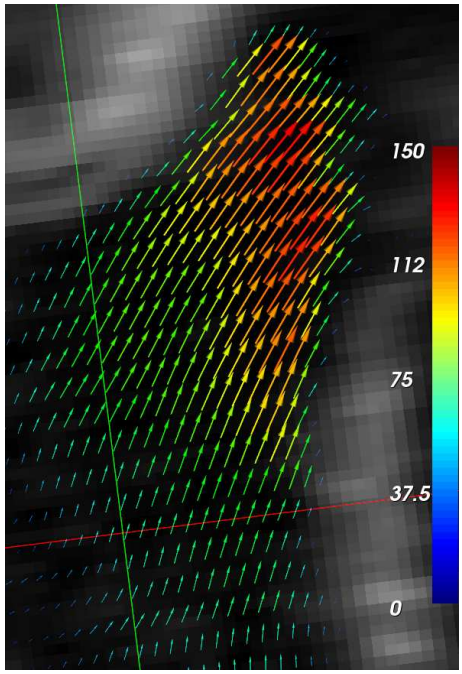

(b) In plane projection of the 3D reconstructed velocity field. Note how velocity magnitude increases in the centre of the outflow tract.

Figure 6.12: 3D velocity field reconstruction for volunteer 1. Velocity magnitude is colour coded. This frame corresponds to the middle of left ventricular systole, where blood is ejected from the ventricle through the aorta.

the first frame (a) corresponds to the instant directly after the R wave (isovolumetric contraction of the left ventricle). Next, the aortic valve opens (b)–(c) with a rapid increase in velocity first and a less steep deceleration later (which explains the lower profile in (c)). The animated sequence over the whole cardiac cycle is included as additional material (Movie 1).

Volunteers 2 and 3 showed poor results, as discussed previously. In particular, velocity vectors had a significantly smaller magnitude than expected, which is consistent with the curves from Fig. 6.11. The velocity vectors were plausibly oriented along the two chamber plane (where the apical and the parasternal windows are located) because the angle between these two views was relatively large. However, the vector components outside of the two chamber plane showed large errors. This was because the third view also provided very little information outside of the two chamber plane (small view angle) and due to high noise levels in the input data.

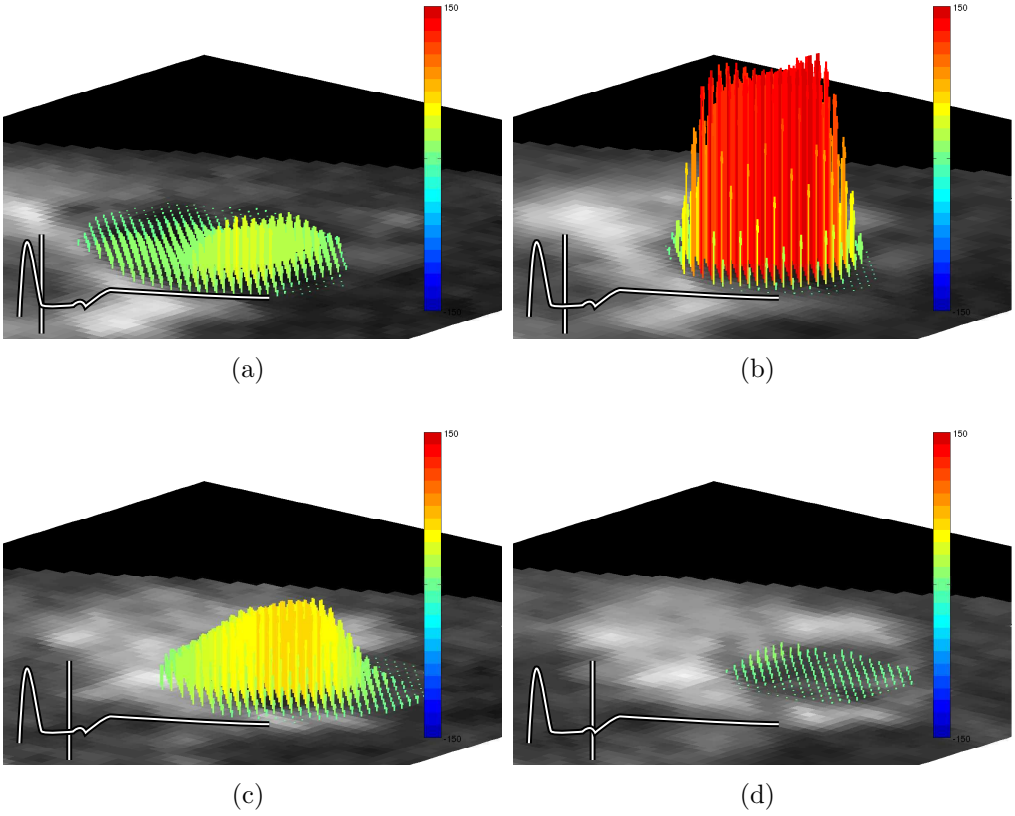

Figure 6.13: Through plane velocity profiles at the aortic valve, measured with our method, for volunteer 1. (a) to (d) represent different instants of the ventricular systole, which can be temporally located within the cardiac cycle by comparing with Fig. 6.11 top. Velocity vectors are colour-coded by through plane velocity magnitude. Movie 2, showing the velocity profile throughout the full cardiac cycle, is provided as additional material.

6.5.3 Results on Patient Data

Quantitative results from the three patients were obtained by comparing flow volume to 2D+t Flow MRI. For patients 1 and 2, representations of the 3D flow are provided for visual inspection and qualitative analysis of the reconstructed velocity fields. For patient 3, 3D+t Flow MRI was also available and intra-cardiac flow could be visualised with both modalities.

6.5.3.1 Quantitative Assessment of Reconstruction Accuracy

Table 6.3 shows the angles measured between each pair of views (each cell shows patient 1 / patient 2 / patient 3). All the angles were equal to or larger than 20° except for the angle between the oblique view and the the first apical view (18°) from patient 1, for which four more views with sufficient angles were available. Best view

angles were obtained with the subcostal view which, unfortunately, was difficult to obtain in adults.

	A2	P	SC	Ob
A1	28°/-/-	77°/-/54°	30°/73°/24°	18°/20°/-
A2		58°/-/-	53°/-/-	27°/-/-
P			80°/-/70°	84°/-/-
SC				46°/69°/-

Table 6.3: View angles measured from three patients (pat. 1/pat. 2/pat. 3). Views stand for: A≡Apical; P≡Parasternal; SC≡Subcostal; Ob≡Oblique. Angles below 20° have been highlighted in grey.

The noise could not be quantified in the same way as for the volunteers, since constraints in the duration of the acquisition, fixed by the approved ethics, prevented us from acquiring additional colour Doppler images for noise calculation. Therefore, noise was estimated by assuming that there was no systolic flow through the tricuspid valve during systole and that any nonzero value was due to noise. The median noise level (and inter-quartile range) was $2.0cm/s$ ($3.5cm/s$) for patient 1, $1.8cm/s$ ($8.5cm/s$) for patient 2 and $2.6cm/s$ ($8.7cm/s$) for patient 3.

Figure 6.14 shows the transtricuspid flow rate curves, calculated with the proposed reconstruction method and compared to 2D+t Flow MRI. The curves were integrated over time to calculate stroke volumes (SVs), which are shown in table 6.4. As predicted given these angles and noise level, and according to the results obtained in our simulation studies, data from the three patients produced good quality results. In the case of patient 1, transtricuspid flow rate curve agreed well compared to 2D+t Flow MRI (Fig. 6.14, top), and the difference in SV was 13.51%. In the case of patient 2 shown in Fig. 6.14 (middle), there was an increase in heart rate of 35% between the MRI and the echo (versus a 2% change in patient 1) because the patient was waking up from anaesthesia during the echo exam, which produced peak fusion in the inflow wave and an increase in the instantaneous flow rate due to increased velocities. The faster cycles provided a smaller SV (by 14.8%) but with similar cardiac output (4.9% difference). This effect has already been observed in HLHS patients by Bellsham-Revell et al. (2011). In the case of patient 3, the two flow rate curves agreed well and the difference in SV was 12.6%.

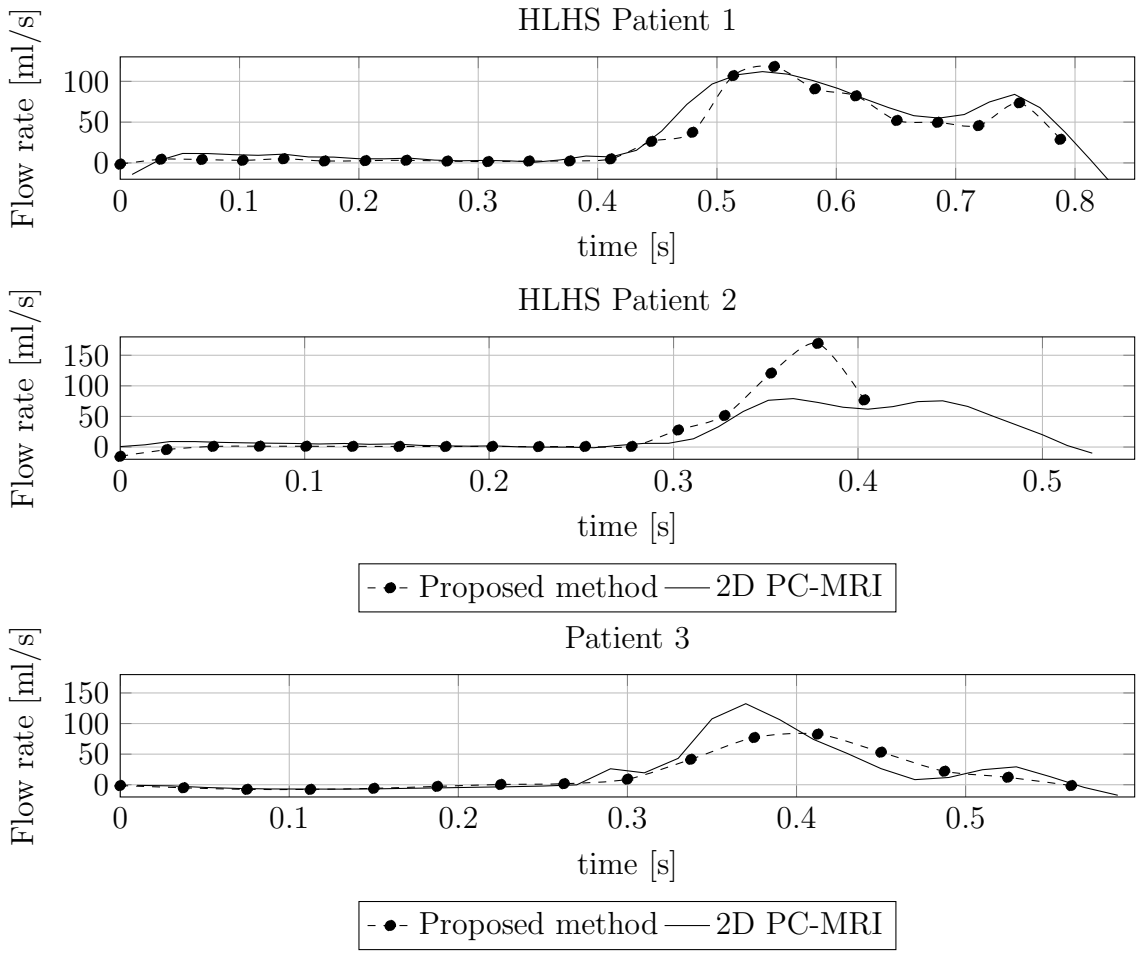

Figure 6.14: Flow rate on two HLHS patient through the tricuspid valve. Plane through which flow rate was computed was set at acquisition time for 2D+t Flow MRI, and a similar plane was manually selected in postprocessing for our proposed method. High temporal discrepancy for patient 2 is due to a 35% increase in heart rate.

6.5.3.2 Qualitative Assessment of Reconstruction Accuracy

Reconstructed velocity fields were produced from each patient dataset for visual inspection. Figure 6.15 shows a few selected diastolic frames from patient 1, where blood motion is illustrated by following the motion of particles initially placed in the right atrium. To relate to anatomy, particles are shown on a compounded B-Mode image (Yao et al., 2011). A movie of the entire cardiac cycle has been included as additional material (Movie 3).

The reconstructed velocity field from patient 2 is represented in Fig. 6.16. In this case, the small size of the patient (3.6kg) enabled the use of a X7-2t probe which has a higher frequency and attains higher spatial and temporal resolution. As a result, the reconstructed flow pattern has finer detail and an inflow vortex in

	Vol. Echo	Vol. MRI	Deviation
Patient 1	$24.2ml$	$28.0ml$	13.51%
Patient 2	$9.9ml$	$11.6ml$	14.8%
Patient 3	$12.7ml$	$14.5ml$	12.6%

Table 6.4: Stroke volume (inflow) in patient data and deviation with respect to the values measured with 2D+t Flow MRI.

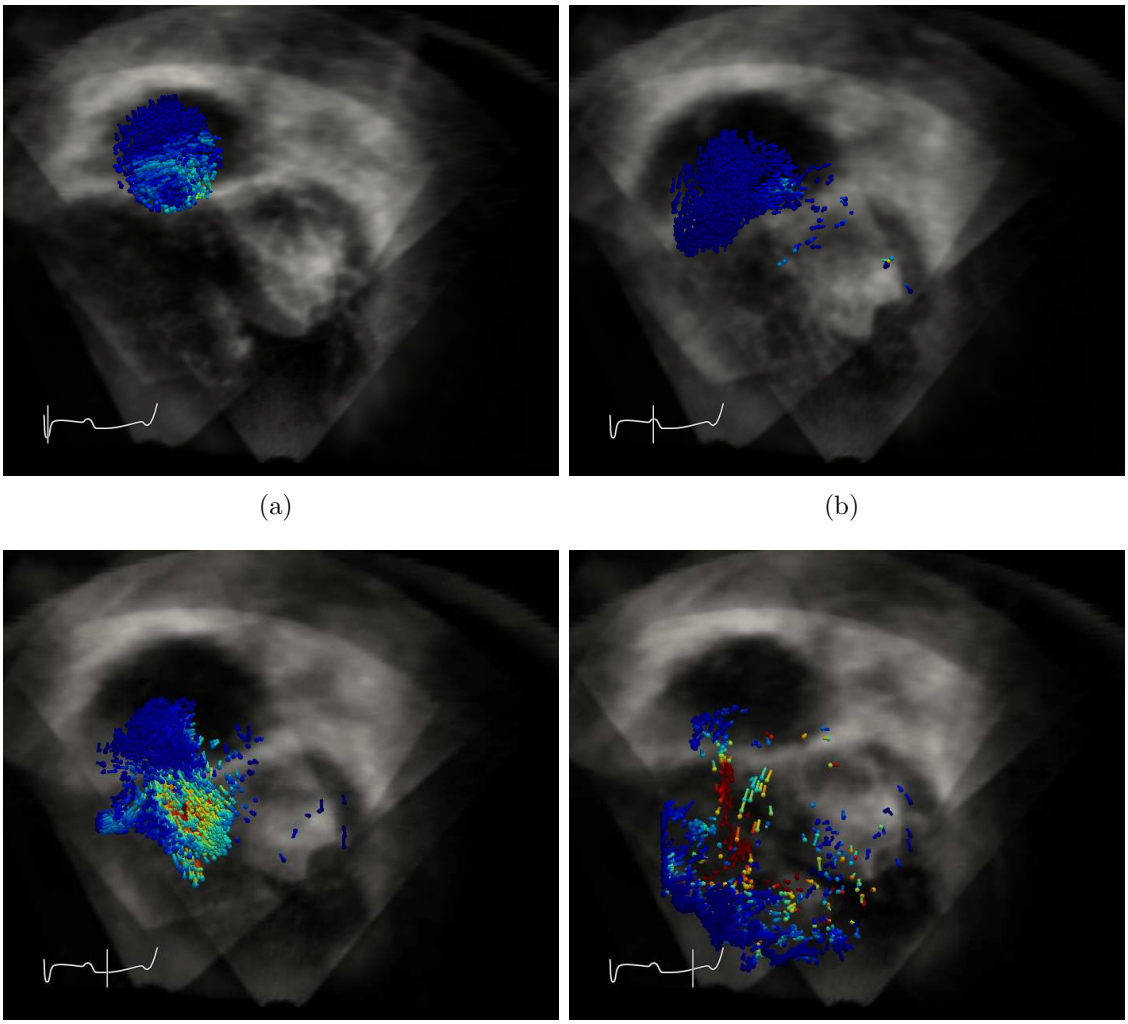

(a) (b)

(c) (d)

Figure 6.15: 3D flow reconstructed from HLHS patient 1. Blood motion is represented by particles which follow the velocity field from the right atrium at each time step. The tricuspid valve is initially closed (a), and it opens when atrial pressure overcomes ventricular pressure (b)–(c). After the passive filling, the atrium contracts sending a second jet of blood into the ventricle (d). Movie 3, showing blood particles tracked over all 24 frames, is provided as additional material.

early diastole is clearly shown, located on the anterior-posterior plane and below the tricuspid valve. Cardiac flow models by de Vecchi et al. (2012), produced also on HLHS patients, have shown that the abnormal geometry of congenital hearts produces single or multiple intraventricular vortices (similar to the vortex shown in

Fig. 6.16) and the shape and dynamic properties of these vortices have a large effect on cardiac efficiency.

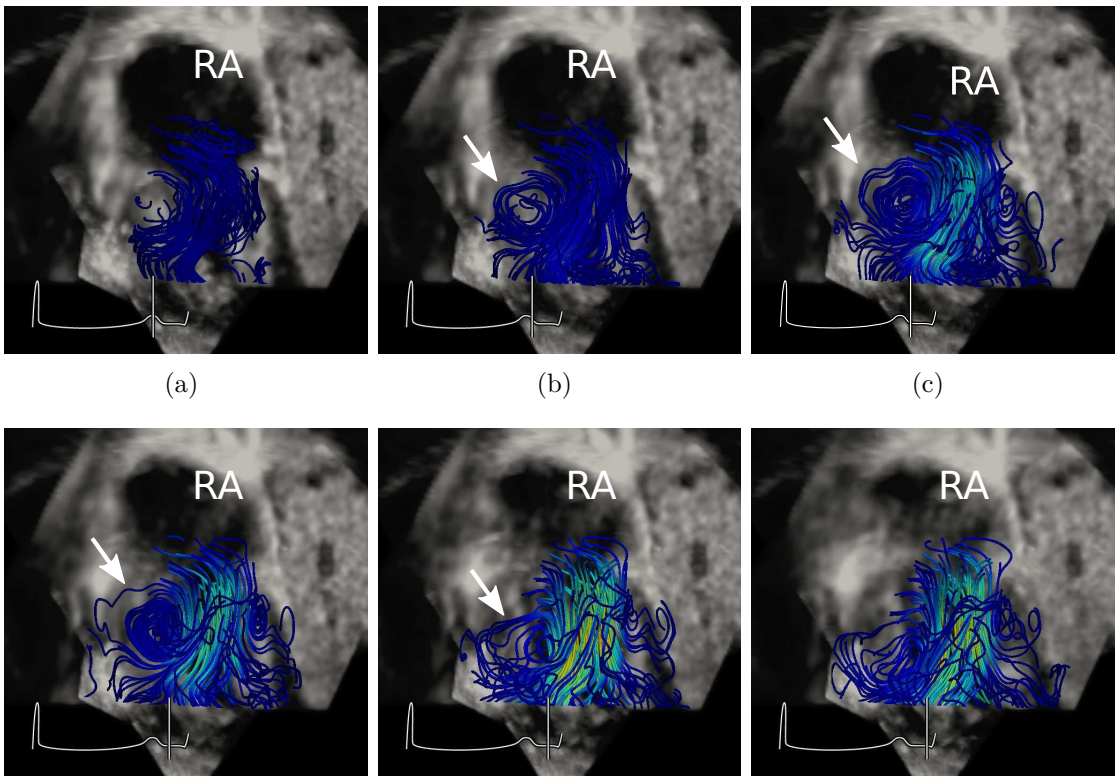

Figure 6.16: 3D flow reconstructed from HLHS patient 2. The selected frames represent the inflow pattern, including vortex formation in the anterior-posterior plane, below the tricuspid valve, as predicted by cardiovascular models on a similar patient group (de Vecchi et al., 2012). The tricuspid valve is initially closed (a), and it opens when atrial pressure overcomes ventricular pressure (b)–(c). After the passive filling, the atrium contracts sending a second jet of blood into the ventricle. The vortex is indicated with a white arrow.

Figure 7.7 shows a 2D slice of the velocity vectors reconstructed from patient 3 using the proposed method (Fig. 6.17(a)) and from 3D+t Flow MRI (Fig. 6.17(b)). The projection plane and the frame were manually selected to try to capture the same location and cardiac phase in both images, during diastole where the inflow vortex is larger. It can be observed that the flow pattern (vortex) is similar in both images, with similar velocity distribution, size and location within the ventricle. A portion of the ventricle, close to the septum in Fig. 7.7 (a) lacks reconstructed data because there was no view overlap. Differences between the two images may be due to differences in projection plane, cardiac phase, patient position and the fact that MRI was acquired over a 10 minute period and echo data over approximately 45 seconds (3 views $\times$3 images $\times$5 seconds).

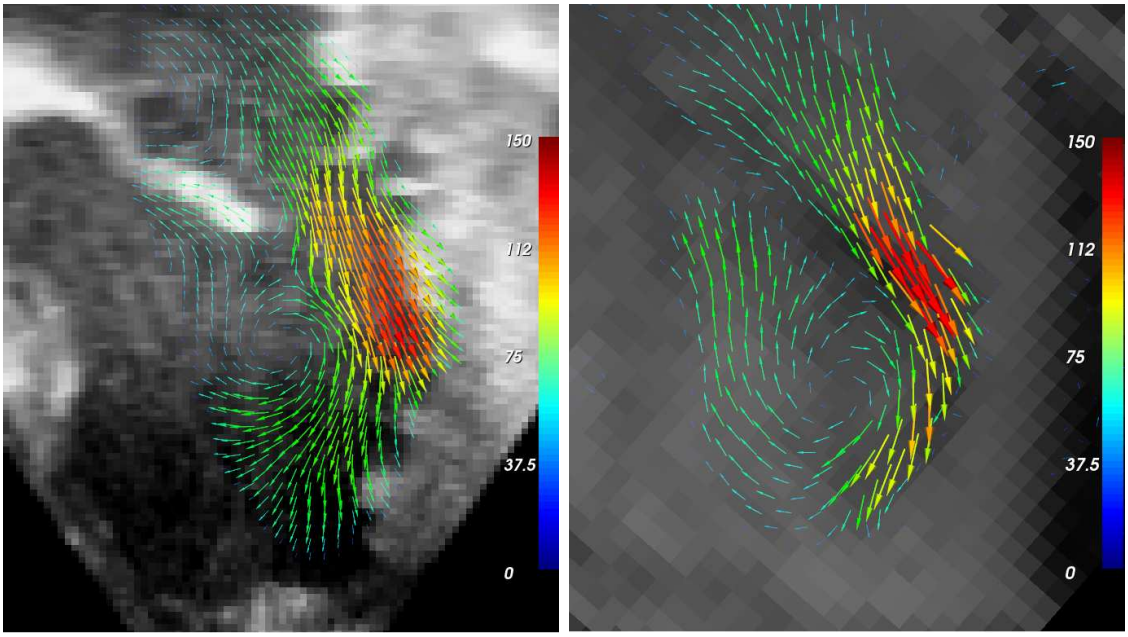

(a) Proposed method. (b) 3D+t Flow MRI.

Figure 6.17: 2D slice of 3D flow reconstructed from patient 3. Blood motion is represented by arrows which follow the velocity field from the left atrium into the left ventricle. (a) Reconstruction with the proposed method. (b) Reconstruction, in a similar plane, from 3D+t Flow MRI acquired from the same patient less than one hour apart.

6.6 Discussion

This chapter has presented a sensitivity analysis to important contributors to inaccuracy for the reconstruction method presented in chapter 5. The accuracy of the method has been studied with realistic simulations using a novel noise model that represents realistic variations in colour Doppler images. The method has been tested on three healthy volunteers and three paediatric patients and compared with the current gold standard technique for non-invasive flow measurements, 2D+t Flow MRI.

The quantitative validation with 2D+t Flow MRI has been carried out using mean absolute difference in stroke volume between the two modalities. Such an approach provides a single, intuitive indicator of reconstruction performance, but would not be able to distinguish between systematic and random errors (for which more than one value would be required, typically mean and standard deviation).

The major contributors to reconstruction errors are noise in colour Doppler images, view angles and registration errors. The results we have obtained allow to propose ranges of these three parameters for which 3D velocity reconstruction will

be accurate: 1) registration error has to be TRE$< 2.5mm$, 2) view angles have to be above 20° and 3) noise in colour Doppler images has to be less than $10cm/s$ (Table 6.1).

The extent to which these parameters can be currently achieved with patients requires further investigation. Registration error is difficult to measure on real data without a ground truth, but the similarity measure we use has been reported to provide TRE below $2mm$ (Grau et al., 2007), for which error in flow reconstruction is dominated by the other sources of error: view angles and noise of input data. View angles are limited by patient's anatomy. Measurements on adult volunteer data (Fig. 6.10 (a)) show that achieving good angles is not always possible (all angles above 20° were only achieved on one volunteer out of three) and therefore noise in input data must be as low as possible. Therefore, further improvement on image quality is required to get the robustness required for clinical practice. The accuracy and the resolution of the reconstructed flow patterns is also limited by the quality and the frequency of the echocardiography (echo) probe. Standard adult probes, as the one used in volunteers, are probably not capable of capturing fine flow structures such as small vortices.

Acquisition of sufficiently high quality reproducible Doppler from a wide enough range of angles for our algorithm is challenging on volunteers, and will likely be more challenging on adult patients. In addition, achieving full coverage of large cardiac structures (e.g. the left ventricle) from three or more views and with sufficiently wide angles is even more difficult. Range of angles is anatomically dependent and so will always be an issue, however, other information than Doppler velocities could help reconstructing velocity vectors. For example, Garcia et al. (2010) calculated 2D velocities from a single colour Doppler image by incorporating ventricle wall motion. The next chapter proposes a new method to use 3D wall motion and multiple 3D colour Doppler images to recover 3D flow over the whole ventricle.

Paediatric patients is a patient group which typically has good acoustic windows and provides high quality images. These patients often present complex anatomics (e.g. congenital patients) hence more detailed information on cardiac flow could aid diagnosis. In addition, the small size of these patients allows the use of higher frequency probes which may enable the reconstruction of more detailed flow patterns. Our method has been tested on three paediatric patients with an average

agreement with flow MRI of 13.6% and has shown potential for flow pattern reconstruction, including vortices and complex intraventricular filling patterns which agreed well with 3D+t Flow MRI and with predictions from computational models. Further work will include a more comprehensive analysis of the precision, accuracy, reproducibility and repeatability of flow reconstruction on a larger set of paediatric patients.

6.7 Conclusion

This chapter has identified the major contributors to inaccuracy in 3D velocity reconstruction, and established the ranges within which flow can be accurately computed.

The advantages of echo over modalities such as MRI in terms of cost and ease of use provides a big impetus to extract additional information from echo. In addition, avoiding general anaesthesia in children is a major attraction of an echo-based method. Our proposed method has potential for quantification of standard blood flow parameters such as SV and flood rate, however it also has the potential to provide additional new information such as 3D velocity field visualisation and through-plane velocity profiles, both of which are currently unavailable in echo.

Chapter 7

3D Intraventricular Flow Mapping from Colour Doppler Images and Wall Motion

“ ‘Every time I see you my heart beats.
Every time I see you my heart beats.
Every time I do not see you, my heart beats too.
Lucky me! Lucky me!’
(With this song I won the award of the Society of Cardiology!)”

Daniel Rabinovich with Les Luthiers (1994)

Contents

The methods described in previous chapters enable 3D velocity reconstruction from multiple 3D colour Doppler images in the region where 3 or more views overlap. In this chapter, previous methods are extended to incorporate ventricular wall motion information into the velocity reconstruction, which increases the coverage and accuracy of the reconstructed velocity field.

This chapter is organised as follows. Section 7.1 motivates the use of wall motion information and introduces the cases in which this information can be useful. Section 7.2 describes how ventricular wall motion can be calculated and incorporated into the method proposed in Sec. 5.5. The experimentes carried out on a paediatric patient are described in Sec. 7.3, followed by the results in Sec. 7.4 comparing intraventricular flow obtained with the proposed method and with 3D+t Flow MRI. Section 7.5 analyses the impact of the described method and the potential benefits of such a technique being widely available, and the future research lines that might arise from the presented work.

7.1 Introduction

As shown in previous chapters, accurate 3D characterisation of cardiovascular flow can have important clinical benefits. Over the past years, researchers and cardiologists have shown increased interest on intracardiac flow structures such as vortices and on new clinical metrics related to cardiac efficiency and vortical structures (Garcia et al., 2010; Sengupta et al., 2012; de Vecchi et al., 2012; Zhang et al., 2013), facilitated by improvements on flow imaging techniques. Examples of these metrics are kinetic energy of blood flow, viscous losses, and vortex parameters such as Q and λ_2 (Jeong and Hussain, 1995) or vortex location. The study of vortices and of the associated metrics requires that flow information over the entire ventricle is available.

The reconstruction method proposed in chapters 5 and 6 can only recover 3D velocity within the region where three or more 3D colour Doppler views overlap. Achieving full ventricular coverage with three views can be difficult because acoustic access is limited by anatomy and because the computational requirements of colour

Doppler images results in a significantly reduced Field of View (FoV) compared to B-Mode images. To illustrate the extent to which lack of coverage can occur in clinical data, the example of patient 3 from chapter 6 is used. This patient, of two months of age, had a small heart (the left ventricle was similar to a truncated ellipsoid of 43mm of height and 25mm of wider diameter) and his chest provided very good acoustic access. An expert echocardiographer acquired 9 3D colour Doppler images trying to obtain full coverage from 3 views over the whole ventricle. Figure 7.1 shows three orthogonal slices of a B-Mode image showing the coverage achieved. Anatomical reference is provided by the background B-Mode image and a white contour which indicates the left ventricular wall. A coloured overlay indicates the number of independent 3D colour Doppler views that overlap at each region (red = 3 or more views, orange = 2 views and yellow = 1 view). The region in which 3 or more colour Doppler views overlapped only covered about 2/3 of the left ventricle (LV). As a result, the crossed-beam approach proposed in chapter 6 was not able to reconstruct 3D velocity over the entire ventricle. This limitation in coverage prevents these kind of techniques from reconstructing full ventricular flow.

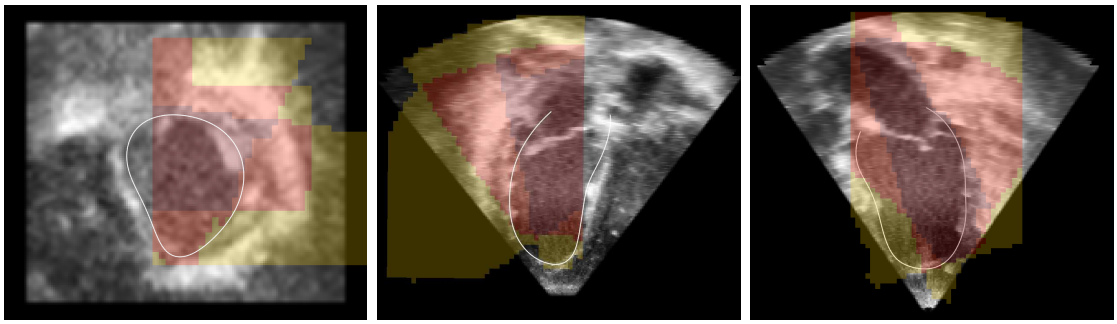

(a) Short axis. (b) 2 chamber. (c) 4 chamber.

Figure 7.1: Coverage of left ventricle from multiple 3D colour Doppler views on a paediatric patient. Anatomical reference is provided by three orthogonal slices of a B-Mode image and a white line representing the ventricular wall. The number of views overlapping in each region is coded by colours: red = 3 or more views, orange = 2 views and yellow = 1 view.

In this chapter, a new method to recover 3D time-resolved velocity vectors within the whole LV is proposed. The method uses a combination of multiple registered 3D colour Doppler images and ventricular wall motion, which is propagated into blood velocity by using mass conservation. Wall motion information could be located relatively far from Doppler data, with a 'blank region' (*i.e.* area with data from 2 or fewer views) in between. In order to keep a low condition number in the involved

matrices, velocities reconstructed with fine grids will be zero in this blank region as explained in Sec. 5.5.3.1. In this chapter, the reconstruction problem is reformulated in a a multi-scale framework which allows recovery of 3D velocity over the entire ventricle, even in regions where there is little or no Doppler data.

In summary, this chapter introduces two main novelties over previous techniques:

- The incorporation of wall motion to achieve full ventricular velocity mapping.
- The multi-scale implementation of the reconstruction method.

The proposed method is applied to a paediatric patient (patient 3 from chapter 6). Quantitative validation is carried out by comparison with the gold standard for non-invasive flow measurement, 2D flow Magnetic Resonance Imaging (MRI). For qualitative validation, flow patterns and 3D velocity profiles were compared to 3D flow MRI measurements.

7.2 Multi-scale Velocity Reconstruction with Wall Motion Information

Wall motion is estimated from a B-Mode sequence as described in Sec. 7.2.1. Then, resulting motion fields are converted into 1D projections (described in Sec. 7.2.2) that can be input into the algorithm from Sec. 5.5. 3D velocity fields over the whole ventricle are calculated with the multi-scale approach described in Sec. 7.2.3.

7.2.1 Wall Motion Estimation

Wall motion was estimated using non-rigid registration on every two consecutive frames of a standard apical B-Mode sequence, where the whole LV was visible, as shown in Fig. 7.2. Registrations were carried out with the Image Registration Toolkit (IRTK) package (Schnabel et al., 2001), using cross-correlation as a similarity measure and a B-spline grid of isotropic spacing set to $10mm$.

Figure 7.2 shows three orthogonal slices of four frames of the 3D B-Mode sequence used for wall motion estimation. The wall segmentation was manually computed from the first frame (first column) and stored as a surface mesh (in the slice in the figure represented with a white contour). This segmentation was propagated

through the cardiac cycle by applying to each node of the mesh the motion fields obtained with the non-rigid registration, as shown in the three other columns which represent 1/4, 1/2 and 3/4 of the cardiac cycle respectively.

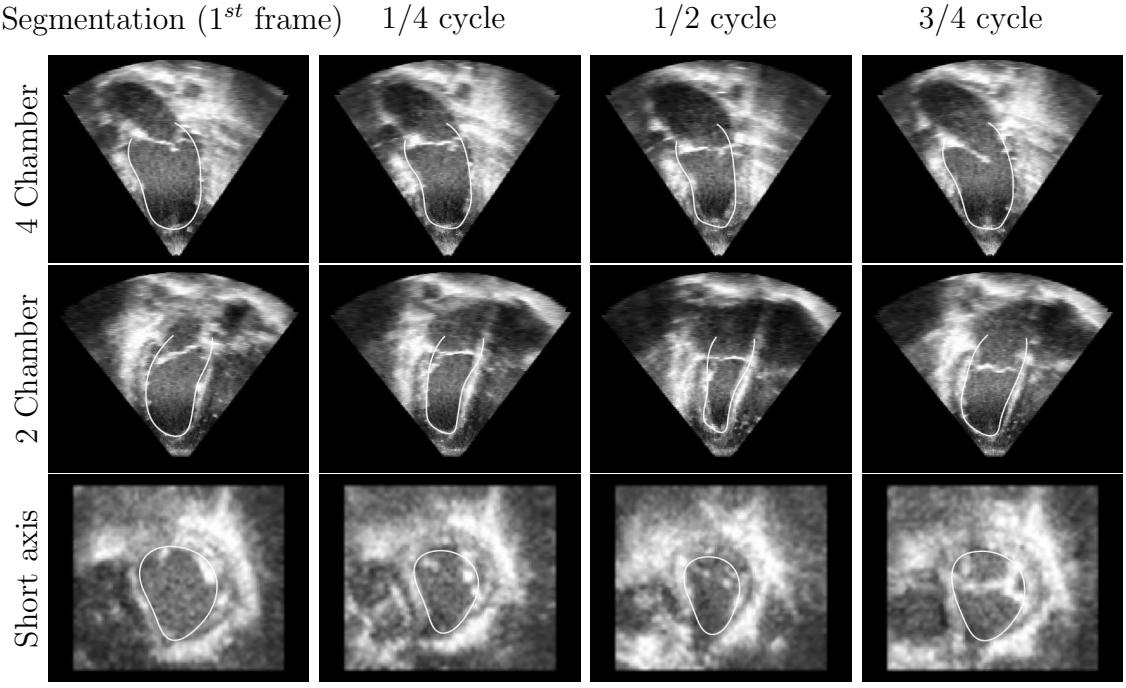

Figure 7.2: Ventricle wall motion detection from 3D B-Mode images. Wall motion was calculated by registering each pair of consecutive frames. The first frame (first column) was manually segmented (ventricular wall is shown in white) and the segmentation was propagated through the rest of the frames through the cardiac cycle with the calculated motion fields.

7.2.2 Incorporation of Ventricle Wall Motion into the Blood Velocity Reconstruction

In the solid-fluid interface at the ventricular wall, it is assumed that the ventricle is impermeable and therefore there is no mass transfer normal to the wall so no through-wall blood flow. If the ventricle wall moves with a velocity $\mathbf{v_w}$, and the blood velocity is $\mathbf{v_b}$, the blood flow $\Phi(W)$ through the wall surface W is dependent on the relative velocities of the wall and the fluid, *i.e.*

$$\Phi(W) = \int_W (\mathbf{v_b} - \mathbf{v_w}) \cdot \mathbf{dw} \tag{7.1}$$

Equating (7.1) to 0 yields $\mathbf{v_b} \cdot \mathbf{dw} = \mathbf{v_w} \cdot \mathbf{dw}$, *i.e.* the component of $\mathbf{v_w}$ and of $\mathbf{v_b}$ orthogonal to the ventricle wall must be identical. If no restriction is imposed

on the other components, this is known as the *free-slip* boundary condition. In consequence, the wall motion calculated in the previous section can be converted into a 1D component of the blood velocity by taking the component of the wall velocity orthogonal to the wall, as depicted in Fig. 7.3.

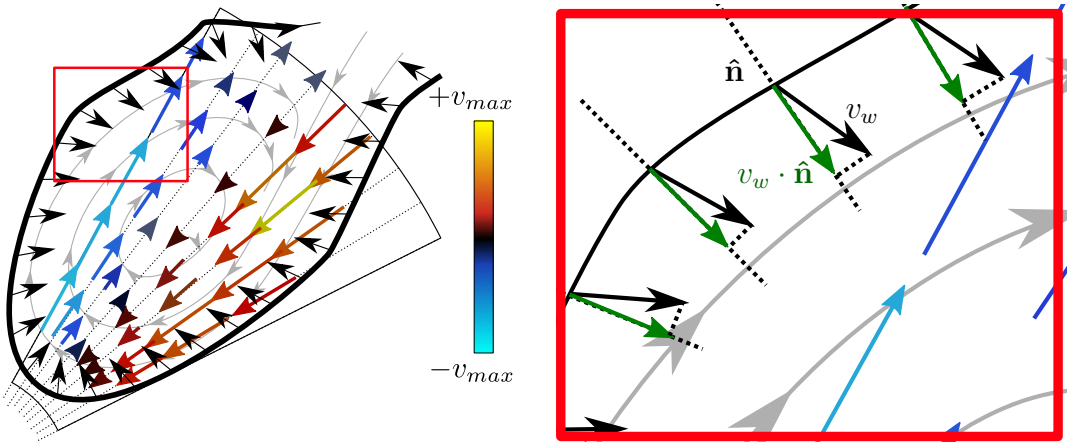

(a) 2D representation of wall motion and measured Doppler velocity magnitude and direction during ventricular filling.

(b) Detail of (a), showing the component of the wall motion orthogonal to the wall ($v_w \cdot \hat{\mathbf{n}}$).

Figure 7.3: Incorporation of ventricle wall motion into the 3D velocity reconstruction. The component of the wall motion v_w along the direction orthogonal to the wall $\hat{\mathbf{n}}$, *i.e.* $v_w \cdot \hat{\mathbf{n}}$ is input into the reconstruction algorithm as a 1D projection of blood velocity along $\hat{\mathbf{n}}$ at the boundary.

Input colour Doppler data for the reconstruction algorithm described in Sec. 5.5 was a list of 3-tuples $\{m, \hat{\mathbf{d}}, P\}$, where m was the blood velocity along the beam direction $\hat{\mathbf{d}}$ at position P. Ventricle wall motion data is introduced by building a new list of 3-tuples $\{\mathbf{v_W} \cdot \hat{\mathbf{n}}, \hat{\mathbf{n}}, P\}$, where $\hat{\mathbf{n}}$ is the direction orthogonal to the wall at each node of the segmentation mesh of coordinates P. This list of 3-tuples can be appended to the 3-tuples made from 3D colour Doppler data and the algorithm incorporates this additional wall motion information in exactly the same way as if it was obtained from colour Doppler images as described in Sec. 5.5 and in chapter 6. The new $\mathbf{S}$ matrix defined in(5.15) will have now one row per input data point from Doppler plus one row per point at which wall velocity has been calculated.

7.2.3 Multi-scale Approach

The velocity reconstruction method proposed in Sec. 5.5 deals with gaps in input data by zeroing the coefficients in the area where there is no velocity information, as described in Sec. 5.5.3.1. This avoids undesired oscillations of the reconstructed

velocity field that might appear if data points are sparse compared to the distance between grid points, but at the same time prevents the reconstruction of velocity in regions without input data. The use of a coarse grid (*i.e.* a grid where the distance between nodes is large compared to the size of internal gaps with no data) can help to fill these gaps with non-zero velocities, however this will result in fine scale flow features being missed. In this chapter, a multi-scale reconstruction approach is proposed which recovers velocity at multiple consecutive scales to achieve both stable and fine scale velocity reconstruction. Previous work on multi-scale B-spline based multidimensional data recovery includes the landmark paper by Lee et al. (1997). For each input data point, they solved for all B-spline grid nodes for which the input data point was within their region of influence. Then, a weighted average scheme was used to calculate the final coefficients of the B-spline nodes. For the case proposed in this paper, many input data points are used simultaneously similarly to the multi-scale B-spline approach proposed by Shi et al. (2012) to characterise deformation fields at multiple resolutions in a free-form deformation registration process.

Multi-scale Approach

3D velocity is reconstructed consecutively using several grids of decreasing distance s between grid nodes. Starting from a coarse grid (Fig. 7.4 (a)) with grid spacing $s = s_0$, 3D velocity vectors are calculated over the whole Region of Interest (RoI). The resulting vector field $\mathbf{w}^0$ is then projected along the beam direction of each view $n = 1 \dots N$, creating N simulated colour Doppler images. These simulated images are subtracted from the N corresponding input colour Doppler images, producing new colour Doppler images which lack coarse features calculated at scale s_0. These new images are used as input for the next scale where $s_1 = s_0/2$ (Fig. 7.4 (b)). This process is iteratively repeated for all scales (Fig. 7.4 (c)). The total velocity field $\mathbf{v}^k$ at a resolution s_k is:

$$\mathbf{v}^k = \sum_{i=0}^{k} \mathbf{w}^i \tag{7.2}$$

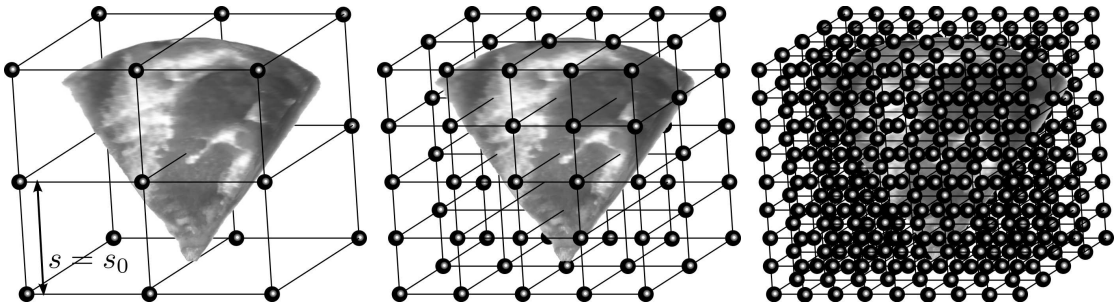

(a) $s = s_0$. (b) $s_1 = s_0/2$. (c) $s_2 = s_0/4$.

Figure 7.4: B-spline grid refinement in the multi-scale approach.

7.3 Experiments

The proposed method was used to recover 3D flow using data from patient 3 from chapter 6: a 2 month old patient following aortic valve replacement for critical aortic stenosis with residual mitral stenosis. In this patient the LV had an approximate height of $43mm$ and a diameter of $25mm$. Flow reconstruction was carried out using 3 resolution scales $s = \{12.5, 6.25, 3.125\}[mm]$.

Three colour Doppler views were acquired with a Philips X7-2 probe during breath-holds, targeting the left ventricular chamber: 1 apical, 1 parasternal and 1 subcostal. At each view, the probe was tilted along three orientations in order to achieve maximum ventricular coverage, resulting in a total of 9 images. A standard B-Mode sequence was acquired in each view for image registration. The patient was under general anaesthesia with active respiratory control. Images were acquired with institutional ethical approval after informed parental consent.

Quantitative and qualitative experiments were carried out:

- **Quantitative analysis.** Point-wise comparison was not possible because an accurate registration between 3D+t Flow MRI and echo was not available. Instead, inflow SV calculated as the time-integral of the flow rate through the mitral valve was calculated using 2D+t Flow MRI and the proposed method and compared.

- **Qualitative analysis.** Ventricular filling flow patterns and velocity distribution were qualitatively compared with 3D+t Flow MRI in terms of velocity profiles and vortex location.

The results were compared to those obtained when no wall motion information

was used, *i.e.* the results reported in Sec. 6.5.3.

7.4 Results

Flow rate was calculated through the mitral valve (MV) using 2D+t Flow MRI and the proposed method. Figure 7.5 shows the resulting flow rate curves for three cases: 2D+t Flow MRI (solid line), 3D velocity reconstruction from 3D colour Doppler data with no wall motion information (round dots, as reported in Sec. 6.5.3) and the method proposed in this chapter, represented with hollow triangles.

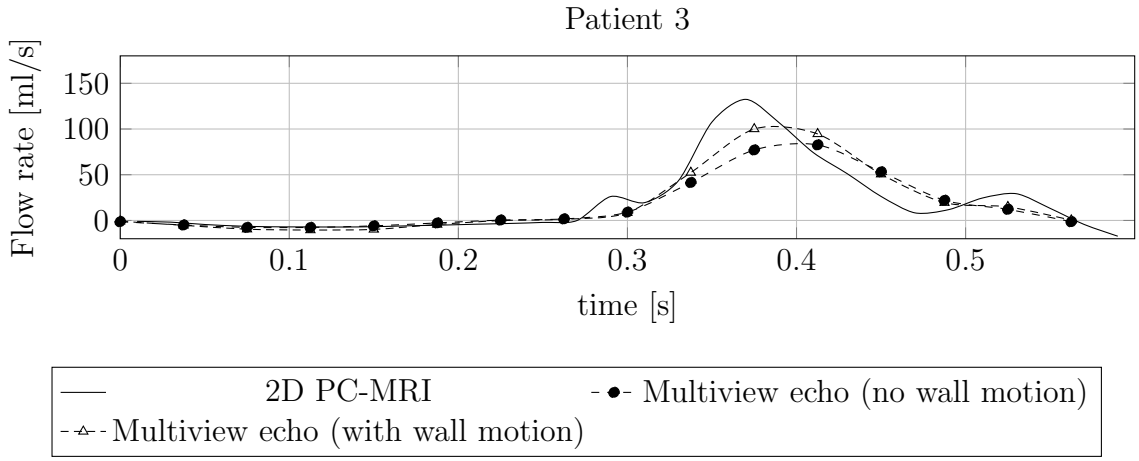

Figure 7.5: Flow rate on a paediatric patient through the mitral valve. Plane through which flow rate was computed was set at acquisition time for 2D+t Flow MRI, and a similar plane was manually selected in postprocessing for our proposed method.

Stroke volume (obtained from time integral of flow rate curves) calculated with 2D+t Flow MRI was 13.0 ml. Stroke volume calculated from velocity fields reconstructed from colour Doppler-derived data without wall motion information was 11.2 ml *i.e.* a mean absolute difference of approximately 15%. Using the method proposed in this chapter, with wall motion information, SV was 12.8 ml *i.e.* a mean absolute difference with respect to 2D flow MRI close to 1%.

Figure 7.6 shows the magnitude of the reconstructed velocity on three orthogonal slices (short axis, 2 chamber and 4 chamber) near the end of diastole when the ventricular vortex is fully developed. Similar planes were manually selected to capture the same location in both modalities. The first column of Fig. 7.6 shows velocity from 4D flow MRI. The 3 rightmost columns show the velocity at three decreasing scales. At the coarser scale ($s = 12.5mm$), the reconstructed velocity

shows a very smooth and homogeneous velocity distribution. At the intermediate scale ($s = 6.25mm$) flow structures are resolved at a similar resolution as 4D flow MRI, including a high-velocity inflow jet. At the finest scale ($s = 3.125mm$) fine flow features emerge, some of which were not present in the MRI data. Further investigation is required to ascertain whether these fine scale structures are underlying flow features or artefacts in the reconstructed field. In the following, the intermediate scale is used when comparing to 4D flow MRI.

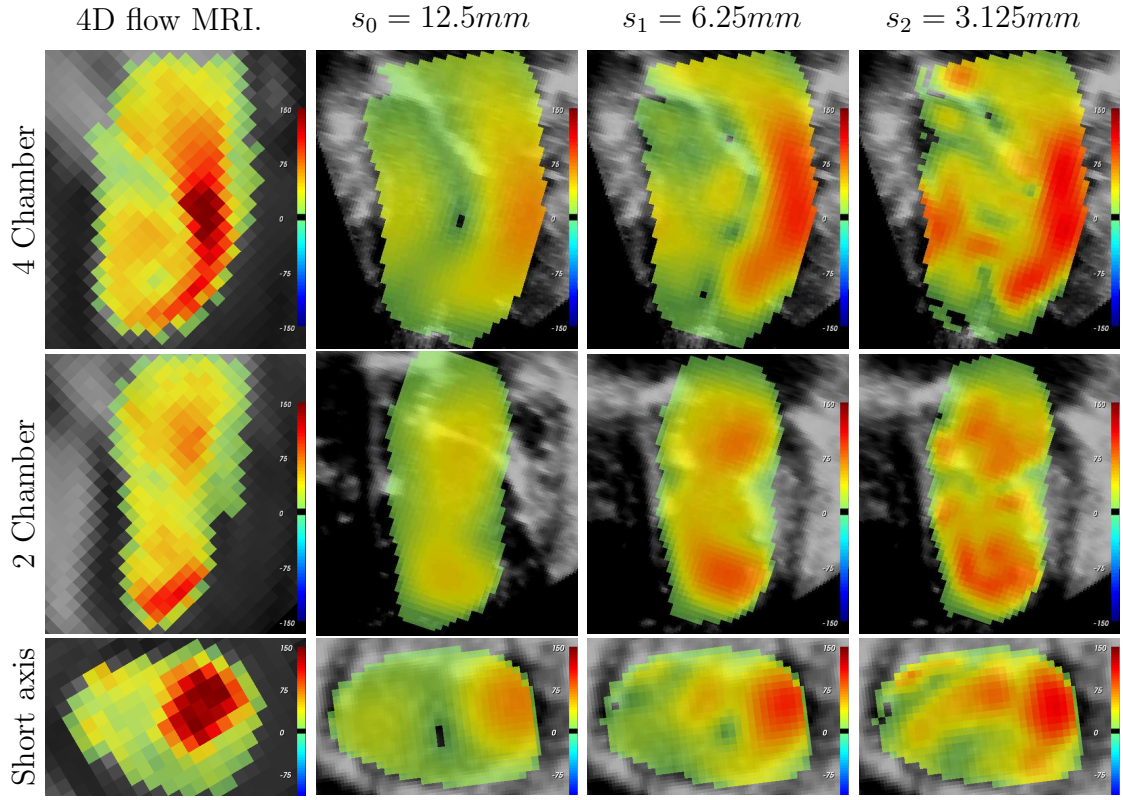

Figure 7.6: Comparison between 3 cross sectional slices of the velocity magnitude, from 4D flow MRI (first column) and the proposed method at three different scales. In all cases the colourmap codes velocity between 0 and 150 cm/s.

Figure 7.7 shows the reconstructed flow patterns in more detail. Figure 7.7(a) shows a 2D slice of the 3D velocity vectors reconstructed using 4D flow MRI. Figure 7.7(b) shows, for comparative purposes, the velocity vectors reconstructed using the crossed-beam method proposed in chapter 6, sliced on a similar plane. The reconstructed vectors were limited to the region where three or more views overlap, and therefore only covered a fraction of the ventricular volume. Figure 7.7(c) shows the velocity vectors reconstructed using the proposed method, *i.e.* crossed-beam plus ventricle wall motion. Incorporation of wall motion allowed recovery of velocity vectors within the whole ventricle obtaining flow patterns similar to those obtained

with 4D flow MRI.

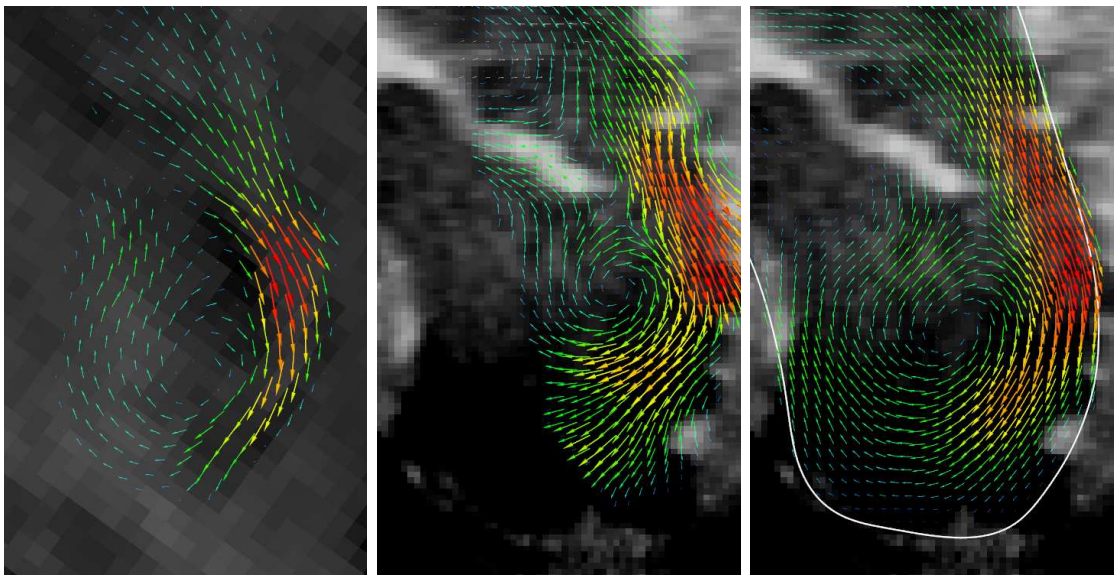

(a) 4D flow MRI.

(b) Flow from multiple colour Doppler views, as described in chapter 6.

(c) Proposed method: flow from multiple colour Doppler views and ventricle wall motion.

Figure 7.7: Reconstructed inflow vortex. (a) 2D slice of 3D flow reconstructed from patient using 3D+t flow MRI. Blood motion is represented by arrows which follow the velocity field from the left atrium into the LV. (b) Reconstruction, in a similar plane, with the method proposed in chapter 6. Velocity can only be reconstructed in the region where three or more views overlap. (c) Reconstruction with the method proposed in this chapter. Whole ventricular coverage is achieved by incorporating ventricle wall motion.

Figure 7.8 shows the formation of the filling vortex on the LV during diastole. The velocity field is represented with streamlines tangent to the velocity vectors at four diastolic time points. Figure 7.8(a) shows the 3D vortex computed from 3D+t Flow MRI measurements, on top of a 2D slice of a 3D cine MRI sequence for anatomical reference. A few erratic streamlines which appear to come out of the ventricle are due to the lack of masking since a good segmentation of the LV was not available from MRI images. Figure 7.8(b) shows the inflow vortex calculated with the proposed method. The segmentation of the ventricle is represented as a semi-transparent surface for anatomical reference. The increasing vortex can be clearly identified and followed through diastole. In both modalities, a main large vortex (I) can be distinguished which progresses from the valve plane towards the apex. In the 3D+t Flow MRI data, a small additional vortex (II) seems to appear below the mitral valve. This small vortex is not distinguishable in the Doppler-derived data at that particular scale.

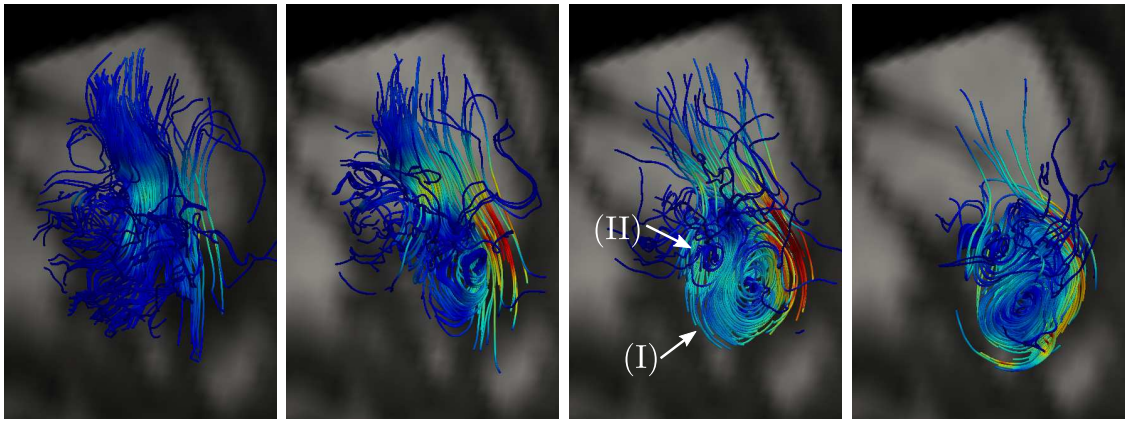

(a) Streamlines representing inflow vortex calculated from 4D flow MRI.

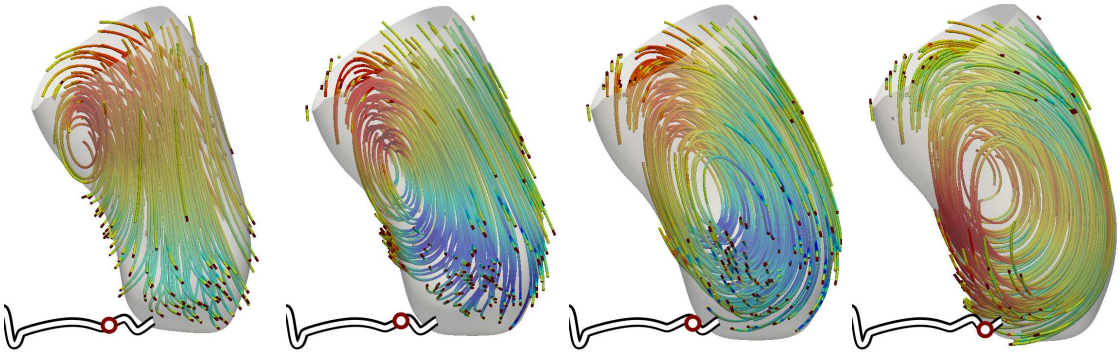

(b) Streamlines representing inflow vortex calculated from the proposed method.

Figure 7.8: Reconstructed inflow vortex represented with streamlines. (a) Vortex formation from the 3D velocity field reconstructed with the proposed method over four diastolic times. (b) Vortex formation calculated from the proposed method at similar time points.

7.5 Discussion

A multi-scale method to reconstruct 3D velocity from multiple 3D colour Doppler images plus information on ventricle wall motion has been proposed in this chapter. Information on ventricle wall motion, combined with a crossed beam 3D flow recovery approach, can help recover 3D velocity data in the regions where less than three colour Doppler images overlap. Full characterization of 3D velocity over the entire ventricle can provide improved understanding of cardiac function compared to standard Doppler techniques and to previously described velocity recovery methods.

Recently, Garcia et al. (2010) proposed to use ventricle wall motion to recover 2D velocities over a plane within the ventricular cavity. In their paper, the azimuthal component of blood velocity was propagated from wall motion provided that radial velocity was measured in the whole ventricle from a colour Doppler image, by using the 2D continuity equation in polar coordinates. Their method, which shows good

performance as long as the reconstruction plane is aligned with the plane of the filling vortex, is not easily extensible to 3D since separation of variables (required for their method) cannot be applied to the 3D continuity equation in spherical coordinates. The method proposed in this chapter incorporates wall motion in a straightforward way with no modification of the underlying algorithm with respect to the framework presented in chapters 5 and 6.

The method has been tested on one paediatric patient and reconstructed velocity has been compared to 3D+t Flow MRI, showing good agreement on estimated flow rate and stroke volume. Although no point-wise comparison of the two modalities was possible, similar velocity distribution and vortex size and location was found.

A representation of the vortex using steamlines revealed some differences between MRI data and the proposed method, particularly a small vortex below the valve which was only detected with MRI. Whether this is physiological or an artefact and the reason why this structure is not appearing with the proposed method needs further verification, and will be addressed with experiments on a larger group of patients.

The availability of 3D velocity fields over the whole ventricle has the potential to enable the calculation of additional cardiac metrics, which cannot be calculated if ventricular coverage is only partial. A few such metrics are the following:

- Rate of kinetic energy ($K = \int_V 1/2\rho \mathbf{v}^\top \mathbf{v}\ dv$) can be used as an indicator of efficiency of the ventricle, for example before and after interventions in Congenital Heart Disease (CHD) as described by de Vecchi et al. (2012). Total kinetic energy can be calculated by integrating K over time..

- Rate of viscous losses ($L = \mu \int_V \nabla\mathbf{v} : \nabla\mathbf{v}\ dv$[1].) indicate the amount of energy dissipated by fluid friction, which when related to total energy also indicates efficiency of the heart. Total viscous losses energy can be calculated by integrating L over time.

- Vortex descriptors, such as the Q and the λ_2 parameters (Jeong and Hussain, 1995) which are based on a singular value decomposition of the velocity gradient tensor (Jacobian), provide means to detect and classify vortical structures,

[1]The tensor operator ':' is the Frobenius product, defined as $A : B = \sum_i \sum_j A_{ij} B_{ji} = tr(A^\top B)$

and potentially study associations between these descriptors and cardiac diseases.

- Vortex plane and vortex angular velocity can also be extracted from the reconstructed velocity field by regression techniques, e.g. the rotation plane is approximately orthogonal to the smallest eigenvector of the velocity vectors within the vortex.

The applicability and benefit that can be obtained from these metrics is still to be determined with a clinical study on a larger set of patients.

The ability to recover 3D velocities in regions where less than three views overlap suggests that it might be possible to recover velocities from less than three views within the whole ventricle. This is important since, as shown in chapter 6 one of the largest contributors to inaccuracy is reduced angle between views. The reduction of the required number of independent views would dramatically increase the applicability of the method because almost always two views with sufficient angle can be achieved, but three or more views separated more than 20° can be difficult to obtain, particularly in adults.

7.6 Conclusion

In this chapter, a new method to recover full 3D intraventricular blood velocity fields from multiple 3D colour Doppler images plus wall motion derived from B-Mode images has been proposed. The method has been tested on one paediatric patient, where the reconstructed velocities were compared to flow MRI showing good agreement in stroke volume, in flow patterns and in velocity distribution.

The present study has been carried out in a single patient and an experiment on a larger set of patients is required to assess the robustness of the method. However, this chapter highlights the potential of the technique to recover complex and detailed 3D flow information with a clinically feasible protocol and is particularly well-suited to small patients where flow MRI is not always possible. The wide spread availability of 3D echo systems further increases the interest and potential impact of the developed method.

Chapter 8

Angle Independent Flow Quantification

"For echocardiography and Doppler to become a 'one-stop shopping' modality for evaluating cardiovascular structure, flow, and function, they will continue to evolve to include, hopefully, all valves (mitral, aortic, pulmonary, and tricuspid). The temporal and spatial resolution should be adequate. The field of view should be large enough to include all heart valves and the great arteries"

"Automated Measurement of Stroke Volumes by Real-Time 3-Dimensional Doppler Echocardiography: Coming of Age?", Ge (2012)

Contents

This chapter contains the second research line that has been followed in this thesis. The ability to compute angle-independent flow rate and volume, without the need of retrieving multiple components of blood velocity, is investigated. The main contributions of this chapter are, on the technical side, three new methods for combining multiple views to build composite surfaces through which flow rate can be calculated; and on the application side, a clinically feasible protocol to accurately calculate angle-independent flow rate and volume from 3D colour Doppler images.

This chapter is organised as follows. Section 8.1 describes the principle of angle independent flow quantification from Doppler measurements and summarises the main contributions of this chapter. Section 8.2 describes the motivation behind view combination to produce a composite surface through which flow rate can be calculated. Sections 8.2.1, 8.2.2 and 8.2.3 describe three algorithms for view combination. Section 8.3 describes how velocity can be integrated over the composite surface to calculate flow rate. Section 8.4 describes how sequences are temporally aligned and interleaved to increase the effective frame rate. Experiments on 4 HLHS patients are described in Sec. 8.5, and results presented in Sec. 8.6.

8.1 Introduction

Many cardiac parameters are calculated from measurements of flow rate, e.g. stroke volume (SV) or cardiac output (Q) (Table 2.1). Widely used techniques for measuring flow rate include intravascular Doppler catheters, 2D+t Flow MRI and echo Doppler systems, as discussed in Sec. 2.3. Doppler systems are inexpensive and wide-spread compared to the other modalities, but the methods based on echo Doppler measurements often lack of accuracy. The main source of inaccuracy is

that the measured velocity depends on the angle of insonation and therefore beam-to-vessel angle has to be compensated for. Even if this angle is compensated, other assumptions have to be made: the direction of the velocity is assumed the same over the entire vessel cross section, and the velocity profile needs to be either measured or assumed e.g. constant or parabolic. Additionally, the cross sectional area of the vessel has to be accurately calculated.

8.1.1 Advanced Angle Independent Flow Quantification from Doppler Velocity Integration over Echo Wavefronts

Recent publications (Ge et al., 2005; Thavendiranathan et al., 2012) have investigated other approaches to overcome angle dependency when measuring flow with Doppler systems. These methods are based on integration of velocity measured from 3D colour Doppler images over spherical surfaces coincident with the echo wavefront. The underlying idea which is common to those publications and the work presented in this chapter is the following.

Flow rate, $\Phi(S)$ is defined as the amount of blood that passes through a surface S per time unit. Figure 8.1 shows a diagram of how $\Phi(S)$ can be measured with 3D colour Doppler echo.

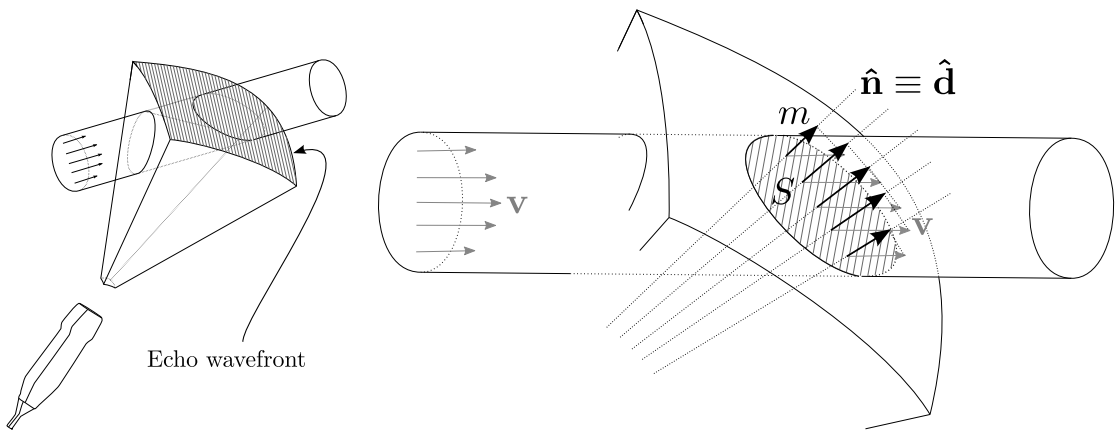

Figure 8.1: Angle-independent flow quantification using 3D colour Doppler. (a) Representation of a transducer imaging a vessel, where the echo frustum completely contains the cross section of the vessel. (b) Detail of the cross sectional surface S and the component m of the velocity $\mathbf{v}$ measured for a particular angle between the beam and the vessel.

Using Gauss' theorem, flow rate can be computed as

$$\Phi(S) = \iint_S \mathbf{v} \cdot d\hat{\mathbf{n}} = \iint_S \|\mathbf{v} \cdot \hat{\mathbf{n}}\| ds \tag{8.1}$$

where $\mathbf{v}$ is the instantaneous velocity vector of blood at each point $s \in S$ and $\hat{\mathbf{n}}$ is the vector normal to S at s. In other words, only the component of the velocity orthogonal to the surface (*i.e.* parallel to $\hat{\mathbf{n}}$) contributes to flow computation. Since intensity in colour Doppler images measures the component of the blood velocity along the echo beam direction $\hat{\mathbf{d}}$, *i.e.* orthogonal to the family of spherical wavefront surfaces (Remark 2), one concludes that flow rate can be computed from integrating colour Doppler intensities m over spherical surfaces centred at the transducer tip. As shown in Fig. 8.1(a), these surfaces are restricted to the frustum-shaped FoV of the echo images. As a result, integrating colour Doppler images over the S yields flow rate independent to the insonation angle and independent to the orientation of the surface, as illustrated in Fig. 8.2.

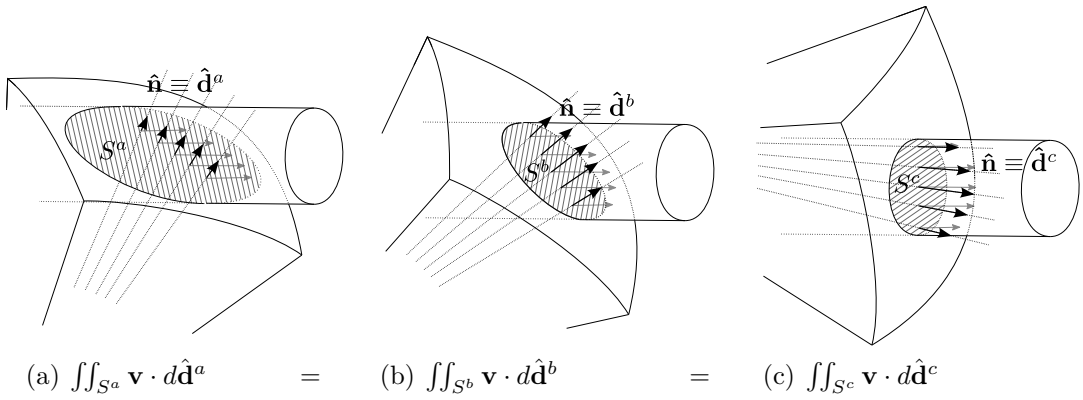

Figure 8.2: Effect of the orientation of the surface through which flow rate is calculated. As the angle between the surface and the rigid vessel decrease from (a) to (c), the cross sectional surface decreases but the magnitude of the projected velocity increases, resulting in the same flow rate and volume.

Flow rate through the surfaces S^a, S^b and S^c is identical. The Doppler velocity measured in Fig 8.2(a) is the lowest of the three, but the surface S^a is the largest. The opposite occurs in Fig. 8.2(c). In a real vessel, where flow is not steady, where the vessel walls move and so the cross sectional area changes, the resulting flow rate curves may be different in the three cases, but the overall flow volume will still be the same.

Although the approaches proposed by Ge et al. (2005) and Thavendiranathan

et al. (2012) do overcome the angle dependency problem, they still have some limitations, particularly:

- These methods rely on 3D colour Doppler images, and the measurement of velocity over a volume reduces the frame rate at which the volume of interest can be sampled. Frame rates high enough for accurate flow quantification are not always attainable, especially for subjects with high cardiac rates.

- The heavy processing demanded by 3D colour Doppler acquisitions also reduce the available FoV. Therefore, it may be difficult and can be impossible to measure flow rate through large vascular structures (e.g. dilated valves in CHD) with a single 3D colour Doppler view.

This chapter describes a new technique for accurate, angle independent flow quantification which enables flow quantification within an enlarged FoV and high temporal resolution. The main novelty in this chapter is the combination of multiple views to produce large FoV, custom composite surfaces through which angle-independent flow can be calculated from multiple 3D colour Doppler images. Three methods to combine multiple 3D colour Doppler views are proposed and discussed.

8.2 View Combination into Composite Surfaces

In the clinic, particularly when using 2D+t Flow MRI to measure flow, care is taken to select a plane orthogonal to the vessel. Although, as explained in Sec 8.1, the orientation of the plane does not affect the calculation of volume, there are two reasons for the extra care taken to choose an orthogonal plane. The first is that the segmentation of the cross section is easier if the surface is orthogonal to the vessel. Secondly, Magnetic Resonance Imaging (MRI) images typically have high resolution in-plane but large slice thickness, *i.e.* MRI signal is averaged over a large area at each side of the slice. If the slice is oblique with respect to the vessel, slice thickness causes that pixels neighbouring the vessel contour extend into the tissue, and the measured velocity value would be an average of actual blood velocity plus signal from tissue. This is known as the *partial volume effect*, and it is reduced by selecting a plane orthogonal to the vessel.

With 3D colour Doppler, the surface through which flow is computed is fixed by the orientation of the transducer, which is restricted by the patient's anatomy and the RoI. In addition, the surface can only be as wide as the FoV of the colour Doppler image (Fig. 8.1), which brings in the main limitation of the method. As shown in Fig. 8.3, if the angle between the vessel and the beam is too large, or the vessel falls outside the FoV, the surface might not completely cut the vessel and the flow measurement is only partial.

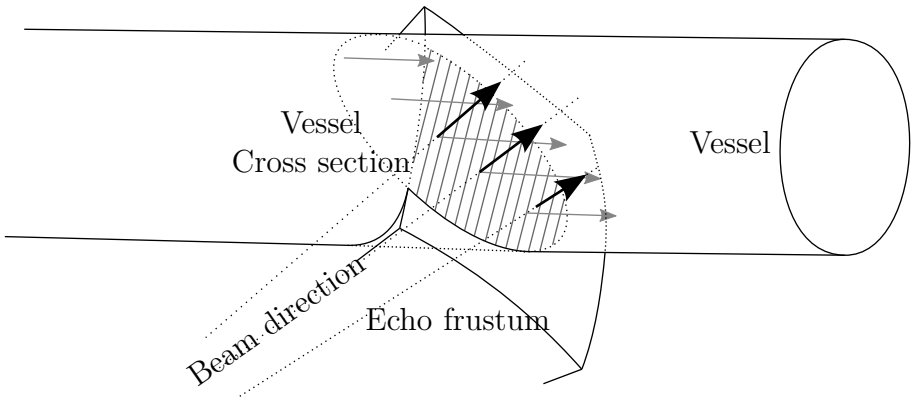

Figure 8.3: Main limitation of angle independent methods. The cross section of the vessel lies outside the FoV of the colour Doppler image, therefore the resulting flow is underestimated.

Lack of coverage can be due to two reasons:

- The RoI (e.g. target valve or structure) is larger than the FoV of the 3D colour Doppler image. Depending on the acquisition settings of the imaging system (depth, number of acquisition beats, density of scan lines, etc) the FoV can be relatively small, especially for colour Doppler images. As a result, including the full cross sectional area of the structure of interest can be impossible. This is relatively common in the case of large valves (mitral, tricuspid) on adult patients or enlarged structures on congenital patients.

- Poor acoustic access prevents from imaging the entire cross section from one view, e.g. a part of the target might be hidden under the shadow projected by air or bones.

A way to overcome these limitations, developed in this chapter and sketched in Fig. 8.4, is to use multiple colour Doppler views. Multiview approaches can enlarge the FoV and can circumvent regions hidden by reduced acoustic access. As represented

in Fig. 8.4(a), the surface through which flow is calculated would then be composed of spherical patches. Figure 8.4(b) shows the contribution of each patch in more detail. Velocities measured from views 1 and 2 are integrated over surfaces S_1 and S_2, and then summed up. This allows for enlarged effective FoV and some flexibility in the effective surface orientation.

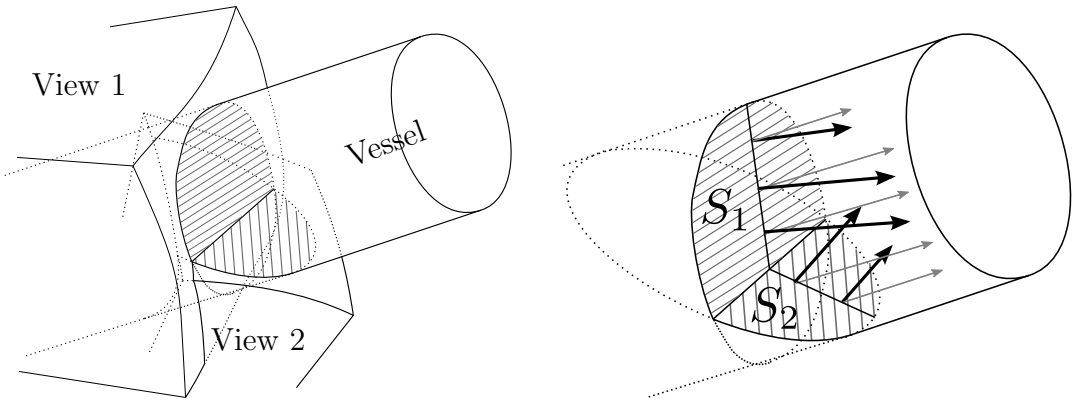

(a) Composite surface from two views.

(b) At each piece velocity is measured along a different direction.

Figure 8.4: Proposed solution to enlarge the effective FoV for angle-independent flow quantifcation.(a) By combining two views, even if each of them only cuts the cross section of the vessel partially, it is possible to produce a composite surface covering the whole cross section. (b) The contribution to flow rate from each piece of the surface is summed up.

Sections 8.2.1, 8.2.2 and 8.2.3 describe three methods to calculate composite surfaces from multiple 3D colour Doppler views. The three methods assume that input views are registered to a common coordinate space. This was achieved with a registration algorithm that used a phase-based similarity measure (Grau et al., 2007) as has been described in Sec. 5.2.

For the sake of clarity of figures and explanations, and without loss of generality, in what follows the theoretical developments are explained in two dimensions. Particularities of the extension to 3D are explicitly clarified when needed. More formally, the problem that the three methods solve can be formulated in 2D as follows:

Problem 1. *Let $b_1, b_2, \ldots, b_K$ be K 2D points, and let S be a 2D target line. What is the combination c of spherical arcs, centred at $\{b_i\}_{i=1\ldots K}$, which best approximates S in the sense of minimising some distance function $d(S, c)$?*

In the above $\{b_i\}$ represent the transducer positions, and the target line S rep-

resents the plane over which flow is to be calculated. A representation of problem 1 and a possible solution are shown in Fig. 8.5. In order to solve it, several parameters have to been set, in particular the choice of distance measure between S and the composite curve c, $d(S, c)$.

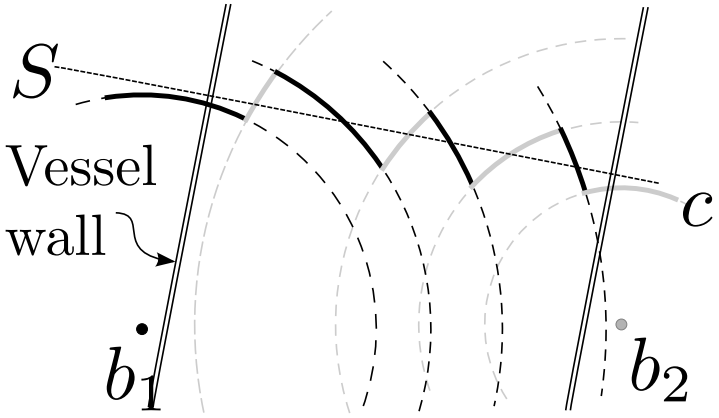

Figure 8.5: Representation of the problem of fitting a line S with a piece-wise arc function c, and a possible solution.

An analytical solution can be found if c can be parameterised in some parameter space:

$$c(\mathbf{a}) = \min_{\mathbf{a}} d(c(\mathbf{a}), S) \tag{8.2}$$

where $\mathbf{a} \in R^n$ is a vector of n parameters. The parameters include the angle of each arc. The problem is ill-posed because the number of parameters (*i.e.* the degrees of freedom) depend on the number of arcs, which might be arbitrarily chosen. An infinite number of arcs would allow for a perfect fit, *i.e.* a zero distance between S and c. Another drawback of the minimisation approach is the extension to 3D, which is non trivial.

Instead of finding an analytical solution following the minimization approach described above, three alternative well-posed solutions are described in the following sections. These approaches are motivated by finding a method which finds an accurate approximation to a 3D target surface S made of spherical patches centred at the view points $\{b_i\}$, with minimal user interaction.

8.2.1 Semi-automatic Combination of Two Views

The simplest solution to the view combination problem is that of combining two views with two spherical patches, each centred at a view point, and separated by

a plane, similar to the solution sketched in Fig. 8.4(b). This section describes a method to implement that solution.

Figure 8.6 shows the process of combining two views. First a standard B-Mode image (which has a wider FoV) is used to segment the region of interest (e.g. the tricuspid valve shown in Fig. 8.6(a)). The user then defines a plane in the overlap of the two FoVs from which each of the two spherical patches of the composite surface will be built (Fig. 8.6(b)). Then, a spherical patch (coincident with the wavefront of the associated view) is extended at each side of P (Fig. 8.6(c)). Finally, The segmentation is used to clip the composite surface (Fig. 8.6(d)).

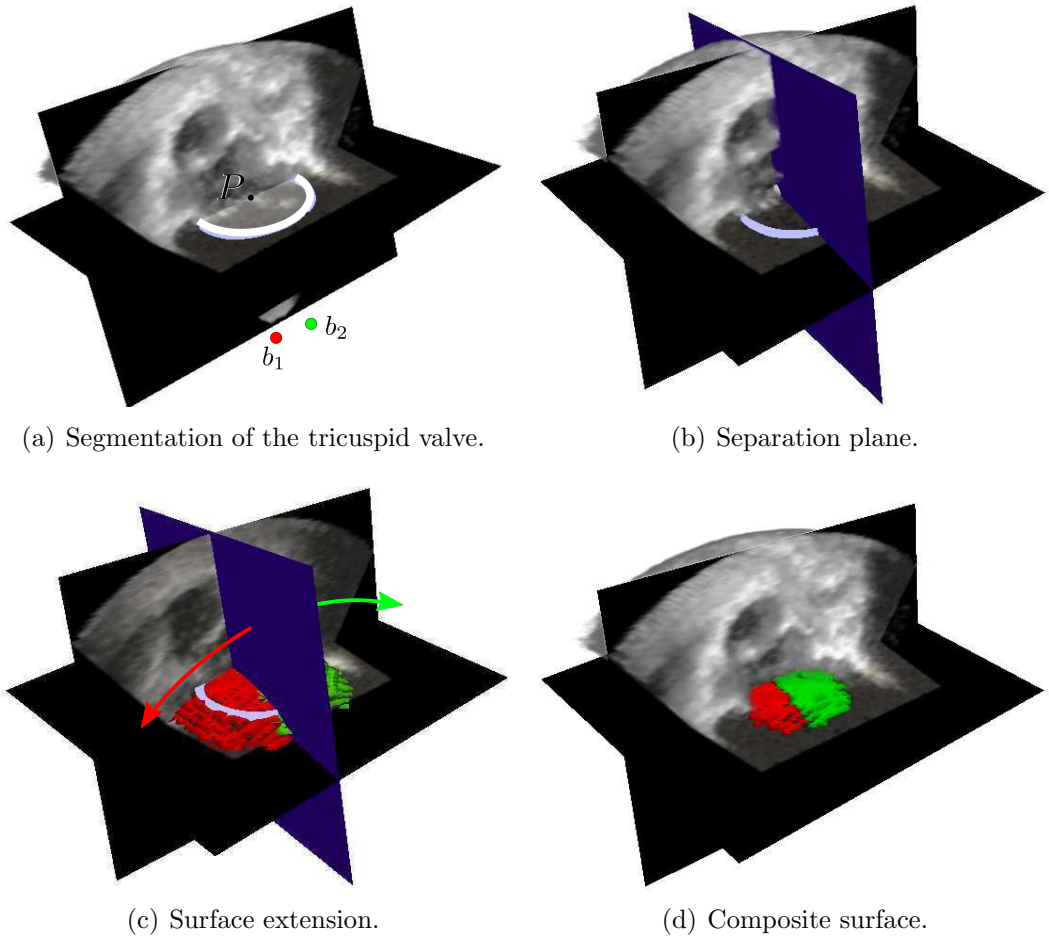

(a) Segmentation of the tricuspid valve.

(b) Separation plane.

(c) Surface extension.

(d) Composite surface.

Figure 8.6: Combination of two views. (a) Segmentation of TV using a B-Mode image. Green and red dots represent the tip of the transducer at each view. (b) Separation plane between views, defined by the user. (c) Spherical surfaces are extended at each side of the separation plane. (d) The extended surfaces are clipped with the segmentation producing the final composite surface.

This method is very simple, but has two main limitations: it can combine no more than two views, and it requires a fair amount of user interaction in order to perform the segmentation of the target and to define the separation plane. The two

alternative methods described in the next two sections address these two limitations.

8.2.2 Multi-resolution Image-Based Approach

This section describes a method to automatically construct a composite surface from K views, given a number of input 3D colour Doppler images and a target surface specified by the user. The method yields a composite surface which approximates the target surface.

8.2.2.1 General Overview of the Method

Instead of the minimization approach, in this section a multi-resolution image-based approach has been investigated. The basic idea is to generate an irregular grid made of circles centred at $\{b_i\}$ and rasterise the target line into that grid so that the target line is approximated by a succession of grid cells. The method, illustrated in Fig. 8.7 consist of the following processing steps:

1. Find the succession of cells that approximate the target line S (Fig. 8.7(a)). This yields a *solid approximation* (in grey) of S.

2. Extract the boundary of the solid approximation (Fig. 8.7(b)). This yields a curve shell enclosing the solid approximation.

3. Clip the boundary with the segmentation of the vessel (Fig. 8.7(c)). This yields two curves, one at each side of the target line.

4. Label the extracted boundary to associate each arc to a centre (Fig. 8.7(d)).

The four steps enumerated above yield two composite curves (one at each side of the target line). In the 3D case, the result is two labelled composite surfaces through which flow can be calculated as described later in Sec. 8.3. A detailed description of the implementation of each processing step is detailed next.

8.2.2.2 Solid Approximation of Target Surface

The solid approximation (*i.e.* ensemble of cells $\{c_i\}$ that enclose the target surface) is obtained via a multi-resolution algorithm. The resolution of the solution depends on the resolution of the sphere-generated grid G_{it} (*i.e.* the step between concentric

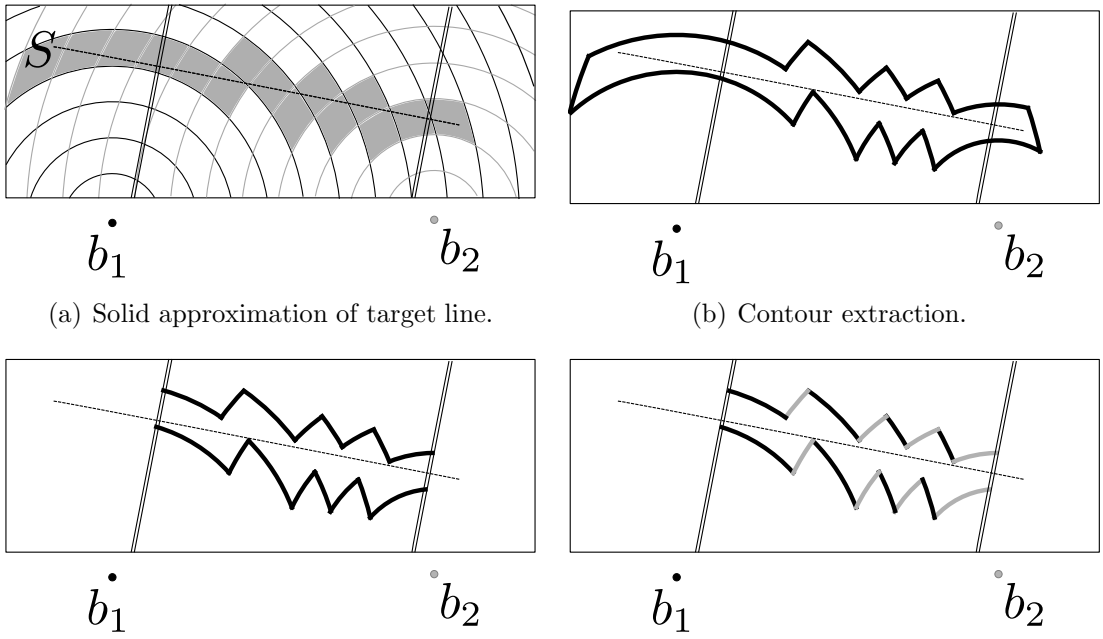

(a) Solid approximation of target line.

(b) Contour extraction.

(c) Contour segmentation.

(d) Contour labelling.

Figure 8.7: Image-based surface combination in 2D.

spheres), which is refined over a number of iterations $it = 0 \ldots$`MAX_IT` indicated by the user. At each iteration only the cells that are potentially part of the solution are refined, saving execution time and memory. The algorithm 1 describes the process.

Algorithm 1 Approximation of a target surface S into a sphere-generated grid.

Input: Target Surface S, View points $\{b_i\}_{i=1\ldots K}$
Output: $c_{ini} \leftarrow$ InitCell($\{b_i\}$,S), $it \leftarrow 0$, $CELLS = \{\}$ ▷ Initialization
RefineCell(c_{ini},it,$CELLS$) ▷ Start multi-scale refinement

```
function RefineCell(c,iteration, CELLS)
    if iteration ≥ MAX_IT then
        CELLS ←append— c
        return
    end if

    G ← CreateGrid(resolution/2,radiusStep/2,{b_i})
    {cells} = Intersect(grid,S)
    for i = 1 to Size(cells) do
        RefineCell(cells_i,iteration+1, CELLS)
    end for
end function
```

First, a single cell c_{ini} enclosing S is initialised (Fig. 8.8). The cell is built as the intersection of K spherical shells centred at $\{b_i\}_{i=1\ldots K}$ where the inner and outer radius are $r_{IN,i} = d_{min}(S, b_i)$ and $r_{OUT,i} = d_{max}(S, b_i)$ respectively. This cell c_{ini} is further refined `MAX_IT` times by subdividing it using grids where distance between

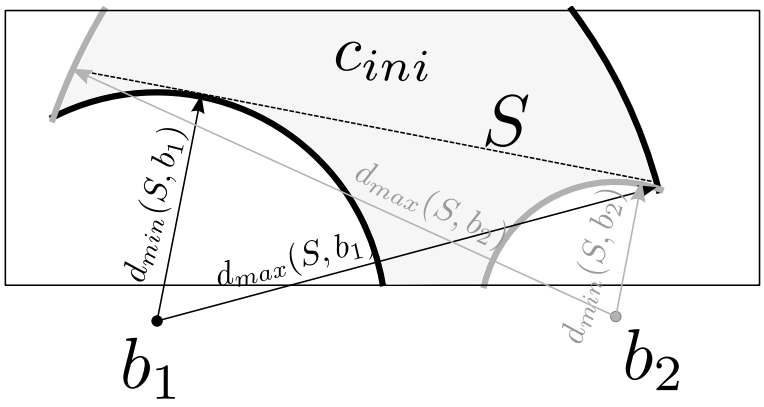

Figure 8.8: Image-based surface combination: definition of the initial cell.

concentric spheres is halved at each iteration. The subdivision process is illustrated in Fig. 8.9. The first row (Fig. 8.9(a) to 8.9(d)) shows a schematic design of the subdivision process at different iterations it. Each step shows the refinement of a cell from the previous level, marked in red. The second row (Fig. 8.9(e) to 8.9(h)) shows the cell grid G_{it} at each iteration it (with each cell labelled with a different colour). The third row (Fig. 8.9(i) to 8.9(l)) shows the binarisation $I_{S,it}$ of the target surface S at the resolution corresponding to the iteration it. At each level, the cells that are kept for the iteration $it+1$ are constituted by the non-zero voxels in $I_{S,it} \cap G_{it}$.

8.2.2.3 Obtaining Two Labelled Surfaces from the Solid Approximation

Once the solid approximation has been computed, the two surfaces can be extracted by the following processing pipeline:

1. **Extract the contour of the solid approximation**.

   This is done by a binarisation of the solid approximation (Fig. 8.10(a)) followed by a morphological edge detector, which yields a 1-voxel thick contour.

2. **Crop the contour.**

   The contour is masked with a segmentation of the vessel (Fig. 8.10(b)).

3. **Labelling: associating each voxel to the view point on which each surface patch is centred**.

   This operation consists of identifying, for each voxel of the contour, which spherical surface it belongs to. The gradient of the solid approximation **g**

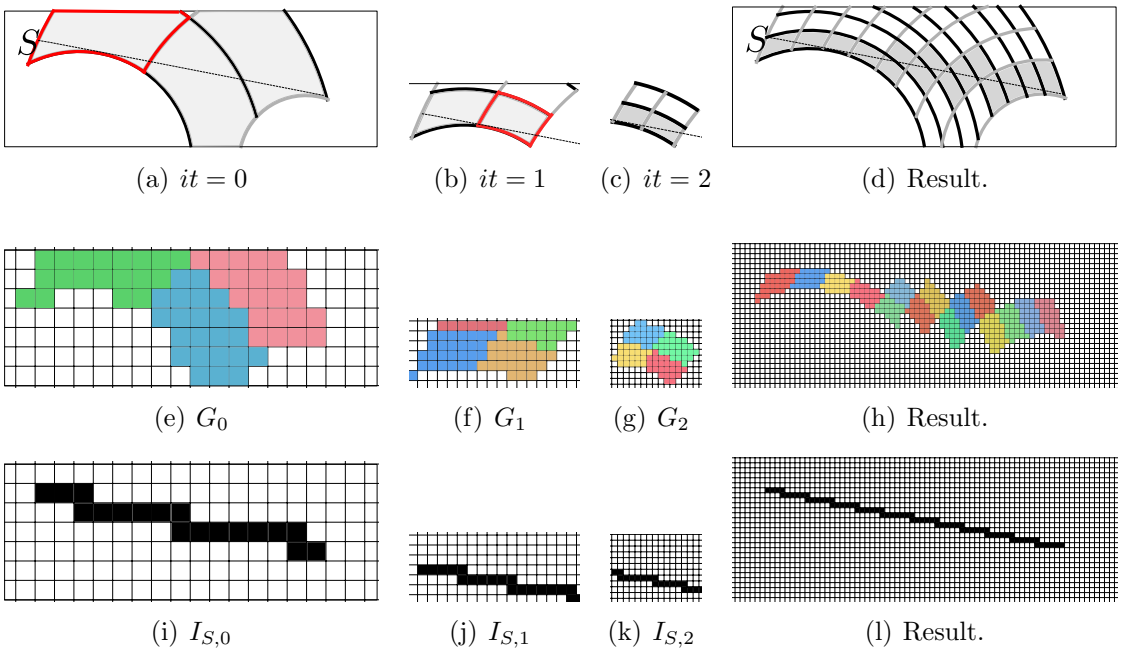

(a) $it = 0$ (b) $it = 1$ (c) $it = 2$ (d) Result.

(e) G_0 (f) G_1 (g) G_2 (h) Result.

(i) $I_{S,0}$ (j) $I_{S,1}$ (k) $I_{S,2}$ (l) Result.

Figure 8.9: Image-based surface combination: cell refinement. The first row shows the theoretical approach to subdividing each cell in 4 smaller cells (8 in 3D) throughout 3 iterations. The second row show the actual implementation of the refinement on images of decreasing voxel size. The third row shows the corresponding refinement of the binarisation of the target surface.

(orthogonal to the solid approximation contour), evaluated only on the contour (Fig. 8.10(c)) is compared to the radial direction $\mathbf{d_1}$ for view point b_1 (Fig. 8.10(d)) and to the radial direction $\mathbf{d_2}$ for view point b_2 (Fig. 8.10(e)). The dot product between $\mathbf{g}$ and each radial direction, *i.e.* $\mathbf{g} \cdot \mathbf{d_1}$ and $\mathbf{g} \cdot \mathbf{d_2}$, represented in Fig. 8.10(f) and Fig. 8.10(g) respectively, indicates how good the alignment is with each view direction, where a value of ± 1 indicates that the alignment with that view direction is perfect and the sign indicates whether the measured velocity is entering $(+)$ the solid approximation or leaving it $(-)$, and 0 means no alignment. Each voxel is then given a label corresponding to the best alignment (dot product closest to ± 1), as shown in Fig. 8.10(h).

The result of this process is an image where a composite spherical surface is represented by labelled voxels. Figure 8.11 shows an example of the resulting surfaces in 3D obtained from two views.

There is mainly one source of inaccuracy when using this method, indicated in Fig. 8.10(h). The resulting composite surface presents ridges where two patches from different views join together. In the image-based approach, these ridges are represented by ridge voxels, which can only be associated to one of the neighbouring

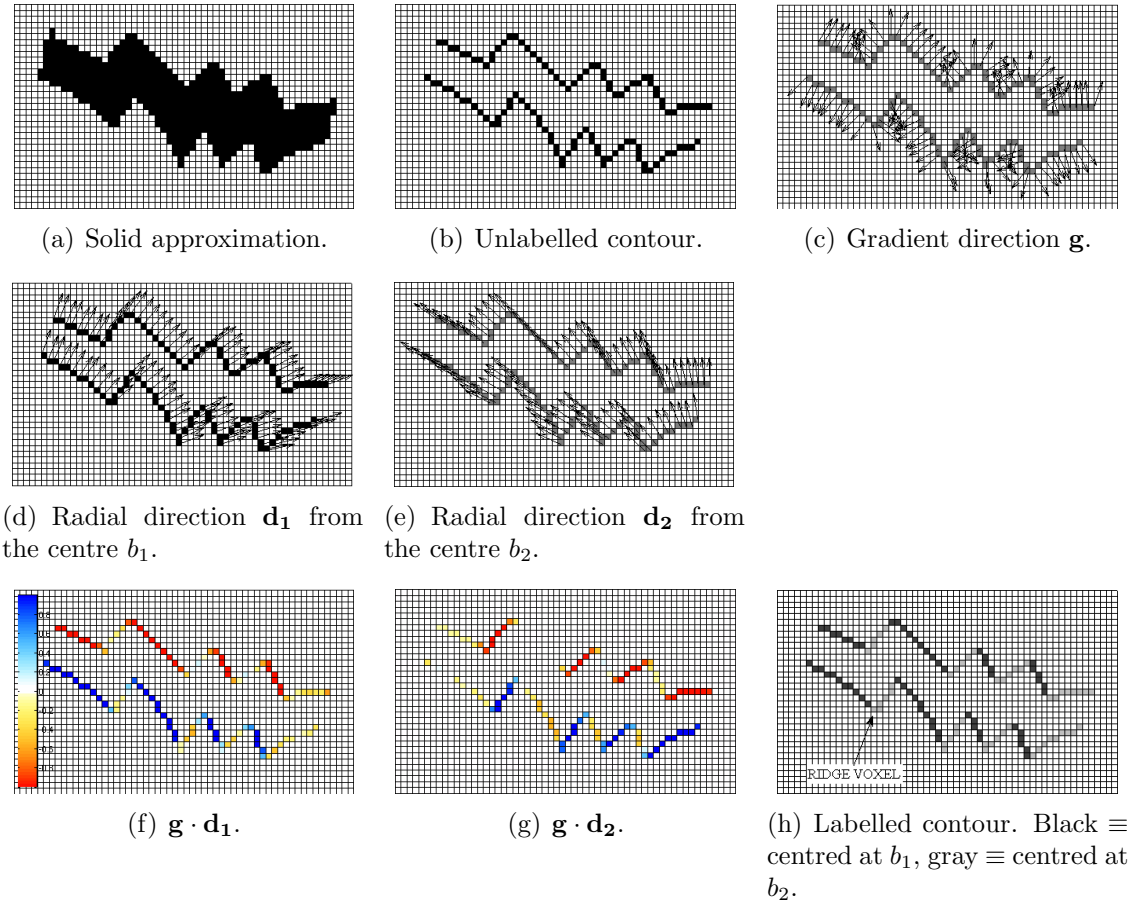

(a) Solid approximation.

(b) Unlabelled contour.

(c) Gradient direction $\mathbf{g}$.

(d) Radial direction $\mathbf{d_1}$ from the centre b_1.

(e) Radial direction $\mathbf{d_2}$ from the centre b_2.

(f) $\mathbf{g} \cdot \mathbf{d_1}$.

(g) $\mathbf{g} \cdot \mathbf{d_2}$.

(h) Labelled contour. Black $\equiv$ centred at b_1, gray $\equiv$ centred at b_2.

Figure 8.10: Surface labelling by aligning the view direction with the surface direction. The centres b_1 and b_2 are those indicated in Fig. 8.8. A label corresponding to a centre is calculated for each voxel of the composite surface as the index of the centre whose radial direction is better aligned with the contour gradient.

spherical patches. As a result, the other patches which share the same ridge will not account for these voxels and will therefore provide a smaller area, underestimating (in absolute value) their contribution to flow rate. This can be minimised by reducing the voxel size, which increases the computational requirements of the method.

8.2.3 Surface-Based Approach

This section describes a method to construct a composite surface from an arbitrary number K of 3D colour Doppler views. Like the method described in the previous section, it is based on building a grid from equally spaced concentric spheres centred at each view position. However, this method does not calculate cells using an image-based processing. Instead, it calculates analytically the intersection between the spherical surfaces, the vessel segmentation and the echo frustums.

In this section, the term *wavefront* is widely used to refer to each of the surfaces

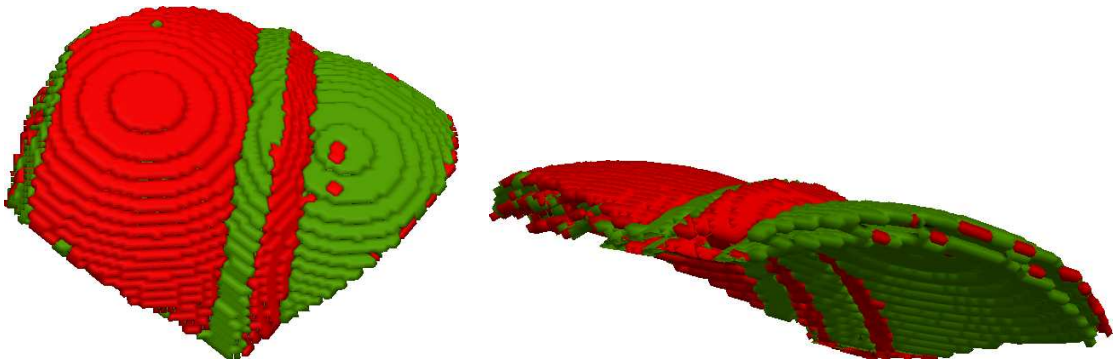

(a) Superior view. (b) Side view.

Figure 8.11: Composite surface obtained with the image-based method. The colour red and green indicates, for each segment, the associated centre.

resulting from the intersection of each concentric sphere centred at a view position and the view frustum (FoV). As an illustrative example, Fig. 8.12(a) and 8.12(b) show wavefronts for two different views.

8.2.3.1 General Overview

The basic idea of the method is to parameterise a set of wavefronts, separated by a user-defined radius step r_s, at each view position. The intersections between these surfaces are analytically calculated and used to build a cell grid, analogously to the grid defined in the previous section. The intersection between the wavefronts yields patches which are contoured by circle arcs. The final composite surface is made of a succession of those patches. Section 8.2.3.2 describes how the circle arcs are found. Section 8.2.3.3 describes how spherical patches are built from circle arcs. Section 8.2.3.4 covers how the right patches are put together to build composite surfaces.

8.2.3.2 Computation of Surface Intersections

In addition to intersecting the wavefronts from different views, the intersection of the wavefronts with the segmentation of the structure of interest (cardiovascular structure) must be calculated. For clarity in the explanations, in this section the structure of interest is a laminar vessel represented by a cylinder.

Intersection between Wavefronts The intersection between two wavefronts, illustrated in Fig. 8.12, was calculated in two steps. For each pair of wavefronts from different views, first the circle between the two spheres in which the wavefronts

lie was calculated. The intersection solution is an arc from this circle which is within the boundary of the FoV of both views. Figure 8.12(c) represents the intersection arcs in thick black lines.

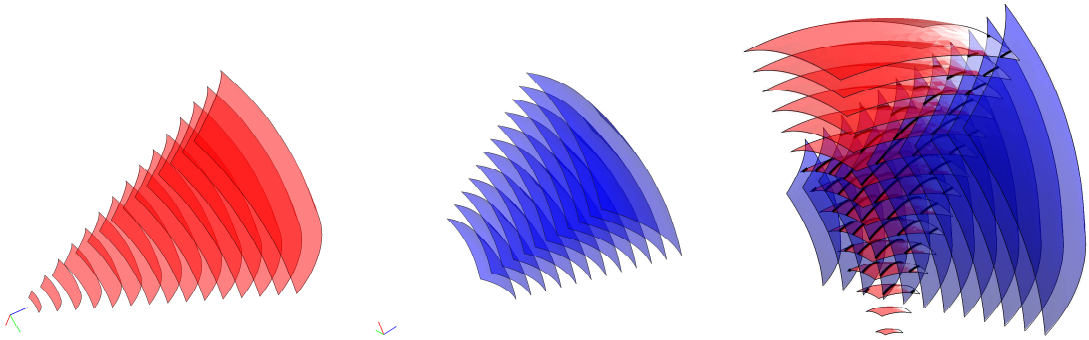

(a) Wavefronts view 1. (b) Wavefronts view 2. (c) Intersection between wavefronts.

Figure 8.12: Calculation of the intersection of wavefronts, illustrated with two views.

Intersection with Segmentation Segmentation of the structure of interest (a laminar vessel) was provided as a triangulated mesh, as shown in Fig. 8.13. The intersection of the wavefronts with a mesh is the combination of the intersection of each wavefront with each triangle of the segmentation mesh. For each triangle, the intersection between the triangle plane and the wavefront sphere yielded a circle. The intersection between the triangle and the wavefront was the arc of the circle which lies both within the triangle and the wavefront surface. Figure 8.13 shows the intersection of a segmented vessel (in green) with two sets of wavefronts from two different views. The intersection arcs are highlighted with thick black lines.

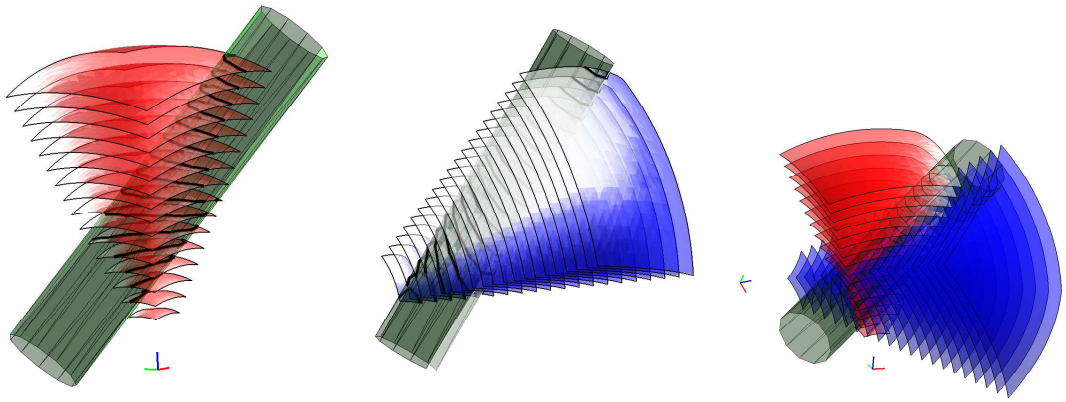

(a) Intersection of view 1 with vessel. (b) Intersection of view 2 with vessel. (c) Intersection of both views with vessel.

Figure 8.13: Calculation of the intersection of wavefronts with the segmentation of a vessel, illustrated with two views.

8.2.3.3 Patch Definition

The combination of all the intersections between all views involved and the segmentation of the structure of interest yields a set of circle arcs. Closed patches were built from the arcs in two steps:

1. **Create a connected graph** where edges are arcs and nodes are the points in which two or more arcs join (Fig. 8.14(a)). This was done by linking arcs with coincident endpoints.

2. **Patches were defined** as all closed loops which do not contain other closed loops inside. For example, Fig. 8.14(b) shows how one of the wavefronts is subdivided into 15 patches. Note how the patch 4 is not subdivided into two smaller patches because the edge inside is not connected to any node. The algorithm which was used to find all closed loops is further described in Appendix D.

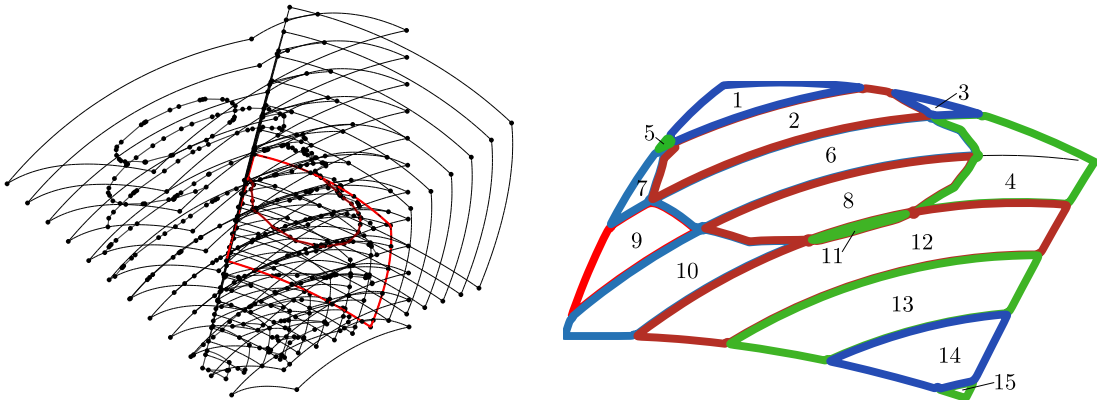

(a) Intersection graph. (b) Example of patches in a wavefront.

Figure 8.14: Generation of spherical patches. In this examples, patches are generated by two views and a segmentation mesh. (a) Graph representing the topology of the intersections between two views and a segmentation of a ventricle. (b) Example of patches in one of the wavefronts, highlighted in red in (a).

A set of closed patches results from the two steps above. Each patch is defined by an ordered succession of circle arcs that lay on a spherical surface.

8.2.3.4 Surface Definition

The patches that form the composite surface are selected in two steps:

1. Find all spherical patches that intersect a target Surface S (Fig. 8.15(a)).

2. From the patches which are inside the segmentation mesh, select the subset of connected patches which are closest to the target mesh S (Fig. 8.15(b)), in the sense of minimising a distance function d. The function d used in this chapter was the mean distance of 2500 regularly distributed points on the patch to the target surface. The distance of a point to a surface was defined as the shortest euclidean distance between the point and the surface.

The result is a composite surface made of spherical patches, labelled according to the view to which they belong (Fig. 8.15(b)).

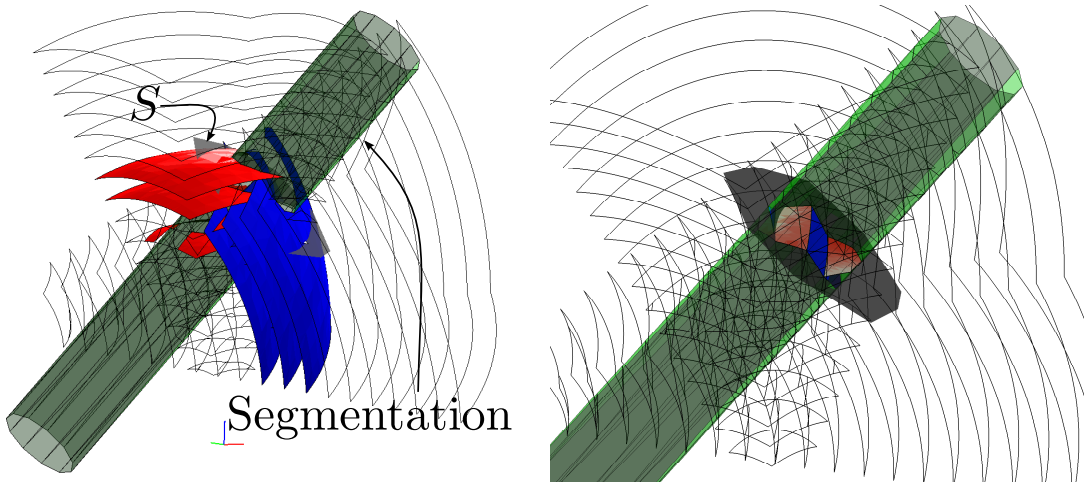

(a) (b)

Figure 8.15: Composite surface definition from spherical patches. (a) Patches that intersect the target mesh. (b) Final composite surface.

8.3 Velocity Integration over a Composite Spherical Surface

Sections 8.2.1, 8.2.2 and 8.2.3 have described 3 methods to produce composite spherical surfaces from multiple views. This surface can be provided as a labelled image (as in the two first approaches) or a set of surface patches (third approach). In either case, the composite surface is used to sample the input 3D colour Doppler images, and the velocity samples are then integrated to calculate flow rate. This section describes a method to calculate (8.1) using the composite surfaces and 3D colour Doppler images.

To calculate flow rate, the integral in (8.1) was calculated as a finite summation:

$$\tilde{\Phi}(S) = \sum_{s \in S} \|\mathbf{v}_s \cdot \hat{\mathbf{n}}_s\| \Delta s \tag{8.3}$$

where s is every sampling position in the surface S, v_s is the Doppler velocity at s (which can be calculated by interpolation of the colour Doppler image), n_s is the beam direction at s and Δs is the area of the surface of influence centre at s. Splitting (8.3) into K terms corresponding to the different views yields

$$\tilde{\Phi}(S) = \sum_{i=1}^{K} \sum_{s \in S_i} m_s \Delta s \tag{8.4}$$

where $\{S_i\}$ are the K contributions to the composite surface, each consisting of an ensemble of spherical patches centred at the ith view position , so that $\cup_i S_i = S$ and $\cap_i S_i = \emptyset$. Since for a given view the vector normal to the surface $\hat{\mathbf{n}}$ is coincident with the beam direction, $\|\mathbf{v}_s \cdot \hat{\mathbf{n}}_s\| = m_s$, where m_s is the Doppler velocity at each voxel in the 3D colour Doppler image.

The calculation of Δs is not trivial. In world coordinates, the surfaces are made of pieces of spheres, which might be irregularly shaped (e.g. the patches in Fig. 8.14(b)). Doing a regular sampling of these pieces (*i.e.* distributing sampling points homogeneously so that each point has the same area of influence) is a difficult problem on its own. The approach adopted in this chapter was simpler: each patch was transformed into frustum coordinates (a variation of usual spherical coordinates) which are the native coordinates of the acquisition system. In frustum coordinates, a spherical patch yields a flat surface orthogonal to the z axis. This surface was then regularly sampled, and the area of influence of each sample was just a square. The mapping between frustum and coordinates is as follows (Ji et al., 2011):

$$\begin{aligned} r &= \sqrt{x^2 + y^2 + z^2} & x &= r \sin\phi \cos\theta \\ \theta &= \tan^{-1}(y, z) & y &= r \sin\theta \cos\phi \\ \phi &= \tan^{-1}(x, z) & z &= r \cos\theta \cos\phi \end{aligned} \tag{8.5}$$

Note how coordinates defined in (8.5) are different to the usual spherical coordinates, since they are designed to sweep a frustum of the shape of a rectangular pyramid rather than a sphere. The surface area $\Delta s(r, \theta_s, \phi_s)$ of a voxel centred at frustum

coordinates (r, θ_s, ϕ_s) could then be calculated as follows:

$$\begin{aligned} dx/d\phi = r\cos\theta\cos\phi &\Rightarrow dx = r\cos\theta\cos\phi d\phi \\ dy/d\theta = r\cos\theta\cos\phi &\Rightarrow dy = r\cos\theta\cos\phi d\theta \\ ds = dx \times dy &= r^2\cos^2\theta\cos^2\phi d\theta d\phi \end{aligned} \tag{8.6}$$

$$\begin{aligned} \Delta s(r,\theta_s,\phi_s) &= \iint ds(\theta_s,\phi_s) = \int_{\theta=\theta_s-\frac{\Delta\theta}{2}}^{\theta_s+\frac{\Delta\theta}{2}} \int_{\phi=\phi_s-\frac{\Delta\phi}{2}}^{\phi_s+\frac{\Delta\phi}{2}} r^2\cos^2\theta\cos^2\phi d\theta d\phi \\ &= r^2\left(\frac{\sin(\Delta\phi+2\phi_s)+\Delta\phi+2\phi_s}{4}) + \frac{\sin(\Delta\phi-2\phi_s)+\Delta\phi-2\phi_s}{4})\right) \\ &\quad \left(\frac{\sin(\Delta\theta+2\theta_s)+\Delta\theta+2\theta_s}{4}) + \frac{\sin(\Delta\theta-2\theta_s)+\Delta\theta-2\theta_s}{4})\right) \end{aligned} \tag{8.7}$$

where $\Delta\theta$ and $\Delta\phi$ are the voxel spacing in θ and ϕ directions respectively. The final value of flow rate is calculated by using (8.4) at each cardiac phase.

8.4 Temporal Interleaving

A 3D echo Doppler sequence can be acquired in a few heart beats. However, the frame-rate is limited by depth and FoV and is generally not fast enough to analyse dynamic flow behaviour.

A method to increase the effective frame rate is to acquire several sequences i, from the same view, delaying the acquisition trigger by a short time Δt_i, and then to interleave these sequences. Instantaneous flow rate is computed frame by frame and then placed at its time location t within the output interleaved cardiac cycle.

During different acquisitions patient's heart rate may differ, which will affect correspondence between frames from different sequences. Sequences have to be compensated correct for such effects before interleaving the frames into a single sequence, *i.e.* the appropriate temporal position of each frame into a common normalised cycle needs to be calculated. A way to estimate the appropriate temporal location is the following. Let f_i be the frame rate and h_i the heart rate for sequence i. Let h_r be the heart rate of the output interleaved sequence. The normalised time position $t'_i(k)$ at which the frame k of the sequence i is located within the output interleaved sequence is:

$$t'_i(k) = \left(k\frac{1}{f_i} + \Delta t_i\right)\frac{h_i}{h_r}$$

A reasonable strategy is to set the output heart rate h_r the same as the heart rate of one of the input sequences, denoted *reference* (i.e. the other input sequences are temporally registered to the time frame of the reference sequence). The choice of the reference does not have a significant impact on the results, and in this thesis the sequence which had a heart rate closest to the average heart rate was chosen as reference.

8.5 Experiments

Flow rate and volume measurements were carried out on four HLHS patients, and compared to measurements obtained with 2D+t Flow MRI. For both modalities, image acquisition was triggered by the R wave of the electrocardiogram. Colour Doppler was acquired using a Philips iE33 with a X3-1 3D probe, which produced colour Doppler sequences with a spatial resolution of $0.7mm$ isotropic (scan converted) and a temporal resolution of 14 to 16 frames per second (fps). PC-MRI data was acquired on a Philips Achieva 1.5T, during free breathing using 3 averages to suppress breathing motion artefacts. Scan time was in the order of 1.5 minutes. 2D+t Flow MRI data had in-plane spatial resolution of $1.05mm$ isotropic, slice thickness $8mm$ and a temporal resolution of 40 phases per cardiac cycle. Data was automatically corrected for phase offsets due to eddy currents (Gatehouse et al., 2010).

Clinical parameters of interest for HLHS are typically tricuspid valve (TV) inflow and neoaortic outflow volumes. For the inflow, two apical views were acquired covering the full cross-section of the TV. For the outflow, full coverage was achieved with a single view. In all three views, 3 separate sequences were acquired with a trigger delay $\Delta t = 0, 20, 40\ ms$. Each Doppler image was acquired in 7 cardiac cycles. The full echocardiographic exam lasted less than 10 min.

Three experiments were carried out to compare the accuracy of the three proposed methods to each other and to the reference technique, 2D+t Flow MRI:

1. **Outflow**. Flow rate through the neo-aortic valve was calculated with 2D+t Flow MRI. Since one view was enough to have full coverage of the vessel cross section, no view combination was required, and flow rate was calculated by surface integration of temporally interleaved 3D colour Doppler images.

2. **Inflow: effect of view combination and interleaving**. Flow rate was calculated through the TV using the semi-automatic method (Sec. 8.2.1). Four measurements were carried out:

   (a) Flow computed using temporal interleaving only.

   (b) Flow computed using combined views but no temporal interleaving.

   (c) Flow computed by using combined views and temporal interleaving.

   (d) Flow computed from a single sequence, with no interleaving and a single view.

   In these experiments, the semi-automatic method to combine two views (Sec. 8.2.1) was used.

3. **Inflow: comparison of the three proposed methods**. The three methods to combine views proposed in this chapter were used to calculate flow rate through the TV.

Flow rate curves were calculated from 2D+t Flow MRI using manually segmented regions and from 3D Doppler data on the composite surfaces calculated as described above using (8.4). Stroke volumes were calculated by time-integral of the flow rate curves.

8.6 Results

Flow rate curves and SVs are reported in this section. When comparing two flow rate curves, one important point must be taken into account. Two curves of the same subject under the same cardiac conditions which are not calculated through the same surface might be different if the tissue boundaries are not rigid (Sec. 8.1.1). This is the case for measurements carried out with 2D+t Flow MRI and with the proposed method using 3D colour Doppler images. For this reason, SV should be taken as a more reliable indicator of accuracy, and only a few flow rate curves are shown for illustrative purposes.

8.6.1 Calculation of Outflow Volume

Figure 8.16 shows the calculated flow rate curves through the outflow tract for patient 1. The reference curve, calculated with 2D+t Flow MRI, is shown as a solid line with dark dots. Four more curves are shown: a dashed curve showing the flow rate estimated from three interleaved 3D colour Doppler sequences (dashed), and the flow rate curve estimated with each sequence separately (dotted).

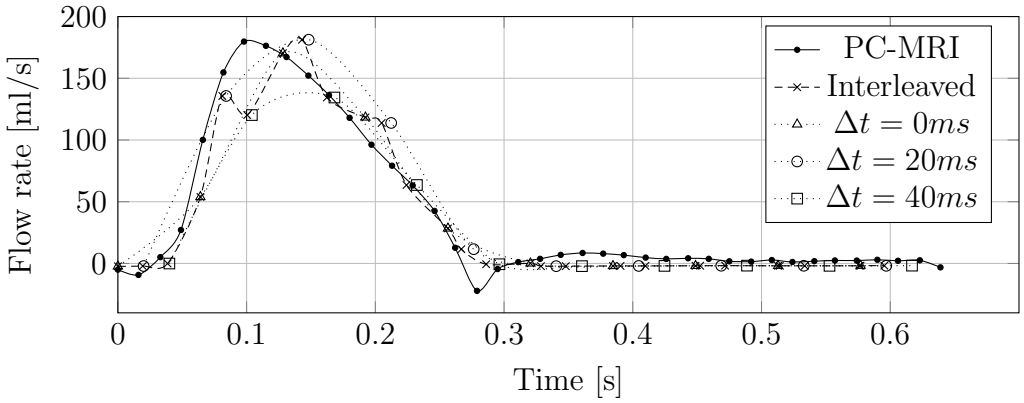

Figure 8.16: Effect of temporal interleaving on flow rate curves. Flow rate curves through the outflow tract for patient 1 are shown in three cases: 2D+t Flow MRI (reference), temporally interleaved 3D colour Doppler sequences, and three individually delayed 3D colour Doppler sequences.

The lack of temporal resolution in the individual sequences means that, depending on the delay, the resulting flow rate curve may, or may not, capture important features such as peaks and troughs of the curve. As a result, computation of SV can be unreliable if temporal resolution is low. Table 8.1 shows the SV through the neo-aortic valve in the four patients, calculated by time integral of flow rate curves. Since three 3D colour Doppler sequences (acquired with different trigger delays) were available for each patient, the calculation of volume without temporal interleaving was carried out separately with each of these images, and the corresponding column in table 8.1 shows the $mean \pm std$ volume.

The use of temporal interleaving reduces the variability of the measurement between a 5% and a 10%, as illustrated in Fig. 8.17. The bars show the relative mean absolute difference in volume compared to 2D+t Flow MRI, and the lines show the average (solid) and the bounds for the standard deviation (dashed) of the absolute difference over all patients. On average, the use of temporal interleaving decreases the disagreement in the estimation of SV compared to the measurement

	no temporal interleaving	temporally interleaved	2D+t Flow MRI
Patient 1	24.0 ± 4.0 ml	22.8 ml	25.3 ml
Patient 2	28.9 ± 1.6 ml	31.3 ml	30.6 ml
Patient 3	21.6 ± 0.3 ml	19.9 ml	18.4 ml
Patient 4	16.8 ± 3.7 ml	12.6 ml	14.7 ml

Table 8.1: Comparative results in outflow stroke volume from 4 patients with and without temporal interleaving.

with MR by around a 30%.

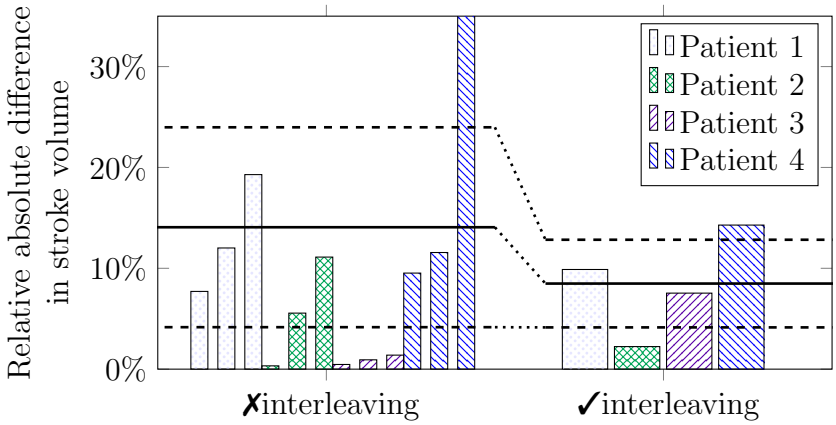

Figure 8.17: Relative dissimilarity in outflow volumes on four HLHS patients, compared to 2D+t Flow MRI. Volumes estimated from integrating flow rate curves. Two cases are covered: using our proposed method with temporal interleaving and using view combination but no temporal interleaving (shown on the left, each bar corresponding to an individual delayed 3D colour Doppler sequence). The black lines show the average (solid) and the bounds of the standard deviation (dashed) of the relative mean absolute difference between the two modalities over all patients.

8.6.2 Calculation of Inflow Volume

Figure 8.18 shows the calculated flow rate curves through the inflow tract for patient 1, classified in two groups. The first group of curves (Fig. 8.18(a)) shows the effect of temporal interleaving on the calculation of flow rate, showing similar results to Fig. 8.16. The second group of curves (Fig. 8.18(b)) shows the impact of view combination on the calculation of flow rate.

In this patient, individual views underestimate flow rate because they lack coverage of the enlarged TV. View combination allows to cover the whole cross section of the valve, and therefore shows an increase in flow rate which is reflected by an increase in calculated inflow SV. Table 8.2 shows the inflow stroke volume through

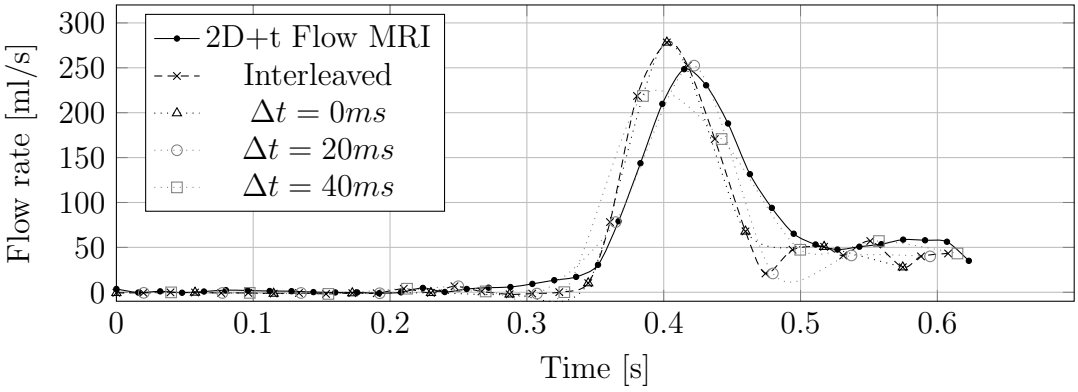

(a) Effect of temporal interleaving on flow rate curves through the inflow tract.

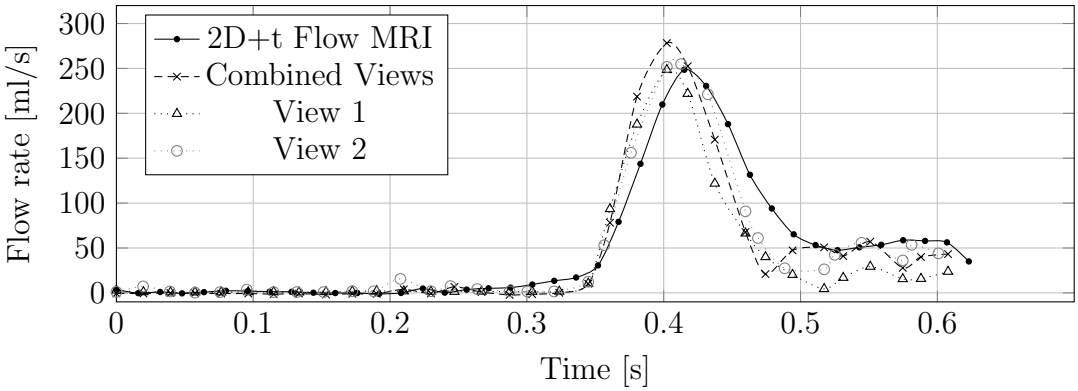

(b) Effect of view combination on flow rate curves through the inflow tract.

Figure 8.18: Flow rate curves comparing different view combination methods using data from patient 1. (a) Curves obtained with 2D+t Flow MRI, with interleaved 3D colour Doppler images, and with non-interleaved 3D colour Doppler images, all using view combination. (b) Curves obtained with 2D+t Flow MRI, with multiview 3D colour Doppler images and with single-view 3D colour Doppler images, all with temporal interleaving.

the TV in the four patients, calculated by time-integral of the flow rate curves calculated from 2D+t Flow MRI and from 3D colour Doppler images (four cases: all combinations of with / without temporal interleaving and with / without multiple views). For the first three columns, because only part of the data was used for each volume calculation, several measurements could be carried out and the table shows the $mean \pm std$ volume. For the fourth column (temporally interleaved and multiview) all data was used (all the delayed sequences and the multiple views) so only a single volume value could be computed.

In general, using temporal interleaving and view combination increases the accuracy of the measurement. The average absolute difference with respect to 2D+t Flow MRI is reduced from 27% to around 7%. This trend can also be seen in Fig.

temporally interleaved	✗	✓	✗	✓	2D+t Flow
Multiview	✗	✗	✓	✓	MRI
Patient 1	24.6 ± 3.8 ml	24.5 ± 4.0 ml	26.8 ± 3.6 ml	26.8 ml	29.6 ml
Patient 2	19.5 ± 2.2 ml	18.9 ± 0.2 ml	21.2 ± 3.7 ml	20.6 ml	21.9 ml
Patient 3	15.1 ± 3.9 ml	15.2 ± 1.8 ml	19.7 ± 4.2 ml	18.8 ml	20.2 ml
Patient 4	10.7 ± 4.0 ml	16.3 ± 0.2 ml	19.9 ± 1.2 ml	23.2 ml	22.3 ml

Table 8.2: Impact of temporal interleaving and view combination in inflow volume calculation from 4 HLHS patients.

8.19, which shows the relative mean absolute difference in stroke volume through the TV compared to 2D+t Flow MRI. Combination of two views increases coverage which yields flow values greater than when a single view is used and closer to the reference value. It should be noted that the variability of the measurement is highly reduced by combining both multiview and interleaving approaches.

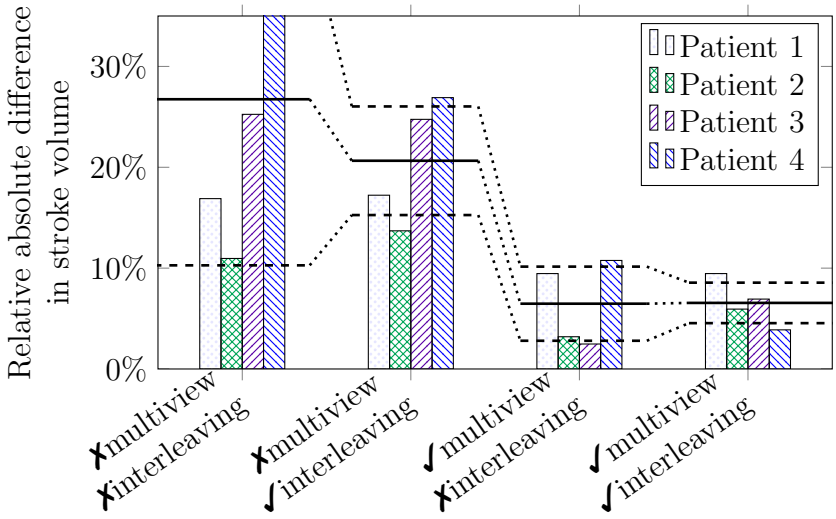

Figure 8.19: Relative absolute difference in inflow volumes on four HLHS patients, compared to 2D+t Flow MRI. Volumes were estimated from integrating flow rate curves. Four cases are covered: using our proposed method with temporal interleaving and view combination; using view combination but no temporal interleaving; using 1 view with temporal interleaving; and using 1 view and no temporal interleaving. The black lines show the average (solid) and the bounds of the standard deviation (dashed) of the absolute difference with flow MR over all patients.

8.6.3 Comparison of View Combination Methods

Figure 8.20 shows the flow rate curves obtained with 2D+t Flow MRI (the reference method) and with the three proposed view combination methods: semi-automatic

combination of two views ('Simple'), image-based method ('Image Based') and surface-based method ('Surface Based'). The curves represent the flow rate through the TV from patient 1. The 'Simple' and the 'Surface Based' methods yield similar flow rate curves close to the curve obtained with 2D+t Flow MRI. The 'Image Based' method produces a curve of similar shape than the other two but smaller flow rate magnitude, *i.e.* flow rate is underestimated mainly because of the ridge voxel effect described in Sec. 8.2.2.

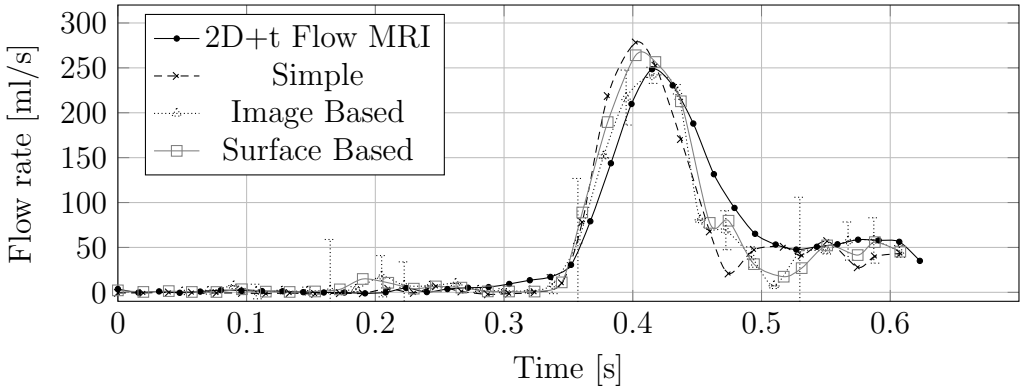

Figure 8.20: Flow rate curves comparing different view combination methods using data from patient 1.

Table 8.3 shows the stroke volume through the TV in the four patients, calculated from 3D colour Doppler images with three different view combination methods.

	Simple	Image Based	Surface Based	2D+t Flow MRI
Patient 1	26.8 ml	26.2 ml	28.2 ml	29.6 ml
Patient 2	20.6 ml	18.9 ml	23.7 ml	21.9 ml
Patient 3	18.8 ml	13.0 ml	19.0 ml	20.2 ml
Patient 4	23.2 ml	15.5 ml	20.8 ml	22.3 ml

Table 8.3: Comparative results in inflow stroke volume from 4 patients for different surface integration methods.

The relative absolute difference in volume with respect to 2D+t Flow MRI is shown in Fig. 8.21. The performance of the semi-automatic method (Sec. 8.2.1) and the surface based method (Sec. 8.2.3) show similar accuracy, with an average absolute difference below 10%. The multi-resolution image-based approach (Sec. 8.2.2) brings in relatively large errors which range from 10% to over 35%.

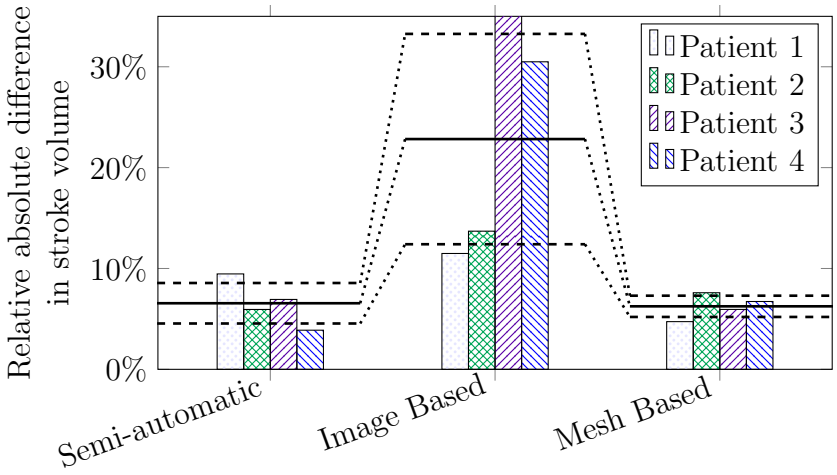

Figure 8.21: Comparison of three methods for multiview surface combination, described in sections 8.2.1, 8.2.2 and 8.2.3 . The bars show the relative absolute difference in inflow volume calculation with respect to 2D+t Flow MRI for 4 HLHS patients. The black lines show the average (solid) and the bounds of the standard deviation (dashed) of the relative absolute difference with flow MR over all patients.

8.7 Discussion

Accurate flow quantification is required to understand and diagnose many cardiac conditions. Currently, non-invasive flow measurements are carried out with 2D+t Flow MRI and with echo Doppler systems. Flow MRI provides accurate and reproducible flow measurements, however it requires anaesthesia in young children and is incompatible with metallic implants. In addition, MRI is expensive compared to echo and therefore accessibility to MRI systems is limited especially for control, follow-up and recurrent studies.

Echo systems enable blood flow quantification based on Doppler measurements. Flow rate and volume are typically measured using Spectral Pulsed-Wave Doppler (sPWD), assuming a velocity profile and a flow direction direction, which can yield to large inaccuracies (Hoskins, 2010). The introduction of 3D colour Doppler systems enabled angle independent flow measurements by integrating Doppler velocity over spherical surfaces which completely intersect the cross section of the target cardiovascular structure. This idea was first raised by Poulsen and Kim (1996b), but has not been exploited until very recently by only a few groups (Ge et al., 2005; Thavendiranathan et al., 2012). One of the reasons for the scarce use of such a promising technique is the lack of automation of the measurement and solid clinical validation. In addition, current 3D colour Doppler images have reduced frame rate

and FoV, and for that reason the method is not always accurate on patients with fast heart rate and when targeting large structures such as atrio-ventricular valves or abnormally enlarged hearts. This is the case in many adults and congenital patients.

This chapter has described a multiview approach for calculating flow rate and volume from 3D colour Doppler images. This technique uses temporally interleaved sequences to increase frame rate and multiple 3D colour Doppler views to increase coverage. Three methods to combine multiple views have been proposed and compared: a semi-automatic method to combine two views, an automatic image-based method and an automatic surface-based method.

The semi-automatic method and the surface-based method achieve a similar level of performance, with an average absolute difference with flow MR between 5% and 10%. The image based method shows a significantly poorer performance, with absolute differences in stroke volume up to over 35%. The main reason for these high errors is that the ridge between two patches is badly defined, as explained in Sec. 8.2.2.3, and a voxel at the border can belong to two patches. Calculation of the partial volume belonging to each patch is non-trivial, and if borders are long or if there are many patches then large errors will occur. A solution would be to attain finer resolution levels, however this would result in a corresponding increase in memory and computational resources required. Since this method does not have any significant advantage over the other two methods, the use of the multi-resolution image-based method is discouraged.

The surface based method has several advantages over the semi-automatic method. First, in the surface based method user interaction is limited to selecting the target surface and segmenting the valve. In the semi-automatic method, in addition to these two actions, the user must verify that the plane separating the two patches lies in the overlap of the two FoVs. Secondly, the semi-automatic method is limited to two patches separated by a circle arc, which reduces the potential coverage of composite surface. With the surface based method, the composite surface can have an arbitrary number of patches. And thirdly, the surface based method allows combination of an an arbitrary number of views, whereas the semi-automatic method is limited to two views.

A comparative summary of the three methods for view combination is shown in table 8.4. the semi-automatic method is mainly limited by only handling two views

and by requiring manual interaction to define the two spherical patches. In general many views can be acquired quickly, therefore the other two methods, which can make use of an arbitrary number of views are preferred. The image-based method shows the largest errors, as discussed before, and increasing image resolution to improve accuracy would exponentially increase memory and execution time. The best overall performance is given by the surface-based method, which achieves absolute differences below 10% compared to 2D+t Flow MRI. The most important limitation of the surface based method is that patch detection (*i.e.* detection of all closed loops in the circle intersection graph) is not scalable with the current implementation (described in appendix D). If the the distance between concentric wavefronts is reduced to increase the resolution of the resulting composite surface, the time to compute all closed loops grows exponentially. Developing an alternative loop search algorithm could solve the problem but is out of the scope of this thesis.

	Semi-automatic	Image based	Surface based
# views	2	arbitrary	arbitrary
Computational complexity	⋆⋆⋆	⋆⋆⋆⋆⋆	⋆⋆
Accuracy	5%- 10%	10%- 40%	5%- 10%
# patches	2	limited by memory	limited by graph depth
User interaction	Segmentation of vessel/valve and manual patch definition	Segmentation of vessel/valve	Segmentation of vessel/valve

Table 8.4: Comparison of the main features of the three methods for surface combination.

Overall, the results have shown that temporal interleaving can improve average accuracy in flow rate and SV calculation by a 30%. However, the more significant improvement is in the robustness in the measurement, which is reflected by the decrease of up to a third in the variability of the volume computation when using temporal interleaving. Robust and accurate flow measurements need high temporal resolution which standard 3D colour Doppler systems are not always able to provide. The results have also shown that combining multiple views can reduce the underestimation of flow rate and volume by increasing cross sectional coverage. Using temporal interleaving and view combination together provides the best results, decreasing mean absolute difference with flow MR in SV by a factor 4 from $27\% \pm 15\%$

to $6\% \pm 3\%$.

The velocity integration technique proposed in this chapter is not free from limitations. Artefacts in colour Doppler images, in particular velocity aliasing, can limit the applicability of the technique. In addition, accuracy of the result is dependent on the accuracy of the registration of multiple views. Variations in heart rate can introduce error due to temporal misalignment, and probably a more sophisticated temporal interleaving scheme, for example piecewise-alignment as proposed by Duchateau et al. (2011) would help reduce this error.

8.8 Conclusion

In this chapter, a technique for flow rate and volume calculation from multiple 3D colour Doppler views has been described. Three different methods for combining the multiple views have been presented and compared, from which the surface-based approach has shown best results, achieving an agreement with flow MR of 5% to 10% in stroke volume compared to 2D+t Flow MRI.

The advantages of view combination and temporal interleaving have been demonstrated on 4 HLHS patients, tripling the accuracy of state-of the art techniques based on surface integration which use none of the two improvements.

Chapter 9

Conclusion

" I have wrought my simple plan
if I give one hour of joy
to the boy who's half a man,
or the man who's half a boy. "

"The Lost World", Sir Arthur Conan Doyle (1912)

Contents

The main aim of this thesis was to investigate multiview approaches to recover full 3D flow and velocity information from multiple 3D colour Doppler images. This chapter summarises the main outcome of this investigation and its main limitations, puts into context the resulting novel contributions and hypothesizes on the future implications and further work that the contributions described in this thesis may lead to.

9.1 Summary and Context of the Contributions

The work carried out in this thesis contributes to knowledge with two main novelties:

1. **A new method for 3D blood velocity reconstruction (chapters 5, 6 and 7)**

   A new method has been proposed to recover a 3D blood velocity vector field from multiple 3D colour Doppler images. The method has been comprehensively tested on a simulation study, from which ranges of view angles, noise in Doppler images and registration accuracy have been established within which reconstruction is accurate. The results showed that if the angle between views is $> 20°$ and the noise in colour Doppler images is $< 10\%$ of the Doppler range, 3D velocity can be reconstructed with an accuracy of 15% compared to the gold standard for non-invasive flow measurements, 2D+t Flow MRI.

   The method has been tested on 3 healthy volunteers and three patients, which have confirmed the results from the simulation study. High quality 3D velocity reconstructions were achieved for one volunteer and all three patients, who had view angles and noise levels within the ranges specified in the simulation study. These successful reconstructions agreed well with flow MRI. Quantitatively, flow rate and volume were within a 15% error with respect to the measurements with 2D+t Flow MRI. Qualitatively, 3D flow patterns through the aortic valve in the volunteer and through the atrio-ventricular valve in two HLHS patients and one congenital patient with mitral stenosis were successfully reconstructed, showing plausible flow patterns similar to those predicted with computational models in similar patients.

   Using wall motion information, full intraventricular velocity mapping was achieved, showing similar velocity distribution than 3D+t Flow MRI and a plausible filling vortex during diastole on a patient with mitral stenosis.

   Placing the proposed 3D blood velocity reconstruction into context. Figure 9.1 relates the 3D velocity reconstruction method proposed in chapters 5, 6 and 7 (marked with a red cross) to the main past and current multidimensional velocity recovery methods using echo discussed in the literature review,

represented as circles where the diameter is approximately proportional to the amount of published material. As shown in Fig. 9.1(a), most of the methods have targeted 2D velocity reconstruction on a 2D plane, and the majority of them by using multiview approaches. Figure 9.1(b) shows that previous efforts have been mainly focused on reconstructing 2D velocities from laminar flows (simple vessels and phantoms). The approach proposed in this thesis is the first to target 3D velocity reconstruction of intracardiac flows from 3D Doppler data.

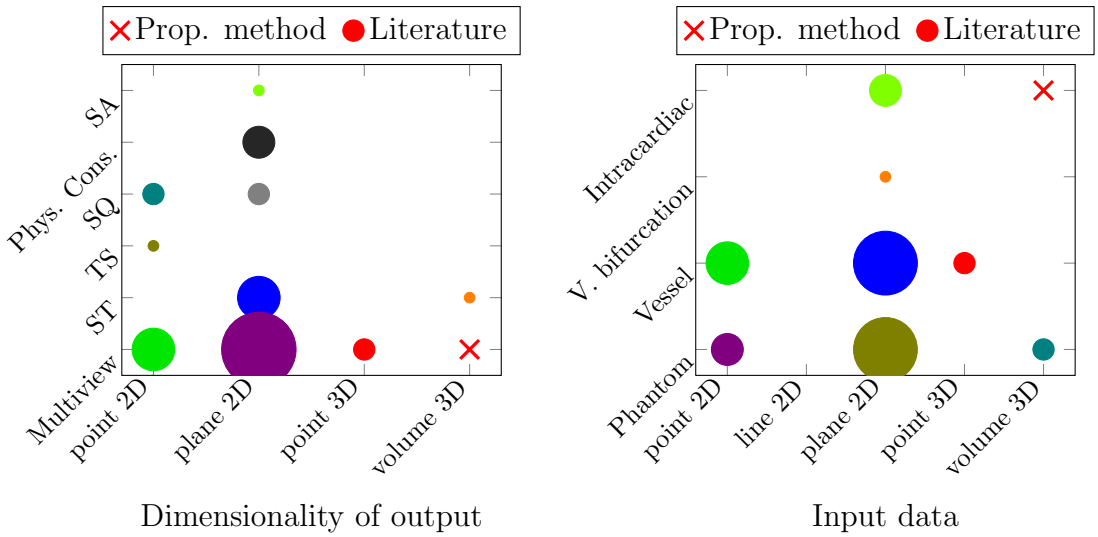

(a) Reconstruction methods and dimensionality of the output.

(b) Region of interest and dimensionality of the output.

Figure 9.1: Representation of the proposed 3D velocity reconstruction method into the context of state-of-the-art techniques. The solid circles represent work by other authors, and the radius of the circles is approximately proportional to the number of publications. The red cross represents the proposed method. Abbreviations: SA = synthetic aperture. SQ = spatial quadrature (≡ transversal oscillation). TS = time shift. ST = speckle tracking. The mapping between the colours in the figures and the corresponding publications is listed below:

(a)
- Daigle et al. (1975); Fox (1978).
- Farthing and Peronneau (1979); Ricci et al. (2009); Tortoli et al. (2006); Wei-qi and Lin-xin (1982)
- Bjaerum et al. (2002); Bohs et al. (1993); Marion et al. (2010); Trahey et al. (1987).
- Bonnefous (1988).
- Arigovindan et al. (2007); Capineri et al. (2002); Maniatis et al. (1994); Overbeck et al. (1992); Pastorelli et al. (2008); Phillips et al. (1995); Xu et al. (1991).
- Anderson (1997); Jensen and Munk (1998).
- Morsy and Von Ramm (1999).
- Nikolov and Jensen (2003).
- Hansen et al. (2009); Udesen and Jensen (2006).
- Garcia et al. (2010); Ohtsuki and Tanaka (2006); Tanaka et al. (2011)

(b)
- Daigle et al. (1975); Fox (1978).
- Farthing and Peronneau (1979); Ricci et al. (2009); Tortoli et al. (2006); Wei-qi and Lin-xin (1982).
- Bjaerum et al. (2002); Hansen et al. (2009); Nikolov and Jensen (2003); Overbeck et al. (1992); Pastorelli et al. (2008); Trahey et al. (1987).
- Bohs et al. (1993); Capineri et al. (2002); Maniatis et al. (1994); Marion et al. (2010); Phillips et al. (1995); Xu et al. (1991).
- Anderson (1997); Bonnefous (1988); Jensen and Munk (1998).
- Morsy and Von Ramm (1999); Niita and Shiina (1998).
- Arigovindan et al. (2007).
- Garcia et al. (2010); Ohtsuki and Tanaka (2006); Tanaka et al. (2011).

2. **A new method to calculate accurate, highly time resolved flow rate**

and volume (chapter 8)

A new multiview approach to angle-independent flow quantification with 3D temporally-interleaved colour Doppler images has been proposed. Three new methods have been proposed to combine multiple time-interleaved views (semi-automatic, image-based and surface-based), so that flow through cross sections larger than the individual FoV could be calculated.

From the three proposed methods, the semi-automatic method and the surface based method showed similar degree of accuracy, largely outperforming the image based method. The surface-based method was preferred to the semi-automatic method because it allows use of an arbitrary number of views (the semi-automatic can only combine two views) and requires less manual interaction.

The surface-based method, using two views and three temporally interleaved sequences achieved an average accuracy of 5% compared to 2D+t Flow MRI in stroke volume through the TV in four HLHS patients.

Placing proposed multiview flow quantification methods into context. Figure 9.2 shows the different techniques to calculate flow with echo Doppler systems proposed over the last 30 years, and the different Doppler technology used with each technique. Technical improvements in echo Doppler systems, in particular the increase in frame rate and the introduction of 2D phased-array transducers, favoured that researchers progressively turned from sPWD to first 2D then 3D colour Doppler systems to calculate flow and volume. The most popular techniques are those which do not depend in the angle of insonation, such as the Proximal Isovelocity Surface Area (PISA) method and integration over spherical surfaces. However, this idea was not really put into practice until 3D colour Doppler systems became more widely available, enabling the first studies with data from volunteers and patients. In this thesis, one step beyond has been taken; the surface integration method has been improved by using multiple views to enlarge the FoV which, as shown in chapter 8, can enable full coverage of large cross sections of the structure of interest (e.g. enlarged valves in CHD) and improves temporal resolution and accuracy

by interleaving time-delayed sequences acquired from multiple views.

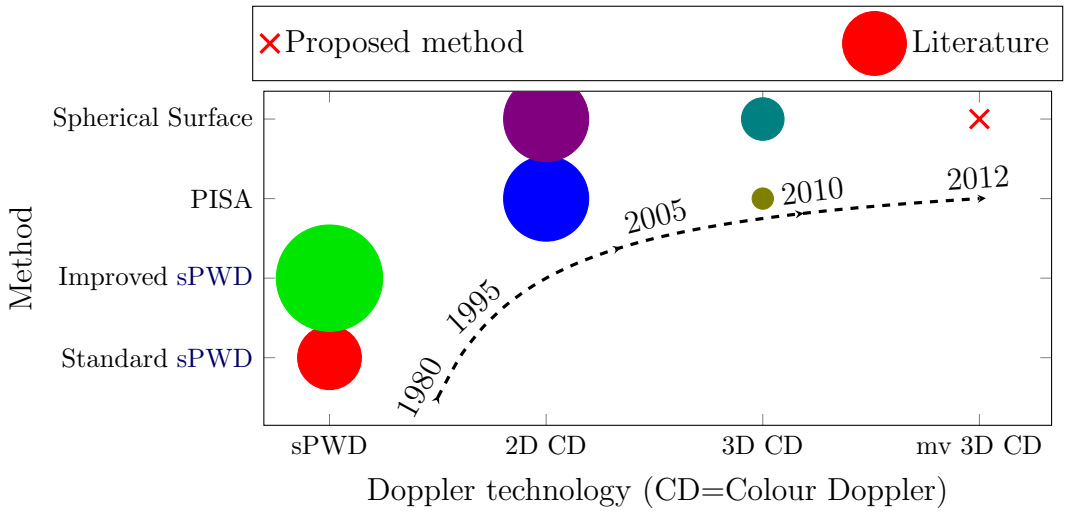

Figure 9.2: Representation of the proposed angle-independent flow quantification method into the context of state-of-the-art techniques. The solid circles represent work by other authors, and the radius of the circles is approximately proportional to the number of publications. The red cross represents the proposed method. The dashed line approximately indicates the time-line for the different publications. The mapping between the colours in the figures and the corresponding publications is listed below:
- Forsberg et al. (1995); Gill (1979); Struyk et al. (1985).
- Embree and O'Brien (1990); Evans et al. (1989b); Foster and Smith (1990); Hottinger and Meindl (1975, 1979).
- Enriquez-Sarano et al. (1995); Hung et al. (1999); Rodriguez et al. (1993); Utsunomiya et al. (1991).
- Goncalves et al. (2011).
- Gibson et al. (1994); Li et al. (2001); Mori et al. (2002); Poulsen and Kim (1996b).
- Ge et al. (2005); Thavendiranathan et al. (2012).

9.2 Clinical Impact

The technical work presented in this thesis has been tested in a small group of patients showing feasibility and very promising results which need to be confirmed in a larger set of patients.

In a recently published guideline report from the American Society of Echocardiography (Lang et al., 2012), clinical uses and potential of 3D echocardiography were analysed. 3D echo was recommended for clinical practice for calculation of left ventricle volume and ejection fraction (EF), mitral valve anatomy and stenosis and guidance of transcatheter procedures. In that report, potential applications of the techniques proposed in this thesis are considered unstudied or within active research (e.g. assessment of the TV and the pulmonary valve (PV), regurgitation in aortic valve (AV), regurgitation of MV).

The acquisition protocol for all methods proposed in this thesis lasted less than 10 minutes in all patients. This means that it could be added to existing clinical protocols at a minimum cost. In addition, for most cardiac patients an echo exam is the first imaging procedure. The developed methods have the potential to aid in the diagnosis and eligibility of the patient for further exams after the first visit to the clinic. This may favour exciting clinical improvements such as earlier diagnosis, better understanding of the cardiac condition (since the reduction in exam time may allow for complementary exams that are otherwise not possible) and cost reduction, since the patient is selected for the right examination and treatment earlier.

9.3 Limitations of the Investigation

A main limitation of the investigations conducted in this thesis is the small number validation datasets used, both from adult volunteers and paediatric patients. Validation using adult volunteer data was discontinued after it was found out that this group of subjects often provided data where quality of 3D colour Doppler images and angle between views were sub-optimal, preventing a reliable assessment of the performance of the different methods proposed in chapters 5, 6, 7 and 8 using volunteer data.

More extensive validation of the algorithms in this thesis was carried out using data from 7 patients (4 datasets used for flow quantification and 3 used for velocity reconstruction). Although availability of patients was relatively high, difficulty of access to Doppler data limited the number of patient datasets that could be precessed within a reasonable time. For that reason, the scope of the thesis is focused on showing feasibility of the proposed methods, and further work will be carried out to validate them clinically.

Some related work (Arigovindan et al., 2007; Garcia et al., 2010; Xu et al., 1991) has used phantoms to validate their work. Phantom studies allow to measure the performance of the method in controlled situations, with ability to vary many parameters at will and carry out a comprehensive analysis of the impact of these parameters on accuracy. However, the difficulty to produce phantoms which reflect the reality of complex flow patterns, cardiac geometry, cardiac wall motion, etc. and the emphasis on translation of this thesis, together with the available amount

of time and resources, favoured the decision to test the developed methods on real patients rather than using phantoms. During this thesis, technical work has been carried out in close collaboration with clinicians to garner knowledge of potential clinical use.

Further work should include a comparison with related methods reviewed in this thesis and, in particular, assessment of the clinical benefit of 3D velocity fields over 2D. For that purpose, 3D velocity fields could be reformatted into arbitrary 2D planes, to be compared directly with 2D velocity obtained using other methods for example those proposed by Arigovindan et al. (2007); Garcia et al. (2010); Xu et al. (1991).

9.4 Future Work

This section describe five research lines which could be a continuation to the presented work.

1. **Clinical validation**

   In order to assess the accuracy, reproducibility and repeatability of the proposed methods, a study on a larger group of patients is needed. In addition, clinical translation of the developed methods would require direct access to raw Doppler data (instead of the current indirect access described in appendix C). Obtaining this access involves the establishment of a research agreement with the manufacturer of the echo system.

2. **4D velocity reconstruction**

   The method for 3D velocity reconstruction proposed in chapter 5 works frame-wise, *i.e.* reconstructs velocity for each time frame independently. This requires that every view is temporally aligned and interpolated to the same temporal grid, and does not impose any consistency on the reconstructed velocity field over time.

   The method could be extended to 4D, using a 4D B-spline grid which would take input data scattered over time. Moreover, a regularisation term dependent on time could be included for temporal consistency (e.g. conservation of mass) similarly to the term penalising divergence.

3. **Incorporating computational modelling techniques into 3D velocity reconstruction**

   In a related field, computational models are capable of predicting intracardiac flow from morphology, cardiac mechanics and boundary conditions (Nordsletten et al., 2010) with no intracardiac flow information (apart from an estimated value for pressure and other parameters such as viscosity and blood density). The introduction of physical constraints into crossed-beam approaches (e.g. penalisation of flow divergence) and incorporation of heart mechanics (e.g. ventricle wall motion information) that have been presented in this thesis could be the first steps towards an intermediate stage between image-based methods and model based method; enabling the recovery of 3D velocities by making best combined use of available data and prior knowledge.

4. **Improved image registration with probe tracking**

   All methods proposed in this thesis use multiple echo Doppler views. In order to spatially align the multiple views, a two-step image registration process has been proposed (sec. 5.2). This process has two disadvantages: first additional standard B-Mode images need to be acquired. Second, there are two registrations for each image, therefore two potential sources of error.

   An improvement over this technique would be to track the probe position at each acquisition (e.g. with an electromagnetic tracker), which would provide a reasonable initialisation for the registration. As a result, automation would be increased, registration error reduced and fewer additional B-Mode images would be needed.

5. **Flow calculation through curved surfaces**

   One current limitation of the flow quantification method proposed in chapter 8 is aliasing of velocities over the Doppler range, which leads to inaccurate flow rates and volumes, and is particularly important in diseased hearts which have stenotic or leaking valves. Dealiasing techniques like the method proposed by Muth et al. (2011) or the semi-automatic method briefly described in chapter 6 can correct for first or second order aliasing, but are likely to fail for higher orders. Aliasing of third, fourth or higher orders are common for regurgitant

jets through the cardiac valves, where calculating flow rate and volume is particularly important.

The image-based method and the surface-based method approximate a user-defined surface with a composite spherical surface combining an arbitrary number of views. The user-surfaces used in this thesis were planes, but the algorithm does not impose any restriction in the shape of the surface. If the user was capable of defining a curved surface contouring the aliased region, flow rate could be calculated without being affected by aliasing. This would probably require developing a new user interface allowing the definition of such surfaces.

9.5 Overall Summary

This thesis has described the conception, development and application of two novel methods for full 3D velocity and flow quantification. The first method provides the means to recover a 3D blood velocity field from multiple 3D colour Doppler images, and has been applied to the recovery of intraventricular flow on three volunteers and three paediatric patients with an accuracy of less than 15% compared to 2D+t Flow MRI. The second method introduces a multiview approach to calcuate accurate, time resolved flow rate and volume through spherical composite surfaces, and has been applied to calculate transvalvular flow in HLHS patients achieving an accuracy of less than 5% compared to 2D+t Flow MRI.

I believe that involvement of system manufacturers and improvements on echo systems will allow clinical translation of the developed techniques, and that in the future echo systems will benefit from the developed methods, or of improved versions of them, to carry out quantitative flow imaging from echo in the clinic. Multiview echo approaches have recently shown great potential for enriched anatomical images and, as shown in this thesis, for quantitative flow analysis. Therefore it would not be surprising that new echo systems had multi-view features such as simultaneous acquisition from multiple transducers and probe tracking. That would be a suitable scenario to bring the techniques developed in this thesis to an accurate, real time system which would open a whole new world of clinical possibilities.

Appendices

Appendix A

Autocorrelation Techniques for Velocity Estimation

When a ultrasound signal is reflected by a moving scatterer, the frequency of the sent wave is shifted as a consequence of the Doppler effect. In a typical Colour Doppler system, the mean frequency can be computed using the Fast Fourier Transform (FFT) (as in Pulsed Wave Doppler (PWD) systems) or the so-called autocorerlation techniques. In colour Doppler images, where many frequency calculations (one per sample) have to be done very rapidly, the average frequency shift is computed by using an autocorrelator which is described in this appendix.

The goal is to estimate the mean velocity, as well as the power and the bandwidth (*i.e.* variance) of the Doppler signal, *i.e.* the mixed signal whose average frequency is proportional to the velocity of the scatterers.

A.1 Introduction

Let $p(t)$ be a received Doppler signal, such that $p(t) = Re\{\bar{p}(t)\}$ where $\bar{p}(t)$ is the complex envelope described in (3.4). Let $P(\omega)$ be the spectrum of $\bar{p}(t)$:

$$P(\omega) = \int_{-\infty}^{\infty} \bar{p}(t) e^{-j\omega t}\, dt \tag{A.1}$$

and reciprocally,

$$\bar{p}(t) = \frac{1}{2\pi} \int_{-\infty}^{\infty} P(\omega) e^{j\omega t}\, d\omega \tag{A.2}$$

The power spectral density of p is a real signal representing the distribution of power over frequency as shown in Fig. A.1, and is defined by

$$S(\omega) = \|P(\omega)\|^2 = P(\omega)P^{\star}(\omega) \tag{A.3}$$

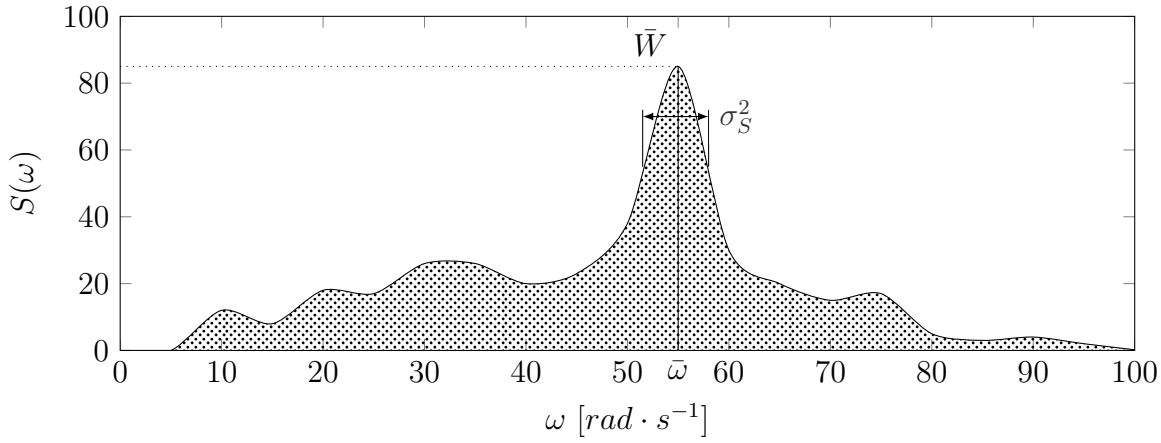

Figure A.1: Example of Spectral Power Density curve of a ficticious Doppler signal, and the parameters that are calculated with autocorrelation techniques.

Figure A.1 shows, as is the general case, that the received echo is formed by the contributions of a number of scatterers within a resolution cell, which may not have exactly the same velocity and direction, and therefore the resulting Doppler signal has a power distributed over a broad spectrum. Autocorrelation techniques enable the calculation of three velocity parameters to characterize this distribution: the mean frequency $\bar{\omega}$ (proportional to the mean velocity), the total power of the signal $\bar{W}$ (which is related to the amount of flow) and the variance of the distribution σ_S^2 (which is related to the number of different velocities measured within the resolution cell). These three parameters can be calculated for the frequency and then related to velocity through (3.18).

A.2 Total Power

The autocorrelation of a signal $\bar{p}$ is

$$p_{xx}(\tau) = \int_{-\infty}^{\infty} \bar{p}(t)\bar{p}(t+\tau)\ dt \tag{A.4}$$

If (A.2) is replaced into the expression above (A.4)

$$\begin{aligned} p_{xx}(\tau) &= \int_{-\infty}^{\infty} \bar{p}(t)\bar{p}^*(t+\tau)\ dt \\ &= \int_{-\infty}^{\infty} \left[\tfrac{1}{2\pi}\int_{-\infty}^{\infty} P(\omega)e^{j\omega t}\ d\omega\right]\left[\tfrac{1}{2\pi}\int_{-\infty}^{\infty} P^\star(\omega')e^{-j\omega'(t+\tau)}\ d\omega'\right]\ dt \\ &= \tfrac{1}{4\pi^2}\int_{-\infty}^{\infty}\int_{-\infty}^{\infty}\int_{-\infty}^{\infty} P(\omega)P^\star(\omega')e^{-j(\omega'-\omega)t}e^{-j\omega'\tau}\ dt\ d\omega\ d\omega' \\ &= \tfrac{1}{4\pi^2}\int_{-\infty}^{\infty}\int_{-\infty}^{\infty} P(\omega)P^\star(\omega')2\pi\delta(\omega'-\omega)e^{-j\omega'\tau}\ d\omega\ d\omega' \\ &= \tfrac{1}{2\pi}\int_{-\infty}^{\infty}\int_{-\infty}^{\infty} P(\omega)\delta(\omega-\omega')\ d\omega P^\star(\omega')e^{-j\omega'\tau}\ d\omega' \\ &= \tfrac{1}{2\pi}\int_{-\infty}^{\infty} P(\omega')P^\star(\omega')e^{-j\omega'\tau}\ d\omega' \\ &= \tfrac{1}{2\pi}\int_{-\infty}^{\infty}\|P(\omega)\|^2 e^{-j\omega\tau}\ d\omega = \tfrac{1}{2\pi}\int_{-\infty}^{\infty} S(\omega)e^{-j\omega\tau}\ d\omega \end{aligned} \tag{A.5}$$

which is known as the Wiener-Khinchin theorem. The total power can be calculated from $S(\omega)$ as the area under the curve

$$\bar{W} = \int_{-\infty}^{\infty} S(\omega)\ d\omega \tag{A.6}$$

which can be calculated from the autocorrelation (A.5) as

$$\bar{W} = 2\pi p_{xx}(0) \tag{A.7}$$

A.3 Mean Frequency

The first-order derivative of the autocorrelation can be calculated from (A.5) as

$$\begin{aligned} \dot{p}_{xx}(\tau) &= \tfrac{\partial}{\partial\tau}\tfrac{1}{2\pi}\int_{-\infty}^{\infty} S(\omega)e^{-j\omega\tau}\ d\omega \\ &= \tfrac{-j}{2\pi}\int_{-\infty}^{\infty} \omega S(\omega)e^{-j\omega\tau}\ d\omega \end{aligned} \tag{A.8}$$

The mean frequency is defined by

$$\bar{\omega} = \frac{\int_{-\infty}^{\infty} \omega S(\omega)\ d\omega}{\int_{-\infty}^{\infty} S(\omega)\ d\omega} \tag{A.9}$$

which can be computed from the autocorrelation and its first-order derivative as

$$\bar{\omega} = -j\frac{\dot{p}_{xx}(0)}{p_{xx}(0)} \tag{A.10}$$

A.4 Frequency Variance

The width of the peak in Fig. A.1 indicates the presence or not of different velocity magnitudes and directions within the resolution cell, which may be an indicator of turbulence in the flow (Kasai et al., 1985). The width of the peak is proportional to the variance σ_S^2 of $S(f)$. To calculate the variance, the second-order derivative of the autocorrelation is needed:

$$\begin{aligned} \ddot{p}_{xx}(\tau) &= \frac{\partial^2}{\partial\tau^2}\frac{1}{2\pi}\int_{-\infty}^{\infty} S(\omega)e^{-j\omega\tau}\, d\omega \\ &= \frac{-1}{2\pi}\int_{-\infty}^{\infty} \omega^2 S(\omega)e^{-j\omega\tau}\, d\omega \end{aligned} \tag{A.11}$$

The variance of the power Doppler spectrum is

$$\sigma_S^2 = \frac{\int_{-\infty}^{\infty}(\omega-\bar{\omega})^2 S(\omega)\, d\omega}{\int_{-\infty}^{\infty} S(\omega)\, d\omega} = \overline{\omega^2} - \bar{\omega}^2 \tag{A.12}$$

which can be computed from the autocorrelation and its first and second-order derivatives as

$$\sigma_S^2 = \left(\frac{\dot{p}_{xx}(0)}{p_{xx}(0)}\right)^2 - \frac{\dot{p}_{xx}(0)}{p_{xx}(0)} \tag{A.13}$$

A.5 Resolving the Velocity Direction

The measured mean frequency is an absolute value, always positive, and therefore does not distinguish whether the velocity direction is towards or away from the transducer. There are several methods to resolve this ambiguity, but the most widespread is quadrature phase detection. This method consists of demodulating two Doppler signals by mixing the received signal with two sinusoidal waves of the transmit frequency ω_0 dephased 90° (*i.e.* $\cos(\omega_0)$ and $\sin(\omega_0)$). A positive or negative shift between phase of the demodulated quadrature signal and the demodulated in-phase signal represents motion away from or towards the probe. Further details on this method and on alternative techniques can be found in (Evans and McDicken, 2000).

Appendix B

Overview of B-splines

Polynomial splines are smooth, parametrised piece-wise functions. In particular, splines are smooth at the value of the parameter where two pieces are connected, called a *knot*. B-splines are a type of polynomial function which is widely used to generate spline curves. This appendix describes the basics of B-splines, including their definition and main properties.

One of the main motivations for splines is to approximate a set of connected points by a smooth curve. One of the first approaches to address this problem were Bézier curves, popularised by Pierre Bézier based in the ideas of Casteljau (Farin, 2002), which are at the origin of B-splines.

B.1 Bézier curves

Bézier curves are polynomial curves (Floater, 2007) which approximate a set of ordered control points C_i, and are anchored to the first and the last point. If there are $n+1$ control points, the resulting Bézier curve is a polynomial of degree n. A Bézier curve of degree $n = 2$, $f_2(t)$, can be mathematically defined as follows:

$$\begin{aligned} f_{0,0}(t) &= (1-t)C_1 + tC_2 \\ f_{0,1}(t) &= (1-t)C_2 + tC_3 \\ f_2(t) &= (1-t)c_{0,0} + tc_{0,0} \end{aligned} \tag{B.1}$$

The resulting curve is represented in Fig. B.1 (a).

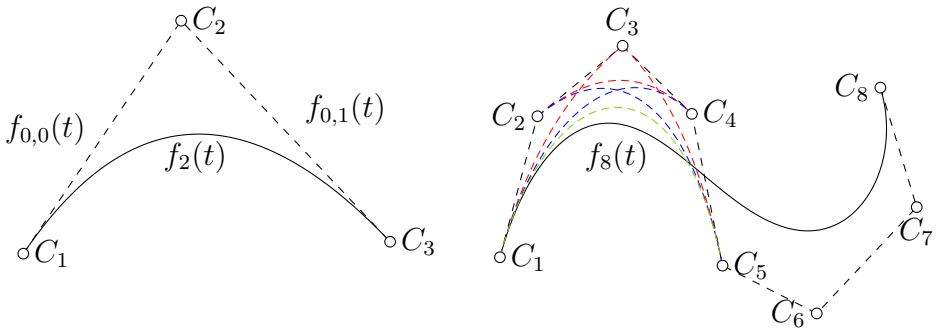

(a) Quadratic Bézier curve. (b) Bézier curve of degree 7

Figure B.1: Bézier curves. (a) Quadratic Bézier curve. (b) Bézier curve of degree 7. Some steps of the recursive process have been depicted with dashed lines: $f_{0,x}$ in black, $f_{1,x}$ in red, $f_{2,x}$ in blue, and $f_{3,x}$ in green.

The recursive formulation in (B.1) can be linearly expanded:

$$f_2(t) = (1-t)^2 C_1 + (1-t)tC_2 + t(1-t)C_2 + t^2 C_3 \tag{B.2}$$

This can be further extended to a polynomial of degree n, which can then be written as a linear representation on some basis

$$f_n(t) = \sum_i C_i b_{i-1,n} \tag{B.3}$$

where $b_{i,n}$ are the Bernstein basis of degree n:

$$b_{i,n} = \begin{pmatrix} n \\ i \end{pmatrix} t^i (1-t)^{n-i}, \qquad i = 0 \dots n \tag{B.4}$$

Figure B.1 (b) shows an example of a Bézier curve of degree $n = 7$, with 8 control points.

B.2 Splines and B-splines

The main problem of Bézier curves is that the degree of the polynomial increases with the number of data points, which may be arbitrarily large, making the computation of the curve too expensive for many practical applications.

A solution is to build a piece-wise function where the pieces are Bézier curves of

a lower degree (typically 2 or 3). To achieve smoothness in the joint between pieces (*i.e.* knots), one must assure at least that the first derivative is continuous (*i.e.* C^1 continuity). In a Bézier curve, the derivative at the ends (*i.e.* the slope of the curve at the endpoints) is parallel to the vector joining the two exteriormost control points (e.g. in Fig. B.1 (a) the tangent at C_3 is parallel to C_2C_3). Therefore, smoothness at knots can be achieved if every piece shares the two end points with the next one. For example, to build a Bézier spline of degree 2, the first ith piece $h_{n,i}$ is built with the control points $\{C_i, C_{i+1}, C_{i+2}\}$, the second one with $\{C_{i+1}, C_{i+2}, C_{i+3}\}$, and so on. Overlapping is managed by introducing an extra knot so that knot positions are not coincident with the value of the parameter t corresponding to control points, as shown in Figure B.2 (a).

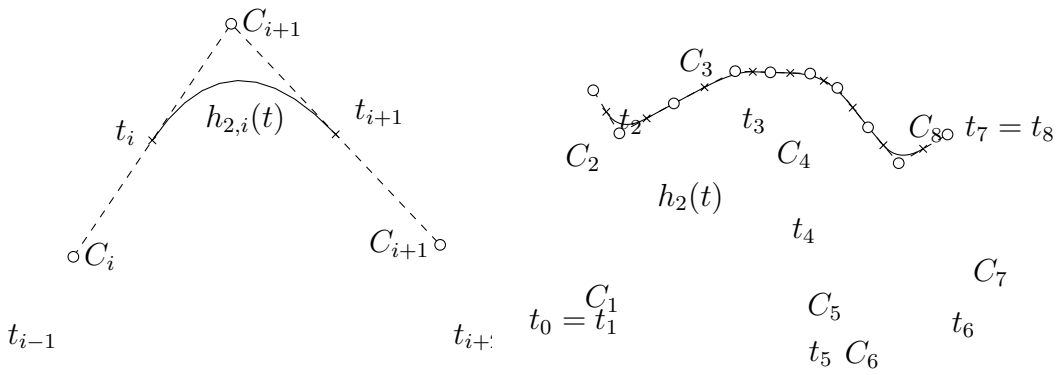

(a) Bézier spline (b) Quadratic Bézier spline.

Figure B.2: Bézier splines. (a) Bézier spline of degree 2. This spline piece is constructed by using 3 control points $\{C_i\}$ and 4 knots $\{t_j\}$. the final result is restricted to the parameter interval $[t_i, t_{i+1}]$ and therefore the next piece does not overlap. (b) Bézier spline curve of degree 2 with 8 control points. The two first and two last knots are made equal so that the curve is anchored in the ending control points.

Figure B.2 (b) shows the resulting quadratic Bézier spline with 8 nodes. the parameter at the first and last node is set $t_0 = t_1$ and $t_7 = t_8$ so that the curve $h_2(t)$ starts and finishes exactly at the end control points. Mathematically, the piece-wise Bézier spline is an extension of the Bézier curve by adding one knot:

$$h_2(t) = \begin{cases} \vdots & \vdots \\ h_{2,i+1}(t) = \frac{t_{i+2}-t}{t_{i+2}-t_{i+1}} h_{1,i+1}(t) + \frac{t-t_{i+1}}{t_{i+2}-t_{i+1}} h_{1,i+2}(t) & if \quad t \in [t_{i+1}, t_{i+2}) \\ \vdots & \vdots \end{cases} \tag{B.5}$$

where

$$h_{1,i}(t) = \frac{t_i - t}{t_i - t_{i-1}} C_i + \frac{t - t_{i-1}}{t_i - t_{i-1}} C_{i+1} \tag{B.6}$$

If (B.5) is recursively developed until $h_n(t)$ is expressed as a function of the control points C_i, which results in the B-spline expansion of $h_n(t)$:

$$h_n(t) = \sum_i C_i \beta^n (t - t_i) \tag{B.7}$$

where $\beta^n(t)$ is the B-spline of degree n, which is a piece-wise polynomial and is mathematically described by the recursive expression

$$\beta^n(t) = \frac{t - t_i}{t_{i+n} - t_i} \beta_i^{n-1}(t - t_i) + \frac{t_{i+1+n} - t}{t_{i+1+n} - t_{i+1}} \beta^{n-1}(t - t_{i+1}) \tag{B.8}$$

Figure B.3 show examples of B-spline for different degrees.

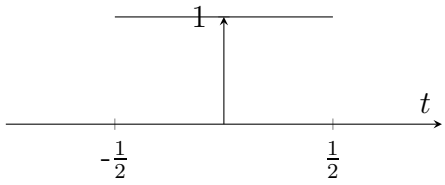

$$\beta^0(t) = \begin{cases} 1 & if \quad -\frac{1}{2} < t < \frac{1}{2} \\ 0 & otherwise \end{cases}$$

(a) B-spline degree 0

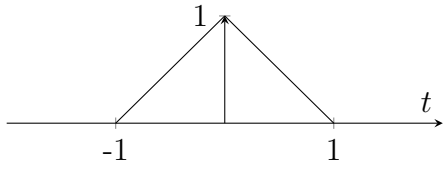

$$\beta^1(t) = \begin{cases} 1 - t & if \quad -\frac{1}{2} < t \leq 0 \\ t & if \quad 0 < t < \frac{1}{2} \\ 0 & otherwise \end{cases}$$

(a) B-spline degree 1

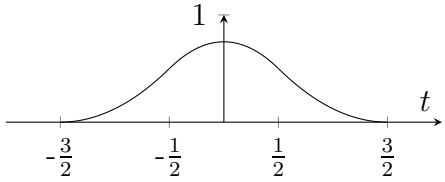

$$\beta^2(t) = \begin{cases} \frac{(t-1)^2}{2} & if \quad -\frac{3}{2} < t \leq -\frac{1}{2} \\ -\frac{2t^2-2t-1}{2} & if \quad -\frac{1}{2} < t \leq \frac{1}{2} \\ \frac{t^2}{2} & if \quad \frac{1}{2} < t < \frac{3}{2} \\ 0 & otherwise \end{cases}$$

(c) B-spline degree 2

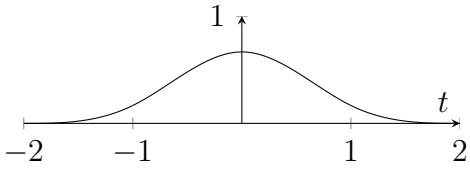

$$\beta^3(t) = \begin{cases} (1-t)^3 & if \quad -2 < t \leq -1 \\ 3t(1-t)^2 & if \quad -1 < t \leq 0 \\ 3t^2(1-t) & if \quad 0 < t \leq 1 \\ t^3 & if \quad 1 < t < 2 \\ 0 & otherwise \end{cases}$$

(d) B-spline degree 3

Figure B.3: B-Spline basis functions.

B.3 B-Spline Approximation

B-splines are extensively used in signal and image processing for many applications. Main uses of B-splines are curve approximation, smoothing, data fitting and interpolation (Unser, 1999).

The main use of B-splines in this thesis is data interpolation over regular B-spline grids. Data interpolation consists of calculating a value for data at a point where data is not available, by using data values of neighbouring data points. B-Spline interpolation on regular grids means that distance between input data is constant. The value at any position P is then calculated as the value of the neighbours weighted by the B-Spline centred at the neighbours. Figure B.4 shows an example of this approach using B-Splines of degree 1 and 3.

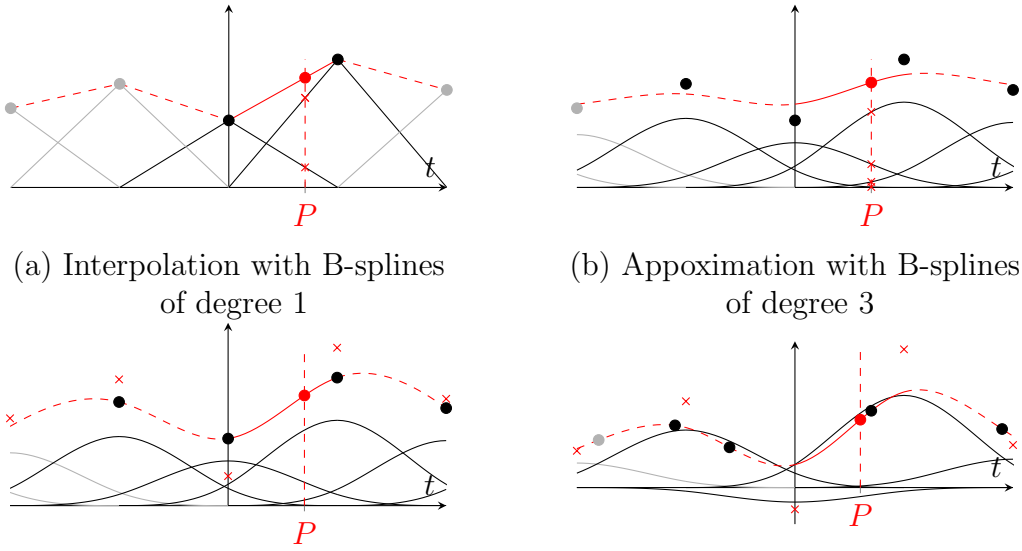

(a) Interpolation with B-splines of degree 1

(b) Appoximation with B-splines of degree 3

(c) Interpolation with B-splines of degree 3

(d) Fitting with B-splines of degree 3

Figure B.4: B-spline approximation and interpolation. (a) B-spline interpolation with B-splines of degree 1, which is equivalent to linear interpolation. (b) Data interpolation by weighting B-splines of degree 3 with input data The resulting curve smooths the input data but does not, in general, pass through the input points. (c) B-spline interpolation, where the interpolated curve passes through the input points. The red crosses represent the interpolation weight for each B-spline. (d) B-spline Fitting of scattered input data points. Depending on the points distribution and the distance between grid nodes, the resulting curve will pass through the points or only close to them.

B.4 B-Spline Interpolation

Using B-splines to weight input data points produces a curve which does not pass through input data points (apart from the anchor points), except in the case of $n = 1$ when this weighting is equivalent to linear interpolation. Image processing operations such as transformation, registration, etc. often require that interpolated data is unchanged at the at the positions where it is defined, *i.e.* that the interpolation curve passes through the input points. To perform B-spline interpolation, the coefficients (*i.e.* weights, and in general different to input datapoints) for each B-spline so that the interpolated curve passes through the input points must be found (Sankar and Ferrari, 1988). In this section we assume that input data is regularly spaced, which is the case in Cartesian images.

Let $[C_1 \dots C_N]$ be the N input values of a discrete signal $C[t]$ sampled at $t \in [t_1, t_2, \dots, t_N]$. The interpolated curve $c_n(t)$ is

$$c_n(t) = \sum_{i=1}^{N} w_i \beta^n(t - t_i) \tag{B.9}$$

The coefficients $\{w_i\}$ can be calculated by solving the linear system of N equations defined by

$$c_n(t_k) = \sum_{i=1}^{N} w_i \beta^n(t_k - t_i) = C[t_k] \quad k = 1 \dots N \tag{B.10}$$

which can be written in matrix form as

$$\begin{bmatrix} C[1] \\ \vdots \\ C[N] \end{bmatrix} = \mathbf{B} \begin{bmatrix} w_1 \\ \vdots \\ w_N \end{bmatrix} \tag{B.11}$$

where $\mathbf{B}$ is the B-spline square sampling matrix which contains the B-spline values at the points where input data is available, of $N \times N$:

$$\mathbf{B} = \begin{bmatrix} \beta^n(t_1 - t_1) & \beta^n(t_1 - t_2) & \beta^n(t_1 - t_3) & \vdots & \beta^n(t_1 - t_N) \\ \beta^n(t_2 - t_1) & \beta^n(t_2 - t_2) & \beta^n(t_2 - t_3) & \vdots & \beta^n(t_2 - t_N) \\ \vdots & \vdots & & & \vdots \\ \beta^n(t_N - t_1) & \beta^n(t_N - t_2) & \beta^n(t_N - t_3) & \vdots & \beta^n(t_N - t_N) \end{bmatrix} \tag{B.12}$$

Because the support of a B-spline is $n+1$ points for a B-spline of degree n, as shown in Fig. B.3 the matrix $\mathbf{B}$ is sparse with at most $n+1$ non zero elements per row (and per column), and has non zero elements close to the diagonal; and because B-splines are symmetric, B is symmetric. Finally, the diagonal is always nonzero, and therefore B^{-1} exists. Thus, the weights $\{w_i\}$ can be retrieved by

$$\begin{bmatrix} w_1 \\ \vdots \\ w_N \end{bmatrix} = \mathbf{B}^{-1} \begin{bmatrix} C[1] \\ \vdots \\ C[N] \end{bmatrix} \tag{B.13}$$

The result of such approach is shown in Fig. B.4 (c).

B.5 B-Spline Fitting of Scattered Data Points

The previous section has shown the simplest case of B-spline interpolation, where input data points are regularly spaced and are used as position for the B-spline control points (nodes). However, N input data points may be scattered within the input domain. In that case, these points can be fitted with a curve $c_n(t)$ expressed on a B-spline basis as described in (B.9), and the coefficients w_i can also be found by solving the linear system in (B.10) and (B.11). However, in this case, the matrix $\mathbf{B}$ is built differently. Each row of $\mathbf{B}$ represents the B-splines sampling for each one of the N input data points, *i.e.* each entry $B_{i,j}$ of $\mathbf{B}$ contains the value of the B-spline basis function centred at node j evaluated at the position of the i-th input data point. Let Δx be the space between grid nodes, p_i the position of the i-th input data point and x_j is the position of the j-th grid node, then

$$B_{i,j} = \beta^n\left(\frac{x_i - p_i}{\Delta x}\right) \tag{B.14}$$

In this case, $\mathbf{B}$ is, in general, not a square matrix. The system in (B.11) can now be solved by a LMS approach:

$$\begin{aligned} \mathbf{c} &= \mathbf{B}\mathbf{w} \longrightarrow \\ \mathbf{w} &= \min_{\mathbf{w}} \textstyle\sum \|\mathbf{B}\mathbf{w} - \mathbf{c}\|^2 = \\ \mathbf{w} &= (\mathbf{B}^\top \mathbf{B})^{-1} \mathbf{B}^\top \mathbf{c} \end{aligned} \tag{B.15}$$

This is now a optimization process which minimises the distance (in the least squares sense) between $c_n(t)$ and the input data points. Therefore, in general the fitted curve does not pass through the points unless the points between two nodes are very few (Fig. B.4 (d)).

Appendix C

Extraction of 3D Colour Doppler Data

3D Colour Doppler data was stored by the Philips iE33 echo system into DICOM files. Unfortunately these files contain the echo data hidden under proprietary tags, often compressed, and its retrieval would require knowledge about data organisation which was unavailable at the time of the thesis. This appendix describes an alternative method for extracting 3D images from the DICOM data.

C.1 Method overview

The only available software capable of reading the DICOM files was Philips QLab. This software allows to open the images and to perform some manipulations. This software also allows to export the current view as a movie file, *i.e.* a video screenshot of one slice of the volume through the cardiac cycle. A movie was generated for each slice, and these slices were then put together to build a 3D volume over time. An overview of the method is represented in Fig. C.1.

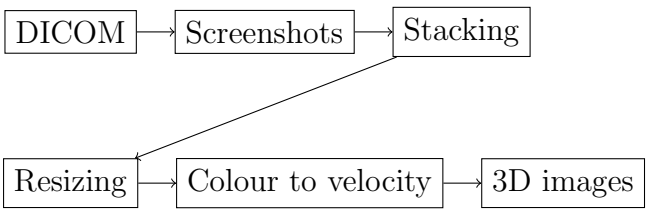

Figure C.1: Overview of data extraction.

C.2 Screenshooting

Two screenshots were taken from each 2D slice: first the B-Mode images with no colour (Fig. C.2(a)), and then the colour image with background suppression (C.2(b)). All slices were navigated with the slice selector slider. QLab reformatted data for visualisation so that the volume had 100 slices in each spatial dimension, therefore each colour Doppler image generated 100 B-Mode plus 100 colour video screenshots.

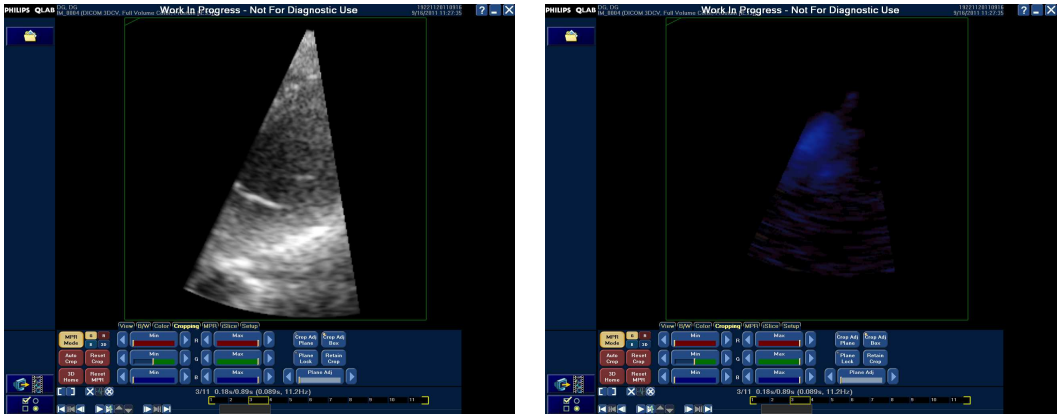

(a) Colour suppression (b) Background suppression

Figure C.2: Image screeenshots from QLab.

C.3 Volume Recomposition

For each temporal frame, 100 slices were put together to build a 3D volume. The size of the resulting volume depended on the screen size where the screenshot was done, and was typically in the order of $800 \times 600 \times 100$ voxels. This was in general different to the true image size (in the DICOM file) which was of the order of $32 \times 32 \times 350$ (in spherical coordinates). The stacked volume was therefore re-sampled to an arbitrarily chosen manageable size ($150 \times 150 \times 100$) using linear interpolation.

C.4 Volume Resizing

The screenshooting and the recomposition processes did not register any information about image size and voxel spacing. In order to retrieve the true size of the image,

a standard B-Mode image was acquired at the same position as the colour Doppler image. This B-Mode image could be extracted directly from the QLab software in a readable format (which included image size and voxel dimensions) via a patch provided by Philips Healthcare. By registering the directly extracted images to the screenshot B-Mode images (using an affine transformation) the size and voxel dimensions of the screenshot images could be determined.

C.5 Mapping Colour to Velocity

The voxels of the colour image reconstructed from screenshots have three components (red green and blue). These values were mapped to velocity values by using a transfer function obtained from a screenshot of the colour bar (Fig. C.3 left). This colour bar maps velocity values to values of red, green and blue. Similar work on conversion from colours to velocities was carried out by Bell et al. (1995), where a particular colourmap was chosen so that inverse mapping was achieved with a simple two-level boolean test. In our case, we dealt with the standard colourmap used by most clinicians (Fig. C.3(b)) which, unfortunately, was not invertible. The RGB colour map was converted to the HSV colour space (Hue, Saturation and Value, Fig. C.3(c)). From the HSV colourmap a function f could be obtained to map colour to velocity (Fig. C.3(d)) as follows:

$$f(H,V) = \begin{cases} -V & if \quad H \leq 0.35 \\ V & if \quad H > 0.35 \end{cases} \tag{C.1}$$

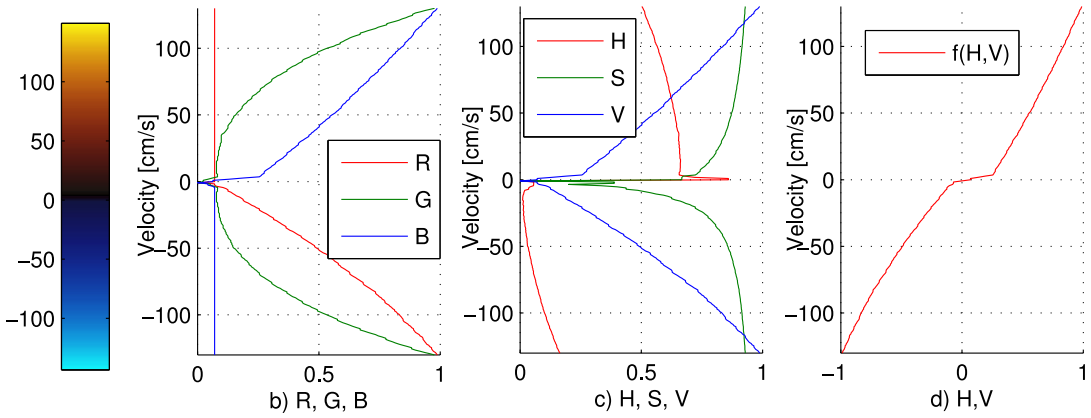

Figure C.3: Mapping colour to velocity.

C.6 Accuracy of Data Extraction

In order to assess how accurate this process was, B-Mode images (which can be exported with a QLab plug-in) were extracted with the method presented in this section and then compared to the exported version. 20 images were compared this way and results showed that the images were very similar: cross-correlation value of $r = 0.98 \pm 8 \cdot 10^{-3}$.

Appendix D

Patch Generation from Intersection Topology

This appendix describes how spherical patches are generated from a graph representing the intersection topology (c.f. Sec. 8.2.3.2).

D.1 Input Data

The input data required for building the patches is the graph $G(V, E)$ describing the topology of the intersection of the wavefronts and the segmentation, where V is the list of nodes (arc endpoints) and E is the list of edges (arcs). In addition, the list W which associates each edge E which the wavefronts on which the arc lies is needed to ensure that each patch is totally contained within a single wavefront.

D.2 Method

Let E be a $n \times 2$ matrix, where n is the number of edges in the graph and the i-th row of e contains the index to two arc endpoints connected by the i-th edge. for each edge $\mathbf{e_i} = [e_{i,1} \quad e_{i,2}]$, do the following:

1. **Find all the patches containing $\mathbf{e_i}$**, *i.e.* the paths going from $e_{i,1}$ to $e_{i,2}$ without passing by $\mathbf{e_i}$.

   This is achieved by a modified Depth-First Search (DFS) method shown in algorithm 2. The algorithm finds, for each edge $\mathbf{e_i}$ in the mesh, all the closed

loops that contain $\mathbf{e_i}$ and are on the same wavefront as $\mathbf{e_i}$.

2. **From all the loops containing $\mathbf{e_i}$, keep the one which has smaller normalised area**. The normalised area of a loop (or a patch) is calculated as the area of the patch in spherical coordinates (where it lies on a plane surface), and is given in deg^2.

Algorithm 2 Modified Depth-First Search algorithm.

Input: Intersection graph $G(V, E)$, Wavefront list W
Output: $\mathbf{p}$

```
E ← GetEdgeMatrix(G)
p = ∅                                   ▷ array containing all the patches (loops)
for each e ∈ E do
    v ← GetViews(e)                     ▷ Views of the wavefronts generating this arc
    for each v ∈ v do
        G_v ← Subgraph(G, v, e, W)      ▷ Subgraph of G restricted to a wavefront
        G'_v ← RemoveEdge(G_v, e)
        p_all = ∅
        p_current = ∅
        ModifiedDFS(G'_v, e_1, e_2, p_current, p_all)   ▷ Calculate all loops passing by e
        S ← SurfaceArea(p_all, G)
        p ← PatchOfMinimalArea(p_all, S)
        p ←append— p
    end for
end for
p ← RemoveRepeatedLoops(p)

function ModifiedDFS(G,e_1,e_2,p_current,p_all)
    p_current ←append— e_1
    if e_1 = e_2 then
        p_all ←append— p_current        ▷ Add another loop to the list
        return
    else
        n ←Neighbours(G, e_1)
        for each n ∈ n : n ∋ p_current do
            ModifiedDFSG,n,e_2,p_current,p_all
        end for
    end if
end function
```

These two steps are repeated for all the edges in E. Then, the repeated patches in $\mathbf{p}$ are removed ($\mathbf{p} \leftarrow$ `RemoveRepeatedLoops`$(\mathbf{p})$ in Alg. 2).

D.3 Performance Remarks

The proposed method for patch generation provides all the patches from a given intersection topology. Since the modified DFS searches for all loops (and not only the first one found) the complexity of the algorithm is extremely high for fine topologies. The experience acquired during experimentation suggests that it becomes impractical for more than 3 views with a radius step smaller than approximately 1/30 the maximum length of the region of interest. A solution to this would involve a study on loop search algorithms, which was out of the scope of this thesis.

Bibliography

Abbott, E.A., 1884. Flatland: A Romance of Many Dimensions. Seely & Co., 46,47 and 48 Essex street, London.

Achim, A., Bezerianos, A., Tsakalides, P., 2001. Novel bayesian multiscale method for speckle removal in medical ultrasound images. Medical Imaging, IEEE Transactions on 20, 772 –783.

Aderson, M., 1998. Multi-dimensional velocity estimation with ultrasound using spatial quadrature. IEEE Trans. Ultrason., Ferroelectr., Frq. Control 45, 852 –861.

Amundsen, B.H., Helle-Valle, T., Edvardsen, T., Torp, H., Crosby, J., Lyseggen, E., Støylen, A., Ihlen, H., Lima, J.A., Smiseth, O.A., Slørdahl, S.A., 2006. Noninvasive myocardial strain measurement by speckle tracking echocardiography: Validation against sonomicrometry and tagged magnetic resonance imaging. J. Am. Coll. Cardiol. 47, 789–793.

Anderson, B., 2007. Echocardiography: the normal examination and echocardiographic measurements. MGA Graphics, Manly, Qld., Australia. 2nd edition.

Anderson, M., 1997. Spatial quadrature: a novel technique for multi-dimensional velocity estimation, in: IEEE Ultrasonics Symposium, pp. 1233–1238.

Anderson, M., 2001. Vector flow estimator isomorphism and wall filter requirements, in: Proc. SPIE, pp. 215–226.

Anderson, M., Trahey, G., 2000. A seminar on k-space applied to medical ultrasound. Departement of Biomedical Engineering, Duke University .

Angelsen, B.A.J., 2000. Ultrasound Imaging: Waves, Signals, and Signal Processing. volume I and II. Emantec AS, Trondheim, Norway.

Arigovindan, M., Suhling, M., Jansen, C., Hunziker, P., M.Unser, 2007. Full motion and flow field recovery from echo Doppler data. IEEE Trans. Med. Imaging 26, 31–45.

Babick, F., Hinze, F., Ripperger, S., 2000. Dependence of ultrasonic attenuation on the material properties. Colloids and Surfaces A: Physicochemical and Engineering Aspects 172, 33–46.

Bamber, J., 1999. Image Formation and Image Processing in Ultrasound. http://www.m-pss.org/summer_school/1999/tuesday/file_29515.pdf. Mayneord Phillips Summer School.

Bargiggia, G.S., Tronconi, L., Sahn, D.J., Recusani, F., Raisaro, A., Servi, S.D., Valdes-Cruz, L.M., Montemartini, C., 1991. A new method for quantitation of mitral regurgitation based on color flow Doppler imaging of flow convergence proximal to regurgitant orifice. Circulation 84, 1481–1489.

Beldi, G., Bosshard, A., Hess, O.M., Althaus, U., Walpoth, B.H., 2000. Transit time flow measurement: experimental validation and comparison of three different systems. Ann. Thorac. Surg. 70(1), 212–217.

Bell, D.S., Bamber, J.C., Eckersley, R.J., 1995. Segmentation and analysis of colour Doppler images of tumour vasculature. Ultrasound Med. Biol. 21, 635–647.

Bellsham-Revell, H., Tzifa, A., Hussain, T., Valverde, I., Bell, A., Beerbaum, P., Simpson, J., Parish, V., Kutty, S., Razavi, R., et al., 2011. Dobutamine stress MRI catheterisation in patients with hypoplastic left heart syndrome after fontan completion: preliminary results. J. Cardiov. Magn. Reson. 13, 1–2.

Bjaerum, S., Martens, D., Kristoffersen, K., Torp, H., 2002. Blood motion imaging-A new technique to visualize 2D blood flow, in: Ultrasonics Symposium, 2002. Proceedings. 2002 IEEE, IEEE. pp. 1507–1510.

Bohs, L., Geiman, B., Anderson, M., Gebhart, S., Trahey, G., 2000. Speckle tracking for multi-dimensional flow estimation. Ultrasonics 38, 369 – 375.

Bohs, L.N., Friemel, B.H., McDermott, B.A., Trahey, G.E., 1993. A real time

system for quantifying and displaying two-dimensional velocities using ultrasound. Ultrasound Med. Biol. 19, 751.

Bohs, L.N., Friemel, B.H., Trahey, G.E., 1995. Experimental velocity profiles and volumetric flow via two-dimensional speckle tracking. Ultrasound Med. Biol. 21, 885–898.

Bohs, L.N., Trahey, G.E., 1991. A novel method for angle independent ultrasonic imaging of blood flow and tissue motion. IEEE Trans. Biomed. Eng. 38, 280–286.

Bonnefous, O., 1988. Measurement of the complete (3D) velocity vector of blood flows. Proc. IEEE Ultrason. Symp. , 795–799.

Bonnefous, O., Pesqué, P., 1986. Time domain formulation of pulse-Doppler ultrasound and blood velocity estimation by cross correlation. Ultrasonic Imaging 8, 73–85.

Budoff, M.J., Cohen, M.C., Garcia, M.J., Hodgson, J.M., Hundley, W.G., Lima, J.A.C., Manning, W.J., Pohost, G.M., Raggi, P.M., Rodgers, G.P., Rumberger, J.A., Taylor, A.J., 2012. ACCF/AHA clinical competence statement on cardiac imaging with computed tomography and magnetic resonance. Circulation 112, 598–617.

Burckhardt, C.B., 1978. Speckle in ultrasound B-Mode scans. IEEE Trans. Sonics Ultrason. 25, 1–6.

Cai, Q., Ahmad, M., 2012. Three-dimensional echocardiography in valvular heart disease. Echocardiography 29, 88–97.

Cape, E.G., Sung, H.W., Yoganathan, A.P., 1989. Quantitative approaches to color Doppler flow mapping of intracardiac blood flow: A review of in vitro methods. Echocardiography 6, 371–383.

Capineri, L., Scabia, M., Masotti, L., 2002. A Doppler system for dynamic vector velocity maps. Ultrasound Med. Biol. 28, 237–248.

Censor, D., 1977. Reflection mechanisms, Doppler effect, and special relativity. Proceedings of the IEEE 65, 572–572.

Chiao, R.Y., Mo, L.Y., Hall, A.L., Miller, S.C., Thomenius, K.E., 2000. B-mode blood flow (B-flow) imaging, in: Ultrasonics Symposium, 2000 IEEE, IEEE. pp. 1469–1472.

Conolly, S., Macovski, A., Pauly, J., Schenck, J., Kwong, K.K., Chesler, D.A., Hu, X., Chen, W., Patel, M., Ugurbil, K., 2000. Magnetic resonance imaging, in: Bronzino, J.D. (Ed.), The Biomedical Engineering Handbook. CRC Press, Boca Raton, FL, U.S.A. volume 1. chapter 63, 2 edition.

Corpetti, T., Heitz, D., Arroyo, G., Mémin, E., Santa-Cruz, A., 2006. Fluid experimental flow estimation based on an optical-flow scheme. Experiments in Fluids 40(1), 80–97.

Daigle, R.E., Miller, C.W., Histand, M.B., McLeod, F.D., Hokanson, D.E., 1975. Nontraumatic aortic blood flow sensing by use of an ultrasonic esophageal probe. J. Appl. Physiol. 38, 1153–1160.

Dantas, R.G., Costa, E.T., Leeman, S., 2005. Ultrasound speckle and equivalent scatterers. Ultrasonics 43, 405–420.

Dendy, P., Heaton, B., 1999. Physics for Diagnostic Radiology. Institute of Physics Publishing, Bristol, UK. 2nd edition.

Doppler, C., 1842. On the coloured light of double stars and certain other stars from the heaven. Royal Bohemian Society of Science .

Duchateau, N., De Craene, M., Piella, G., Silva, E., Doltra, A., Sitges, M., Bijnens, B.H., Frangi, A.F., 2011. A spatiotemporal statistical atlas of motion for the quantification of abnormal myocardial tissue velocities. Med. Image Anal. 15, 316–328.

Dunmire, B., Beach, K.W., Labs, K., Plett, M., Strandness, D.E., 2000. Cross-beam vector Doppler ultrasound for angle-independent velocity measurements. Ultrasound Med. Biol. 26, 1213–1235.

Edler, I., Lindstr om, K., 2004. The history of echocardiography. Ultrasound Med. Biol. 30, 1565 – 1644.

Embree, P., O'Brien, W.D., J., 1990. Volumetric blood flow via time-domain correlation: experimental verification. IEEE Trans. Ultrason., Ferroelectr., Frq. Control 37, 176–189.

Enriquez-Sarano, M., Akins, C.W., Vahanian, A., 2009. Mitral regurgitation. Lancet 373, 1382–1394.

Enriquez-Sarano, M., Jr., F.A.M., Hayes, S.N., Bailey, K.R., Tajik, A.J., Seward, J.B., 1995. Effective mitral regurgitant orifice area: Clinical use and pitfalls of the proximal isovelocity surface area method. J. Am. Coll. Cardiol. 25, 703–709.

Evangelista, A., Flachskampf, F., Lancellotti, P., Badano, L., Aguilar, R., Monaghan, M., Zamorano, J., Nihoyannopoulos, P., 2008. European association of echocardiography recommendations for standardization of performance, digital storage and reporting of echocardiographic studies. EHJ 9, 438–448.

Evans, D.H., McDicken, W.N., 2000. Doppler Ultrasound. Physics, Instrumentation and Signal Processing. Wiley-Blackwell, West Sussex, England, UK. 2nd edition.

Evans, J., Skidmore, R., Baker, J., Wells, P., 1989a. A new approach to the noninvasive measurement of cardiac output using an annular array Doppler technique–ii. practical implementation and results. Ultrasound Med. Biol. 15, 179–187.

Evans, J., Skidmore, R., Luckman, N., Wells, P., 1989b. A new approach to the noninvasive measurement of cardiac output using an annular array Doppler technique–i. theoretical considerations and ultrasonic fields. Ultrasound Med. Biol. 15, 169–178.

Fan, P., Anayiotos, A., Nanda, N., Yoganathan, A., Cape, E., 1994. Intramachine and intermachine variability in transesophageal color Doppler images of pulsatile jets. in vitro studies. Circulation 89, 2141–2149.

Faran, J.J., 1951. Sound scattering by solid cylinders and spheres. Journal of the Acoustical Society of America 23, 405–418.

Farin, G., 2002. A history of curves and surfaces in cagd. Handbook of Computer Aided Geometric Design , 1–23.

Farthing, S., Peronneau, P., 1979. Flow in the thoracic aorta. Cardiovascular Research 13, 607–620.

Fishman, A.P., 2000. The fick principle and the steady state. Am. J. Respir. Crit. Care Med. 161, 692–693.

Fitzpatrick, J.M., 2001. Detecting failure, assessing success, in: Hajnal, J.V., Hill, D.L., Hawkes, D.J. (Eds.), Medical Image Registration. CRC Press, Boca Raton, FL, U.S.A.. chapter 6, pp. 117–139.

Floater, M.S., 2007. Splines and B-splines an introduction, in: Lecture notes on Spline methods. University of Oslo.

Fontan, F., Baudet, E., 1971. Surgical repair of tricuspid atresia. Thorax 26, 240–248.

Forsberg, F., Liu, J.B., Russell, K.M., Guthrie, S.L., Goldberg, B.B., 1995. Volume flow estimation using time domain correlation and ultrasonic flowmetry. Ultrasound Med. Biol. 21, 1037–1045.

Foster, J., Smith, M., 1990. An Angle Independent Pattern Recognition Algorithm for Ultrasound Image Blood Flow Estimation. IEEE Southeastcon'90. Proceedings .

Foster, S., Embree, P., O'Brien, W.D., J., 1990. Flow velocity profile via time-domain correlation: error analysis and computer simulation. IEEE Trans. Ultrason., Ferroelectr., Frq. Control 37, 164–175.

Fox, M., 1978. Multiple crossed-beam ultrasound Doppler velocimetry. IEEE Trans. Sonics Ultrason. 25, 281–286.

Fox, M., Gardiner, W., 1988. Three-dimensional Doppler velocimetry of flow jets. Biomedical Engineering, IEEE Transactions on 35, 834–841.

Fresnel, A.J., 1816. Oeuvres. Ann. Chim. et Phys. 1, 89–129.

Fuster, V., Kelly, B. (Eds.), 2010. Promoting Cardiovascular Health in the Developing World: A Critical Challenge to Achieve Global Health. National Academies Press (US), Washington, U.S.A.. chapter 2.

Gao, H., Claus, P., Amzulescu, M., Stankovic, I., D'hooge, J., Voigt, J., 2012. How to optimize intracardiac blood flow tracking by echocardiographic particle image velocimetry? exploring the influence of data acquisition using computer-generated data sets. European Heart Journal–Cardiovascular Imaging 13, 490–499.

Garcia, D., del Álamo, J.C., Tanné, D., Yotti, R., Cortina, C., Bertrand, É., Antoranz, J.C., Pérez-David, E., Rieu, R., Fernández-Avilés, F., Bermejo, J., 2010. Two-dimensional intraventricular flow mapping by digital processing conventional color-Doppler echocardiography images. IEEE Trans. Med. Imaging 54, 1167–1178.

Gatehouse, P.D., Keegan, J., Crowe, L.A., Masood, S., Mohiaddin, R.H., Kreitner, K.F., Firmin, D.N., 2005. Applications of phase-contrast flow and velocity imaging in cardiovascular MRI. Eur. Radiol. 15(10), 2172–2184.

Gatehouse, P.D., Rolf, M.P., Graves, M.J., Hofman, M.B., Totman, J., Werner, B., Quest, R.A., Liu, Y., von Spiczak, J., Dieringer, M., Firmin, D.N., van Rossum, A., Lombardi, M., Schwitter, J., Schulz-Menger, J., Kilner, P.J., 2010. Flow measurement by cardiovascular magnetic resonance: a multi-centre multi-vendor study of background phase offset errors that can compromise the accuracy of derived regurgitant or shunt flow measurements. J. Cardiov. Magn. Reson. 12, 1–8.

Ge, S., 2012. Automated measurement of stroke volumes by real-time three-dimensional Doppler echocardiography: Coming of age? J. Am. Soc. Echocardiogr. 1, 66–67.

Ge, S., Bu, L., Zhang, H., Schelbert, E., Disterhoft, M., Li, X., Li, X., Sahn, D., Stolpen, A., Sonka, M., 2005. A real-time 3-dimensional digital Doppler method for measurement of flow rate and volume through mitral valve in children: A validation study compared with magnetic resonance imaging. J. Am. Soc. Echocardiogr. 18, 1–7.

Geva, T., 2006. Magnetic resonance imaging: Historical perspective. J. Cardiov. Magn. Reson. 8, 573–580.

Gibson, W., Cobbold, R., Johnston, K., 1994. Principles and design feasibility of a Doppler ultrasound intravascular volumetric flowmeter. IEEE Trans. Biomed. Eng. 41, 898–908.

Giese, D., Schaeffter, T., Kozerke, S., 2012. Highly undersampled phase-contrast flow measurements using compartment-based k–t principal component analysis. Magn. Reson. Med. 2, 434–443.

Gill, R., 1979. Pulsed Doppler with B-mode imaging for quantitative blood flow measurement. Ultrasound Med. Biol. 5, 223–235.

Gill, R.W., 1985. Measurement of blood flow by ultrasound: Accuracy and sources of error. Ultrasound Med. Biol. 11, 625–641.

Glenn, W.W.L., 1958. Circulatory bypass of the right side of the heart. New Engl. J. Med. 259, 117–120.

Goncalves, A., Sousa, C., de Agustín, J.A., Marcos-Alberca, P., Fernández-Golfín, C., Zamorano, J.L., 2011. Full-volume color flow quantification in mitral regurgitation. US Cardiology 8, 94–97.

Grau, V., Becher, H., Noble, J.A., 2007. Registration of multiview real-time 3-D echocardiographic sequences. IEEE Trans. Med. Imag. 26, 1154–1165.

Gupta, S., Chauhan, R., Sexana, S., 2004. Wavelet-based statistical approach for speckle reduction in medical ultrasound images. Medical and Biological Engineering and Computing 42, 189–192.

Guyton, A.C., Hall, J.E., 2006. Textbook of Medical Physiology. Elsevier, Philadelphia, Pennsilvanya, U.S.A.. 11th edition.

Hall, S.A., Brickner, M.E., Willett, D.L., Irani, W.N., Afridi, I., Grayburn, P.A., 1997. Assessment of mitral regurgitation severity by Doppler color flow mapping of the vena contracta. Circulation 95, 636–642.

Hamdan, A., Charalampos, K., Roettgen, R., Wellnhofer, E., Gebker, R., Paetsch, I., Jahnke, C., Schnackenburg, B., Tang, M., Gerds-Li, H., Fleck, E., 2009. Magnetic resonance imaging versus computed tomography for characterization of pul-

monary vein morphology before radiofrequency catheter ablation of atrial fibrillation. Am. J. Cardiol. 104, 1540 – 1546.

Hangiandreou, N.J., 2003. Physics tutorial for residents: Topics in US: B-mode US: Basic concepts and new technology. Radiographics 23, 1019 – 1033.

Hansen, K., Udesen, J., Gran, F., Jensen, J., Nielsen, M., 2008. Fast blood vector velocity imaging using ultrasound: In-vivo examples of complex blood flow in the vascular system, in: Ultrasonics Symposium, 2008. IUS 2008. IEEE, pp. 1068 –1071.

Hansen, K., Udesen, J., Thomsen, C., Jensen, J., Nielsen, M., 2009. In vivo validation of a blood vector velocity estimator with MR angiography. IEEE Trans. Ultrason., Ferroelectr., Frq. Control 56, 91–100.

Hoffman, J.I.E., Kaplan, S., 2002. The incidence of congenital heart disease. J. Am. Coll. Cardiol. 39, 1890–1900.

Hope, T.A., Markl, M., Wigstrøm, L., Alley, M.T., Miller, D.C., Herfkens, R.J., 2007. Comparison of flow patterns in ascending aortic aneurysms and volunteers using four-dimensional magnetic resonance velocity mapping. J. Magn. Reson. Imaging 26, 1471–1479.

Hoskins, P., 2010. Principles of Doppler ultrasound, in: Hoskins, P.R., Thrush, A., Martin, K., Wittingham, T. (Eds.), Diagnostic Ultrasound. Physics and Equipment. Cambridge University Press. chapter 7, pp. 84–95.

Hoskins, P., Loupas, T., McDicken, W., 1990. A comparison of three different filters for speckle reduction of Doppler spectra. Ultrasound Med. Biol. 16, 375–389.

Hoskins, P.R., Criton, A., 2010. Colour flow and tissue imaging, in: Hoskins, P.R., Thrush, A., Martin, K., Wittingham, T. (Eds.), Diagnostic Ultrasound. Physics and Equipment. Cambridge University Press. chapter 10, pp. 121–123.

Hoskins, P.R., Thrush, A., Martin, K., Wittingham, T. (Eds.), 2010. Diagnostic Ultrasound. Physics and Equipment. Cambridge University Press. 2nd edition.

Hottinger, C., Meindl, J., 1975. Unambiguous measurement of volume flow using ultrasound. Proceedings of the IEEE 63, 984–985.

Hottinger, C.F., Meindl, J.D., 1979. Blood flow measurement using the attenuation-compensated volume flowmeter. Ultrasonic Imaging 1, 1–15.

Hung, J., Lang, R., Flachskampf, F., Shernan, S.K., McCulloch, M.L., Adams, D.B., Thomas, J., Vannan, M., Ryan, T., 2007. 3D echocardiography: A review of the current status and future directions. J. Am. Soc. Echocardiogr. 20, 213–233.

Hung, J., Otsuji, Y., Handschumacher, M.D., Schwammenthal, E., Levine, R.A., 1999. Mechanism of dynamic regurgitant orifice area variation in functional mitral regurgitation: Physiologic insights from the proximal flow convergence technique. J. Am. Coll. Cardiol. 33(2), 538–545.

Huygens, C., 1690. Traité de lumière. Pierre Vander, Leyde.

Jensen, J., Munk, P., 1998. A new method for estimation of velocity vectors. IEEE Trans. Ultrason., Ferroelectr., Frq. Control 45, 837–851.

Jensen, J.A., Lacasa, I.R., 1999. Estimation of blood velocity vectors using transverse ultrasound beam focusing and cross-correlation. Proc. IEEE Ultrason. Symp. , 1493–1497.

Jensen, J.A., Nikolov, S.I., 2002. Transverse flow imaging using synthetic aperture directional beamforming. Proc. IEEE Ultrason. Symp. 2, 1523–1527.

Jensen, J.A., Nikolov, S.I., G., K.L., Pedersen, M.H., 2006. Synthetic aperture ultrasound imaging. Ultrasonics 44, e5–e15.

Jeong, J., Hussain, F., 1995. On the identification of a vortex. Journal of Fluid Mechanics 285, 69–94.

Ji, S., Roberts, D.W., Hartov, A., Paulsen, K.D., 2011. Real-time interpolation for true 3-dimensional ultrasound image volumes. J. Ultrasound. Med. 30, 243–252.

Judge, T.P., Kennedy, J.W., Bennett, L.J., Willis, R.E., Murray, J.A., Blackmon, J.R., 1971. Quantitative hemodynamic effects of heart rate in aortic regurgitation. Circulation 44, 355–367.

Kadah, Y., Farag, A., Zurada, J., Badawi, A., Youssef, A.B., 1996. Classification algorithms for quantitative tissue characterization of diffuse liver disease from ultrasound images. IEEE Trans. Med. Imaging 15, 466 –478.

Kadota, L., 1985. Theory and application of thermodilution cardiac output measurement: a review. Heart Lung. 14, 605–616.

Kasai, C., Namekawa, K., Koyano, A., Omoto, R., 1985. Real-time two-dimensional blood flow imaging using an autocorrelation technique. IEEE Trans. Sonics Ultrason. 32, 458–463.

Kilner, P.J., Yang, G.Z., Wilkes, A.J., Mohiaddin, R.H., Firmin, D.N., Yacoub, M.H., 2000. Asymmetric redirection of flow through the heart. Nature 404, 759–761.

Kim, W.Y., , Bisgaard, T., Nielsen, S.L., Poulsen, J.K., Pedersen, E.M., Hasenkam, J.M., Yoganathan, A.P., 1994. Two-dimensional mitral flow velocity profiles in pig models using epicardial Doppler echocardiography. Journal of the American College of Cardiology 24, 532–545.

Kitabatake, A., Inoue, M., Asao, M., Ito, H., Masuyama, T., Tanouchi, J., Morita, T., Hori, M., Yoshima, H., Ohnishi, K., 1984. Noninvasive evaluation of the ratio of pulmonary to systemic flow in atrial septal defect by duplex Doppler echocardiography. Circulation 69, 73–79.

Lai, W., Shirali, G., Humes, R., Pignatelli, R., 2006. Guidelines and standards for performance of a pediatric echocardiogram: a report from the task force of the pediatric council of the american society of echocardiography. J. Am. Soc. Echocardiogr. 19, 1413–1430.

Lang, R.M., Badano, L.P., Tsang, W., Adams, D.H., Agricola, E., Buck, T., Faletra, F.F., Franke, A., Hung, J., de Isla, L.P., Kamp, O., Kasprzak, J.D., Lancellotti, P., Marwick, T.H., McCulloch, M.L., Monaghan, M.J., Nihoyannopoulos, P., Pandian, N.G., Pellikka, P.A., Pepi, M., Roberson, D.A., Shernan, S.K., Shirali, G.S., Sugeng, L., Cate, F.J.T., Vannan, M.A., Zamorano, J.L., Zoghbi, W.A., 2012. EAE/ASE recommendations for image acquisition and display using three-dimensional echocardiography. J. Am. Soc. Echocardiogr. 25, 3–46.

Laniado, S., Yellin, E., Yoran, C., Strom, J., Hori, M., Gabbay, S., Terdiman, R., Frater, R., 1982. Physiologic mechanisms in aortic insufficiency. i. the effect of

changing heart rate on flow dynamics. ii. determinants of austin flint murmur. Circulation 66, 226–235.

Laven, P., 2010. Separating diffraction from scattering: the million-dollar challenge. J. Nano. 4, 041593–041593–18.

Lee, S., Wolberg, G., Shin, S., 1997. Scattered data interpolation with multilevel b-splines. Visualization and Computer Graphics, IEEE Transactions on 3, 228–244.

de Leval, M.R., 2005. The Fontan circulation: a challenge to William Harvey? Nature Clinical Practice Cardiovascular Medicine 2, 202–208.

Li, J., Li, X., Mori, Y., Rusk, R.A., Lee, J.S., Davies, C.H., Hashimoto, I., El-Sedfy, G.O.M., Li, X.N., Sahn, D.J., 2001. Quantification of flow volume with a new digital three-dimensional color Doppler flow approach: an in vitro study. J. Ultrasound. Med. 20, 1303–1311.

Liang, Z.P., 1996. A model-based method for phase unwrapping 15, 893–897.

Lizzi, F.L., Feleppa, E.J., 2000. Image processing and pre-processing for medical ultrasound. 29th Applied Imagery Pattern Recognition Workshop .

Long, Q., Xu, X., Ramnarine, K., Hoskins, P., 2001. Numerical investigation of physiologically realistic pulsatile flow through arterial stenosis. Journal of Biomechanics 34, 1229 – 1242.

Lovato, L., Giardini, A., La Palombara, C., Russo, V., Gostoli, V., Gargiulo, G., Picchio, F., Fattori, R., 2007. Role and effectiveness of cardiovascular magnetic resonance in the diagnosis, preoperative evaluation and follow-up of patients with congenital heart diseases. La radiologia medica 112, 660–680.

Lovstakken, L., 2007. Signal Processing in Diagnostic Ultrasound: Algorithms for Real-time Estimation and Visualization of Blood Flow Velocity. Ph.D. thesis. Norwegian University of Science and Technology.

Machado, A., 1921. Campos de Castilla.

Mahle, W.T., Spray, T.L., Wernovsky, G., Gaynor, J.W., Clark, B.J., 2000. Survival after reconstructive surgery for hypoplastic left heart syndrome : A 15-year experience from a single institution. Circulation 102, III–136–III–141.

Maniatis, T.A., Cobbold, R.S., Johnston, K., 1994. Two-dimensional velocity reconstruction strategies for color flow Doppler ultrasound images. Ultrasound Med. Biol. 20, 137–145.

Marion, A., Aoudi, W., Basarab, A., Delachartre, P., Vray, D., 2010. A comparative study of four vector velocity estimation methods applied to flow imaging. Physics Procedia 3, 225–233.

Marion, A., Vray, D., 2009. Spatiotemporal filtering of sequences of ultrasound images to estimate a dense field of velocities. Pattern Recognition 42, 2989–2997.

Markl, M., Harloff, A., Bley, T.A., Zaitsev, M., Jung, B., Weigang, E., Langer, M., Hennig, J., Frydrychowicz, A., 2007. Time-resolved 3D MR velocity mapping at 3T: Improved navigator-gated assessment of vascular anatomy and blood flow. J. Magn. Reson. Imaging 25, 824–831.

Markl, M., Kilner, P.J., Ebbers, T., 2011. Comprehensive 4D velocity mapping of the heart and great vessels by cardiovascular magnetic resonance. J. Cardiov. Magn. Reson. 13, 1–22.

Martin, K., 2010. Properties, limitations and artefacts of B-mode images, in: Hoskins, P.R., Thrush, A., Martin, K., Wittingham, T. (Eds.), Diagnostic Ultrasound. Physics and Equipment. Cambridge University Press. chapter 5, pp. 64–74.

Martin, K., Ramnarine, K., 2010. Physics, in: Hoskins, P.R., Thrush, A., Martin, K., Wittingham, T. (Eds.), Diagnostic Ultrasound. Physics and Equipment. Cambridge University Press. chapter 10, pp. 121–123.

McRobbie, D.W., Moore, E.A., Graves, M.J., Prince, M.R., 2006. MRI from Picture to Proton. Cambridge University Press. 2 edition.

Meunier, J., Bertrand, M., 1995. Ultrasonic texture motion analysis: theory and simulation. IEEE Trans. Med. Imaging 14, 293–300.

Migliavacca, F., Yates, R., Pennati, G., Dubini, G., Fumero, R., de Leval, M.R., 2000. Calculating blood flow from Doppler measurements in the systemic-to-

pulmonary artery shunt after the norwood operation: a method based on computational fluid dynamics. Ultrasound Med. Biol. 26, 209 – 219.

Moran, P.R., 1982. A flow velocity zeugmatographic interlace for NMR imaging in humans. Magn. Reson. Med. 1, 197 – 203.

Mori, Y., R., R.A., Jones, M., Li, X.N., Irvineand, T., Zetts, A.D., Sahn, D.J., 2002. A new dynamic three-dimensional digital color Doppler method for quantification of pulmonary regurgitation: Validation study in an animal model. J. Am. Coll. Cardiol. 40, 1179–1185.

Morsy, A., Von Ramm, O., 1999. FLASH correlation: a new method for 3-D ultrasound tissue motion tracking and blood velocity estimation. IEEE Trans. Ultrason., Ferroelectr., Frq. Control 46, 728 –736.

Möser, M., 2009. Engineering Acoustics: An Introduction to Noise Control. Berlin, Heidelberg: Springer-Verlag Berlin Heidelberg. 2nd edition.

Mulet-Parada, M., Noble, J., 2000. 2D+T acoustic boundary detection in echocardiography. Med. Image Anal. 4, 21 – 30.

Muth, S., Dort, S., Sebag, I.A., Blais, M.J., Garcia, D., 2011. Unsupervised dealiasing and denoising of color-Doppler data. Med. Image Anal. 15, 577–588.

Newhouse, V.L., Censor, D., T. Vontz, J.A.C., Goldeberg, B.B., 1987. Ultrasound Doppler probing of flows transverse with respect to beam axis. IEEE Trans. Biomed. Eng. 34, 779–788.

Ng, A., Swanevelder, J., 2011. Resolution in ultrasound imaging. Continuing Education in Anaesthesia, Critical Care & Pain 11, 186–192.

Nichols, W.W., O'Rouke, M.F., 1997. McDonald's Blood Flow in Arteries. Oxford University Press. 4th edition edition.

Niita, N., Shiina, T., 1998. Real-time three-dimensional velocity vector measurement using the Weighted Phase Gradient method. Japanese journal of applied physics. Pt. 1, Regular papers & short notes 37, 3058–3063.

Nikolov, S., Jensen, J., 2003. In-vivo synthetic aperture flow imaging in medical ultrasound. IEEE Trans. Ultrason., Ferroelectr., Frq. Control 50, 848–856.

Nikolov, S.I., Jensen, J.A., 2001. Velocity estimation using synthetic aperture imaging. Proc. IEEE Ultrason. Symp. , 1409–1412.

Nock, L., Trahey, G., 1992. Synthetic receive aperture imaging with phase correction for motion and for tissue inhomogeneities. i. basic principles. IEEE Trans. Ultrason., Ferroelectr., Frq. Control 39, 489–495.

Noonan, J.A., Nadas, A.S., 1958. The hypoplastic left heart syndrome; an analysis of 101 cases. Pediatr. Clin. North Am. 5, 1029–56.

Nordsletten, D., McCormick, M., Kilner, P., Hunter, P., Kay, D., Smith, N., 2010. Fluid–solid coupling for the investigation of diastolic and systolic human left ventricular function. International Journal for Numerical Methods in Biomedical Engineering 27, 1017–1039.

Norwood, W.I., Lang, P., Hansen, D.D., 1983. Physiologic repair of aortic atresia – hypoplastic left heart syndrome. New Engl. J. Med. 308, 23–26.

Oh, J.K., Seward, J.B., Tajik, A.J., 2007. The Echo Manual. Lippincott Williams & Wilkins, Rochester, MN, U.S.A.. 3rd edition.

Ohtsuki, S., Tanaka, M., 2006. The flow velocity distribution from the Doppler information on a plane in three-dimensional flow. Journal of visualization 9, 69–82.

Omoto, R., Yokote, Y., Takamoto, S., Kyo, S., Ueda, K., Asano, H., Namekawa, K., Kasai, C., Kondo, Y., Koyano, A., et al., 1984. The development of real-time two-dimensional doppler echocardiography and its clinical significance in acquired valvular diseases. with special reference to the evaluation of valvular regurgitation. Japanese heart journal 25, 325.

Overbeck, J.R., Beach, K.W., jr., D.S., 1992. Vector Doppler: Accurate measurement of blood velocity in two dimensions. Ultrasound Med. Biol. 18, 19–31.

Pastorelli, A., Torricelli, G., Scabia, M., Biagi, E., Masotti, L., 2008. A real-time 2-D vector Doppler system for clinical experimentation. IEEE Trans. Med. Imaging 27, 1515–1524.

Paulsen, P.K., Hasenkam, J.M., 1983. Three-dimensional visualization of velocity profiles in the ascending aorta in dogs, measured with a hot-film anemometer. Journal of Biomechanics 16, 201–210.

Pedersen, H., Kozerke, S., Ringgaard, S., Nehrke, K., Kim, W.Y., 2009. k-t PCA: Temporally constrained k-t BLAST reconstruction using principal component analysis. Magn. Reson. Med. 62, 706–716.

Pemberton, J., Hui, L., Young, M., Li, X., Kenny, A., Sahn, D.J., 2005. Accuracy of 3-dimensional color Doppler-derived flow volumes with increasing image depth. J. Ultrasound. Med. 24, 1109–115.

Péronneau, P., Bournat, J.P., Bugnon, A., Barbet, A., Xhaard, M., 1974. Theoretical and practical aspects of pulsed Doppler flowmetry: real-time application to the measure of instantaneous velocity profiles in vitro and in vivo. Cardiovascular Applicationsof Ultrasound , 66–84.

Phillips, P.J., Kadi, A.P., von Ramm, O.T., 1995. Feasibility study for a two-dimensional diagnostic ultrasound velocity mapping system. Ultrasound Med. Biol. 21, 217–229.

Picot, P., Embree, P., 1994. Quantitative volume flow estimation using velocity profiles. IEEE Trans. Ultrason., Ferroelectr., Frq. Control 41, 340–345.

Poulsen, J., Kim, W., 1996a. Measurement of volumetric flow with no angle correction using multiplanar pulsed Doppler ultrasound. IEEE Trans. Biomed. Eng. 43, 589–599.

Poulsen, J., Kim, W., 1996b. Measurement of volumetric flow with no angle correction using multiplanar pulsed Doppler ultrasound. IEEE Trans. Biomed. Eng. 43, 589–599.

Rabben, S.I., 2011. Technical principles of transthoracic three-dimensional echocardiography, in: Textbook of Real-Time Three Dimensional Echocardiography. Springer-Verlag. chapter 2, 1st edition. pp. 9–24.

Rao, N., Mehra, S., Zhu, H., 1990. Ultrasound speckle statistics variations with imaging systems impulse response, in: Ultrasonics Symposium, 1990. Proceedings., IEEE 1990, pp. 1435 –1440 vol.3.

Rhode, K., Lambrou, T., Hawkes, D., Seifalian, A., 2005. Novel approaches to the measurement of arterial blood flow from dynamic digital x-ray images. Medical Imaging, IEEE Transactions on 24, 500 –513.

Ricci, S., Diciotti, S., Francalanci, L., Tortoli, P., 2009. Accuracy and reproducibility of a novel dual-beam vector doppler method. Ultrasound Med. Biol. 35, 829 – 838.

Richter, Y., Edelman, E.R., 2006. Cardiology is flow. Circulation 113, 2679–2682.

Riva, C.E., Feke, G.T., Ben-Sira, I., 1978. Fluorescein dye-dilution technique and retinal circulation. Am. J. Physiol. 234, H315–H322.

Robbins, J.M., Bird, T.M., Tilford, J.M., Cleves, M.A., Hobbs, C.A., Grosse, S.D., Correa, A., 2003. Hospital stays, hospital charges, and in-hospital deaths among infants with selected birth defects – united states. MMWR Morb Mortal Wkly Rep 56, 25–29.

Rodriguez, L., Thomas, J.D., Monterroso, V., Weyman, A.E., Harrigan, P., Mueller, L.N., Levine, R.A., 1993. Validation of the proximal flow convergence method. calculation of orifice area in patients with mitral stenosis. Circulation 88, 1157–1165.

Roger, V.L., Go, A.S., Lloyd-Jones, D.M., Adams, R.J., Berry, J.D., Brown, T.M., Carnethon, M.R., Dai, S., de Simone, G., Ford, E.S., Fox, C.S., Fullerton, H.J., Gillespie, C., Greenlund, K.J., Hailpern, S.M., Heit, J.A., Ho, P.M., Howard, V.J., Kissela, B.M., Kittner, S.J., Lackland, D.T., Lichtman, J.H., Lisabeth, L.D., Makuc, D.M., Marcus, G.M., Marelli, A., Matchar, D.B., McDermott, M.M., Meigs, J.B., Moy, C.S., Mozaffarian, D., Mussolino, M.E., Nichol, G., Paynter,

N.P., Rosamond, W.D., Sorlie, P.D., Stafford, R.S., Turan, T.N., Turner, M.B., Wong, N.D., Wylie-Rosett, J., 2011. Heart disease and stroke statistics – 2011 update. Circulation 123, e18–e209.

Roger, V.L., Go, A.S., Lloyd-Jones, D.M., Benjamin, E.J., Berry, J.D., Borden, W.B., Bravata, D.M., Dai, S., Ford, E.S., Fox, C.S., et al., 2012. Heart disease and stroke statistics –2012 update a report from the american heart association. Circulation 125, e2–e220.

Rojo-Álvarez, J.L., Bermejo, J., Rodríguez-González, A.B., Martínez-Fernández, A., Yotti, R., García-Fernández, M.A., Antoranz, J.C., 2007. Impact of image spatial, temporal, and velocity resolutions on cardiovascular indices derived from color-Doppler echocardiography. Med. Image Anal. 11, 513–525.

Sanders, S.P., Yeager, S., Williams, R.G., 1983. Measurement of systemic and pulmonary blood flow and QP/QS ratio using Doppler and two-dimensional echocardiography. Am. J. Cardiol. 51, 952–956.

Sankar, P., Ferrari, L., 1988. Simple algorithms and architectures for B-spline interpolation. Pattern Analysis and Machine Intelligence, IEEE Transactions on 10, 271–276.

Scabia, M., Calzolai, M., Capineri, L., Masotti, L., Fort, A., 2000. A real-time two-dimensional pulsed-wave Doppler system. Ultrasound Med. Biol. 26, 121–131.

Schnabel, J., Rueckert, D., Quist, M., Blackall, J., Castellano-Smith, A., Hartkens, T., Penney, G., Hall, W., Liu, H., Truwit, C., et al., 2001. A generic framework for non-rigid registration based on non-uniform multi-level free-form deformations, in: Medical Image Computing and Computer-Assisted Intervention–MICCAI 2001, Springer. pp. 573–581.

Schumacher, M., Yin, L., Swaid, S., Oldenburger, J., Gilsbach, J.M., Hetzel, A., 2001. Intravascular ultrasound Doppler measurement of blood flow velocity. J. Neuroimaging 11, 248–252.

Segadal, L., Matre, K., 1987. Blood velocity distribution in the human ascending aorta. Circulation 76, 90–100.

Sengupta, P.P., Pedrizzetti, G., Kilner, P.J., Kheradvar, A., Ebbers, T., Tonti, G., Fraser, A.G., Narula, J., 2012. Emerging trends in CV flow visualization. J. Am. Coll. Cardiol. 5, 305–316.

Shahin, A., Ménard, M., Eboueya, M., 2000. Cooperation of fuzzy segmentation operators for correction aliasing phenomenon in 3D color Doppler imaging. Artificial Intelligence in Medicine 19, 121–154.

Shannon, C.E., 1949. Communication in the presence of noise. Proc. Institute of Radio Engineers 37, 10–21.

Shi, W., Zhuang, X., Pizarro, L., Bai, W., Wang, H., Tung, K.P., Edwards, P., Rueckert, D., 2012. Registration using sparse free-form deformations. Medical Imaging Computing and Computer-Assisted Intervention—MICCAI '12 , 659–666.

Shpilfoygel, S.D., Close, R.A., Valentino, D.J., Duckwiler, G.R., 2000. X-ray videodensitometric methods for blood flow and velocity measurement: A critical review of literature. Med. Phys. 27(9), 2008–2023.

Simpson, I., Valdes-Cruz, L., Yoganathan, A., Sung, H., Jimoh, A., Sahn, D., 1989. Spatial velocity distribution and acceleration in serial subvalve tunnel and valvular obstructions: An in vitro study using Doppler color flow mapping. J. Am. Coll. Cardiol. 13(1), 241–248.

Sloth, E., Houlind, K.C., Oyre, S., Kim, W.Y., Pedersen, E.M., Jórgensen, H.S., Hasenkam, J.M., 1994. Three-dimensional visualization of velocity profiles in the human main pulmonary artery with magnetic resonance phase-velocity mapping. American Heart Journal 128, 113–1138.

Stadlbauer, A., van der Riet, W., Globits, S., Crelier, G., Salomonowitz, E., 2009. Accelerated phase-contrast MR imaging: comparison of k-t BLAST with SENSE and Doppler ultrasound for velocity and flow measurements in the aorta. J. Magn. Reson. Imaging 29, 817–824.

Struyk, P., Pijpers, L., Wladimiroff, J., Lotgering, F., Tonge, M., Bom, N., 1985. The time-distance recorder as a means of improving the accuracy of fetal blood flow measurements. Ultrasound Med. Biol. 11, 71–77.

Sun, Y., Aska, P., Janerot-Sjöberga, B., Eidenvalla, L., Loyda, D., Wrannea, B., 1995. Estimation of volume flow rate by surface integration of velocity vectors from color Doppler images. J. Am. Soc. Echocardiogr. 8, 904–914.

Swillens, A., Segers, P., Torp, H., Lóvstakken, L., 2010. Two-dimensional blood velocity estimation with ultrasound: speckle tracking versus crossed-beam vector Doppler based on flow simulations in a carotid bifurcation model. IEEE Trans. Ultrason., Ferroelectr., Frq. Control 57, 327–339.

Szabo, T.L., 1998. Transducer Arrays for Medical Ultrasound Imaging. J. Ultrasound. Med. , 91–111.

Tanaka, M., Sakamoto, T., Sugawara, S., Nakajima, H., Kameyama, T., Katahira, Y., Ohtsuki, S., Kanai, H., 2010. Spiral systolic blood flow in the ascending aorta and aortic arch analyzed by echo-dynamography. Journal of Cardiology 56, 97–110.

Tanaka, M., Sakamoto, T., Sugawara, S., Nakajima, H., Kameyama, T., Tabuchi, H., Katahira, Y., Ohtsuki, S., Kanai, H., 2011. Physiological basis and clinical significance of left ventricular suction studied using echo-dynamography. Journal of Cardiology 58, 232–244.

Tanter, M., Bercoff, J., Sandrin, L., Fink, M., 2002. Ultrafast compound imaging for 2-D motion vector estimation: application to transient elastography. IEEE Trans. Ultrason., Ferroelectr., Frq. Control 49, 1363–1374.

Tay, P., Garson, C., Acton, S., Hossack, J., 2010. Ultrasound despeckling for contrast enhancement. IEEE Trans. Image Processing 19, 1847 –1860.

Thavendiranathan, P., Liu, S., Datta, S., Walls, M., Nitinunu, A., Van Houten, T., Tomson, N., Vidmar, L., Georgescu, B., Wang, Y., Srinivasan, S., De Michelis, N., Raman, S., Ryan, T., Vannan, M., 2012. Automated quantification of mitral inflow and aortic outflow stroke volumes by three-dimensional real-time volume color-flow Doppler transthoracic echocardiography: comparison with pulsed-wave doppler and cardiac magnetic resonance imaging. J. Am. Soc. Echocardiogr. 1, 56–65.

Thijssen, J.M., 2003. Ultrasonic speckle formation, analysis and processing applied to tissue characterization. Pattern Recognition Letters 24, 659–675.

Thrush, A., 2010. Spectral Doppler ultrasound, in: Hoskins, P.R., Thrush, A., Martin, K., Wittingham, T. (Eds.), Diagnostic Ultrasound. Physics and Equipment. Cambridge University Press. chapter 9, pp. 105–115.

Torp, H., Kristoffersen, K., Angelsen, B.A.J., 1994. Autocorrelation techniques in color flow imaging: Signal model and statistical properties of the autocorrelation estimates. IEEE Trans. Ultrason., Ferroelectr., Frq. Control 41, 604–612.

Tortoli, P., Bambi, G., Ricci, S., 2006. Accurate Doppler angle estimation for vector flow measurements. IEEE Trans. Ultrason., Ferroelectr., Frq. Control 53, 1425–1431.

Trahey, G., Allison, J.W., Ramm, O.T.V., 1987. Angle independent ultrasonic detection of blood flow. IEEE Trans. Biomed. Eng. 34, 965–967.

Tsai-Goodman, B., Geva, T., Odegard, K.C., Sena, L.M., Powell, A.J., 2004. Clinical role, accuracy, and technical aspects of cardiovascular magnetic resonance imaging in infants. Am. J. Cardiol. 94, 69 – 74.

Tsujino, H., Jones, M., Shiota, T., Qin, J.X., Greenberg, N.L., Cardon, L.A., Morehead, A.J., Zetts, A.D., Travaglini, A., Bauer, F., Panza, J.A., Thomas, J.D., 2001. Real-time three-dimensional color Doppler echocardiography for characterizing the spatial velocity distribution and quantifying the peak flow rate in the left ventricular outflow tract. Ultrasound Med. Biol. 27, 69 – 74.

Turnbull, H., Scott, J., Hall, A. (Eds.), 1959. The Correspondence of Isaac Newton. volume I. Cambridge University Press.

Tustison, N., Gee, J., 2006. Generalized n-D C k B-spline scattered data approximation with confidence values. Medical Imaging and Augmented Reality , 76–83.

Tuthill, T., Sperry, R., Parker, K., 1988. Deviations from Rayleigh statistics in ultrasonic speckle. Ultrasonic Imaging 10, 81 – 89.

Udesen, J., Gran, F., Hansen, K., Jensen, J., Thomsen, C., Nielsen, M., 2008. High frame-rate blood vector velocity imaging using plane waves: Simulations

and preliminary experiments. IEEE Trans. Ultrason., Ferroelectr., Frq. Control 55, 1729–1743.

Udesen, J., Jensen, J.A., 2006. Investigation of transverse oscillation method. IEEE Trans. Ultrason., Ferroelectr., Frq. Control 53, 959–971.

Uejima, T., Koike, A., Sawada, H., Aizawa, T., Ohtsuki, S., Tanaka, M., Furukawa, T., Fraser, A.G., 2010. A new echocardiographic method for identifying vortex flow in the left ventricle: Numerical validation. Ultrasound Med. Biol. 36, 772 – 788.

Unser, M., 1999. Splines: a perfect fit for signal and image processing. IEEE Signal Proc. Mag. 16, 22–38.

Uribe, S., Beerbaum, P., Sørensen, T.S., Rasmusson, A., Razavi, R., Schaeffter, T., 2009. Four-dimensional (4D) flow of the whole heart and great vessels using real-time respiratory self-gating. Magn. Reson. Med. 62, 984–992.

Utsunomiya, T., Ogawa, T., Tang, H.A., Doshi, R., Patel, D., Quan, M., Henry, W.L., Gardin, J.M., 1991. Doppler color flow mapping of the proximal isovelocity surface area: a new method for measuring volume flow rate across a narrowed orifice. J. Am. Soc. Echocardiogr. 4, 338–348.

Vargas-Barron, J., Sahn, D.J., Valdes-Cruz, L.M., Lima, C.O., Goldberg, S.J., Allen, E.G.A.D., 1984. Clinical utility of two-dimensional Doppler echocardiographic techniques for estimating pulmonary to systemic blood flow ratios in children with left to right shunting atrial septal defect, ventricular septal defect or patent ductus arteriosus. J. Am. Coll. Cardiol. 3, 169–178.

de Vecchi, A., Nordsletten, D.A., Remme, E.W., Bellsham-Revell, H., Greil, G., Simpson, J.M., Razavi, R., Smith, N.P., 2012. Inflow typology and ventricular geometry determine efficiency of filling in the Hypoplastic Left Heart. Annals of Thoracic Surgery 94, 1562–1569.

Walker, W., Trahey, G., 1995. A fundamental limit on delay estimation using partially correlated speckle signals. Ultrasonics, Ferroelectrics and Frequency Control, IEEE Transactions on 42, 301–308.

Wei-qi, W., Lin-xin, Y., 1982. A double beam Doppler ultrasound method for quantitative blood flow velocity measurement. Ultrasound Med. Biol. 8, 421–425.

Weisel, R.D., Berger, R.L., Hechtman, H.B., 1975. Measurement of cardiac output by thermodilution. New Engl. J. Med. , 682–684.

Wells, P., 1975. Absorption and dispersion of ultrasound in biological tissue. Ultrasound Med. Biol. 1, 369 – 376.

Wells, P.N.T., 1998. Current Doppler Technology and Techniques. J. Ultrasound. Med. , 113–128.

Wells, P.N.T., 2006. Ultrasound Imaging. Phys. Med. Biol. 51, R83 – R98.

Whittingham, T., Martin, K., 2010. Transducers and beam-forming, in: Hoskins, P.R., Thrush, A., Martin, K., Wittingham, T. (Eds.), Diagnostic Ultrasound. Physics and Equipment. Cambridge University Press. chapter 3, pp. 23–46.

Wigstrom, L., Sjoqvist, L., Wranne, B., 1996. Temporally resolved 3D phase-contrast imaging. Magn. Reson. Med. 36, 800–803.

Wilkinson, J.L., 2001. Haemodynamic calculations in the catheter laboratory. Heart 85, 113–120.

Wilson, R.F., Marcus, M.L., White, C.W., 1987. Prediction of the physiologic significance of coronary arterial lesions by quantitative lesion geometry in patients with limited coronary artery disease. Circulation 75, 723–732.

Xu, S., Ermert, H., Hammentgen, R., 1991. Phased array pulse Doppler tomography. Proc. IEEE Ultras. Symp. , 1273–1276.

Yamani, H., Cai, Q., Ahmad, M., 2012. Three-dimensional echocardiography in evaluation of left ventricular indices. Echocardiography 29, 66–67.

Yao, C., Simpson, J., Schaeffter, T., Penney, G., 2011. Multi-view 3D echocardiography compounding based on feature consistency. Phys. Med. Biol. 56, 6109–6128.

Yoganathan, A.P., Lemmon, J.D., Ellis, J.T., 2007. Biomechanics. Principles and Applications. CRC Press. chapter 9: Heart Valve Dynamics. pp. 184–208.

Zemp, R., Abbey, C., Insana, M., 2003. Linear system models for ultrasonic imaging: application to signal statistics. Ultrasonics, Ferroelectrics and Frequency Control, IEEE Transactions on 50, 642 –654.

Zhang, H., Liu, L., Chen, L., Ma, N., Zhou, L., Liu, Y., Li, Z., Liu, C., Hou, R., Zhu, S., 2013. The evolution of intraventricular vortex during ejection studied by using vector flow mapping. Echocardiography 30, 27–36.

Zoghbi, W.A., Enriquez-Sarano, M., Foster, E., Grayburn, P.A., Kraft, C.D., Levine, R.A., Nihoyannopoulos, P., Otto, C.M., Quinones, M.A., Rakowski, H., Stewart, W.J., Waggoner, A., Weissman, N.J., 2003. American society of echocardiography: recommendations for evaluation of the severity of native valvular regurgitation with two-dimensional and Doppler echocardiography. J. Am. Soc. Echocardiogr. 16, 777–802.

Publications

2013

Peressutti, D., Penney, G.P., James Housden, R., Kolbitsch, C., **Gomez, A.**, Rijkhorst, E.J., Barratt, D.C., Rhode, K.S., King, A.P., 2013. A novel bayesian respiratory motion model to estimate and resolve uncertainty in image-guided cardiac interventions. Med. Image Anal. 17, 488–502.

Gomez A., Pushparajah, K., Simpson, J., Schaeffter, T., Penney, G., 2013. Accurate, highly time resolved flow rate and volume quantification with multiview 3D colour Doppler echo. 47th Annual Meeting of the Association for European Paediatric and Congenital Cardiology (AEPC) .

Gomez, A., Pushparajah, K., Simpson, J.M., Giese, D., Schaeffter, T., Penney, G., 2013a. A sensitivity analysis on 3D velocity reconstruction from multiple registered echo Doppler views. Med. Image Anal. 17, 616–631.

Gomez, A., Vecchi, A.D., Pushparajah, K., Simpson, J., Giese, D., Schaeffter, T., Penney, G., 2013b. 3D intraventricular flow mapping from colour Doppler images and wall motion, in: Medical Image Computing and Computer-Assisted Intervention–MICCAI, pp. 476–483.

2012

Gómez, A, Giese, D., Pushparajah, K., Simpson, J., Schaeffter, T., Penney, G., 2012a. Quantification of transvalvular flow through composite Gaussian surfaces from temporally interleaved multi-view 3D colour Doppler images, in: Proceedings of MICCAI STACOM 2012.

Gómez, A, Pushparajah, K., Simpson, J., Schaeffter, T., Penney, G., 2012b. Quantification of intracardiac flow through composite Gaussian surfaces from temporally interleaved 3D colour Doppler, in: Proceedings of Bioengineering12.

Gómez, A, Pushparajah, K., Simpson, J., Schaeffter, T., Penney, G., 2012c. Three dimensional intracardiac blood velocity and flow from compounded 3D echo colour Doppler images. Eur Assoc Cardiovasc Imaging 13, i3 (Young Investigator Award – euroEcho 2012).

2011

Gómez, A, Simpson, J., C., Y., Schaeffter, T., Penney, G., 2011. 3D flow reconstruction from multiple registered echo Doppler views, in: Biomedical Imaging: From Nano to Macro, 2011 IEEE International Symposium on, pp. 879 –882.

2010

Gómez, A., Simpson, J., Yao, C., Schaeffter, T., Penney, G., 2010. Reconstruction of 3D Flow from Multiple Echo Doppler Views. Proc. Medical Image Understanding and Analysis '10 .